

DISS. ETH NO. 27108

Advancing CO₂ Capture and Conversion by Improving CO₂ Sorbents and Dry Reforming Catalysts

A thesis submitted to attain the degree of
DOCTOR OF SCIENCES of ETH ZÜRICH
(Dr. sc. ETH Zürich)

presented by

ALEXEY KURLOV

M.Sc. Materials Science, ETH Zürich

born on 16.01.1990

citizen of the Russian Federation

accepted on the recommendation of

Prof. Dr. Christoph R. Müller

Prof. Dr. Michel W. Barsoum

Prof. Dr. Maria Lukatskaya

2020

Acknowledgments

First and most importantly, I would like to thank my supervisor Prof. Dr. Christoph R. Müller for not only giving me the opportunity to do my PhD in the LESE group, but also his continuous support, encouragements and constructive criticism throughout my PhD.

I am grateful to Prof. Dr. Michel W. Barsoum (Drexel University) and Prof. Dr. Maria Lukatskaya (ETH Zürich) for accepting to be co-referees on this thesis and for carefully reading the manuscript.

I would like to express my gratitude to the European Synchrotron Radiation Facility (ESRF, Grenoble, France) and the Swiss Light Source (SLS, PSI, Villigen, Switzerland) for the provision of multiple beamtimes. Special thanks go to Dr. Herman Emerich, Dr. Dragos Stoian and Dr. Wouter van Beek from the Swiss-Norwegian Beamlines (ESRF) and Dr. Thomas Huthwelker from the Phoenix beamline (SLS) for their support during the experiments.

I am deeply grateful to all our collaborators, Javier Pérez-Ramírez, Sharon J. Mitchell, Dmitry Lebedev, Christopher P. Gordon, André R. Studart, Xing Huang and Aleix Comas-Vives for their help and valuable discussion.

I am greatly indebted to the help of my colleagues in the Laboratory of Energy Science and Engineering. Special thanks go to Dr. Agnieszka Kierzkowska, Dr. Paula Macarena Abdala, and Dr. Alexey Fedorov. To Aga for training me during my first year of my PhD, allowing the labs to run smoothly and her continuous support. Paula is acknowledged for her kind assistance and superb input on X-ray absorption and diffraction measurements and data analysis. Alexey is gratefully acknowledged for his tremendous assistance, guidance and valuable discussions during the last 3 years of my PhD. Many thanks to all my past and present lab members: Abera, Alessandro, Alex B., Alex P., Ali, Andac, Athanasia, Annelies, Awais, Cristina, Chris, Christopher, Davood, Debajeet, Denis, Elena, Evgenia D., Evgenia K., Felix, Giancarlo, Guang, Hui, James, Jens, Jian, Manouchehr, Margarita, Max, Meng, Nicholas, Nora, Pedro, Qasim, Sena, Sergey, Stephan, Sung Min, Tejansh, Tian, Yi-Hsuan, Yong and Zixuan. I am grateful for the good working atmosphere we all created, for all the collaborations, discussions and support with and from every one of you and, of course, for all the fun activities we had.

The research work presented in this dissertation was funded by ETH Zurich and the Swiss Office of Energy (BFE) and I am very grateful to these bodies for their financial support.

I would like to thank my beloved parents, sisters and grandparents for their love and support they have shown me through all the years that I have been away from home for my studies. Finally, my deepest gratefulness goes to my wife, Elizaveta. Thanks a lot for your love, support and patience throughout this challenging journey.

Abstract

The ever-rising emissions of CO₂ from the combustion of fossil fuels result in a constant increase of the CO₂ concentration in the atmosphere that in turn is linked to global warming. Therefore, the development of technologies that allow for a reduction in the anthropogenic CO₂ emissions is of great importance. In this context, CO₂ capture and storage (CCS) as well as CO₂ capture and utilization (CCU) have been proposed to mitigate the rise of the atmospheric CO₂ concentration. Currently, the only CO₂ capture technology that is implemented industrially is amine scrubbing. However, amine scrubbing is associated with high CO₂ capture costs and the formation of hazardous amine-derived by-products. A promising alternative concept for CO₂ capture is calcium looping, i.e. a CO₂ capture process that is based on the reversible carbonation reaction: $\text{CaO (s)} + \text{CO}_2 \text{ (g)} \leftrightarrow \text{CaCO}_3 \text{ (s)}$, $\Delta H_{298\text{ K}}^0 = \pm 178 \text{ kJ mol}^{-1}$. However, despite the considerable advantages for using CaO as a CO₂ sorbent, such as a high theoretical CO₂ uptake ($0.78 \text{ g}_{\text{CO}_2} \text{ g}_{\text{CaO}}^{-1}$) and a high abundance of naturally-occurring CaO precursors, it suffers from a rapid decay of its CO₂ uptake with the number of carbonation/calcination cycles. This limitation makes the development of more effective and stable CaO-based CO₂ sorbents a key requirement for the practical deployment of the calcium looping process. In addition, strategies to transform the captured CO₂ into value-added chemicals or energy carriers must be developed to close ultimately the carbon cycle. The dry reforming of methane (DRM) is a reaction that converts methane and carbon dioxide into a synthesis gas according to: $\text{CH}_4 + \text{CO}_2 \rightarrow 2\text{H}_2 + 2\text{CO}$, $\Delta H_{298\text{ K}}^0 = 247 \text{ kJ mol}^{-1}$. It is an attractive alternative to the steam reforming of methane ($\text{CH}_4 + \text{H}_2\text{O} \rightarrow 3\text{H}_2 + \text{CO}$, $\Delta H_{298\text{ K}}^0 = 206 \text{ kJ mol}^{-1}$) as it converts two major greenhouse gases (CH₄ and CO₂) into a valuable product mixture that is suitable for further transformation to value-added chemicals (e.g., *via* the Fischer-Tropsch process). Currently, no DRM process is operated industrially, primarily due to the lack of stable and inexpensive DRM catalysts. The major disadvantages of the current state-of-the-art catalysts are either their high price (noble metal-based DRM catalysts) and/or their deactivation with time on stream by carbon deposition or loss of active metal *via* the formation of mixed oxide phases with the support (for instance, for Ni-based, Al₂O₃-supported catalysts). Therefore, the engineering of novel catalyst formulations relying on earth-abundant metals with high operational stability is required.

This doctoral Thesis focuses on the development of highly effective CO₂ sorbents for CO₂ capture and novel catalysts for CO₂ conversion, primarily *via* the DRM. Chapter 2 of this Thesis describes a readily scalable route, based on wet mechanochemical activation, to prepare CaO-based CO₂ sorbents. A thorough optimization of the ball-milling parameters allowed to effectively stabilize the morphology of CaO with as little as 15 wt.% of MgO. Characterization of the sorbent by electron microscopy demonstrated that small MgO nanoparticles decorating the surface of CaO particles mitigated sintering and reduced, in turn, to a large degree the deactivation of the sorbent. Furthermore, the effect of adding Na₂CO₃ to CaO sorbents was investigated critically (Chapter 3). The addition of alkali compounds has been proposed as a route for sorbent stabilization, however, reports concerning the effectiveness of this method are contradictory. It was found that the introduction of 1 wt.% Na₂CO₃ reduced substantially the CO₂ uptake performance of CaO under industrially relevant

conditions (i.e. performing the calcination step at 900 °C in a CO₂-rich atmosphere). A detailed characterization of the Na₂CO₃-containing sorbent using a thermogravimetric analysis (TGA), Na K-edge X-ray absorption spectroscopy (XAS) and advanced electron microscopy identified the irreversible formation of a Na₂Ca(CO₃)₂ phase under operation conditions to be a key factor responsible for the degradation of the performance of the sorbent with cycling. Chapter 4 describes a protocol to produce a CaO-based CO₂ sorbent with a hierarchical pore structure *via* a microfluidic emulsification technique. The structure of the sorbent was stabilized through the addition of a uniform Al₂O₃ coating *via* atomic layer deposition (ALD). The improved mass transport characteristics of the hierarchical porous structure makes the new material a promising material for sorption-enhanced applications, e.g. to produce hydrogen.

Turning to the CO₂ utilization through the DRM, β-Mo₂C was chosen as an alternative to conventional noble metals- or Ni-based catalysts. To maximize Mo utilization, the β-Mo₂C phase was derived from two dimensional (2D) MoO₃ supported on carbon spheres *via* a carburization reaction. Electron microscopy revealed that the original 2D morphology was not preserved during the carburization process. The combination of *in situ* XANES/XRD (under DRM reaction conditions) and advanced transmission electron microscopy linked the catalyst deactivation observed during DRM, and appearance of a competing reverse water gas shift reaction to the transformation of β-Mo₂C/C to Mo₂C_xO_y/C (Chapter 5).

Chapter 6 describes how a novel class of 2D materials, MXenes, and in particular 2D molybdenum oxycarbide (Mo₂CT_x, where T_x are surface termination groups), was adapted for applications in heterogeneous catalysis. The combination of TGA, XPS, XANES and XRD revealed that the Mo₂CT_x structure was preserved up to ca. 550 °C in reducing conditions, followed by sintering forming β-Mo₂C owing to the complete de-functionalization of the T_x groups on the Mo-terminated surface. As a prove of concept for the new application of this class of materials in heterogeneous catalysis, the high stability and activity of Mo₂CT_x was demonstrated for the water gas shift (WGS) reaction with a selectivity > 99 % towards CO₂ and H₂ at 500 °C. To prevent the sintering of Mo₂CT_x and to enable its exploitation at the higher temperatures required for the DRM reaction, a novel two dimensional oxycarbide catalyst, Mo₂CO_x, derived from Mo₂CT_x supported on SiO₂, was developed *via* high temperature reduction and oxidation processes (by H₂ and CO₂, respectively). The obtained catalyst was found to be highly active for the DRM and, contrary to the conventional Mo₂C-based catalysts, its activity could be controlled by the oxygen surface coverage (as determined by changes in the Mo oxidation state). The active state of this 2D Mo₂CO_x catalyst was evaluated thoroughly by *ex situ* and *in situ* XAS, XPS and electron microscopy and complemented by density functional theory calculations. The 2D (MXene) morphology of the catalyst was retained after multiple high temperature pretreatment steps and under reactant atmospheres (such as exposure to H₂, CO₂, and DRM atmosphere at 800 °C), revealing a remarkable resistivity of the 2D Mo₂CO_x sheets against oxidation and sintering at these high temperatures and harsh conditions. This work shows how morphology can be exploited to impart stability and maximize metal utilization in two dimensional Mo₂CO_x catalysts.

Zusammenfassung

Die stetig steigenden CO₂-Emissionen durch der Verbrennung fossiler Brennstoffe führen zu einem konstanten Anstieg der CO₂-Konzentration in der Atmosphäre, welche mit der globalen Erwärmung in Zusammenhang gebracht wird. Die Entwicklung von Technologien zur Reduzierung der anthropogenen CO₂-Emissionen ist daher von großer Bedeutung. In diesem Zusammenhang wurden verschiedene Technologien zur CO₂-Abscheidung und -Speicherung (CCS) sowie zur CO₂-Abscheidung und -Nutzung (CCU) vorgeschlagen, um den Anstieg der CO₂-Konzentration in der Atmosphäre zu mildern. Derzeit ist die einzige industriell implementierte CO₂-Abscheidungstechnologie die Aminwäsche. Die Aminwäsche ist jedoch mit hohen Kosten für die CO₂-Abscheidung und der Bildung potentiell gefährlicher, auf Aminen basierender Nebenprodukte verbunden. Ein vielversprechendes alternatives Verfahren für die CO₂-Abscheidung ist das sogenannte Calcium Looping-Verfahren, welches auf einer reversiblen Karbonisierungsreaktion basiert: $\text{CaO (s)} + \text{CO}_2 \text{ (g)} \leftrightarrow \text{CaCO}_3 \text{ (s)}$, $\Delta H_{298\text{ K}}^0 = \pm 178 \text{ kJ mol}^{-1}$. Trotz der Vorteile von CaO für die CO₂-Abscheidung, wie einer hohen theoretischen CO₂-Aufnahmekapazität ($0.78 \text{ g}_{\text{CO}_2} \text{ g}_{\text{CaO}}^{-1}$) und einem grossen Vorkommen natürlicher CaO-Vorläufersubstanzen (z.B. Kalkstein), nimmt die CO₂-Aufnahmekapazität von CaO nach nur wenigen Karbonisierungs- / Kalzinierungszyklen aufgrund der hohen Prozesstemperaturen (ca. 650-900 °C) rasch ab. Dies macht die Entwicklung hochwirksamer und stabiler CO₂-Sorbentien auf CaO-Basis zu einer Schlüsselvoraussetzung für den praktischen Einsatz des Calcium Looping-Verfahrens. Darüber hinaus sollten Strategien entwickelt werden, um das gebundene (und dann freigesetzte) CO₂ in wertschöpfende Chemikalien oder Energieträger umzuwandeln, die es ermöglichen würden die Gesamteffizienz eines CCU-Prozesses zu erhöhen. Die Trockenreformierung von Methan (DRM) ist eine Reaktion, die Methan und Kohlendioxid in ein Synthesegas umwandelt: $\text{CH}_4 + \text{CO}_2 \rightarrow 2\text{H}_2 + 2\text{CO}$, $\Delta H_{298\text{ K}}^0 = 247 \text{ kJ mol}^{-1}$. Die Trockenreformierung ist eine attraktive Alternative zur Dampfreformierung von Methan ($\text{CH}_4 + \text{H}_2\text{O} \rightarrow 3\text{H}_2 + \text{CO}$, $\Delta H_{298\text{ K}}^0 = 206 \text{ kJ mol}^{-1}$), da die beiden wichtigsten Treibhausgase (CH₄ und CO₂) in ein hochwertiges Produktgemisch umgewandelt werden, welches dann zu höheren Kohlenwasserstoffen verarbeitet werden kann (z.B. über das Fischer-Tropsch-Verfahren). Derzeit wird kein DRM-Verfahren industriell betrieben, hauptsächlich aufgrund des Mangels an stabilen und kostengünstigen DRM-Katalysatoren. Die Hauptnachteile der aktuell modernsten Katalysatoren sind ihr hoher Preis (für DRM-Katalysatoren auf Edelmetallbasis) und / oder die mit Prozessdauer zunehmende Deaktivierung durch Kohlenstoffabscheidungen auf der Katalysatoroberfläche, oder der Verlust des katalytisch-aktiven Metalls durch die Bildung von Mischoxid-Phasen mit dem Trägermaterial (z.B. bei Katalysatoren auf Ni-Basis auf einem Al₂O₃-Trägermaterial). Die Entwicklung neuartiger Materialien aus häufig vorkommenden Metallen mit hoher Betriebsstabilität ist daher erforderlich.

Diese Doktorarbeit konzentriert sich auf die Entwicklung hochwirksamer CO₂-Sorbentien zur CO₂-Abscheidung sowie neuartiger Katalysatoren für die anschließende CO₂-Nutzung, hauptsächlich über die DRM-Reaktion. Kapitel 2 dieser Arbeit beschreibt ein skalierbares Verfahren auf Grundlage der nassen mechanochemischen Aktivierung zur Herstellung von CO₂-Sorbentien auf CaO-Basis. Die Optimierung der Kugelmahlparameter

ermöglichte es, die Porenstruktur von CaO mit nur 15 Gew. % MgO wirksam zu stabilisieren. Die elektronenmikroskopische Charakterisierung des CO₂-Sorbents zeigte, dass kleine MgO-Nanopartikel auf der Oberfläche der CaO-Partikeln deren Sintern hemmen und so die Deaktivierung des CO₂-Sorbents abschwächen. Zusätzlich wurde die Wirkung von Na₂CO₃, das häufig als Stabilisator für Sorbentien auf CaO-Basis verwendet wird, auf die zyklische CO₂-Aufnahmekapazität kritisch untersucht und in Kapitel 3 beschrieben. Berichte bezüglich der Wirksamkeit dieses Ansatzes sind jedoch widersprüchlich. Es wurde festgestellt, dass die CO₂-Aufnahmekapazität von CaO nach Hinzufügen von lediglich 1 Gew. % Na₂CO₃ deutlich abnahm unter industriell relevanten Reaktionsbedingungen (d.h. die Durchführung der Kalzinierung bei 900 °C in einer CO₂-reichen Atmosphäre). Durch die detaillierte Charakterisierung der Na₂CO₃-haltigen CaO-Sorbentien unter Verwendung einer Thermowaage (TGA), Na K-Kanten-Röntgenabsorptionsspektroskopie (XAS) und Elektronenmikroskopie konnte die irreversible Bildung einer Na₂Ca(CO₃)₂-Phase unter Betriebsbedingungen festgestellt werden, welche ein Schlüsselfaktor für die Verschlechterung der zyklischen CO₂-Aufnahmekapazität ist. Kapitel 4 beschreibt, wie ein auf CaO basierender CO₂-Sorbent mittels mikrofluidischer Emulgiertechnik zu einer porösen hierarchischen Makrostruktur zusammengesetzt wurde. Eine weitere Stabilisierung der Mikrostruktur des CO₂-Sorbents wurde durch die gleichmäßige Al₂O₃-Beschichtung mittels Atomlagenabscheidung (ALD) erreicht. Die hierarchisch poröse Struktur des Materials ermöglicht einen verbesserten Massentransport innerhalb des CO₂-Sorbents und macht es somit zu einem vielversprechenden Material für Anwendungen, in denen CO₂ im Prozess abgeschieden werden muss, z.B. bei der Herstellung von Wasserstoff.

In Bezug auf die CO₂-Nutzung durch eine DRM-Reaktion wurde β -Mo₂C als Alternative zu herkömmlichen Edelmetallen oder Katalysatoren auf Ni-Basis ausgewählt. Um die Ausnutzung der katalytisch aktiven Mo-Phase zu maximieren, wurde die β -Mo₂C-Phase durch die Aufkohlungsreaktion von zweidimensionalem (2D) MoO₃, das auf Kohlenstoffkugeln aufgetragen wurde, hergestellt. Elektronenmikroskopische Untersuchungen ergaben, dass die 2D-Morphologie während des Aufkohlungsprozesses nicht erhalten werden konnte. Durch die Kombination von in-situ Röntgen-Nahkanten-Absorptions-Spektroskopie (XANES) / Röntgendiffraktometrie (XRD) (unter DRM-Reaktionsbedingungen) und Transmissionselektronenmikroskopie konnte die Katalysatordeaktivierung während der DRM-Reaktion in Zusammenhang mit dem Auftreten der konkurrierenden umgekehrten Wassergas-Konvertierungsreaktion (rWGS) gebracht werden, durch die katalytisch aktive Phase β -Mo₂C/C teilweise zu Mo₂C_xO_y/C umgewandelt wurde (Kapitel 5).

Kapitel 6 beschreibt, wie eine neuartige Gattung von 2D-Materialien, MXene und insbesondere 2D-Molybdänoxycarbide (mit der allgemeinen Formel Mo₂CT_x, wobei T_x für Oberflächenabschlussgruppen steht), für Anwendungen in der heterogenen Katalyse angepasst wurde. Die Kombination von TGA, Röntgenphotoelektronenspektroskopie (XPS), XANES und XRD ergab, dass die Mo₂CT_x-Struktur unter reduzierenden Bedingungen bis zu einer Temperatur von ca. 550 °C erhalten bleibt, gefolgt vom Sintern zu β -Mo₂C aufgrund der vollständigen Desfunktionalisierung der T_x-Gruppen von der Mo-terminierten Oberfläche. Die hohe Stabilität und Aktivität des Mo₂CT_x-Katalysators wurde für die Wassergas-Konvertierungsreaktion (WGS) mit einer Selektivität von > 99 % gegenüber CO₂ und H₂ bei

500 °C nachgewiesen. Um das Sintern von Mo_2CT_x zu verhindern und somit dessen Nutzung bei höheren, für die DRM-Reaktion erforderlichen Temperaturen zu ermöglichen, wurde ein neuartiger zweidimensionaler Oxycarbidkatalysator Mo_2CO_x , der von Mo_2CT_x auf einem SiO_2 Trägermaterial abgeleitet wurde, über Hochtemperaturreduktions- und Oxidationsprozesse (durch H_2 bzw. CO_2) entwickelt. Der Katalysator erwies sich in der DRM-Reaktion als hochaktiv und im Gegensatz zu den herkömmlichen Katalysatoren auf Mo_2C -Basis konnte seine Aktivität durch die Sauerstoffoberflächenbedeckung gesteuert werden, wie durch die Änderungen der Mo-Oxidationsstufe festgestellt werden konnte. Der aktive Zustand dieses 2D- Mo_2CO_x -Katalysators wurde gründlich durch ex-situ- und in-situ-XAS-, XPS- und Elektronenmikroskopie untersucht und durch Berechnungen der Dichtefunktionaltheorie (DFT) ergänzt. Die zweidimensionale (MXene) Morphologie des Katalysators wurde auch nach mehreren Hochtemperatur-Vorbehandlungsschritten und unter dem Einfluss verschiedener Reaktanten (wie z.B. H_2 , CO_2 und denen der DRM-Reaktion bei 800 °C) beibehalten, was einen bemerkenswerten Widerstand der 2D- Mo_2CO_x -Schichten gegen die Oxidation und das Sintern bei diesen hohen Temperaturen und extremen Bedingungen darstellt. In dieser Arbeit wird daher aufgezeigt, wie die Morphologie der Materialien genutzt werden kann, um ihnen Stabilität zu verleihen und die Metallausnutzung in zweidimensionalen Mo_2CO_x -Katalysatoren zu maximieren.

Table of Contents

Abstract	iii
Zusammenfassung	v
Chapter 1: Introduction	1
1.1. General background.....	1
1.2. Calcium looping.....	4
1.2.1. Fundamentals of the calcium looping process	4
1.2.2. Stabilized CaO-based materials	8
1.2.3. Alkali-based dopants.....	9
1.3. Methane reforming.....	10
1.3.1. Fundamentals of the dry reforming of methane.....	11
1.3.2. State of the art DRM catalysts	12
1.3.3. Molybdenum carbide as an alternative methane reforming catalyst.....	13
1.3.4. MXenes – promising materials for heterogeneous catalysis applications	16
1.4. Sorption-enhanced steam methane reforming.....	18
1.4.1. Sorption-enhanced steam methane reforming.....	19
1.4.2. Bi-functional materials for SE-SMR.....	21
1.5. The objectives and structure of this dissertation	23
Chapter 2: Mechanochemically activated, calcium oxide-based, magnesium oxide-stabilized carbon dioxide sorbents	25
2.1. Abstract.....	26
2.2. Introduction	26
2.3. Experimental section	30
2.3.1. Materials	30
2.3.2. Characterization.....	30
2.3.3. CO ₂ capture tests	31
2.4. Results and discussion	32
2.4.1. Optimization of the mechanochemical activation	32
2.4.2. Phase identification using X-ray diffraction.....	33
2.4.3. Morphological characterization of ball-milled CaO.....	34
2.4.4. CO ₂ uptake characteristics of ball-milled, unsupported CaO	37
2.4.5. Stabilization of CaO by MgO	39
2.4.6. Phase characterization using X-ray diffraction	40
2.4.7. Morphological characterization of MgO-stabilized CaO	40
2.4.8. Optimization of the Ca-to-Mg ratio	41
2.4.9. Long-term stability of MgO-stabilized CaO.....	42
2.5. Conclusions	47
Chapter 3: Na ₂ CO ₃ -modified CaO-based CO ₂ Sorbents: The Effects of Structure and Morphology on CO ₂ Uptake.....	49
3.1. Abstract.....	50
3.2. Introduction	50
3.3. Experimental section	52
3.3.1. Material preparation.....	52
3.3.2. Characterization.....	53
3.3.3. CO ₂ capture tests	54
3.4. Results and discussion	55

3.4.1.	Synthesis and structural characterization of the as-prepared sorbents	55
3.4.2.	Cyclic CO ₂ uptake	55
3.4.3.	Morphological characterization of the calcined sorbents	58
3.4.4.	The effect of sintering on the CO ₂ uptake of the pure CaO sorbent	60
3.4.5.	Structure and morphology of the cycled sorbents	60
3.4.6.	XAS analysis: the nature of the Na containing phases in the cycled materials	61
3.4.7.	Discussion.....	63
3.5.	Conclusions	64
Chapter 4:	CaO-based CO ₂ sorbents with a hierarchical porous structure made <i>via</i> microfluidic droplet templating	65
4.1.	Abstract.....	66
4.2.	Introduction	66
4.3.	Experimental section	68
4.3.1.	Materials	68
4.3.2.	Atomic layer deposition (ALD) of Al ₂ O ₃	68
4.3.3.	Characterization.....	69
4.3.4.	CO ₂ capture tests	69
4.4.	Results and discussion	70
4.4.1.	Sorbent synthesis.....	70
4.4.2.	CO ₂ capture performance	73
4.4.3.	Characterization of reacted sorbents	74
4.5.	Conclusions	76
Chapter 5:	Molybdenum carbide and oxycarbide from carbon-supported MoO ₃ nanosheets: phase evolution and DRM catalytic activity assessed by TEM and <i>in situ</i> XANES/XRD methods.....	77
5.1.	Abstract.....	78
5.2.	Introduction	78
5.3.	Experimental section	80
5.3.1.	Materials	80
5.3.2.	Characterization.....	80
5.3.3.	Catalytic Testing.....	82
5.4.	Results and discussion	82
5.5.	Conclusions	91
Chapter 6:	<i>In Situ</i> XANES/XRD study of the structural stability of two-dimensional molybdenum carbide Mo ₂ CT _x : implications for the catalytic activity in the water-gas shift reaction	92
6.1.	Abstract.....	93
6.2.	Introduction	93
6.3.	Experimental section	94
6.3.1.	Materials	94
6.3.2.	Characterization.....	95
6.3.3.	Catalytic Testing.....	97
6.4.	Results and discussion	98
6.5.	Conclusions	107

Chapter 7:	Two-dimensional silica-supported molybdenum oxycarbide 2D-Mo ₂ CO _x : exploiting morphology to enable high activity and stability in the dry reforming of methane.....	109
7.1.	Abstract.....	110
7.2.	Introduction	110
7.3.	Experimental section	113
7.3.1.	Materials	113
7.3.2.	Characterization.....	113
7.3.3.	Catalytic Testing.....	116
7.3.4.	Computational Details	116
7.4.	Results and discussion	117
7.4.1.	Synthesis and characterization of silica-supported 2D-Mo ₂ CT _x , 2D-Mo ₂ C and 2D-Mo ₂ CO _x materials.....	117
7.4.2.	Correlating catalytic activity of 2D-Mo ₂ CO _x /SiO ₂ in DRM to the oxygen coverage of its surface.	123
7.4.3.	Theoretical modelling of DRM reaction pathways on 2D-Mo ₂ CO _x /SiO ₂	128
7.5.	Conclusions	132
Chapter 8:	Conclusions and Outlook	134
8.1.	Conclusions	134
8.2.	Outlook	136
Appendices	137
A.	Experimental setups and procedures	137
A.1.	Ball milling	137
A.2.	Microfluidic setup.....	137
A.3.	X-ray diffraction.....	138
A.4.	X-ray absorption spectroscopy.....	139
B.	Supplementary information for Chapter 3	142
C.	Supplementary information for Chapter 4	152
D.	Supplementary information for Chapter 5	156
E.	Supplementary information for Chapter 6	170
F.	Supplementary information for Chapter 7	182
References	208
Curriculum vitae.....	228

Chapter 1: Introduction

1.1. General background

The global economic and population growth leads to a continuous increase in the global energy demand (in 2018 the annual increase in the global energy demand was 2.3 % or 328 Mtoe).¹ Currently, fossil fuels, i.e. coal, oil and natural gas, are the main energy carriers contributing to more than 80 % of the total primary energy supply (TPES, Figure 1.1a).

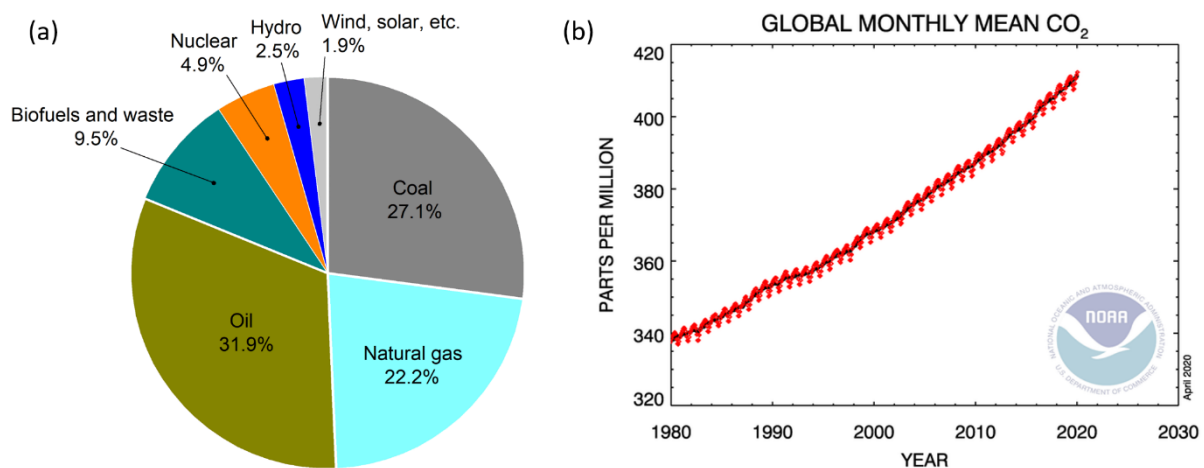


Figure 1.1. a) TPES by source in 2017 (International Energy Agency (IEA), World Energy Balances 2019); b) CO₂ concentration in the atmosphere (NOAA/ESRL).

The combustion of fossil fuels for electricity generation, in industrial processes, and for transportation releases large quantities of CO₂ into the atmosphere. Currently, more than 33 Gt of CO₂ are emitted annually. In 2016, the CO₂ concentration in the atmosphere exceeded the milestone value of 400 ppm and currently is at 412 ppm (Figure 1.1b). This value is ca. 47 % higher than the pre-industrial level of ca. 280 ppm.²⁻³ There is ample evidence that the increasing concentration of greenhouse gases (GHG), with CO₂ being the dominating gas, is linked to global warming with potentially severe consequences for the global climate, such as droughts and rising sea levels.⁴ According to estimations of the Organisation for Economic Co-operation and Development (OECD), global, annual CO₂ emissions will reach 50 Gt CO₂ in 2050 in case that countermeasures are not being implemented. This accelerated rate of CO₂ emissions will translate into a rise in the average global temperature in the range of 3 to 6 °C (compared to the pre-industrial temperature level).⁵ To limit the global temperature increase to below 2 °C (a globally accepted temperature growth limitation to avoid potentially

catastrophic changes to the planet), the annual CO₂ emissions have to be reduced to ca. 14 Gt CO₂,⁶ a value that is more than two times lower compared to the 33 Gt CO₂ that were emitted in 2018.¹

To reach this challenging goal, an arsenal of measures have to be implemented including i) the improvement of the energy efficiency of current technologies, ii) a gradual transition from fossil fuels to renewable energy carriers, and iii) the implementation of technologies for carbon capture and utilization (CCU), and storage (CCS), potentially even capturing CO₂ from the air. According to the International Energy Agency (IEA), by 2050 CCS is expected to contribute by up to 12 % to the global CO₂ reduction target (Figure 1.2).⁶

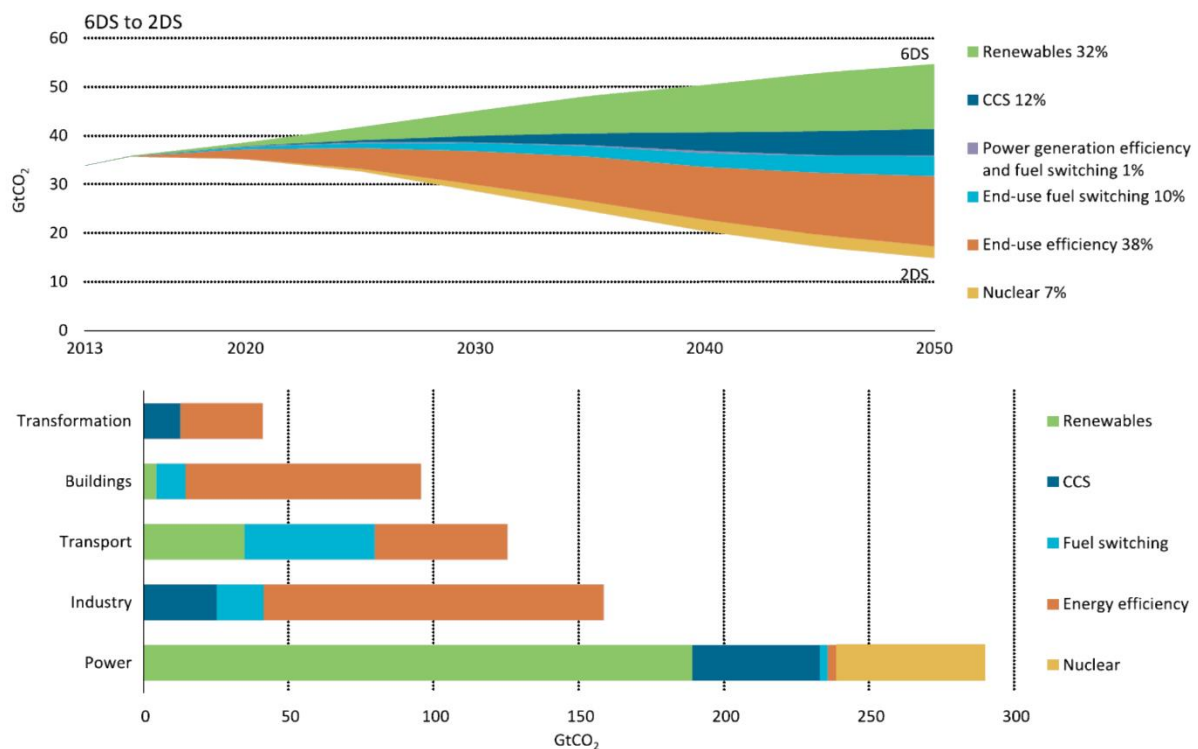
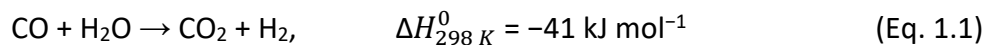


Figure 1.2. Contribution of different technologies to the key sectors to global CO₂ reduction targets for the IEA's 6-degrees and 2-degrees scenarios (2013-2050). (Adopted from ref. ⁶)

In CCUS, CO₂ is captured from large point sources, e.g. fossil-fuel fired power stations. While in CCU processes the CO₂ captured is converted to valuable products, e.g. methanol, biofuels, and other forms of hydrocarbons, in CCS the CO₂ is compressed and subsequently stored. Saline aquifers as well as depleted oil and gas reservoirs or coal are considered as possible CO₂ storage sites.⁷ The captured CO₂ can (and indeed is) be further utilized for the enhanced oil recovery.⁸⁻⁹ While enhanced oil recovery might aid in the current situation to

implement CCS technologies on the large scale, it is questionable whether it will lead to an overall net reduction of CO₂ emissions. The costs of transportation and storage of CO₂ are estimated to be relatively low, whereas the costs of CO₂ capture account for ca. 70–80 % of the total CCS costs.¹⁰ For example, the costs for the currently most mature CO₂ capture technology, i.e. scrubbing using monoethanolamine (MEA), range between 32 and 77 \$ t_{CO₂}⁻¹.¹¹ Hence, there are large global research programs to reduce the costs of CO₂ capture by exploring alternative CO₂ sorbents.

Overall, the different CO₂ capture technologies can be divided into three main categories: (i) post-combustion capture, (ii) pre-combustion capture and (iii) oxy-fuel combustion (Figure 1.3). In post-combustion capture, CO₂ is removed from the flue gas (containing ca. 15 % CO₂) after the combustion process. This technology can be retrofitted to most of the operating power plants. In pre-combustion capture, the fossil fuel is decarbonized prior to its combustion. In most cases this involves first a gasification step which yields a synthesis gas (i.e. a mixture of CO and H₂). The water gas shift reaction (Eq. 1.1), converts CO further to CO₂ which is subsequently separated from the H₂ prior to its combustion. In oxy-fuel combustion, fuel is burned in a mixture of O₂ (ca. 30 %) and (recycled) CO₂, yielding a flue gas containing only steam and CO₂.¹² This technology requires an expensive air separation unit to supply oxygen of high purity.



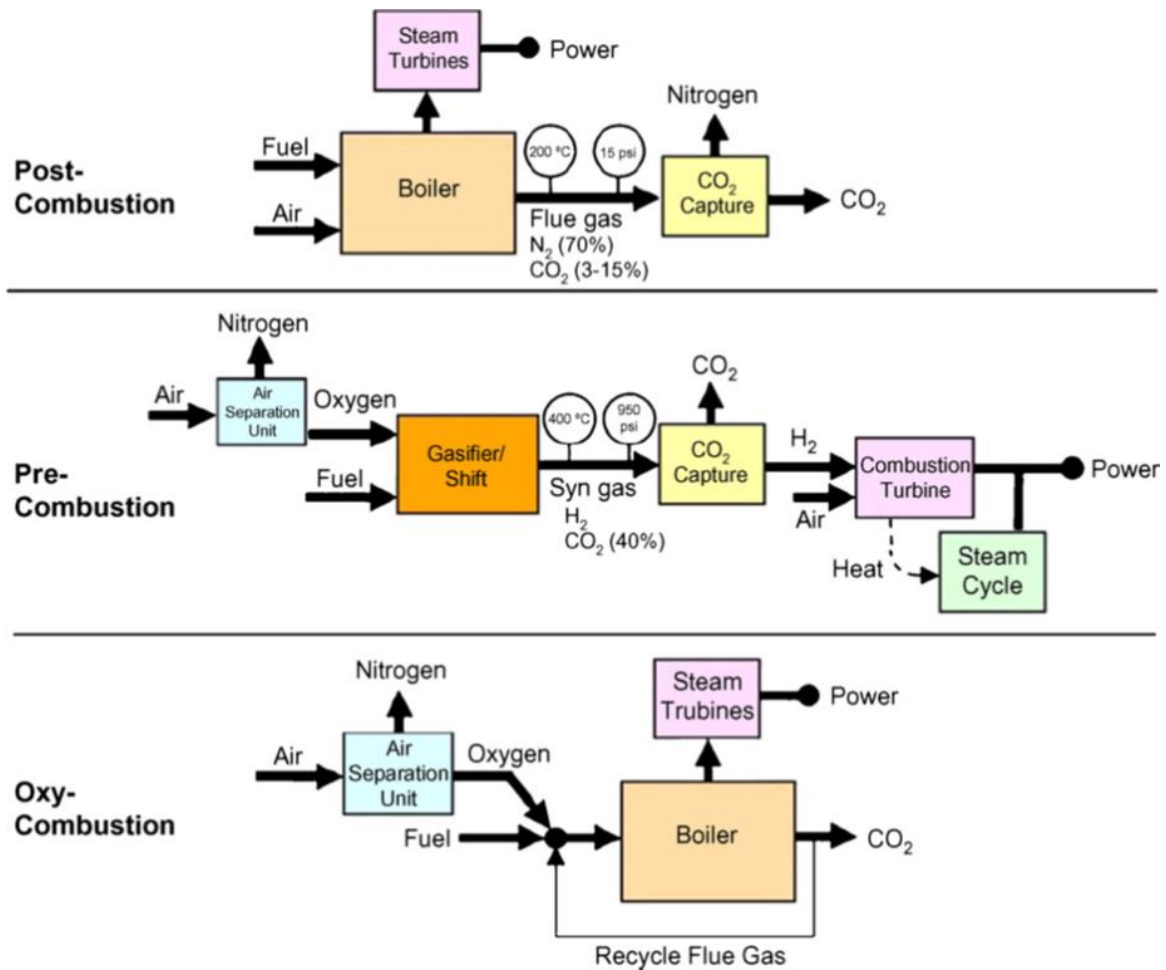


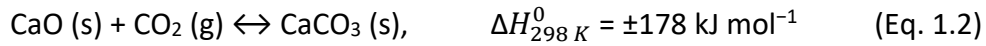
Figure 1.3. Schematic illustrating post-combustion, pre-combustion, and oxy-combustion CCS concepts. (Adopted from ref. ⁸)

1.2. Calcium looping

Currently, the only commercially implemented CO₂ capture technology (for the purification of natural gas) is amine scrubbing.¹³ However, beside its high costs, thermal degradation of the amines and formation of hazardous by-products, i.e. secondary nitrosamines are key disadvantages.¹⁴⁻¹⁵ Therefore, substantial research activities are directed towards the development of less costly and more environmentally friendly CO₂ capture technologies, including e.g. amine-functionalized host structures,¹⁶⁻¹⁷ nanoporous materials such as zeolites¹⁸⁻¹⁹ or metal-organic frameworks²⁰⁻²¹ and alkali-earth metal oxides, e.g. MgO²²⁻²⁴ and CaO.^{22,25-27} In this work, we explore CaO-based CO₂ sorbents for the so-called calcium looping (CaL) process.

1.2.1. Fundamentals of the calcium looping process

CaL is based on the following reversible carbonation-calcination cycle (Eq. 1.2):



The key advantages of CaL are (i) a high theoretical CO₂ uptake capacity of CaO (0.78 g_{CO₂} g_{CaO}⁻¹), (ii) a high abundance of naturally-occurring precursors, e.g. limestone or dolomite, and (iii) fast kinetics for both the carbonation (CO₂ capture) and calcination (CO₂ release) reactions. Owing to these favorable characteristics, it has been estimated that CaL could reduce the costs of CO₂ capture by 60 % compared to amine scrubbing.¹¹

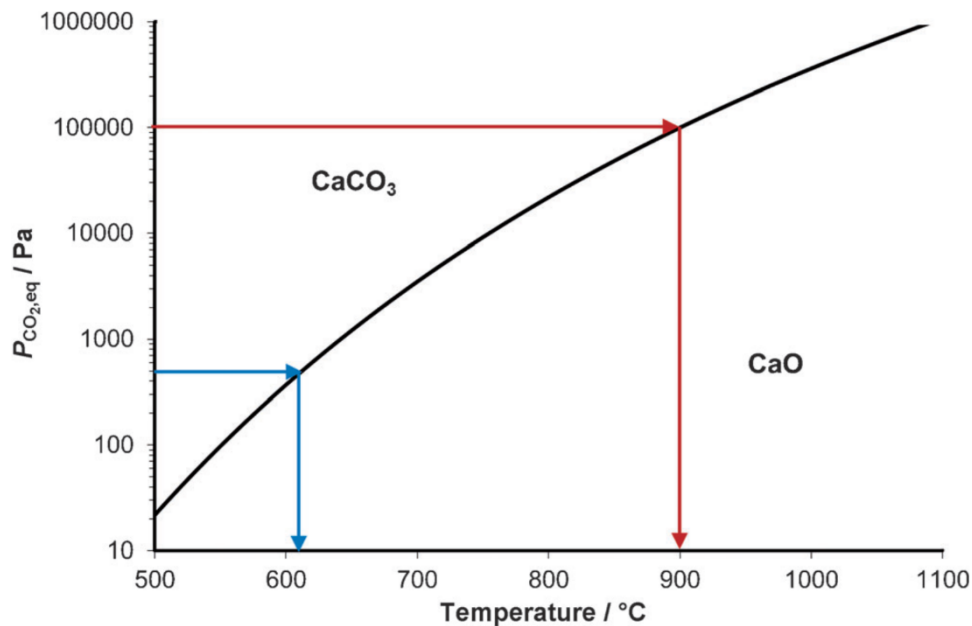


Figure 1.4. Equilibrium partial pressure of CO₂ over the CaO-CaCO₃ pair as determined by correlation of Baker.²⁸ Blue arrows indicate the carbonation temperatures with a 0.005 bar CO₂ slip, while red arrows indicate the minimum calcination temperature required to produce a pure stream of CO₂. (Adopted from ref. ²⁵)

The optimal operational temperatures for the calcination and carbonation reactions are determined by the CaCO₃-CaO equilibrium (Figure 1.4). The temperature of the carbonation reaction is determined largely by the acceptable CO₂ slip in the exhaust gas and the carbonation rate, that is a CO₂ removal efficiency at low temperatures comes at the cost of lower carbonation kinetics. As a compromise, the carbonation step is typically performed between 600 and 650 °C, yielding a CO₂ slip of 0.002-0.01 bar CO₂. The calcination temperature is determined by the requirement to obtain a pure stream of CO₂. To obtain a partial pressure of CO₂ of 1 bar, a calcination temperature of ca. 900 °C is required (Figure 1.4).

From a practical standpoint, the CaL process is operated in two bubbling fluidized beds (separate carbonator and calciner reactors) or a circulating fluidized bed (Figure 1.5). The cyclic CaL process can be described as followed: CaO is introduced in the carbonator in which it is exposed to a gas mixture containing largely N₂, unburnt oxygen and CO₂. The CO₂ reacts with CaO to form CaCO₃, and the CO₂-depleted flue gas exits the reactor. Next, the carbonated sorbent is transferred to the calciner for the regeneration, resulting in the release of a pure stream of CO₂. The regenerated sorbent is transferred back to the carbonator, starting a new cycle. Owing to the high exothermicity of the carbonation reaction and its high operational temperature, the heat released can be utilized for electricity generation, contributing notably to the reduced costs of CO₂ capture. The endothermic calcination reaction requires heat, which can be supplied e.g. through oxy-fuel combustion (Figure 1.5).

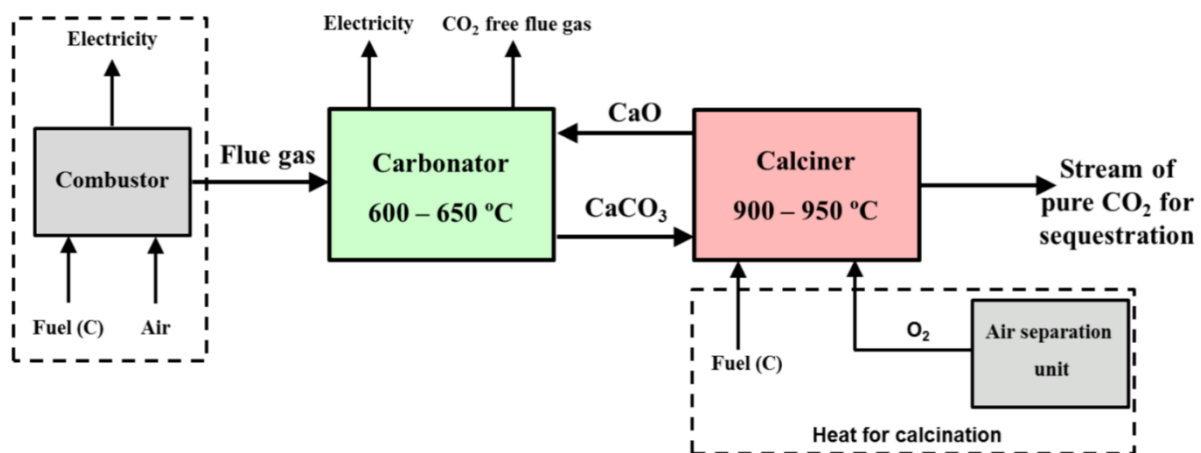


Figure 1.5. Schematic diagram of the CaL process. (Adopted from ref. ²⁹)

A major drawback of the CaL technology is the rapid decay of the CO₂ uptake performance of the benchmark material limestone (and indeed most other CaO-based sorbents) over repeated cycles of carbonation and calcination.³⁰⁻³¹ For example, the CO₂ uptake capacity of limestone (initial CO₂ uptake of ca. 0.5 g_{CO2} g_{sorbent}⁻¹) was observed to decrease by ca. 85 % over the first 20 cycles, stabilizing, however at 0.075–0.08 g_{CO2} g_{sorbent}⁻¹ during the following 500 cycles.³¹ The reduction in CO₂ uptake has been assigned largely to thermal sintering, as the Tamman temperature (the temperature at which atoms in the bulk become mobile; roughly equal to half of the melting temperature in Kelvin) of CaCO₃ ($T_T = 533$ °C) is significantly lower than the operating temperature of the process (650–950 °C).^{25,32} Sintering leads to drastic morphological changes, i.e. a decrease in the pore

volume and surface area of the material. However, large pore volumes are required for rapid CO₂ uptake as the molar volume of the product CaCO₃ (36.9 cm³ mol⁻¹) is approximately two times higher than that of CaO (16.8 cm³ mol⁻¹). Indeed, the carbonation reaction proceeds in two stages, i.e. an initial, fast, kinetically-controlled reaction stage that is followed by a slow, diffusion-limited reaction stages (Figure 1.6). In the kinetically-controlled regime, CO₂ reacts with the CaO surface forming a layer of CaCO₃ that fills the small pores of the sorbent. Upon reaching a critical product layer thickness, estimated by different models to vary from 22³³ and 50 nm³⁴ to 90 nm,³⁵ the carbonation reaction becomes diffusion-limited with notably lower reaction rates as the diffusion coefficient of CO₂ in CaCO₃ (0.003 cm² s⁻¹) is two orders of magnitude lower than that in CaO (0.3 cm² s⁻¹).³³

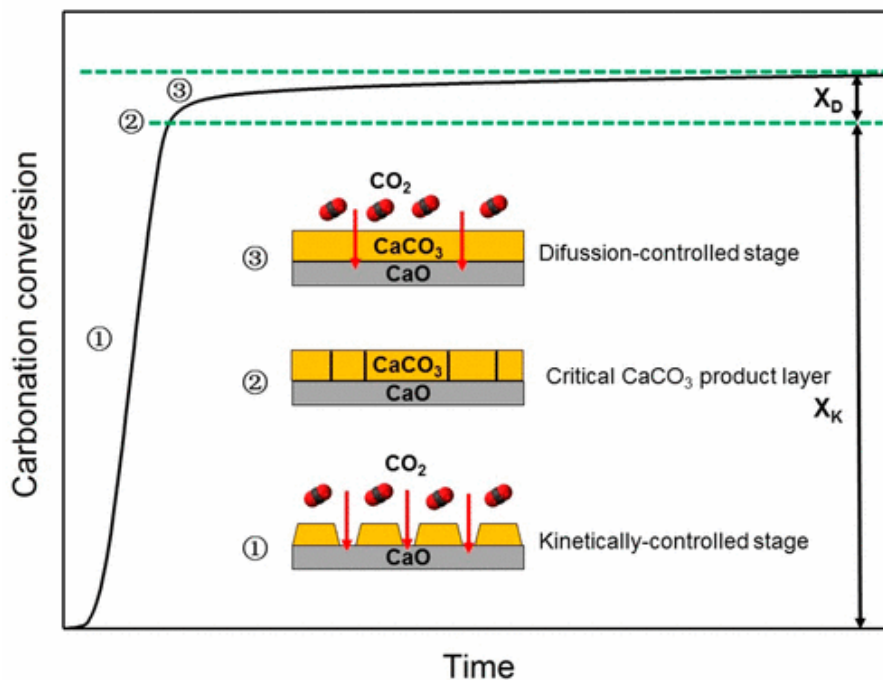


Figure 1.6. Visualization of the two reaction regimes of the carbonation reaction. A fast, kinetically controlled reaction regime (with a CaO conversion of X_K) is followed by a slow, diffusion-limited reaction regime (with a CaO conversion of X_D). (Adopted from ref. ³⁶⁻³⁷)

Hence, the development of highly effective CaO-based CO₂ sorbents requires the structural stabilization of CaO. This can be generally achieved by several routes: (i) The development of highly porous (generally nano-sized) synthetic CaO, (ii) the introduction of stabilizers such as MgO and Al₂O₃, and (iii) doping with alkali metals salts, e.g. Na₂CO₃ and K₂CO₃.

1.2.2. Stabilized CaO-based materials

A frequently explored approach to mitigate the rapid decay of the cyclic CO₂ uptake of CaO due to sintering is the stabilization of CaO with a high T_T material.³⁸⁻³⁹ Stabilizer materials can be divided into two main categories, viz. (i) inactive stabilizers that do not form mixed oxides with CaO, e.g. MgO⁴⁰ and Y₂O₃,⁴¹ and (ii) reactive stabilizer that form mixed oxides with CaO, e.g. Al₂O₃⁴² and ZrO₂.³⁸ Generally, stabilizers do not capture CO₂ at the operating conditions of the CaL process. Therefore, there is a trade-off between achieving a high cyclic stability and high CO₂ uptake. Among the many supports investigated, MgO and Al₂O₃ have shown the most promising results so far.

MgO possesses a high Tammann temperature of $T_T = 1276$ °C and seems to stabilize the structure of CaO most effectively in a homogeneous mixture with CaO (preferably at the nanoscale).⁴⁰ It is worth mentioning that even though MgO can adsorb CO₂ at moderate temperatures (300–450 °C),⁴³ it is inert in regards to the CO₂ capture in CaL applications and is utilized ultimately as a stabilizer. Various synthesis methods such as dry and wet (mechanical) mixing,⁴⁴⁻⁴⁶ recrystallization,⁴⁰ sol-gel⁴⁷ and carbon-gel templating⁴⁸ have been utilized to prepare such materials. Based on observations by TEM, the stabilization mechanism has been attributed to the homogeneous distribution of MgO nanoparticles (< 100 nm) decorating the CaO/CaCO₃ surfaces and thereby strongly reducing the thermal sintering of the CaO/CaCO₃ particles.⁴⁹ For example, it has been reported that as little as 8 wt.% MgO can effectively stabilize a CaO-based sorbent, yielding after 10 carbonation/calcination cycles a CO₂ uptake of 0.47 g_{CO₂} g_{sorbent}⁻¹ compared to 0.14 g_{CO₂} g_{sorbent}⁻¹ for unsupported material.⁴⁰

Al₂O₃ is arguably the most widely studied stabilizer. It falls into the class of reactive stabilizers as it forms mixed oxides with CaO. Common synthesis techniques have included mechanical mixing,⁵⁰⁻⁵¹ co-precipitation,⁵²⁻⁵³ sol-gel⁵⁴⁻⁵⁵ and carbon-gel⁴² templating, and, more recently, advanced deposition techniques such as chemical vapor deposition (CVD)⁵⁶ and atomic layer deposition (ALD).⁵⁷ Generally, Ca-Al mixed oxides, mainly mayenite (Ca₁₂Al₁₄O₃₃) and tricalcium aluminate (Ca₃Al₂O₆), form during the initial calcination step. Similar to MgO-stabilized sorbents, the higher and more stable CO₂ uptake of Al₂O₃-stabilized sorbents has been attributed to the stabilization of the pores within the sorbent (such that a relatively high surface area and a large pore volume are preserved) by well-dispersed Ca-Al

mixed oxides reducing appreciably the thermal sintering of CaO/CaCO₃ particles/grains/crystallites. Nevertheless and similar to MgO-stabilized materials, also Al₂O₃-stabilized CaO deactivates with an increasing cycle number, albeit at a reduced rate compared to the unstabilized reference materials.^{53,57-58} Recently studies using *in situ* X-ray diffraction (XRD) and nuclear magnetic resonance (NMR) techniques attributed this deactivation to the partial “de-mixing” of Ca-Al mixed oxides, resulting in the formation and segregation of Al₂O₃ nanoparticles on the sorbent’s surface and reducing thereby significantly the sintering resistivity of the material.⁵⁸

1.2.3. Alkali-based dopants

Depending on the alkaline earth metal oxide, sorbent promotion by alkali metal (salts) can result in a significant increase in the rate of CO₂ uptake. Recently, this approach has been successfully demonstrated for the intermediate temperature MgO-based CO₂ sorbent.^{23-24,59} For example, while unpromoted MgO shows a negligible CO₂ uptake capacity (0.025 g_{CO2} g_{sorbent}⁻¹ at 300 °C), the CO₂ uptake of MgO promoted with 5 mol.% of (Li-Na-K)NO₃ exceeded 0.45 g_{CO2} g_{sorbent}⁻¹ at identical carbonation conditions. Inspired by these results, several studies aimed at promoting also CaO by alkali salts.

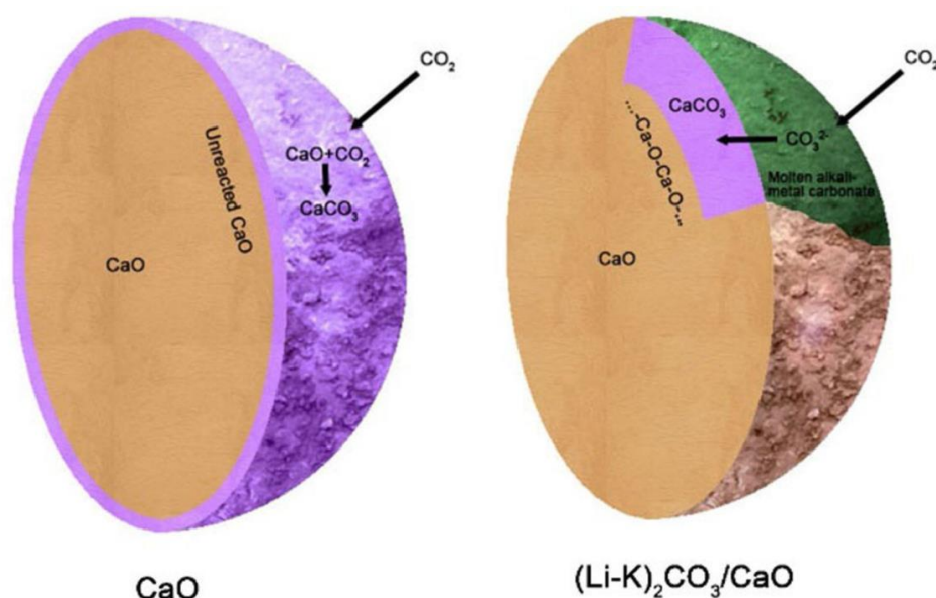


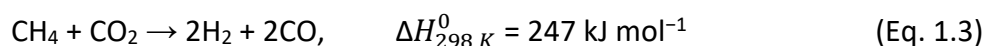
Figure 1.7. Schematic representation of the possible interactions of CO₂ with (Li-K)₂CO₃/CaO and CaO particles. (Adopted from ref. ⁶⁰)

However, unlike for MgO, the results for CaO are contradictory. For example, Reddy and Smirniotis reported that all alkali metal salts except Li strongly increased the CO₂ uptake

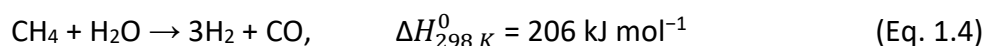
capacity of CaO, although no cyclic stability data was reported.⁶¹ Furthermore, also NaCl and, to a lesser extent Na₂CO₃, were reported to enhance limestone-derived sorbent towards CO₂ uptake.⁶² A further report arguing about the positive effect of the promotion of CaO by alkali metal carbonates reported that when CaO was coated with (Li-K)₂CO₃, a three times higher CO₂ uptake compared to pure CaO was obtained after 23 carbonation/calcination cycles.⁶⁰ It was postulated that the alkali salt coating prevents the formation of a rigid CaCO₃ layer, which retains access for CO₂ to unreacted CaO (Figure 1.7). Additionally, the formation of a Ca-Na double carbonate, i.e. Na₂Ca(CO₃)₂, has been reported to increase the kinetics of the carbonation/calcination reactions when compared to pristine CaO while, at the same time, increasing the sorbent's cyclic stability.⁶³⁻⁶⁴ However, other studies reported a severe reduction of the CO₂ uptake of limestone by ca. 60 % upon the addition of Na₂CO₃.⁶⁵ In addition to the conflicting reports on the effect of the addition of alkali salts on the CO₂ uptake of CaO, in all of the studies described above the cyclic CO₂ uptake was determined under mild conditions that are of little relevance for practical use, i.e. the calcination step was performed in pure N₂ at $T \leq 800$ °C. Therefore, understanding the effect of alkali metal salts on the CO₂ uptake of CaO-based sorbents requires more work.

1.3. Methane reforming

A route to valorize the captured CO₂ is to utilize it as a feedstock in the production of valuable chemicals or fuels.⁶⁶⁻⁶⁷ For instance, the direct hydrogenation of CO₂ to methanol, a high energy density liquid fuel, is currently actively studied.⁶⁸⁻⁶⁹ Additionally, CO₂ can be converted to CO, which is, with H₂, the required reactant for the production of liquid hydrocarbons *via* the Fischer-Tropsch (FT) process.⁷⁰ In this context, the dry reforming of methane (DRM) is of great interest as it converts two major greenhouse gases, i.e. CH₄ and CO₂, into a synthesis gas, viz. a mixture of carbon monoxide and hydrogen (Eq. 1.3).

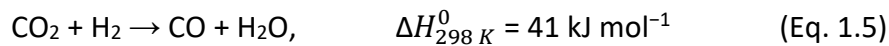


An alternative route for synthesis gas production is steam methane reforming (SMR). In contrast to the DRM process, SMR utilizes H₂O to reform CH₄ (Eq. 1.4). Additionally, SMR is an important process for the production of H₂ for pre-combustion CO₂ capture technologies.



1.3.1. Fundamentals of the dry reforming of methane

The DRM process has been developed since the 1920s and currently attracts attention owing to increased research activities on the mitigation of CO₂ emissions. The theoretical H₂ : CO ratio of one (Eq. 1.3) makes DRM attractive for downstream industrial applications, e.g. synthesis of long chain hydrocarbons *via* FT.⁷¹ However, multiple side-reaction can occur simultaneously with the DRM process,⁷² influencing the H₂ : CO ratio obtained.



One of the major side reactions occurring in parallel with the DRM is the reverse water gas shift (RWGS) reaction (Eq. 1.5). In this reaction, the H₂ produced reacts further with the unconverted CO₂ to yield CO and steam, thus decreasing the H₂ : CO ratio below 1. Figure 1.8a plots the equilibrium distribution of the DRM reaction, when only considering H₂, CO, and H₂O as possible products.⁷³ According to these thermodynamic equilibrium calculations, the extend of the RWGS reaction is limited at high temperatures, leading to a H₂ : CO ratio close to 1 for $T > 820 \text{ }^\circ\text{C}$.⁷⁴

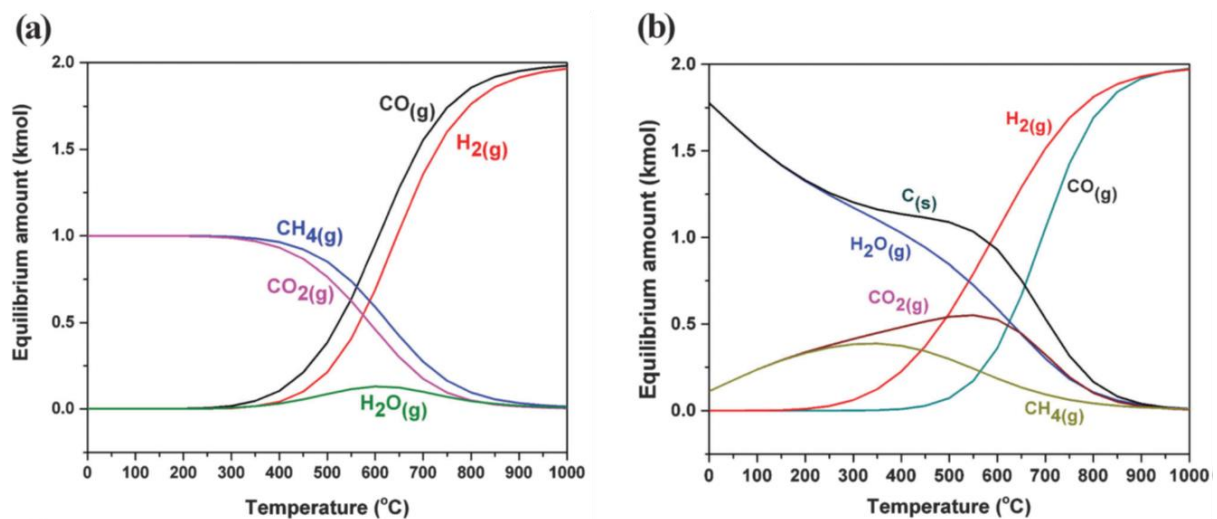
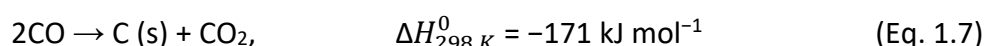
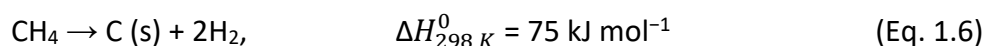


Figure 1.8. Thermodynamic equilibrium plots for DRM at 1 bar (CH₄ : CO₂ = 1) (a) not considering or (b) considering the formation of carbon. (Adopted from ref. ⁷³)



Another significant side reaction occurring in parallel to the DRM reaction is carbon formation (often referred to as coking), which leads to catalyst deactivation. Carbon can be formed through two separate side reactions, viz. CH₄ decomposition (Eq. 1.6) and CO

disproportionation, also referred to as Boudouard reaction (Eq. 1.7). CH₄ decomposition occurs at $T > 557$ °C, while the Boudouard reaction is favored for $T < 700$ °C.⁷⁴ These two side-reactions increase the final H₂ : CO ratio. Including the possibility of solid carbon formation in the thermodynamic equilibrium calculations (Figure 1.8b) predicts a H₂ : CO ratio close to 1 for $T > 900$ °C.

1.3.2. State of the art DRM catalysts

Catalysts based on earth-abundant metals, e.g. Ni and Co, and noble metals, e.g. Pt, Rh and Ru, are among the most studied DRM catalysts.^{71,75-76} Generally, noble metals exhibit a high DRM activity and also show a high stability due to their resistivity to coking.⁷⁷⁻⁷⁸ However, due to the very high price of noble metals, they are mainly used as promoters for the less expensive catalysts such as Ni.⁷⁹⁻⁸⁰ Owing to its high activity and significantly lower price compared to noble metals, Ni is considered to be the most suitable candidate for DRM in practical applications. However, Ni-based catalysts exhibit two major drawbacks that ultimately lead to catalyst deactivation, i.e. a high affinity to carbon deposition (Figure 1.9a) and catalyst sintering at high temperatures (ca. 900 °C) owing to the low Tammann temperature of metallic Ni (ca. 590 °C).^{75,81} Both deactivation routes reduce the quantity of surface Ni, which has been identified as the catalytically active phase for DRM (Figure 1.9b).⁸² To overcome the limitations of Ni-based DRM catalysts, several approaches have been investigated such as the synthesis of highly dispersed Ni nanoparticles on various supports, the promotion of Ni-based catalyst by alkali metals or bi-metallic catalyst formulations, e.g. Ni-Rh,⁷⁹ Ni-Co⁸³ or Ni-Fe.⁸²

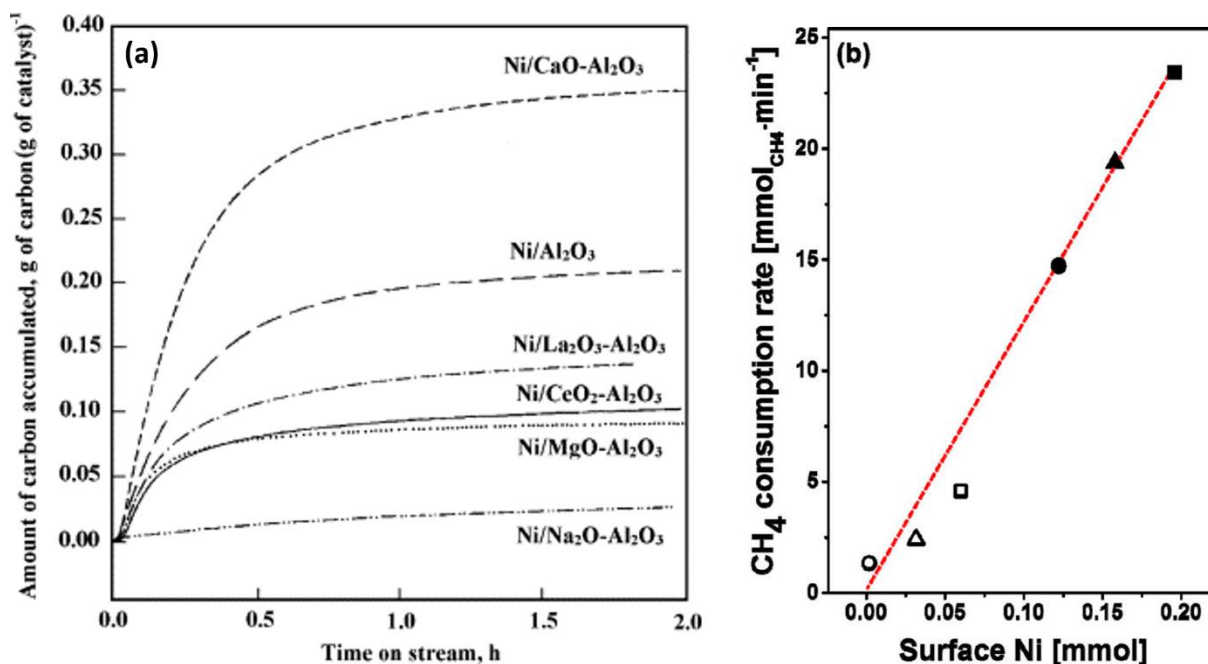


Figure 1.9. a) Carbon deposition on Ni-based catalysts during the DRM for different supports as determined by thermogravimetric analysis (TGA); CH₄ : CO₂ = 1 and 700 °C (adopted from ref. ⁸¹); b) rate of methane consumption (after 1 h time-on-stream (TOS)) as a function of the quantity of surface Ni. (Adopted from ref. ⁸²)

1.3.3. Molybdenum carbide as an alternative methane reforming catalyst

In the 1970s, transition metal carbides, i.e. Mo₂C⁸⁴ and WC,⁸⁵ have been reported to possess noble metal-like catalytic activity. Since that time, transition metal carbides have been researched with the objective to substitute noble metal catalysts in a variety of industrially relevant reactions. For example, molybdenum carbide (Mo₂C) has been shown to be catalytically active in the WGS,⁸⁶⁻⁸⁹ methane aromatization,⁹⁰⁻⁹¹ Fischer–Tropsch,⁹²⁻⁹⁴ and hydrogenation reactions.⁹⁵⁻⁹⁶ Molybdenum carbide exhibits several advantages compared to the state of the art transition metal-based catalysts. In particular, due to its high T_T (ca. 1200 °C) it is resistant to thermal sintering, one of the main deactivation routes of transition metal-based catalysts. At the same time, carbide-based catalysts are highly resistant to carbon deposition⁹⁷ and do not suffer significantly from sulphur poisoning.⁹⁸⁻⁹⁹ However, the high oxophilicity of molybdenum carbide is its major drawback. Oxidative feeds (e.g. gas feed containing O₂ or CO₂) will lead to the rapid oxidation of Mo₂C to MoO₂, i.e. to catalyst deactivation.

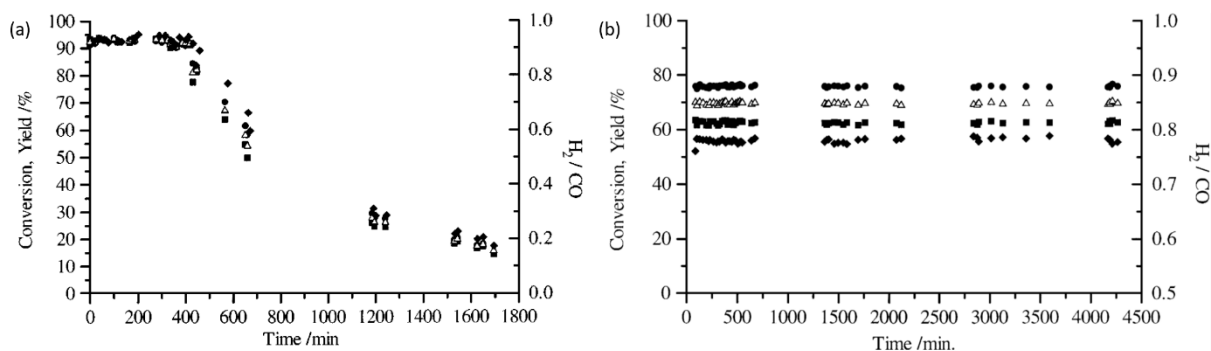


Figure 1.10. Stability study of β -Mo₂C under DRM conditions (850 °C, GHSV = 2.9×10^3 h⁻¹, CH₄ : CO₂ = 1) at a) 1 bar and b) 8.3 bar. (■) C[CH₄]; (●) C[CO₂]; (△) Y[CO] and (◆) H₂/CO. (Adopted from ref. ⁹⁷)

Nevertheless, in the late 1990s Mo₂C was reported to be an active catalyst for DRM. ^{97,100} In particular, unsupported high surface area (30 m² g⁻¹) β -Mo₂C was reported to show a high catalytic activity both at ambient (1 bar) and elevated (8 bar) pressures with CH₄ conversion exceeding, respectively, 90 % and 60 % at 850 °C (Figure 1.10a,b).⁹⁷ However, catalyst deactivation was observed when the DRM reaction was performed at atmospheric pressure. Operating the DRM at ca. 8 bar gave a stable catalytic performance without deactivation for more than three days (Figure 1.10b). XRD analysis of the spent catalyst revealed that deactivation was most likely due to the oxidation of β -Mo₂C to MoO₂, viz. $\text{Mo}_2\text{C} + 5 \text{CO}_2 \rightarrow 2 \text{MoO}_2 + 6 \text{CO}$. Since then, multiple reports have confirmed the deactivation of the Mo₂C-based catalyst due to oxidation under DRM conditions. Several strategies have been developed to mitigate this oxidative deactivation, including:

(i) *Operating DRM at elevated pressure.* One of the main strategies to attenuate the oxidative deactivation of Mo₂C-based catalysts is operating the DRM reaction at elevated pressures, ca. 2-10 bar.^{97,101-102} The improved catalyst stability has been attributed to a reduction in mass transfer rates with increasing pressures, thus maintaining the product gases within the catalyst boundary layer protecting in turn Mo₂C against oxidation.¹⁰³ However, operating DRM at elevated pressures complicates the overall process making it less attractive for practical applications.

(ii) *Stabilization of well-dispersed Mo₂C particles on a support.* Another route is the stabilization of Mo₂C on a support, e.g. zirconia, alumina or carbon.¹⁰⁴⁻¹⁰⁸ For example, ZrO₂ has been reported to effectively stabilize Mo₂C. The stabilization effect increases with decreasing Mo-loading and was attributed to the preferential binding of CO₂ to the support

in preference to CO_2 activation on the Mo_2C surface.¹⁰⁴ Recently, the encapsulation of Mo_2C within carbon nanotubes has been reported as another successful method of stabilization.¹⁰⁷

(iii) *Promotion of Mo_2C -based catalyst with late transition metals.* The promotion of Mo_2C with a DRM active phase, e.g. Ni or Co, has been studied widely and shown to enhance the stability of Mo_2C .¹⁰⁹⁻¹¹⁴ For example, a Ni-modified Mo_2C catalyst was evaluated for DRM at atmospheric pressure and it was found that at the optimal Ni : Mo ratio of 1 : 2, a stable catalytic performance could be achieved (Figure 1.11a).¹¹² It was suggested that CH_4 dissociation occurred on Ni sites, while CO_2 activation took place on Mo_2C . Based on these observations, a catalytic redox cycle was proposed (Figure 1.11b). However, this approach compromises the motivation for the use of Mo_2C as a replacement for DRM catalysts based on late transition metals.

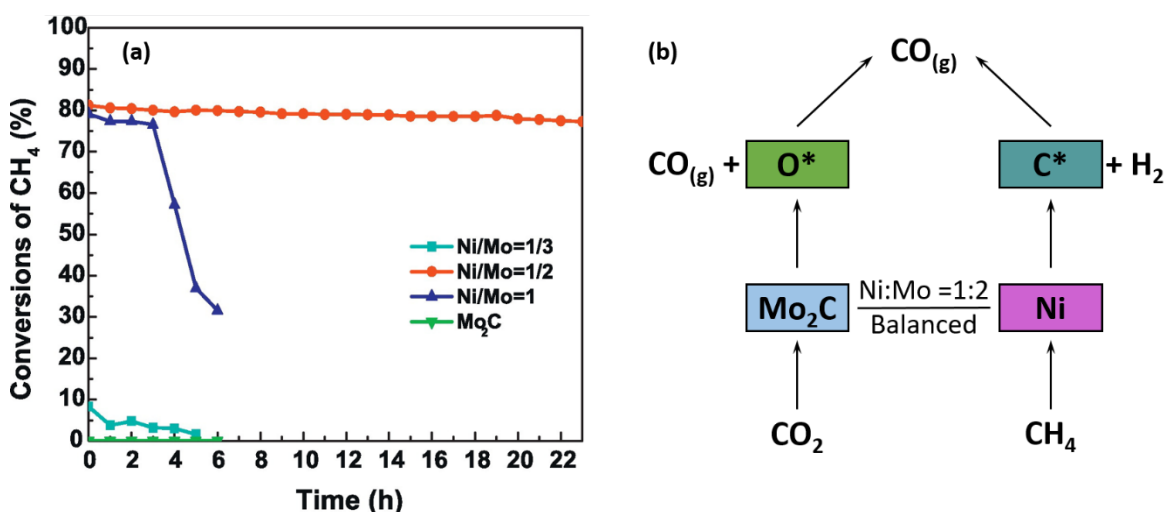


Figure 1.11. a) Stability study of Ni– Mo_2C catalysts for the DRM at 1 bar; b) proposed catalytic oxidation–re carburization cycle over a Ni– Mo_2C -based catalyst. (Adopted from ref. ¹¹²)

From a mechanistic standpoint, it is important to underline that it is not likely that the actual active sites for DRM are located on a pristine Mo_2C surface (Mo-terminated). It is believed that the metal-terminated Mo_2C surface evolves under DRM reaction conditions, owing to its high oxophilicity, forming a molybdenum oxycarbide surface layer or phase ($\text{Mo}_2\text{C}_x\text{O}_y$). The stability and nature of this oxycarbide surface layer or phase plays an important role in the catalyst performance. For example, it has been reported that the oxygen coverage of the molybdenum carbide surface influences its activity and selectivity in CO_2 -assisted propane dehydrogenation.¹¹⁵ Therefore, a further in-depth evaluation of $\text{Mo}_2\text{C}_x\text{O}_y$

active species under reaction conditions is required for a successful development of efficient Mo₂C-based catalysts.

1.3.4. MXenes – promising materials for heterogeneous catalysis applications

Recently, a new family of well-defined two-dimensional (2D) carbides, nitrides, and carbonitrides has been discovered.¹¹⁶⁻¹¹⁷ Its general formula is $M_{n+1}X_nT_x$, where M is an early transition metal, $n = 1, 2, 3$, X is C and/or N, and T_x are surface oxo, hydroxy and/or fluoro groups.^{116,118} Since the discovery of Ti₃C₂T_x, the first MXene reported in 2011,¹¹⁶ a large number of potential MXene phases was predicted theoretically and many of them have been synthesized (Figure 1.12).¹¹⁹

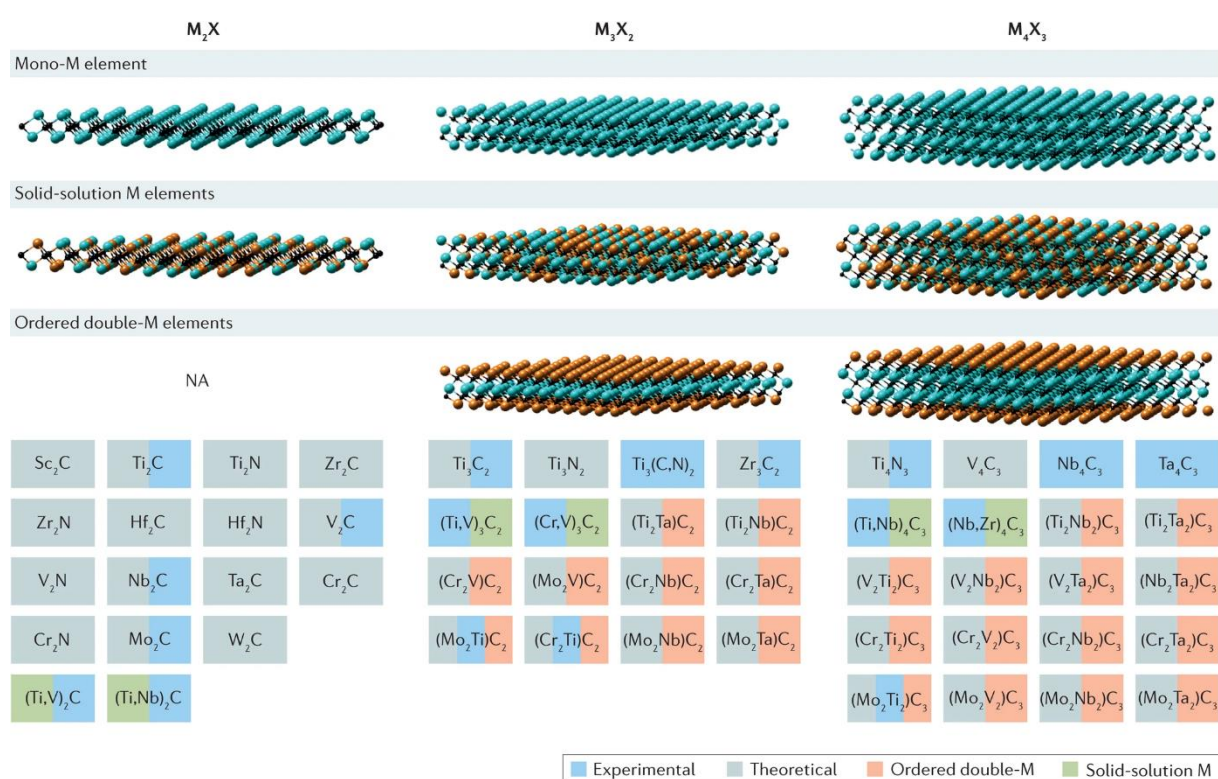


Figure 1.12. MXenes phases reported by 2017. (Adopted from ref. 119)

Synthetically, MXenes are prepared by the selective etching of an A element from a respective ternary layered MAX phase with the general formula $M_{n+1}AX_n$, where A is an A-group element (mostly IIIA and IVA), while M and X are as defined above.¹²⁰ Selective etching is typically performed by the immersion of an MAX phase into an aqueous solution of HF.^{116,121} HF treatment results in a replacement of the A element by T_x surface groups. The full transformation of the MAX phase into a MXene is accompanied by a weakening (or complete disappearance) of all but the (0 0 l) XRD peaks (Figure 1.13a).¹¹⁷ Additionally, a shift of the

(0 0 *l*) peaks towards lower 2θ values is expected, indicating the increase of the value of the lattice parameter *c* due to the incorporation of *T_x* groups. MXenes often feature an accordion-like morphology resembling exfoliated graphite (Figure 1.13b). A counterexample is the morphology of Mo₂CT_x that is comprised of dense MXene nanoplatelets.¹²²

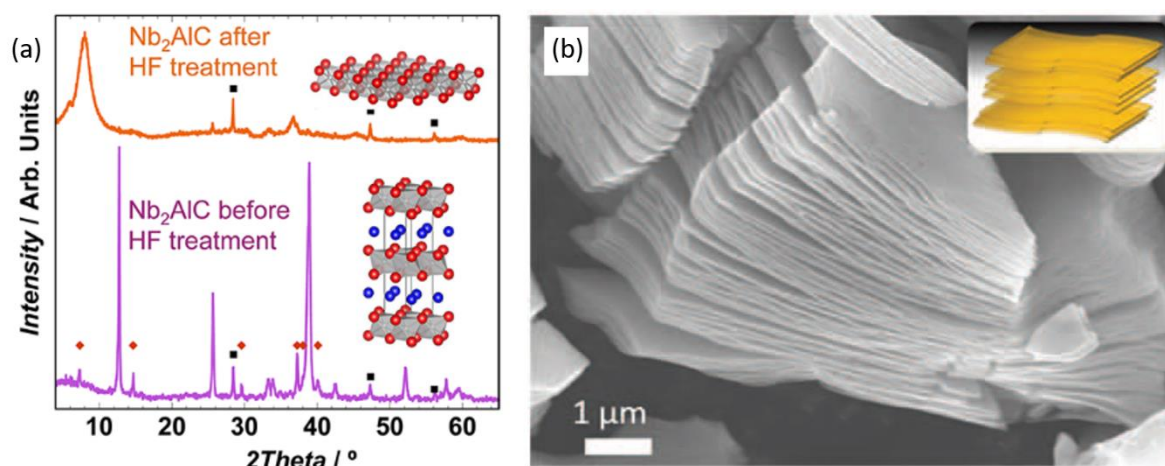


Figure 1.13. a) XRD diffraction patterns of Nb₂AlC before and after HF treatment; (■) Si (internal standard) and (♦) Nb₄AlC₃ (adopted from ref. ¹²³) b) SEM image of Ti₃C₂T_x with an accordion-like structure. (Adopted from ref. ¹²⁴)

A combination of unique properties such as 2D morphology, tunability of the surface chemistry, high elastic moduli along the basal plane, high electron conductivity and intercalation of ions between individual layers makes MXenes promising materials for a large variety of applications (Figure 1.14).¹²⁵ So far, MXenes have been exploited predominantly for energy storage, viz. Li or Na-ion batteries¹²⁶⁻¹²⁸ and supercapacitors.^{124,129-130} In the field of catalysis, MXenes have been explored for photo-,¹³¹⁻¹³² electro-¹³³⁻¹³⁷ and heterogeneous catalytic applications,^{122,138-139} however the main focus remains on electrocatalysis. For example, it has been reported recently that Co-substituted Mo₂CT_x has a high activity for the hydrogen evolution reaction (HER) with an excellent operational stability when compared to the best non-noble metal-based HER catalysts reported so far.¹³³

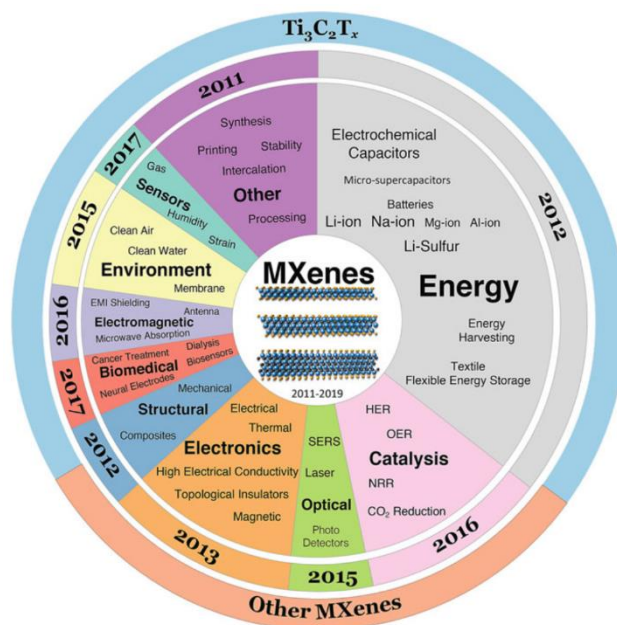


Figure 1.14. Selected applications and properties of MXenes (data from 2011 to 2019). (Adopted from ref. ¹²⁵)

In traditional heterogeneous catalysis such as the WGS reaction, MXenes have been utilized commonly as a support material for late transition metals, such as Pt, providing reactive metal-support interactions (RMSIs).¹³⁸⁻¹³⁹ Additionally, it was demonstrated that MXenes can efficiently stabilize single atom catalysts, such as Pt, Pd, Ru, Rh and Ir.^{137,140} Surprisingly, there is only a very limited number of reports describing the use of pure MXenes as active catalysts, e.g. $Ti_3C_2T_x$ catalyzing the dehydrogenation of ethylbenzene.¹⁴¹ The wide exploitation of catalysts based on MXenes in heterogeneous catalysis is currently limited by several factors, including concerns about their structural and thermal resistance under oxidative and/or reducing conditions. For example, $Ti_3C_2T_x$ has been reported to degrade to titania already under mild oxidizing conditions, especially in aqueous media.¹⁴²⁻¹⁴⁵ That being said, MXenes such as Mo_2CT_x can serve as model compounds and/or precursors for the aforementioned active $Mo_2C_xO_y$ phase in Mo_2C -based DRM catalysts.

1.4. Sorption-enhanced steam methane reforming

As mentioned above, the steam methane reforming (SMR) (Eq. 1.4) is a key reaction in pre-combustion CO_2 capture systems converting methane into a synthesis gas. Since the SMR is highly endothermic, high operation temperatures, i.e. 850-1000 °C, are required for high methane conversions.¹⁴⁶ A typical CO concentration in the effluent gas of a steam

reformer is ca. 10%.¹⁴⁷ Hence, to increase the purity of H₂ further, CO must be either separated from H₂ or converted further to CO₂ (followed by CO₂ capture). CO conversion is achieved by the water-gas shift (WGS) reaction (Eq. 1.1); first at a high temperature (300-500 °C) followed by a low temperature (180-300 °C) operation, reducing the CO concentration down to 3-0.5 vol%.¹⁴⁷ The residues of CO can be further removed *via* a CO preferential oxidation (PROX) method.¹⁴⁸ Finally, to yield a pure stream of H₂, CO₂ is removed by e.g. amine scrubbing. Overall, the entire process is complex requiring several reactor units that operate also at different temperatures, leading to high operational costs (Figure 1.15a).

1.4.1. Sorption-enhanced steam methane reforming

To significantly reduce the complexity of H₂ production (and hence also the pre-combustion CO₂ capture) process, the so-called sorption-enhanced steam methane reforming (SE-SMR) process has been proposed (Figure 1.15b).¹⁴⁹

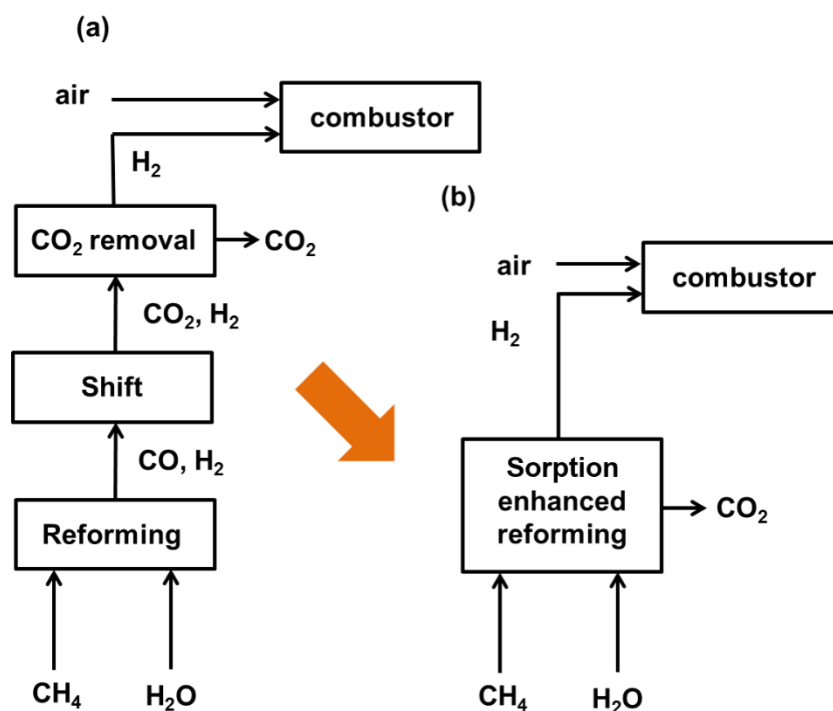
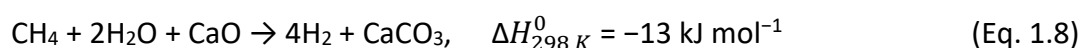


Figure 1.15. Block diagrams illustrating (a) the “conventional” pre-combustion process and (b) the sorption-enhanced steam methane reforming process.

The SE-SMR process combines the SMR (Eq. 1.4), WGS (Eq. 1.1) and CO₂ capture (Eq. 1.2) reactions proceeding simultaneously in a single reactor (Eq. 1.8).



Compared to "conventional" pre-combustion CO₂ capture using methane as a fuel, the SE-SMR reaction would allow for a substantial process intensification reducing significantly the number of unit operations (Figure 1.15). Additionally, the process can be operated at significantly lower temperatures (ca. 600 °C),¹⁵⁰ thus reducing catalyst deactivation through thermal sintering. Finally, due to Le Chatelier's principle¹⁵¹ the immediate removal of CO₂ *via* the carbonation reaction shifts the equilibrium to the product side, thus allowing very high methane conversions and hydrogen yields.

The availability of highly efficient and stable CaO-based CO₂ sorbents is a key requirement for the SE-SMR process.¹⁵²⁻¹⁵³ Due to the finite CO₂ capacity of the sorbent, the SE-SMR process has to operate, similar to adsorption processes, in a semi-batch mode; allowing for the periodic regeneration of the sorbent. Typically, the SE-SMR reaction proceeds in three distinct stages, viz. pre-breakthrough, breakthrough, and post-breakthrough stages (Figure 1.16).¹⁴⁹

- (i) The pre-breakthrough stage is characterized by the production of high purity H₂ and complete CH₄ conversion;
- (ii) The breakthrough stage is characterized by a reduction in H₂ purity due to the saturation of the sorbent with CO₂;
- (iii) In the post-breakthrough stage, owing of the complete conversion of CaO to CaCO₃, the reaction approaches the behavior of the conventional SMR combined with WGS.

The stability of the CaO-based sorbent plays a key role to the efficiency of the SE-SMR process, as the extend of the period of high H₂ yield (pre-breakthrough stage) is critically affected by the CO₂ uptake capacity of the sorbent (Figure 1.16). Additionally, the cyclic regeneration of the sorbent imposes an additional requirement on the reforming catalyst, which has to remain stable in an oxidative environment, i.e. a pure stream of CO₂.

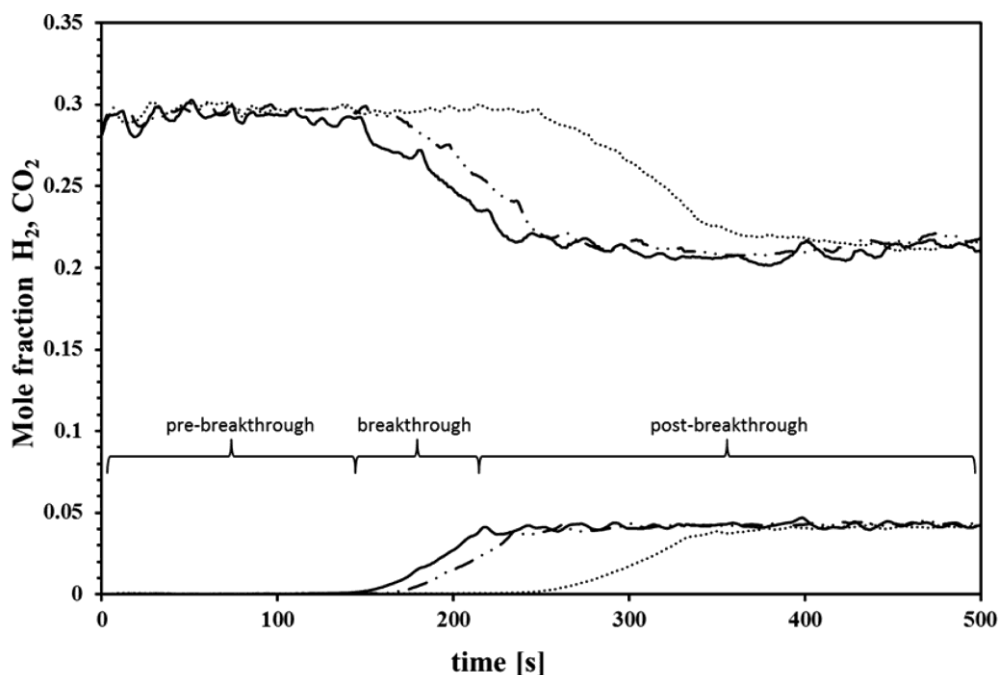


Figure 1.16. SE-SMR (550 °C) breakthrough curves as a function of cycle number using a Ni-Ca-based bi-functional material. (····) 1st cycle, (- ·-) 5th cycle, and (—) 10th cycle. (Adopted from ref. ¹⁵⁴)

1.4.2. Bi-functional materials for SE-SMR

The SE-SMR process requires both a very active and stable CO₂ sorbent and a methane reforming catalyst. Generally, transition metals-based catalyst such as Pt, Ru,¹⁵⁵ Rh¹⁵⁶ and Ni,^{154,157} have been reported for SE-SMR applications. In a “simple” implementation, the CO₂ sorbent is physically mixed with the SMR catalyst.¹⁵⁷⁻¹⁶⁰ For example, a continuous stream of high purity H₂ (>95 %) was obtained over a mixture of a NiO/Al₂O₃ catalyst and a CaO/Ca₁₂Al₁₄O₃₃ CO₂ sorbent, operated in two parallel fixed bed reactors (Figure 1.17).¹⁶⁰ However, a physical mixing of respective CO₂ sorbent and catalyst comes with several disadvantages such as (i) lower rates of heat and mass-transfer and (ii) a large quantity of inactive supports/stabilizers for both the reforming catalyst and the CO₂ sorbent, leading to a higher reactor volume for a given H₂ yield.

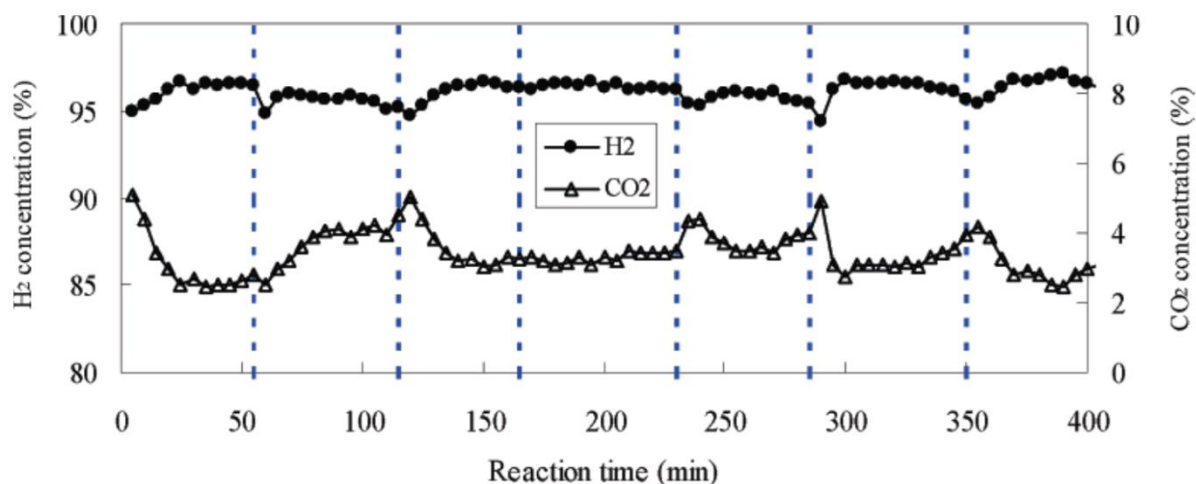


Figure 1.17. Evolution of H₂ and CO₂ (dry basis) with time on stream during the SE-SMR reaction over a physical mixture of a NiO/Al₂O₃ catalyst and a CaO/Ca₁₂Al₁₄O₃₃ sorbent operated in two fixed-bed reactors. (Adopted from ref. ¹⁶⁰)

To overcome those shortcomings, recent works have focused on the development of novel bi-functional materials that contain both the catalysts and the CO₂ sorbent.^{154-155,161-163} It has been argued that the close proximity of the reforming and CO₂ abstraction sites increase the heat and mass-transfer characteristics allowing for a more effective coupling of the endothermic reforming and the exothermic carbonation reaction. Furthermore, the quantity of an inert support/stabilizer material can be reduced appreciably. An important aspect to consider in the development of bi-functional materials is the prevention of irreversible reactions between the catalyst and the sorbent.

In bi-function materials, Ni is often the catalyst of choice and is typically introduced *via* impregnation of the (supported) CaO-based sorbent with a nickel salt solution.¹⁶² Alternatively, bi-functional materials can be synthesized in a single-pot approach by co-precipitation.¹⁵⁴ However, a disadvantage of the current formulations of bi-functional materials is the high loading of Ni, i.e. 40-50 wt.% of Ni that has been required to obtain high SRM activity, hence, reducing significantly the weight normalized CO₂ uptake of the bi-functional material. Additionally, Ni-based, bi-functional materials for the SE-SMR commonly suffer from deactivation due to carbon deposition.

As an alternative, noble metal-based bi-functional materials have been proposed for the SE-SMR process.¹⁵⁵⁻¹⁵⁶ For example, it has been reported that owing to its high activity, as little as 1.7 mol.% of Ru on Ca₃Al₂O₆-CaO (synthesized by a citrate sol-gel route) was sufficient to obtain an excellent SE-SMR performance.¹⁵⁵ Additionally, Ru/Ca₃Al₂O₆-CaO

showed a negligible degree of carbon deposition when compared to the Ni-based counterpart. However, the high price of noble metals reduces the attractiveness of such materials for practical applications. In this context, the development of alternative noble metal-free, bi-functional materials for the SE-SMR is of great interest.

1.5. The objectives and structure of this dissertation

The main goal of this dissertation is to advance different CCUS concepts by developing novel materials for the capture of CO₂ and its conversion. The work was divided into two main parts. The first part of the work (Chapters 2-4) reported is dedicated to the development of novel CaO-based CO₂ sorbents that show an enhanced cyclic stability. The second part (Chapters 5-7) is concerned with the development of highly active noble-metal free catalysts for the dry reforming of methane. The dissertation is organized as follows:

Chapter 1 introduces calcium looping and the reforming of methane.

Chapter 2 presents a scalable route using mechanochemical activation through ball-milling to synthesize highly effective CaO-based sorbents. A thorough optimization of the ball-milling parameters allowed to stabilize effectively the morphology of CaO by as little as 15 wt.% of MgO.

Chapter 3 explores the effect of doping CaO with alkali metal salts on its CO₂ uptake. Combining Na K-edge X-ray absorption spectroscopy (XAS) and electron microscopy techniques identified the formation of a dense layer of Na₂Ca(CO₃)₂ as a possibly reason for the loss in CO₂ uptake.

Chapter 4 describes a microfluidic approach to prepare hierarchically porous (HP) CaO-based CO₂ sorbents. Even without the addition of a stabilizer, the macrostructure was found to be stable over repeated carbonation and calcination reactions. It is shown that the addition of Al₂O₃ by atomic layer deposition (ALD) increases the stability of the microstructure of the sorbent, making HP-CaO-based sorbent a promising material for SE-SMR applications.

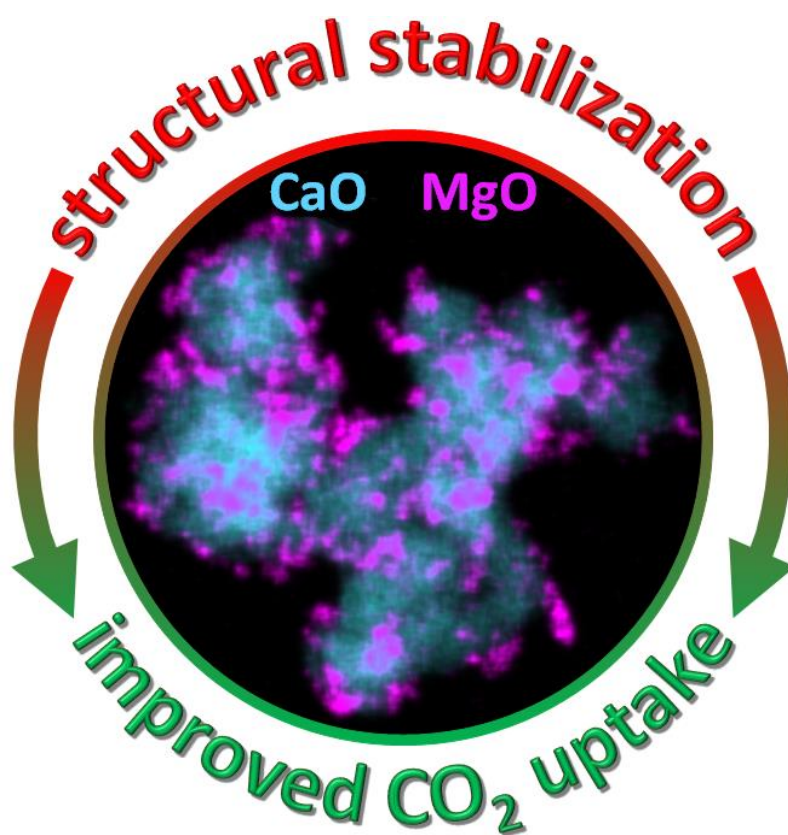
Chapter 5 reports on a Mo₂C-based catalyst, synthesized *via* two dimensional, MoO₃ nanosheets, supported on carbon spheres. The carburization process as well as the catalyst state under DRM reaction was followed by *in situ* XANES/XRD and advanced transmission electron microscopy.

In Chapter 6, a procedure to synthesize a phase-pure Mo_2CT_x is developed. Its structural and thermal stability is investigated by combined *in situ* XANES and XRD to determine the range of suitable operational temperatures of prospective MXene-based catalysts. The catalytic activity of Mo_2CT_x for the WGS reaction is demonstrated as a prove of concept.

Chapter 7 focuses on the development of novel two dimensional Mo_2CT_x -derived catalyst supported on SiO_2 . It is demonstrated that supporting exfoliated 2D- Mo_2CT_x films on SiO_2 eliminates sintering that has been observed for bulk Mo_2CT_x , thus, opening a window for high-temperature MXenes applications. 2D- Mo_2CT_x films supported on SiO_2 reveal a high catalytic activity for DRM. A combination of XAS and XPS experiments allows to assign oxycarbide 2D- Mo_2CO_x as a catalytically active phase.

Finally, the main conclusion of this work and an outlook for future work are presented in Chapter 8.

Chapter 2: Mechanochemically activated, calcium oxide-based, magnesium oxide-stabilized carbon dioxide sorbents



The results of this chapter are published as:

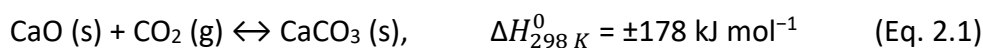
A. Kurlov, M. Broda, D. Hosseini, S. J. Mitchell, J. Pérez-Ramírez, C. R. Müller, Mechanochemically Activated, Calcium Oxide-Based, Magnesium Oxide-Stabilized Carbon Dioxide Sorbents, *ChemSusChem*, **2016**, 9, 2380-2390

2.1. Abstract

Carbon dioxide capture and storage (CCS) is a promising approach to reduce anthropogenic CO₂ emissions and mitigate climate change. However, the costs associated with the capture of CO₂ using the currently available technology, that is, amine scrubbing, are considered prohibitive. In this context, the so-called calcium looping process, which relies on the reversible carbonation of CaO, is an attractive alternative. The main disadvantage of naturally occurring CaO-based CO₂ sorbents, such as limestone, is their rapid deactivation caused by thermal sintering. Here, we report a scalable route based on wet mechanochemical activation to prepare MgO-stabilized, CaO-based CO₂ sorbents. We optimized the synthesis conditions through a fundamental understanding of the underlying stabilization mechanism, and the quantity of MgO required to stabilize CaO could be reduced to as little as 15 wt.%. This allowed the preparation of CO₂ sorbents that exceed the CO₂ uptake of the reference limestone by 200 %.

2.2. Introduction

Increasing anthropogenic greenhouse gases, in particular CO₂ emissions, are most likely the underlying reason for climate change.⁴ In this context, the implementation of CO₂ capture and storage (CCS) technologies¹⁶⁴⁻¹⁶⁶ is widely considered to reduce appreciably the release of CO₂ into the atmosphere in the near- to mid-term.¹⁶⁷ CCS involves capturing CO₂ from large point sources, e.g., fossil-fuel fired power stations, and subsequently storing it in suitable formations, e.g., saline aquifers.¹⁶⁸⁻¹⁶⁹ The Intergovernmental Panel on Climate Change (IPCC) predicts that by 2050 CCS can reduce the annual emissions of CO₂ by ~ ca. 8 Gt.¹⁰ However, currently the only commercially available CO₂ capture technology, aqueous amine scrubbing,¹³ is prohibitively expensive (32 – 77 \$ per t CO₂).¹¹ Therefore, substantial research activities are directed towards the development of less costly CO₂ capture technologies, which largely focus on solid sorbents. Attractive classes of materials for physisorption approaches include amine-functionalized supports^{16-17,170-171} and nanoporous materials as zeolites¹⁸⁻¹⁹ or metal-organic frameworks.^{20-21,172-175} Alternatively, CaO-based CO₂ sorbents are widely studied for high-temperature thermochemical CO₂ capture processes, such as calcium looping.²⁵⁻²⁷ The calcium looping process relies on the following reversible carbonation – calcination reaction pair (Eq. 2.1):



A key advantage of calcium looping is the very high theoretical CO₂ uptake capacity of CaO of 0.78 g_{CO₂} g_{sorbent}⁻¹ as well as the low price and natural abundance of limestone. Taking these favorable characteristics into account, MacKenzie et al.¹¹ predicted calcium looping to reduce the CO₂ capture costs by 60 % compared to amine scrubbing.

However, naturally occurring CaO-based CO₂ sorbents such as limestone have a major drawback, viz. the rapid decay of the CO₂ uptake over repeated cycles of carbonation and calcination.³⁰⁻³¹ Grasa and Abanades³¹ reported that the CO₂ capture capacity of limestone decreased by 600 % over the first 20 cycles, but stabilized at 0.075 – 0.08 g_{CO₂} g_{sorbent}⁻¹ during the following 500 cycles. The deactivation of limestone has been assigned mainly to thermal sintering, as the Tamman temperature of CaCO₃ ($T_T = 533 \text{ }^\circ\text{C}$) is significantly lower than the operating temperature of the process, (650 – 950 °C).^{25,32} Sintering of CaCO₃ is associated with a dramatic decrease in pore volume and surface area of the material.^{32,176} However, for CaO-based CO₂ capture, materials with a large pore volume are required as the ratio of the molar volume of the product (CaCO₃) and the active phase (CaO) is approximately 2 : 1. Thus, for the reaction not to become diffusion limited (the ratio of the diffusion coefficients of CO₂ in CaO and CaCO₃ is approximately 100 : 1)³³ a highly porous material is key to maximize the CO₂ uptake capacity and uptake kinetics during the comparatively short residence time in a circulating fluidized bed reactor (typically in the order of a few minutes).¹⁷⁷ Our current understanding, albeit not proven by direct measurements, is that the transition from kinetic to diffusion control takes place once a CaCO₃ layer of ~ 50 nm thickness forms on the unreacted CaO particle.³⁴

Owing to the importance of porosity, a critical requirement in the development of an effective CaO-based CO₂ sorbent is the structural stabilization of CaO, which is typically achieved by introducing an (inert) stabilizing/support material.^{38,42,45,50,52,178-189} A selection of previous attempts (tested cycles ≥ 30) to stabilize the cyclic CO₂ uptake of CaO is given in **Error! Reference source not found..**

These works exemplify three major shortcomings in the development of synthetic CaO-based CO₂ sorbents: (i) the reliance on cumbersome, complex synthetic procedures such as templating that cannot be controlled or scaled up easily; (ii) the preparation of materials

with a relatively low content of CaO (often < 70 wt.%); and/or (iii) the assessment of the performance of the cyclic CO₂ uptake and release under unrealistic conditions, e.g. the calcination reaction is often performed in N₂ and/or at temperatures below 900 °C, or pure CO₂ is used for carbonation. These “mild” testing conditions lead to artificially high CO₂ uptakes that can, however, not be expected under conditions encountered in practical units.

Table 2.1. Selection of attempts to improve the cyclic CO₂ uptake of CaO through the introduction of structural stabilizers.

Sorbent	Synthesis method	CaO content [wt.%]	Temperature		Gas atmosphere		CO ₂ uptake, 30 th cycle [g _{CO2} g _{sorbent} ⁻¹]	Ref.
			Carb. [°C]	Calc. [°C]	Carb.	Calc.		
CaO/ZrO ₂	Flame spray pyrolysis	60	700	700	30 vol.% CO ₂	100 vol.% He	0.50	38
CaO/Al ₂ O ₃	Carbon template	91	750	750	25 vol.% CO ₂	100 vol.% N ₂	0.56	42
CaO/Al ₂ O ₃	Co-precipitation	88.5	600	700	100 vol.% CO ₂	100 vol.% N ₂	0.48	178
CaO/Al ₂ O ₃	Wet mixing	35	650	800	33 vol.% CO ₂	100 vol.% N ₂	0.16	50
CaO/mayenite	Co-precipitation	85	650	900	15 vol.% CO ₂	15 vol.% CO ₂	0.22	52
CaO/mayenite	Latex template	75	650	950	15 vol.% CO ₂	100 vol.% CO ₂	0.44	179
CaO/SiO ₂	Mechanical mixing	48	700	800	15 vol.% CO ₂	100 vol.% N ₂	0.15 (10 th cycle)	180
CaO/SiO ₂	Mechanical mixing	85	650	850	15 vol.% CO ₂	air	0.18	181
CaO/SBA-15	Impregnation	49	700	910	100 vol.% CO ₂	100 vol.% N ₂	0.31	182
CaO/TiO ₂	Impregnation	41	650	850	100 vol.% CO ₂	100 vol.% N ₂	0.14	183
CaO/TiO ₂	Impregnation	90	600	750	20 vol.% CO ₂	100 vol.% N ₂	0.23	184
CaO/TiO ₂	Hydrolysis	90	600	725	20 vol.% CO ₂	100 vol.% N ₂	0.40	185
CaO/Y ₂ O ₃	Impregnation	14.3	740	740	25 vol.% CO ₂	100 vol.% Ar	0.07	186
CaO/MgO	Mechanical mixing	59	650	900	100 vol.% CO ₂	100 vol.% N ₂	0.47	45
CaO/cement	Wet mixing	90	850	850	100 vol.% CO ₂	100 vol.% N ₂	0.37	187
CaO/cement	Extrusion	25	650	900	15 vol.% CO ₂	100 vol.% N ₂	0.10	188
CaO/kaolin	Pelletizing	90	650	920	15 vol.% CO ₂	100 vol.% CO ₂	0.13	189

Recently, a few studies have attempted to address the above-listed shortcomings and reported interesting attempts to use e.g. inexpensive and scalable synthesis techniques like granulation¹⁸⁷⁻¹⁸⁹ or mechanochemical activation,⁴⁵ to prepare CaO-based CO₂ sorbents. For example, Manovic and Anthony¹⁸⁷ used a wet mixing technique to prepare CaO-based CO₂ sorbents stabilized by a cement binder. However, a shortcoming of this work was that the performance was evaluated under unrealistic conditions. Furthermore, the mechanism by which the structural additive stabilized CaO was not investigated in detail.

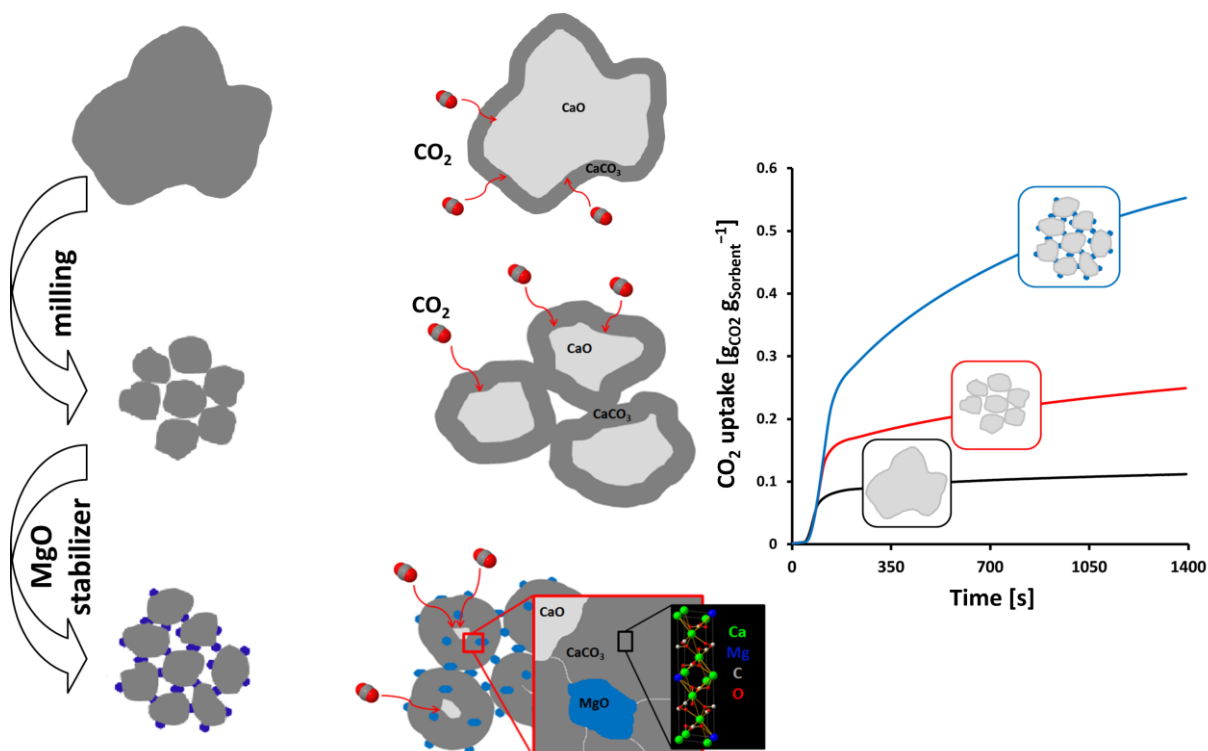


Figure 2.1. Schematic illustration of the strategy to improve the CO₂ uptake of CaO-based sorbents through mechanochemical activation with MgO.

Hence, this work is concerned with the development of MgO-stabilized, CaO-based CO₂ sorbents using the single-step, scalable route of wet-milling (Figure 2.1). To obtain a high CO₂ uptake, the amount of support material was limited to ~ 15 wt.%. By decorating the surface of small CaO grains with (high Tammann temperature) MgO nanoparticles sintering is expected to be reduced significantly. Thus, the porous structure of the material and the small grain size of the CaO particles (obtained through ball milling) are largely preserved, leading, in turn, to a rapid CO₂ uptake. The combined effects of the mechanochemical activation and stabilization with MgO yield a CaCO₃ product layer with a higher diffusivity for CO₂. This favorable characteristic will improve appreciably the CO₂ uptake in the second, diffusion

controlled, stage of the carbonation reaction. By determining in detail the structural, morphological, and porous properties of the materials and the cyclic CO₂ uptake characteristics, a fundamental understanding of the effect of MgO is obtained, allowing us to optimize the CO₂ sorbent. The best material developed here exceeded the CO₂ uptake of the reference limestone by 200 % when tested under *realistic* reaction conditions relevant to those at the industrial scale.

2.3. Experimental section

2.3.1. Materials

Commercial CaCO₃ (Fischer Chemicals, CAS: 471-34-1, analytical reagent grade) and MgCO₃ (Acros Organics, CAS: 39409-82-0, extra pure) powders were used as received without further treatment. The CaCO₃ and MgCO₃ precursors were mixed in appropriate quantities to obtain the desired ratios of Ca : Mg. Wet ball milling was performed in a Pulverisette 7 planetary micro mill (Fritsch, Germany) using 45 cm³ silicon nitride jars filled with 110 silicon nitride balls of 5 mm diameter. A fixed amount (7 g) of the precursor powders and deionized water (10 cm³) were used in each jar. The milling time was varied from 5 min to 48 h and the milling speed from 200 to 800 rpm. After milling, the suspension obtained was collected in a crystallization dish and dried in an oven overnight at 100 °C. The following nomenclature is used for the samples: (100 – x)Ca/xMg-yh(m)-z (h and m correspond to the units hours and minutes, respectively), where **x** refers to the quantity of MgCO₃ (mol.%), **y** indicates the milling time in minutes or hours and **z** is the milling speed in rotations per minute. For example, 80Ca/20Mg-30m-500 is a sample that contains a Ca:Mg ratio of 8 : 2 and was milled for 30 min at 500 rpm, and Ca-48h-200 is pure CaCO₃ that was milled for 48 h at 200 rpm. Natural Rheinkalk limestone (Rheinkalk limestone pit, Germany) was used as the reference material.

2.3.2. Characterization

The crystallinity and phase composition of the sorbents was analyzed using X-ray powder diffraction (XRD) (Bruker, AXS D8 Advance). The X-ray diffractometer was equipped with a Lynxeye superspeed detector and operated at 40 mA and 40 kV. All samples were scanned within the 2θ range of 5 – 90° using a step size of 0.025°. The qualitative phase analysis was performed using the Eva software package (Bruker Corporation). The crystallites

size was determined by applying the Scherrer equation to three individual reflections (012, 104 and 113) for each sample.

Changes in particle size were assessed by laser diffraction using a Mastersizer 3000 instrument (Malvern Instruments) and the distributions were calculated by Mie theory. Measurements were conducted in water and the measurable size range was 0.01 – 3500 μm . To break up any loosely bound agglomerates and obtain reproducible data, the suspensions (< 1 vol.%) were sonicated for 10 min prior to the measurements.

The particle size and morphology of the precursors and the CO₂ sorbents synthesized was examined using scanning electron microscopy (SEM) (LEO Gemini 1530, Zeiss). Prior to imaging the samples were sputtered with a thin (3 – 5 nm) layer of Pt. The particle size distribution of the ball-milled material was calculated from SEM images using the ImageJ software analysing 300 – 500 particles per sample.

N₂ sorption (Quantachrome NOVA 4000e) was used to determine the surface area and pore volume of the CO₂ sorbents. Prior to the measurements, each sample (1 g) was degassed at 300°C for at least 2 h. The Brunauer-Emmett-Teller (BET)¹⁹⁰ and the Barrett-Joyner-Halenda (BJH)¹⁹¹ models were used to calculate the surface area and pore volume, respectively.

Mercury intrusion porosimetry was performed using a Micromeritics Autopore IV 9510 operated in the pressure range from vacuum to 418 MPa. Samples were degassed *in situ* prior to the measurement. A contact angle of 130° for mercury and a pressure equilibration time of 10 s were used. The pore size distribution was determined by application of the Washburn equation.¹⁹²

To visualize the mixing between the active phase (CaO) and the support, scanning transmission electron micrographs and elemental maps were acquired using a FEI Talos F200X electron microscope (200 kV). The microscope was equipped with a high brightness Schottky FEG and a Super-X integrated EDS system, which includes four silicon drift detectors (SDDs) symmetrically placed around the sample.

2.3.3. CO₂ capture tests

The materials synthesized were investigated under both mild and realistic conditions using a thermogravimetric analyzer (TGA, Mettler Toledo TGA/DSC 1). Prior to the cyclic CO₂

uptake experiments, all samples were calcined at 800 °C for 2 h in air. In a typical TGA experiment 10 – 11 mg of sample were placed in an alumina crucible (70 µL).

Mild conditions were used for fast screening at a constant temperature of 750 °C. The samples were heated to 750 °C using a ramp of 10 °C min⁻¹ under a N₂ flow of 20 cm³ min⁻¹. Additionally, a constant N₂ purge (25 cm³ min⁻¹) was applied over the microbalance. Carbonation was performed for 20 min in an atmosphere containing 40 vol.% CO₂ in N₂ (flow rate 75 cm³ min⁻¹), and calcination was performed for 20 min by switching the gas to pure N₂ (flow rate: 45 cm³ min⁻¹). For each CO₂ sorbent the carbonation and calcination cycle was repeated 25 times.

The most promising CO₂ sorbents developed were investigated under *realistic conditions* in additional TGA experiments. Here, the carbonation reaction was performed for 20 min in 20 vol.% CO₂ in N₂ (total flow rate: 150 cm³ min⁻¹) at 650 °C. Subsequently, the materials were calcined for 10 min in pure CO₂ at 900 °C (flow rate: 30 cm³ min⁻¹). All heating and cooling steps were performed at a rate of 50 °C min⁻¹. The cyclic carbonation-calcination experiments were repeated 30 times. The cyclic CO₂ uptake, expressed in g_{CO₂} g_{sorbent}⁻¹, was calculated from the measured weight change as:

$$CO_2 \text{ uptake} = \frac{m_{carb} - m_{calc}}{m_{calc}} \quad (\text{Eq. 2.2})$$

2.4. Results and discussion

The X-ray diffractograms of the CaCO₃ and MgCO₃ precursors are shown in Figure 2.2a and b. CaCO₃ contained only the polymorph calcite (average crystallite size of 45 ± 5 nm), whereas MgCO₃ (Acros Organics) contained only hydromagnesite (Mg₅(CO₃)₄(OH)₂ · 4H₂O) (average crystallite size of 25 ± 5 nm).

2.4.1. Optimization of the mechanochemical activation

To optimize the synthesis conditions, a set of calcite samples were first milled for different durations and at different rotation speeds to assess the impact of these two operation parameters on the particle characteristics (size, morphology and associated surface area and pore volume).

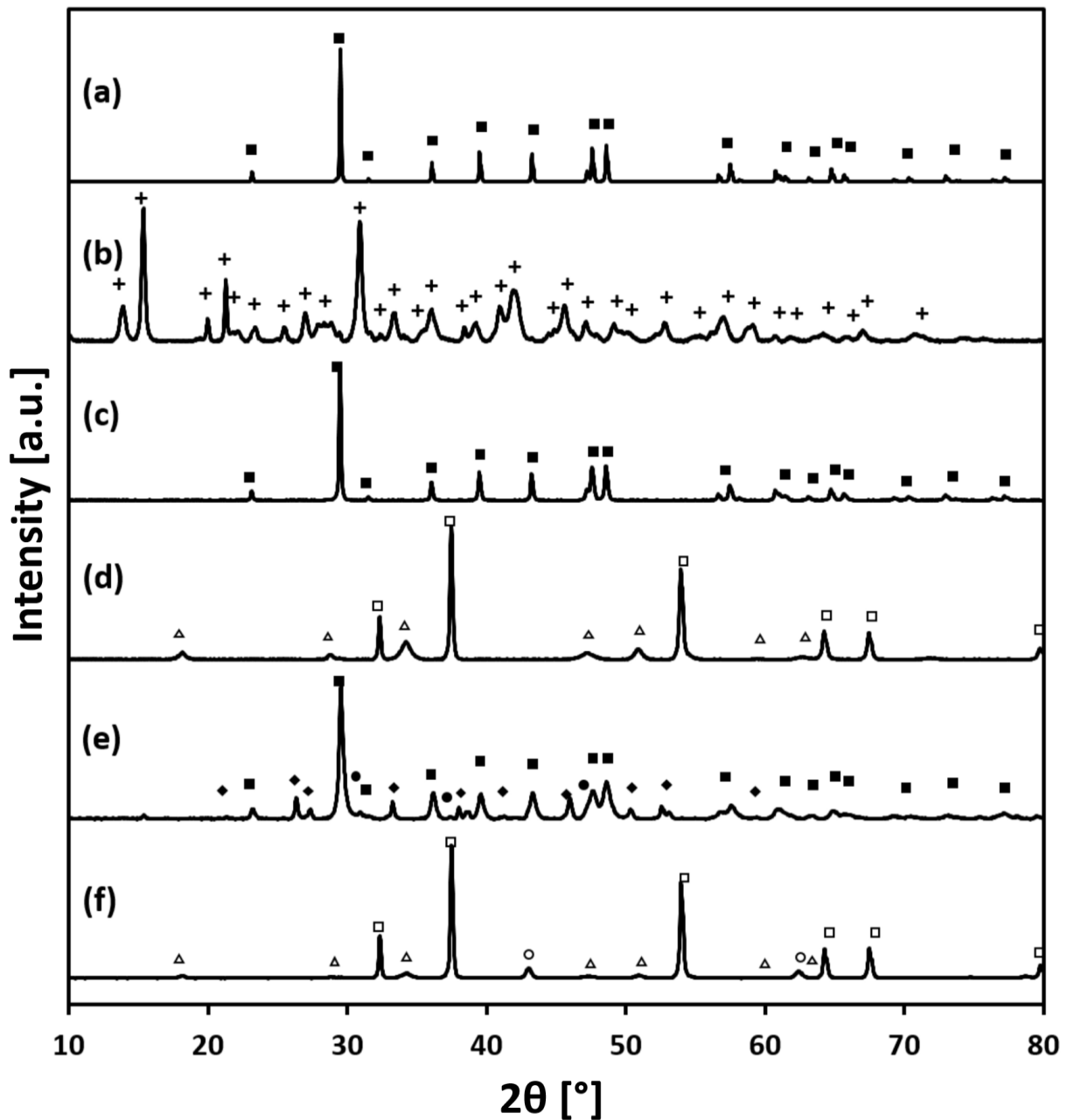


Figure 2.2. XRD patterns of a) CaCO_3 precursor, b) MgCO_3 precursor, c) Ca-48h-500, d) Ca-48h-500 calcined at $800\text{ }^\circ\text{C}$ for 2 h, e) 80Ca/20Mg-48h-500, f) 80Ca/20Mg-48h-500 calcined at $800\text{ }^\circ\text{C}$ for 2 h; The following phases were identified: (+) calcite, CaCO_3 ; (+) hydromagnesite, $\text{Mg}_5(\text{CO}_3)_4(\text{OH})_2 \cdot 4\text{H}_2\text{O}$; (♦) aragonite, CaCO_3 ; (●) magnesite, MgCO_3 ; (□) lime, CaO ; (▲) portlandite, $\text{Ca}(\text{OH})_2$; (○) magnesia, MgO .

2.4.2. Phase identification using X-ray diffraction

The resulting materials were analyzed by XRD after calcination at $800\text{ }^\circ\text{C}$ (Figure 2.2). The milling conditions did not affect the formation of phases and calcite was seen in all materials. Also, the crystallite size ($45 \pm 5\text{ nm}$) was not altered by ball-milling. Contradictory to our observations, Burns and Bredig¹⁹³ and Li et al.¹⁹⁴ reported that the dry mechanical

milling of calcite results in the formation of the CaCO_3 polymorph aragonite, owing to the high shear forces and local pressures encountered during milling.¹⁹³ Specifically, Burns and Bredig¹⁹³ reported the formation of traces of aragonite after 30 min of grinding (electric mortar grinder), whereas Li et al.¹⁹⁴ observed the formation of aragonite after 6 h of dry milling in a vibrational ball mill. However, in this work, the wet ball-milling of pure calcite did not lead to the formation of aragonite (for milling times up to 48 h). It can be speculated that the absence of the calcite-aragonite phase transition is due to lower local shear forces and pressures experienced when milling in water. After calcination at 800 °C for 2 h in air, calcite was decomposed to lime (CaO) (Figure 2.2d). The presence of a small fraction of calcium hydroxide ($\text{Ca}(\text{OH})_2$) was due to the highly hygroscopic nature of lime.

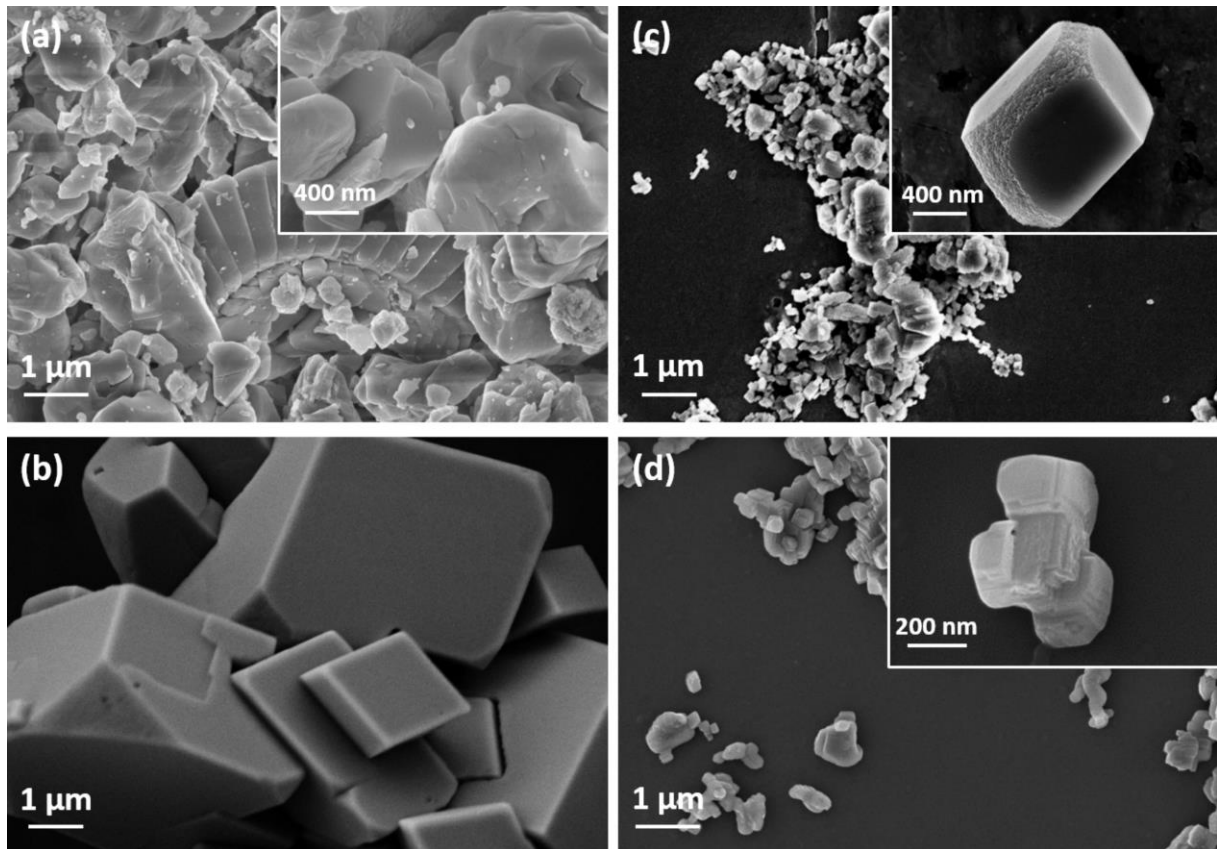


Figure 2.3. Scanning electron micrographs of: a) limestone, b) CaCO_3 precursor, c) Ca-1h-500, d) Ca-48h-500.

2.4.3. Morphological characterization of ball-milled CaO

The morphology and particle size distribution of ball-milled calcite were characterized by scanning electron microscopy (SEM), by imaging and analyzing approximately 300 – 500 particles per sample (Figure 2.3). The particle diameter was calculated from the projected

particle area, assuming a spherical shape. Figure 2.3 shows also electron micrographs of the reference limestone (a) and calcite precursor (b). Fresh, uncalcined limestone was composed of grains of 1 – 2 μm in size. The particles of the commercial calcite precursor were of cubic shape and had an original particle size in the range of $10 \pm 5 \mu\text{m}$ (the particle size distribution of ball-milled calcite was also determined by laser scattering as shown in Figure 2.4). As expected, the median particle size (D50) obtained from the SEM images decreased continuously with increasing milling time from 10 μm for the original calcite precursor down to $\sim 350 \text{ nm}$ after 48 h of milling. The same trend was observed for the particle sizes determined by laser diffraction, in Figure 2.4b and d, viz. the median particle diameter decreased from 10 μm for the original precursor to $\sim 500 \text{ nm}$ for Ca-48h-500. Examples of the particle size distributions obtained by laser diffraction and SEM imaging are given in Figure 2.4b and c, respectively. Generally, the results obtained by the two techniques were in remarkably good agreement. The slightly larger particle diameters obtained by laser diffraction were probably due to the formation of some particle agglomerates, which were not broken apart during the ultrasonic treatment. The calcite sample milled for 48 h possessed a mono-modal size distribution, whereas broad bi-modal particle size distributions were observed for samples that were milled for shorter durations. Consistently, examination of SEM images of Ca-1h-500 (Figure 2.3c) revealed a mixture of fine and larger particles with respective mean particle sizes of 0.4 μm and 1 μm , taken as the maximum values of the distributions. The larger particles had rounded-off edges and a coarse (“damaged”) surface morphology, whereas the original precursor particles showed well-defined facets and edges.

A detailed particle size analysis of the samples prepared under varying milling speeds (fixed milling time) by laser diffraction (Figure 2.4d) revealed that the CaCO_3 milled at 200 rpm (Ca-12h-200) consisted of particles with a median particle size of $\sim 1 \mu\text{m}$. Comparatively samples prepared using higher milling speeds of 500 and 800 rpm (Ca-12h-500 and Ca-12h-800) exhibited a smaller median particle size ($\sim 650 \text{ nm}$).

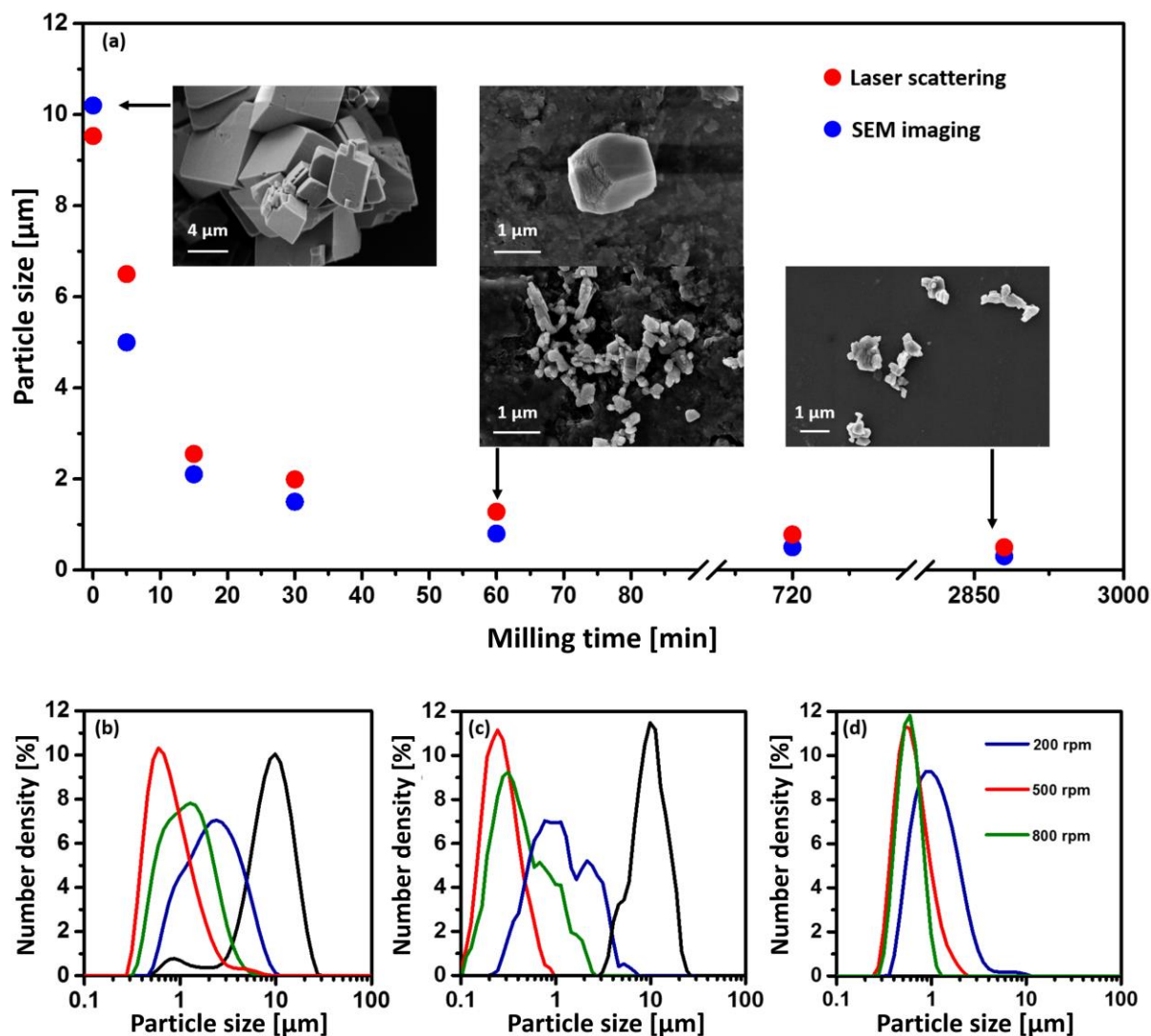


Figure 2.4. Median particle size as a function of milling time for pure CaCO_3 particles (uncalcined). Particle size distribution obtained by using b) laser diffraction and c) SEM: (—) CaCO_3 precursor, (—) Ca-15m-500, (—) Ca-1h-500, and (—) Ca-48h-500 d) particle size distribution (laser scattering) of pure calcite particles milled for 12 h at various milling speeds.

Turning now to the effect of milling conditions on the textural properties, **Error! Reference source not found.** summarizes the results from the BET surface area and the BJH pore volume measurements representing morphological characteristics of the various ball-milled calcite samples (after the initial calcination at 800°C for 2 h) as determined by N_2 sorption. Independent of the milling conditions, all materials were found to possess a very similar surface area ($15 \pm 2 \text{ m}^2 \text{ g}^{-1}$), indicating that the pore structure was largely independent of the particle size, at least within the range studied here.

Table 2.2. Porosity of the reference materials and CaO-based CO₂ sorbents developed (calcined state).

Sorbent (calcined)	BET surface area [m ² g ⁻¹]	BJH pore volume [cm ³ g ⁻¹]
Limestone	8	0.11
CaCO ₃	17	0.27
Ca-15m-500	12	0.13
Ca-30m-500	13	0.18
Ca-2h-500	13	0.14
Ca-12h-500	15	0.20
Ca-48h-500	16	0.13
Ca-48h-200	13	0.11
Ca-12h-800	13	0.11

2.4.4. CO₂ uptake characteristics of ball-milled, unsupported CaO

Subsequently, the cyclic CO₂ uptake of the different, ball-milled, pure calcite samples was determined and compared to the reference limestone and the unmilled calcite precursor. The cyclic CO₂ uptake was determined under both mild (isothermal) and realistic CO₂ capture conditions to assess whether the performance trends observed can be extrapolated. Figure 2.5a shows the results of the experiments performed isothermally under mild reaction conditions. There is a clear relationship between the milling time and the CO₂ capture uptake values of ball-milled calcite. A decreasing rate of deactivation was observed for increasing milling times corresponding to smaller median particle diameters. After 10 carbonation/calcination cycles the maximum CO₂ uptake obtained for Ca-48h-500 was 0.57 gCO₂ g_{sorbent}⁻¹, a value that was 130 % and 80 % higher compared to the calcite precursor and limestone references, respectively.

The carbonation reaction of CaO occurs in two stages. In the first, kinetically-controlled, reaction stage, pores are filled and a dense CaCO₃ layer forms on the outer surface of the CaO particles or grains. Once the product (CaCO₃) layer has reached a critical thickness, reported to be ca. 50 nm,³⁴ the further carbonation of unreacted CaO is controlled by the slow diffusion of reactant through the carbonate (the ratio of the CO₂ diffusion coefficients in CaO and CaCO₃ is D_{CaO} : D_{CaCO₃} = 100 : 1).³³ Based on this reaction model, reducing the particle size of CaO would lead to a higher CO₂ uptake in the kinetically-controlled stage yielding higher overall CO₂ uptakes. The experimental data (Figure 2.5) were in good agreement with

the model, viz. an increasing CO₂ uptake (after 10 cycles) is attained with increasing milling time and, hence, a smaller particle diameter.

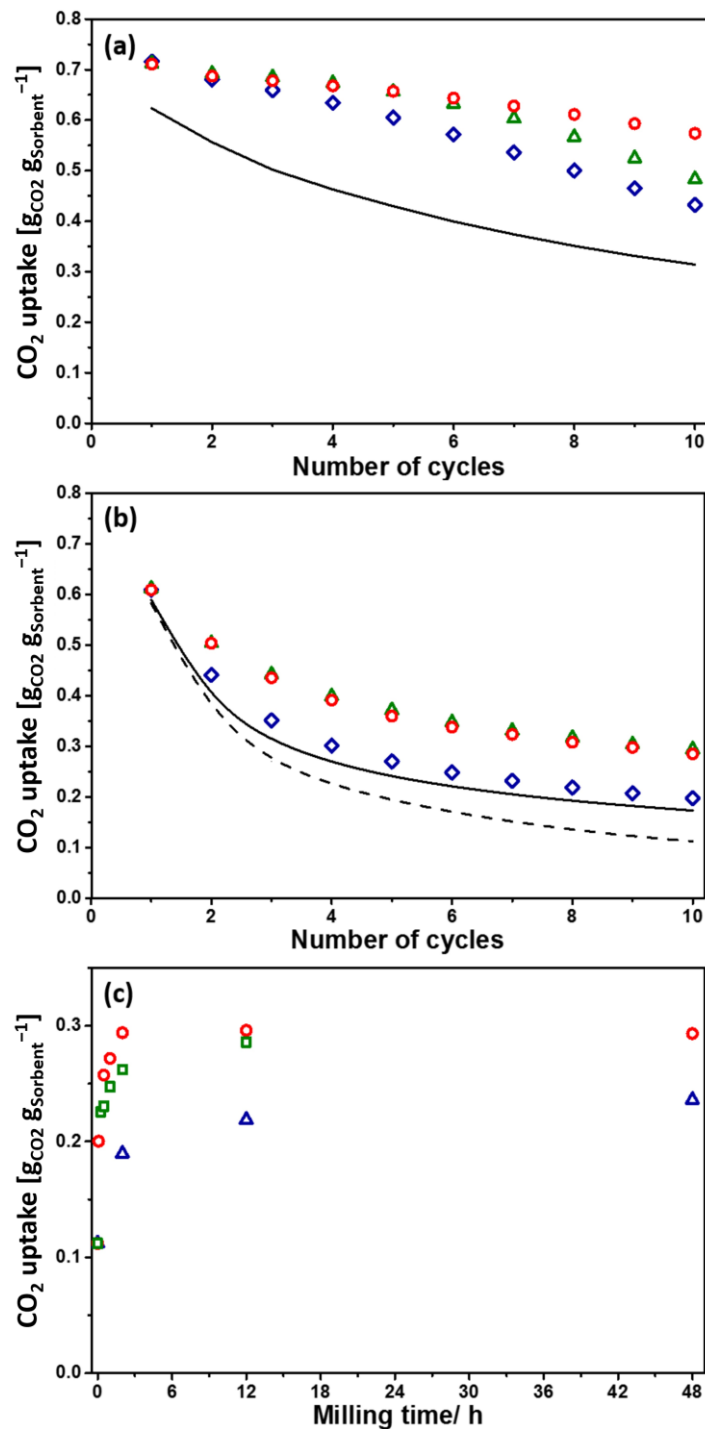


Figure 2.5. CO₂ capture characteristics of ball-milled CaCO₃ as a function of milling time under (a) isothermal (750 °C, calcination in pure N₂, carbonation in 40 vol.% CO₂) and (b) realistic CO₂ capture conditions (calcination at 900 °C in pure CO₂; carbonation at 650 °C in 20 vol.% CO₂): (◇) Ca-15m-500, (△) Ca-2h-500, (○) Ca-48h-500, (—) limestone, (---) unmilled CaCO₃ precursor; (c) CO₂ uptake after 10 carbonation/calcination cycles (realistic CO₂ capture conditions) as a function of the milling time for different rotation speeds: (△) 200 rpm, (○) 500 rpm, (□) 800 rpm.

Increasing the calcination temperature to 900 °C and performing the regeneration in pure CO₂ atmosphere (Figure 2.5b) resulted in a faster decrease in CO₂ uptake of the sorbents compared to isothermal measurements (Figure 2.5a). This can be attributed to the accelerated thermal sintering of CaCO₃ ($T_T = 533$ °C) at the higher calcination temperature and concentration of CO₂.¹⁹⁵ Nonetheless, the trends were similar and ball milling of the calcite precursor improved appreciably the performance of the CO₂ sorbents compared to the reference limestone and unmilled CaCO₃. However, in contrast to the measurements conducted under isothermal conditions, the effect of milling time levelled off, i.e., durations exceeding 2 h did not result in a further improvement in the CO₂ uptake. The CO₂ uptake (after 10 cycles) of the best material (Ca-12h-500) was 0.29 g_{CO2} g_{sorbent}⁻¹, a value that was 75 % and 170 % higher than that of the references limestone (0.17 g_{CO2} g_{sorbent}⁻¹) and the unmilled CaCO₃ precursor (0.11 g_{CO2} g_{sorbent}⁻¹), respectively.

The effect of both the milling speed and the duration on the CO₂ uptake of pure CaCO₃ is plotted in Figure 2.5c, where the CO₂ uptake was determined after 10 cycles and the calcination was in pure CO₂ at 900 °C. CaCO₃ milled at the lowest speed of 200 rpm possessed the lowest CO₂ uptake (0.23 g_{CO2} g_{sorbent}⁻¹ for Ca-48h-200). Increasing the milling speed from 200 to 500 or 800 rpm increased the CO₂ uptake, albeit the difference between the milling speeds of 500 and 800 rpm was small, viz. 0.29 and 0.26 g_{CO2} g_{sorbent}⁻¹ for Ca-2h-500 and Ca-2h-800, and 0.29 and 0.28 g_{CO2} g_{sorbent}⁻¹ for Ca-12h-500 and Ca-12h-800, respectively. Furthermore, operating the ball mill at 800 rpm led to overheating and limited the maximal milling time to 12 h. Based on these results, a milling speed of 500 rpm and a milling time of 48 h were chosen as optimal milling conditions for the further experiments.

2.4.5. Stabilization of CaO by MgO

Despite optimizing the milling conditions, the cyclic CO₂ uptake of unsupported CaO decreased appreciably over multiple carbonation/calcination cycles, due to the thermal sintering of CaCO₃.²⁵ To increase the cyclic stability of the CO₂ sorbents, attempts were made to effectively stabilize CaO through the introduction of high Tammann temperature MgO ($T_T = 1276$ °C). In the following experiments the Ca : Mg ratio was varied while, based on the results presented above, the milling conditions were kept constant (500 rpm, 48 h).

2.4.6. Phase characterization using X-ray diffraction

In contrast to the pure calcite samples, X-ray diffraction revealed the formation of aragonite when mixtures of calcite and magnesium carbonate (used as the precursor) were ball milled (Figure 2.2). A possible explanation for this observation is that the addition of harder magnesite particles (3.5 – 4.5 hardness on the Mohs scale for magnesite compared to 3 for calcite) increased sufficiently the local shear forces and pressures during ball milling and initiated the transformation of calcite to aragonite. It was observed that the addition of MgCO_3 reduced the crystallite size of calcite to 25 ± 5 nm (the crystallite size of aragonite was 30 ± 5 nm) compared to the pure calcite samples ball milled under identical conditions (45 ± 5 nm). The smaller crystallite size of calcite may be explained by the partial transformation of calcite to aragonite, with the transformation occurring at the grain boundary of the calcite particles.¹⁹⁶⁻¹⁹⁷ We could not observe the formation of any solid solution between calcium- and magnesium-carbonate phases, e.g., dolomite.²⁵ After the initial calcination (800 °C for 2 h), only calcium and magnesium oxides with trace amounts of calcium hydroxide were detected (Figure 2.2).

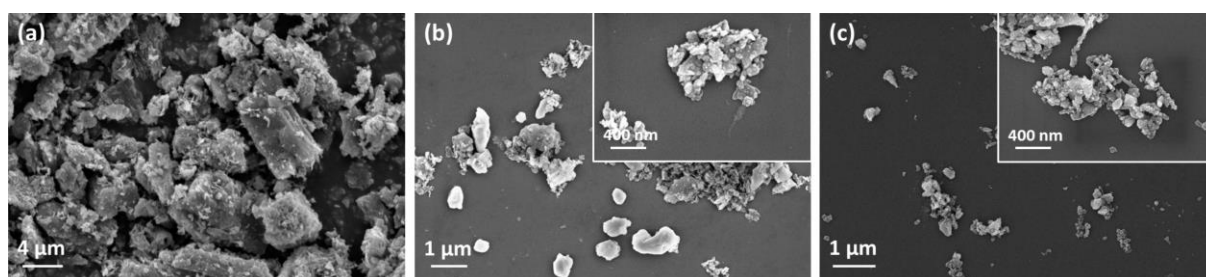


Figure 2.6. Scanning electron micrographs of: (a) the original MgCO_3 precursor, (b) MgCO_3 milled for 48 h and (c) 80Ca/20Mg-48h-500.

2.4.7. Morphological characterization of MgO-stabilized CaO

For reference, scanning electron micrographs of the as-received and milled MgCO_3 are shown in Figure 2.6a and b. The MgCO_3 precursor was comprised of a mixture of comparatively large particles with diameters $> 5 \mu\text{m}$ and fines with diameters $\sim 1 \mu\text{m}$. Laser diffraction analysis evidenced a broad particle size distribution, ranging from 0.8 to 45 μm , with a median particle size of 14 μm . However, it is worth noting that after 48 h of ball-milling the sample was comprised mostly (number fraction of 95 %) of fines with a median diameter of 90 ± 45 nm, and only a very small number fraction (~ 5 %) of large particles (0.5 – 1 μm). Turning now to mixtures of magnesium and calcium carbonate, a typical electron micrograph

of a mixture of calcium and magnesium carbonates (80 : 20 molar ratio) milled for 48 h is shown in Figure 2.6c. Based on analysis of the SEM images, only particles with a diameter < 400 nm are present.

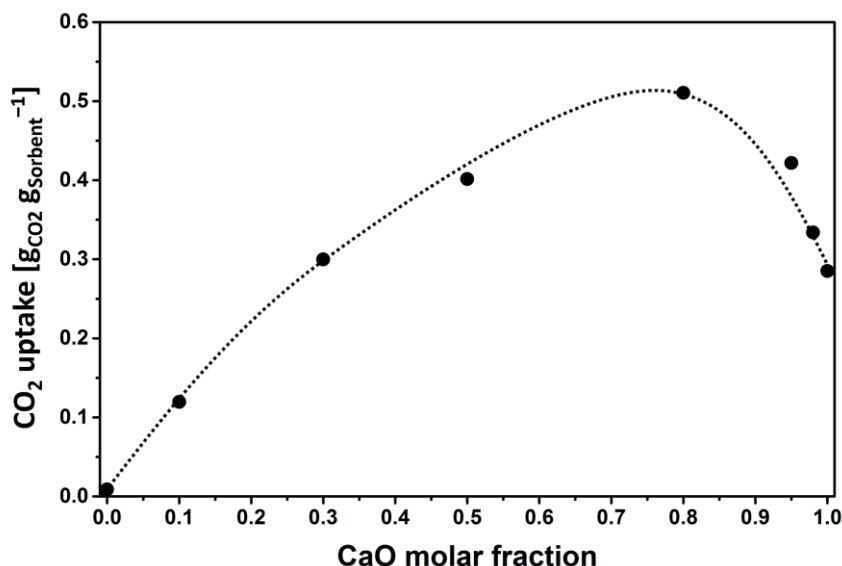


Figure 2.7. CO₂ uptake of MgO-stabilized CaO-based sorbents (ball milled for 48 h at 500 rpm) after 10 carbonation/calcination cycles (calcination at 900 °C in pure CO₂; carbonation at 650 °C in 20 vol.% CO₂) as a function of the CaO molar fraction.

2.4.8. Optimization of the Ca-to-Mg ratio

To determine the minimum quantity of MgO required to effectively stabilize CaCO₃ particles and prevent them from sintering, CO₂ sorbents with different Ca:Mg ratios were prepared (the ball milling conditions were kept constant, i.e., 48 h at 500 rpm). The cyclic CO₂ uptake of the sorbents synthesized was assessed in a TGA under realistic conditions (calcination at 900 °C in a pure CO₂ atmosphere; carbonation at 650 °C in 20 vol.% CO₂). Figure 2.7 shows the CO₂ uptake (after 10 cycles) as a function of the CaO content. The addition of a small quantity of MgO (2 – 5 mol.%) increased appreciably the CO₂ uptake of the CaO-based CO₂ sorbents. The highest CO₂ uptake after 10 cycles, 0.55 gCO₂ gSorbent⁻¹, was obtained for 80Ca/20Mg-48h-500, which exceeds the value of the reference materials limestone and unmilled CaCO₃ precursor by 220 % and 400 %, respectively. The uptake of CO₂ by 80Ca/20Mg-48h-500 was also 100 % higher than that of unsupported, but ball milled CaCO₃ (Ca-48h-500). From Figure 2.7, the optimal Ca:Mg ratio was determined to be 8 : 2, which agrees well with an estimate obtained from the percolation theory, initially developed to predict the conductivity behaviour and conductivity threshold in a binary system of

conductive and insulating spheres.¹⁹⁸⁻¹⁹⁹ According to Kryuchkov,¹⁹⁹ the critical packing fraction of the filler (here the support MgCO_3) depends on the ratio of the particle sizes of the conductive (i.e., MgCO_3) and non-conductive materials (here the active material CaCO_3) and can be calculated by Eq.2.3:

$$V_{cr} = 1 / (5.55 + 3d_i/d_c) + 0.04 \quad (\text{Eq. 2.3})$$

In which d_i is the diameter of the “insulating” particles (i.e., CaCO_3) and d_c is the diameter of the “filler” (i.e., MgCO_3). Using the particles sizes determined for CaCO_3 and MgCO_3 ($d_{\text{CaCO}_3} = 350 \pm 50 \text{ nm}$, $d_{\text{MgCO}_3} = 90 \pm 45 \text{ nm}$) a threshold volume fraction of 10 vol.% MgCO_3 is obtained; which is similar to the experimental value of 14.5 vol.% MgCO_3 (Ca : Mg = 8 : 2) (Figure 2.7). Increasing the fraction of MgCO_3 further, reduces the fraction of active CaO in the material, leading to a lower CO_2 uptake (Figure 2.7).

2.4.9. Long-term stability of MgO-stabilized CaO

After determining the optimal Ca:Mg ratio (80:20), the long term CO_2 uptake stability (30 cycles) of 80Ca/20Mg-48h-500 and the reference materials were assessed, i.e., the best mechanically activated but unsupported CO_2 sorbent (Ca-48h-500), the unmilled CaCO_3 precursor, an unmilled mixture of CaCO_3 and MgCO_3 (80Ca/20Mg) and limestone.

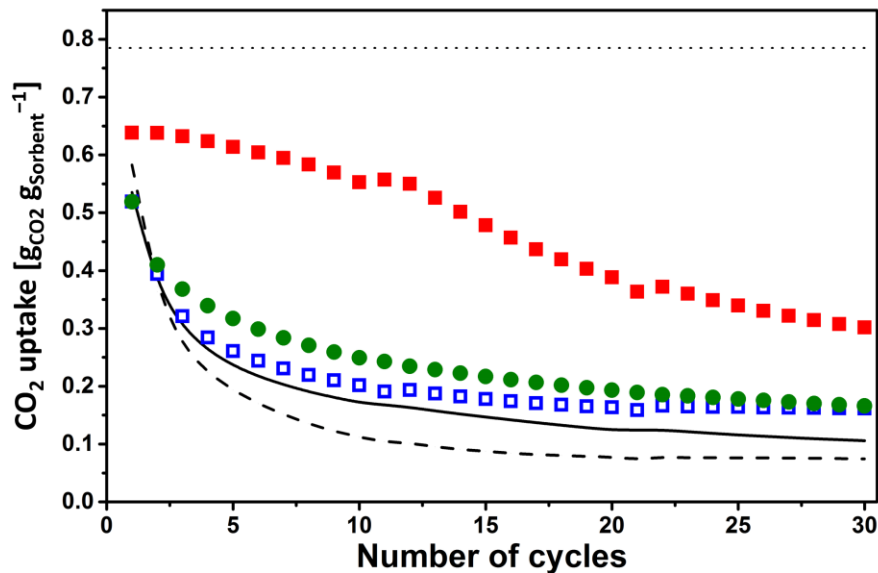


Figure 2.8. Long-term CO_2 uptake characteristics under realistic CO_2 capture conditions (calcination at 900°C in pure CO_2 ; carbonation at 650°C in 20 vol.% CO_2): (■) 80Ca/20Mg-48h-500, (●) Ca-48h-500, (□) unmilled CaCO_3 - MgCO_3 mixture (80Ca/20Mg), (---) unmilled CaCO_3 precursor, (—) limestone, (⋯) theoretical, maximal CO_2 uptake for pure CaO.

The cyclic CO₂ uptakes of the different CO₂ sorbents tested are compared in Figure 2.8. Milled, but unsupported CaCO₃, limestone and unmilled CaCO₃ and CaCO₃/MgCO₃ mixture showed a rapid decrease of the CO₂ uptake over the first few cycles. After approximately 20 cycles the CO₂ uptake stabilized and the following asymptotic values were obtained: 0.16 gCO₂ g_{sorbent}⁻¹ for Ca-48h-500 and 80Ca/20Mg, 0.07 gCO₂ g_{sorbent}⁻¹ for the unmilled CaCO₃ precursor, and 0.1 gCO₂ g_{sorbent}⁻¹ for limestone, respectively. It is worth mentioning that during the first 10 cycles the unmilled mixtures of calcium and magnesium carbonates (80Ca/20Mg) showed a faster decrease of the CO₂ uptake than Ca-48h-500. However, after 30 cycles, the CO₂ uptake of both sorbents reached the same value, viz. 0.16 gCO₂ g_{sorbent}⁻¹. On the contrary, MgO-supported ball-milled CaO showed a significantly improved stability. In particular, the decrease in the CO₂ uptake over the first 10 cycles was comparatively small. After 30 cycles the CO₂ uptake of 80Ca/20Mg-48h-500 was 0.3 gCO₂ g_{sorbent}⁻¹, a value that was approximately 82, 90, 330 and 190% higher than that of the reference materials Ca-48h-500, 80Ca/20Mg, unmilled CaCO₃ precursor, and limestone, respectively.

Table 2.3. Pore volumes and median macropore diameter of Ca-48h-500 and 80Ca/20Mg-48h-500 after drying, calcination at 800 °C, 10 and 30 carbonation/calcination cycles.

Ca-48h-500				
	as prepared	calcined	10 cycles	30 cycles
Mesopore (3.8 – 50 nm)/ macropore (> 50 nm) volume [cm³ g⁻¹]	0.01/ 2.30	0.22/ 2.47	0.01/ 1.56	0.00/ 1.58
Median macropore diameter [nm]	270	320	434	555
80Ca/20Mg-48h-500				
	as prepared	calcined	10 cycles	30 cycles
Mesopore (3.8 – 50 nm)/ macropore (> 50 nm) volume [cm³ g⁻¹]	0.77/ 2.59	0.15/ 3.70	0.01/ 1.96	0.00/ 1.62
Median macropore diameter [nm]	80	180	250	315

To assess the morphological stability of the different CO₂ sorbents tested (limestone, the unmilled CaCO₃ precursor, 80Ca/20Mg and 80Ca/20Mg-48h-500), the cycled materials were recovered after 10 and 30 carbonation/calcination cycles in their calcined state and analysed using mercury porosimetry and electron microscopy.

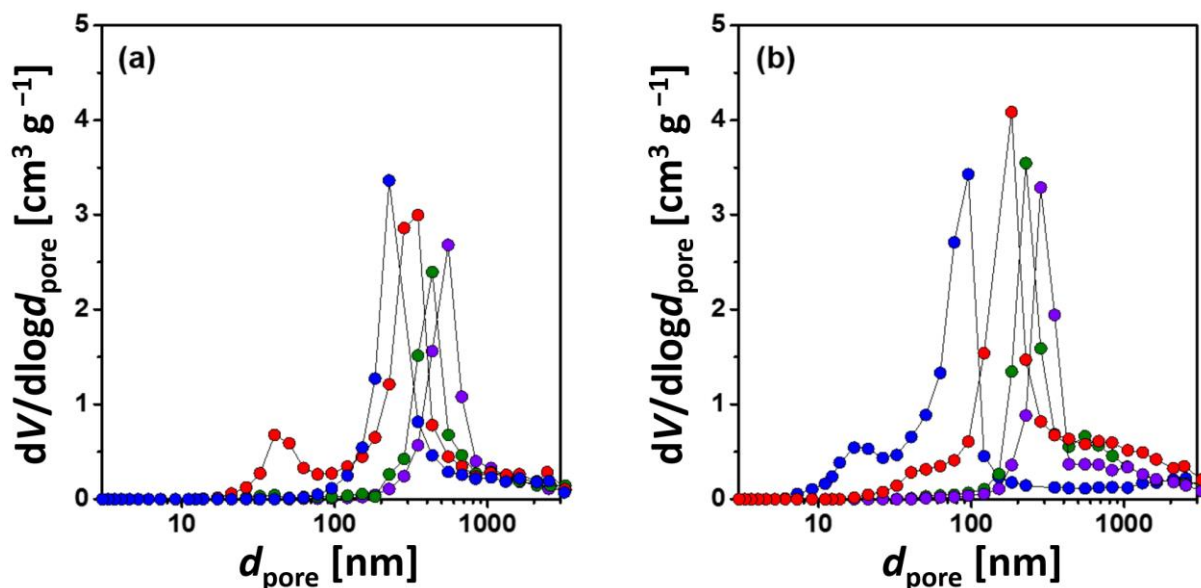


Figure 2.9. Pore size distribution of a) Ca-48h-500 and b) 80Ca/20Mg-48h-500 after drying (●), calcination at 800 °C (●), 10 cycles (●) and 30 cycles (●) derived from mercury porosimetry.

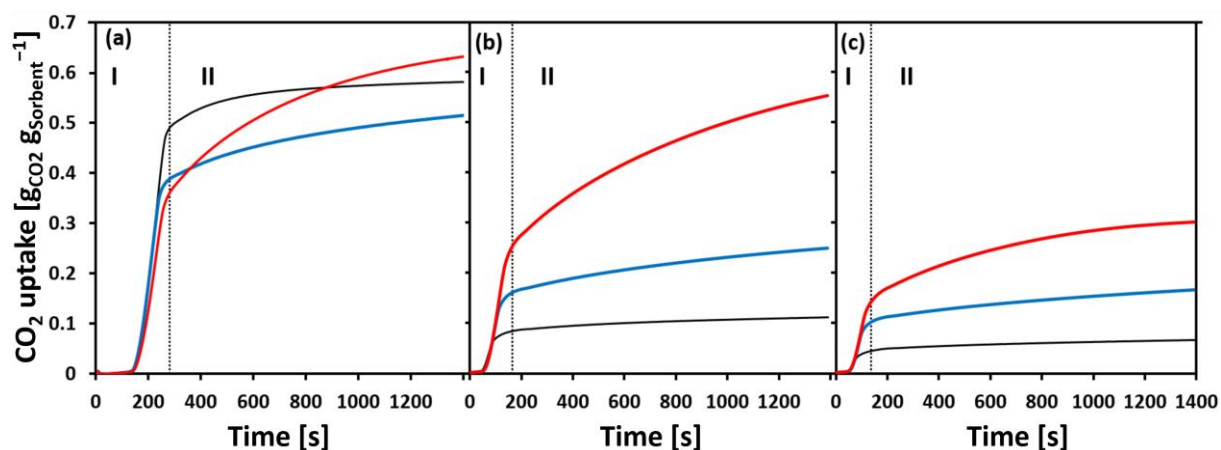


Figure 2.10. CO₂ uptake as a function of time (—) of CaCO₃ precursor, (—) Ca-48h-500 and (—) 80Ca/20Mg-48h-500 during the (a) 1st, (b) 10th and (c) 30th carbonation step. In the plots (I) marks the fast kinetically-controlled carbonation stage whereas (II) marks the slow diffusion-limited reaction regime.

The mercury porosimetry measurements (Figure 2.9, Table 2.3, as-prepared material) revealed that the addition of MgCO₃ to the milling processes reduced significantly the median macropore diameter of the material (from 270 nm for Ca-48h-500 to 80 nm for 80Ca/20Mg-48h-500). This reduction was accompanied by an increase in the total pore volume. Furthermore, while Ca-48h-500 contained essentially only macropores, the addition of MgCO₃ also introduced mesopores in the samples (median mesopore diameter ~ 20 nm). As expected, calcination at 800 °C shifted the median macropore diameter to larger values,

i.e., 320 and 180 nm for the unsupported and supported material, respectively. However, the total pore volume increased owing to the release of CO₂ through the decomposition of the carbonates. Subsequent carbonation/calcination cycles further increased the median macropore diameter, which after 30 cycles reached values of 315 nm and 555 nm for 80Ca/20Mg-48h-500 and Ca-48h-500, respectively. This increase in the average pore diameter with cycle number has been observed previously for limestone and has been attributed to sintering.²⁰⁰⁻²⁰¹ Our results demonstrate, however, that the addition of MgO can reduce appreciably the rate and extent of sintering. This improved morphological stability of CaO leads, in turn, to an improved CO₂ uptake stability, as recorded by our TGA experiments (Figure 2.8 and Figure 2.10). It is noteworthy that after 30 cycles the CO₂ uptake of 80Ca/20Mg-48h-500 was approximately double that of unsupported Ca-48h-500 (Figure 2.8), despite the fact that these materials possessed a similar total pore volume. Thus, the macropore size appears to be a more influential descriptor for the CO₂ uptake of a CaO-based CO₂ sorbent than the total pore volume. Owing to the formation of a low CO₂-diffusivity, carbonate product layer, the median pore diameter (and possibly also the incorporation of MgO into the CaO matrix) influences significantly the transition from the kinetically-controlled (I) to the diffusion-limited (II) reaction regime. Indeed, we observe a higher CO₂ uptake of MgO-supported CaO in the kinetically-controlled stage when compared to unsupported milled CaCO₃ and calcite precursor (Figure 2.10). Moreover, a significantly faster and more prominent CO₂ uptake during the diffusion-limited (II) reaction regime was observed for MgO-supported CaO when compared to the reference materials (Figure 2.10). Using a random pore model,²⁰² the following apparent diffusion coefficients through the product layer were estimated: $1.0 \times 10^{-16} \text{ m}^2 \text{ s}^{-1}$ for Ca-48h-500 and $3.3 \times 10^{-16} \text{ m}^2 \text{ s}^{-1}$ for 80Ca/20Mg-48h-500. However, the differences in the diffusion coefficients are too small to state conclusively that the addition of MgO also affects the CO₂ diffusivity in the product layer at this stage.

The severe sintering of the reference limestone, unmilled calcite precursor and unmilled mixture of CaCO₃ and MgCO₃ (Ca : Mg = 8 : 2), was visualized by electron microscopy and the images are shown in Figure 2.11a-i. After 30 cycles, the porosity of the materials markedly decreased, resulting in low CO₂ uptakes (Figure 2.8).

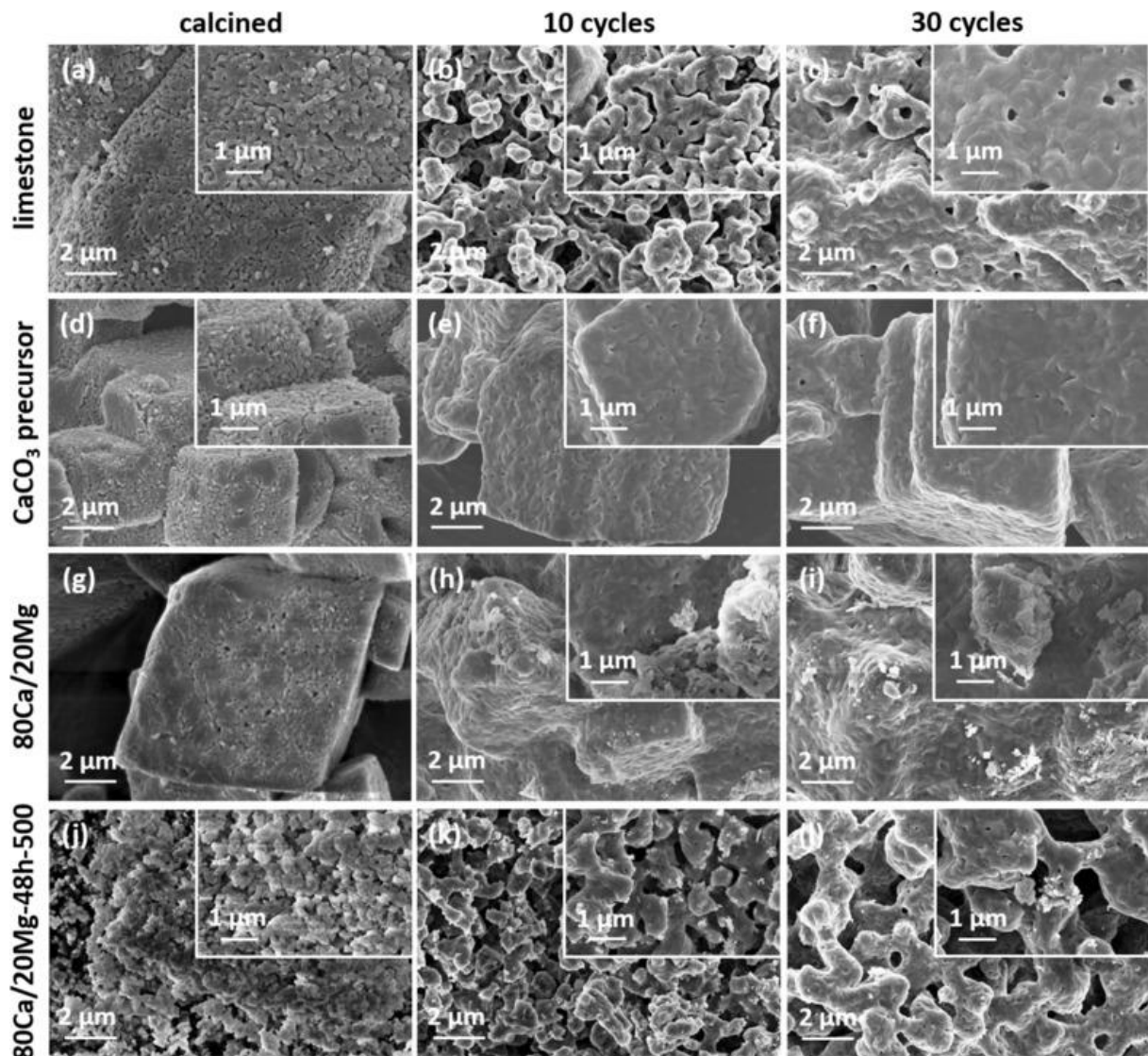


Figure 2.11. Scanning electron micrographs of limestone, unmilled CaCO_3 precursor, 80Ca/20Mg and 80Ca/20Mg-48h-500 after calcination at 800 °C for 2 h, 10 and 30 carbonation/calcination cycles.

On the contrary, after 30 cycles 80Ca/20Mg-48h-500 still retained a macroporous structure, confirming the effective stabilization of CaO by MgO (Figure 2.11l). The structural stabilization of the CaCO_3/CaO particles by MgO on a nanometer level was also visualized by STEM and elemental mapping, in Figure 2.12. Comparatively, large CaO particles (light blue) are surrounded by smaller MgO particles (violet). Thus, a small quantity of sintering-resistant MgO particles reduced effectively the contacting area between neighbouring CaCO_3 particles, minimizing, in turn, sintering. Nonetheless, even 80Ca/20Mg-48h-500 showed a decaying CO_2 uptake with cycle number (Figure 2.8). This observation can be explained by the partial agglomeration of MgO particles, which decorate the surface of partially sintered CaCO_3 particles with increasing cycle number. The latter can be followed in the SEM and STEM

images of the cycled materials (Figure 2.11k and l and Figure 2.12d and f, respectively). Thus, to increase the thermal stability of the material further, the size of the stabilizing MgO particles would have to be reduced to a few nanometers. However, such small particles could probably only be produced using alternative, most likely wet-chemical, approaches, which are typically poorly scalable and relatively expensive.

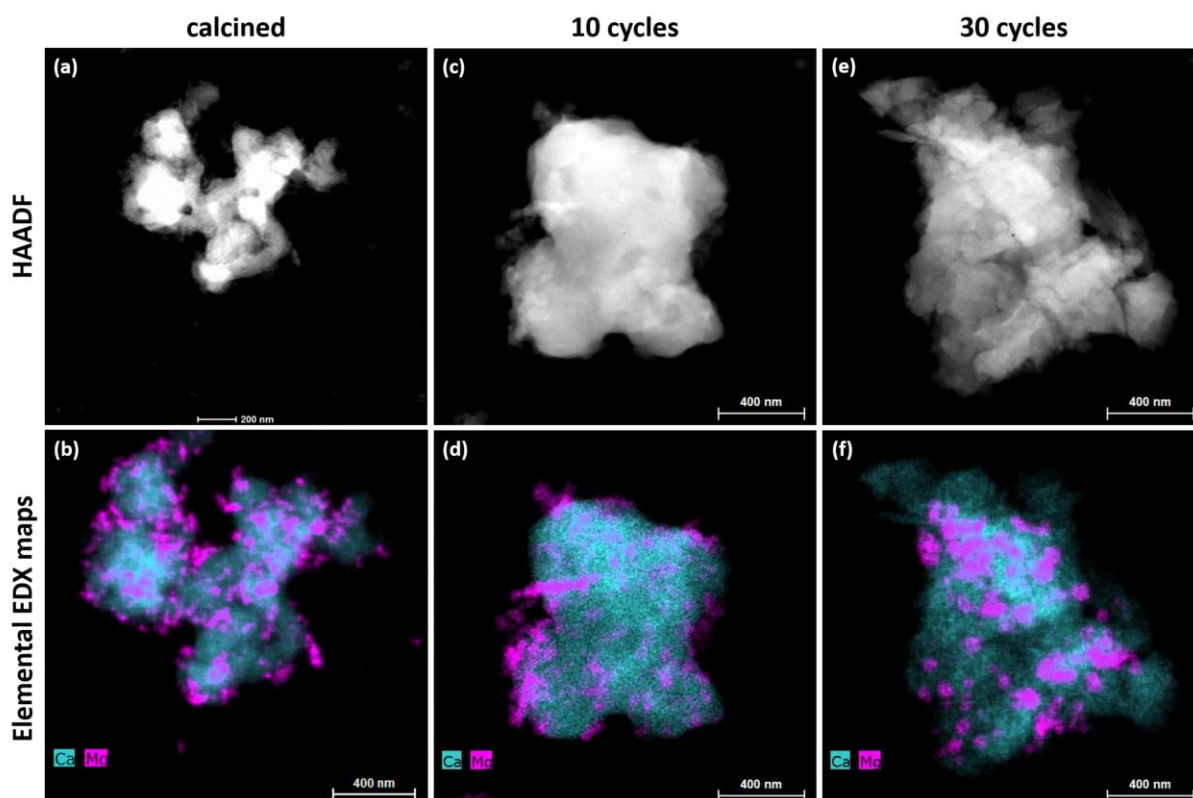


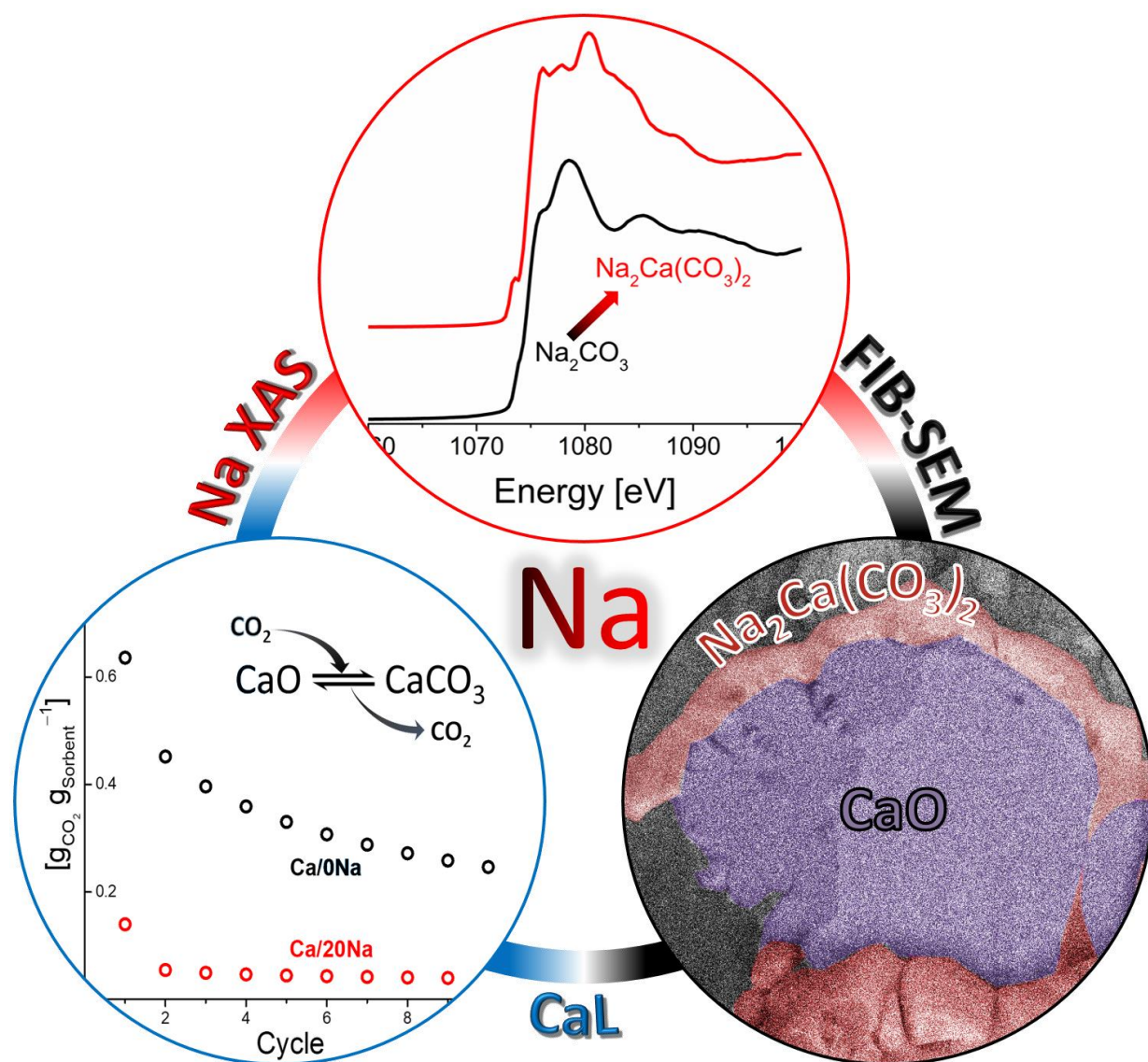
Figure 2.12. HAADF STEM images and Ca and Mg EDX mapping of 80Ca/20Mg-48h after calcination at 800 °C in the air, and after 10 and 30 carbonation/calcination cycles.

2.5. Conclusions

In this work, wet mechanochemical activation was demonstrated as a scalable route to synthesize highly effective CaO-based CO₂ sorbents exhibiting a superior uptake capacity over numerous cycles with respect to state-of-the-art sorbents. This was achieved by optimizing the duration and speed of wet ball milling of a pure CaCO₃ precursor, to attain favorable particle characteristics. Using electron microscopy techniques, we could demonstrate that CaO/CaCO₃ particles were effectively stabilized against sintering by small MgO nanoparticles decorating the surface of larger CaO particles. This understanding of the synthesis and stabilization process allowed us to reduce the amount of the inert support

(MgO) to 15 wt.%. The best CO₂ sorbent exceeded the CO₂ uptake of the reference limestone by 200 % under industrially relevant carbonation and calcination conditions.

Chapter 3: Na_2CO_3 -modified CaO -based CO_2 Sorbents: The Effects of Structure and Morphology on CO_2 Uptake



The results of this chapter are published as:

A. Kurlov, A. M. Kierzkowska, T. Huthwelkerb, P. M. Abdala, C. R. Müller, Na_2CO_3 -modified CaO -based CO_2 Sorbents: The Effects of Structure and Morphology on CO_2 Uptake, *Phys. Chem. Chem. Phys.*, **2020**, 22, 24697-24703

3.1. Abstract

Calcium looping (CaL) is a CO₂ capture technique based on the reversible carbonation/calcination of CaO that is considered promising to reduce anthropogenic CO₂ emissions. However, the rapid decay of the CO₂ uptake of CaO over repeated cycles of carbonation and calcination due to sintering limits its implementation at the industrial scale. Thus, the development of material design strategies to stabilize the CO₂ uptake capacity of CaO is paramount. The addition of alkali metal salts to CaO has been proposed as a strategy to mitigate the rapid loss of its cyclic CO₂ uptake capacity. However, there are conflicting results concerning the effect of the addition of alkali metal carbonates on the structure and CO₂ capacity of CaO. In this work we aim at understanding the effect of the addition of Na₂CO₃ to CaO on the sorbent's structure and its CO₂ uptake capacity. We demonstrate that under industrially-relevant conditions the addition of as little as 1 wt.% of Na₂CO₃ reduces severely the CO₂ uptake of CaO. Combining TGA, XAS and FIB-SEM analysis allowed us to attribute the performance degradation to the formation of the double salt Na₂Ca(CO₃)₂ that induces strong sintering leading to a significant loss in the sorbent's pore volume. In addition, during the carbonation step the formation of a dense layer of Na₂Ca(CO₃)₂ that covers unreacted CaO prevents its full carbonation to CaCO₃.

3.2. Introduction

The continuous global economic growth results in a constant increase in the energy demand. Currently, over 80 % of the total primary energy supply is derived from fossil fuels, i.e. coal, oil and natural gas.²⁰³ The combustion of fossil fuels releases large volumes of CO₂ into the atmosphere which in turn is most likely linked to global warming.⁴ Besides energy saving strategies and the transition to renewable energy carriers, CO₂ capture and storage (CCS) is expected to provide an appreciable contribution to the global reduction targets in CO₂ emissions. Currently, the only industrially available CO₂ capture technology is amine scrubbing.¹³ However, amine scrubbing is expensive and associated with the formation of hazardous by-products such as nitrosamines.¹⁴⁻¹⁵ Therefore, alternative CCS technologies are currently explored, with calcium looping (CaL) being one of the most promising candidates. CaL is based on the reversible carbonation–calcination reaction pair:



and stands out due to the very high theoretical CO₂ uptake capacity of CaO (0.78 g_{CO₂} g_{sorbent}⁻¹), low predicted CO₂ capture costs (ca. 23.7 USD t_{CO₂}⁻¹)¹¹ and the high abundance and inexpensiveness of naturally-occurring CaO precursors, e.g. limestone.²⁵ However, the Tammann temperature of CaCO₃ ($T_T = 533$ °C), which is lower than the operating temperatures of the process (600-950°C), is a major drawback of CaL. The low Tammann temperature results in material sintering and the loss of pore volume, which in turn leads to lower CO₂ uptakes.³⁰⁻³² To yield a high CO₂ uptake, a CaO-based CO₂ sorbent requires a high pore volume in the micro- and mesoporous range as the molar volume of the product, CaCO₃, is approximately twice as high as that of CaO.²⁵ Several material design strategies have been proposed to reduce the sintering-induced material deactivation, such as the stabilization of CaO with high- T_T materials (e.g. Al₂O₃ or MgO)^{25,38,42,56-57,204-205} or the addition of alkali metal salts.⁶⁰⁻⁶⁵ Currently, there is very limited understanding of the effect of the addition of alkali metal salts on the CO₂ capture performance of CaO; indeed, several works have reported conflicting results.^{60-62,65} For example, it has been reported that the addition of alkali metal chlorides and hydroxides (with the exception of Li-based salts) strongly increases the CO₂ uptake capacity of CaO, although no cyclic stability data was reported.⁶¹ A further study confirmed the positive effect of the addition of NaCl and, to a lesser extent of Na₂CO₃, on the CO₂ uptake of limestone-derived CaO when tested in a thermogravimetric analyzer (TGA); yet a negative effect was observed when the cyclic CO₂ capture tests were performed in a laboratory-scale fluidized bed.⁶² Further, a significant drop in the CO₂ uptake of limestone was observed when Na₂CO₃ was added.⁶⁵ Upon the addition of Na₂CO₃, the double carbonate Na₂Ca(CO₃)₂ can form under reaction conditions.⁶³⁻⁶⁴ The formation of Na₂Ca(CO₃)₂ has been linked to an increase in the kinetics of both the carbonation and calcination reactions and an increased cyclic stability of the sorbent when compared to pristine CaO.⁶³⁻⁶⁴

Recent work has explored the effect of the addition of the double salt (Li-K)₂CO₃ to CaO on its CO₂ uptake.⁶⁰ After 23 carbonation/calcination cycles a three times higher CO₂ uptake was observed when compared to pure CaO.⁶⁰ It was speculated that the addition of (Li-K)₂CO₃ prevents the formation of a CaCO₃ layer that would otherwise impose a high diffusion resistance for CO₂, thus providing a direct access for CO₂ to unreacted CaO. However, a limitation of the studies described above is that the cyclic CO₂ uptake of alkali

metal salt-promoted CaO was determined under mild reaction conditions that are of little relevance for practical use, i.e. the calcination step was performed in pure N₂ at $T \leq 850$ °C. Furthermore, there has been very little insight into the morphological and structural modifications that arise from the addition of alkali metal salt promoters. Hence, in this work we study in detail the effect of the addition of the alkali salt Na₂CO₃ on the CO₂ uptake of CaO under industrially relevant conditions. The CO₂ uptake performance of sorbents is complemented by a detailed characterization of the alkali metal salt-induced structural and morphological changes of the sorbent using a combination of electron microscopy and X-ray absorption spectroscopy (XAS). These experiments allowed us to link the sorbents' decreasing CO₂ uptake to sintering that is induced by the formation of the low melting point double carbonate Na₂Ca(CO₃)₂. Furthermore, Na₂Ca(CO₃)₂ was found to be stable under both carbonation and calcination conditions and to cover the surface of unreacted CaO preventing in turn the carbonation reaction to proceed rapidly.

3.3. Experimental section

3.3.1. Material preparation

Commercial CaCO₃ (Fischer Chemicals, CAS: 471-34-1, analytical reagent grade) and Na₂CO₃ (Acros Organics, CAS: 497-19-8, 99.5 % purity) were used for the synthesis of the CO₂ sorbents (Figure B.1). To achieve a homogeneous distribution of the sodium salt modifier, a wet ball-milling technique following a reported method was employed.²⁰⁵ Specifically, 7 g of the precursor powders, mixed with 10 mL of deionized water, were ball-milled in a 45 mL Si₃N₄ jar containing 5 mm Si₃N₄ balls. The ball-milling time was 48 h at 500 rpm. After ball milling, the suspension obtained was dried in an oven overnight at 100 °C. The following nomenclature is used for the samples: Ca/xNa, whereby x refers to the quantity of Na₂CO₃ (wt.%). The following values for x were used: 1, 3, 6, 10 and 20 wt.%. Pure ball-milled CaCO₃ was used as the reference material for the CO₂ uptake experiments (referred to as Ca/0Na).

The reference Na₂Ca(CO₃)₂ material was synthesized from a stoichiometric mixture of Na₂CO₃ and CaCO₃ at 800 °C in a CO₂ atmosphere for 2 h.

3.3.2. Characterization

The mass ratio of Na : Ca in the sorbents was determined by inductively coupled plasma optical emission spectroscopy (ICP OES) using an Agilent 5100 VDV instrument; the samples were digested in aqua regia.

The crystallinity and phase composition of the sorbents were analyzed by X-ray powder diffraction (XRD). The XRD data were collected using a PANalytical Empyrean X-ray diffractometer equipped with a Bragg–Brentano HD mirror, which was operated at 45 kV and 40 mA using CuK α radiation ($\lambda = 1.54 \text{ \AA}$). The materials were examined within the 2θ range of $5\text{--}90^\circ$ using a step size of 0.0167° . The scan time per step was 1 s.

N₂ physisorption (Quantachrome NOVA 4000e) was used to determine the surface area and pore volume of the CO₂ sorbents in both the as-prepared and calcined states. Prior to the measurements, all samples were degassed at 300 °C for at least 2 h. The Brunauer-Emmett-Teller (BET)¹⁹⁰ and the Barrett-Joyner-Halenda (BJH)¹⁹¹ models were used to calculate the surface area and pore volume, respectively.

The particle size and morphology of the CO₂ sorbents synthesized was examined using scanning electron microscopy (SEM). SEM was performed on a LEO Gemini 1530 (Zeiss, Germany) at 5 kV acceleration voltage. Prior to imaging, all samples were sputtered with a thin (ca. 3 nm) layer of Pt. Energy-dispersive X-ray spectroscopy (EDX) mapping was obtained at 20 kV acceleration voltage on samples without a Pt coating. Cross-sections of the synthesized materials were prepared by focused ion beam (FIB) equipped with a Ga ion source and imaged with a high-resolution FE-SEM (Zeiss, FIB-SEM NVision 40). For elemental mapping, an Edax EDX detector was used.

X-ray absorption spectroscopy (XAS) experiments were performed at the Phoenix Beamlines (X07MA/B) at the Swiss Light Source (SLS, PSI, Villigen, Switzerland). Data were collected in fluorescence mode (Vortex four-element Si-drift diode detector). For the reference materials, total electron yield signals were also acquired and compared to the fluorescence-detected data to account for self-absorption. The incident intensity I_0 was measured as the total electron yield signal using a 0.5 μm thin polyester foil coated with Ni. All XAS measurements were performed in a vacuum chamber (ca. $2.5 \cdot 10^{-5}$ mbar) using materials supported on a copper plate, while metallic indium was used for sample fixation.

The data were acquired in the range of 950-1600 eV and 3900-4800 eV for the Na and Ca K-edges, respectively. XAS data processing was performed using the Athena software (Demeter 0.9.25 software package)²⁰⁶. Energy calibration was performed using NaCl (1075.6 eV at the inflexion point).²⁰⁷

3.3.3. CO₂ capture tests

The materials synthesized were first assessed with regards to their CO₂ uptake performance in a TGA (Mettler Toledo TGA/DSC 3). In a typical TGA experiment 10-14 mg of sample was placed in a 900 μL sapphire crucible. Prior to the cyclic CO₂ uptake experiments, all samples were calcined at 800 °C for 2 h in N₂. The carbonation reaction was performed for 20 min in 125 cm³ min⁻¹ using 20 vol.% CO₂ in N₂ at 650 °C (including a purge flow of 25 cm³ min⁻¹ of N₂ over the microbalance; total flow rate: 150 cm³ min⁻¹, measured at ambient temperature and pressure). Subsequently, the materials were calcined for 10 min at 900 °C in 30 cm³ min⁻¹ of CO₂ (while maintaining a mandatory purge flow of 25 cm³ min⁻¹ of N₂ over the microbalance). This condition is referred to as CO₂-rich atmosphere. All heating and cooling steps were performed at a rate of 50 °C min⁻¹ in either a CO₂-rich atmosphere or 20 vol.% CO₂. The carbonation-calcination cycle was repeated 10 times in each experiment. The cyclic CO₂ uptake, expressed in g_{CO2} g_{sorbent}⁻¹, was calculated from the measured weight change as:

$$CO_2 \text{ uptake} = \frac{m_{carb} - m_{calc}}{m_{calc}} \quad (\text{Eq. 3.2})$$

where m_{carb} is the sample mass measured at the end of the carbonation stage and m_{calc} is the sample mass measured at the end of the calcination stage. Replacing m_{carb} with $m(t)$, the sample mass measured during the carbonation reaction, gives a CO₂ uptake as a function of time t .

Temperature-programmed carbonation/ calcination (TPC) experiments were performed as follows. After an initial calcination step (800 °C, 2 h, N₂) the sample was cooled down to 50 °C in N₂. Next, the sample was heated up from 50 °C to 1000 °C at a rate of 10 °C min⁻¹ in a flow of 20 vol.% CO₂ in N₂ (total flow rate: 150 cm³ min⁻¹).

3.4. Results and discussion

3.4.1. Synthesis and structural characterization of the as-prepared sorbents

A series of $\text{CaCO}_3\text{-Na}_2\text{CO}_3$ materials with Na_2CO_3 loadings ranging from 1 to 20 wt.% were synthesized *via* a wet ball-milling route ($\text{Ca}/x\text{Na}$, where x is the wt.% of Na_2CO_3 added, Table B.1).²⁰⁵ X-ray powder diffraction (XRD) analysis of the as-prepared (ball-milled) materials revealed only Bragg peaks due to the CaCO_3 calcite phase (R-3c space group) when the Na_2CO_3 loading was below 10 wt.% (e.g., $\text{Ca}/3\text{Na}$). No crystalline phase of Na_2CO_3 was detected, likely due to the low Na_2CO_3 content and/or its amorphous nature (Figure 3.1a and B.2). The XRD patterns of materials with higher Na_2CO_3 loading, i.e. $\text{Ca}/10\text{Na}$ and $\text{Ca}/20\text{Na}$, showed peaks due to both calcite and Na_2CO_3 (C2/m space group) (Figure 3.1a and B.2). Scanning electron microscopy (SEM, Figure B.3) analysis of the ball-milled materials showed that the addition of Na_2CO_3 to the sorbents did not have any appreciable influence on the morphology of the materials. For instance, after ball milling, $\text{Ca}/3\text{Na}$ and $\text{Ca}/20\text{Na}$ consisted of submicrometer-sized particles with a particle size comparable to that of $\text{Ca}/0\text{Na}$, i.e. $0.35 \pm 0.15 \mu\text{m}$ (Figure B.3 and Figure B.4). Energy-dispersive X-ray spectroscopy (EDX) analysis confirm a uniform distribution of Na (Na_2CO_3) within the material, as the elemental maps of Ca and Na overlapped with each other and no Na-rich agglomerates were observed (Figure B.4). N_2 physisorption analysis revealed that regardless of the sodium content, the sorbents possessed BET surface areas in the range of 9 - 11 $\text{m}^2 \text{g}^{-1}$ and BJH pore volumes in the range of 0.04 - 0.06 $\text{cm}^3 \text{g}^{-1}$ (Figure B.5).

3.4.2. Cyclic CO_2 uptake

The cyclic CO_2 uptake performance of the ball-mill derived $\text{Ca}/x\text{Na}$ materials (Figure 3.1b) was determined under gas atmospheres and temperatures close to that prevailing in the envisioned large-scale CaL process, i.e. the calcination step was performed at 900 °C in a CO_2 -rich atmosphere; and the carbonation at 650 °C in 20 vol.% CO_2 in N_2 . $\text{Ca}/0\text{Na}$ (i.e. the pure ball-milled calcite) exhibited a relatively high initial CO_2 uptake ($0.65 \text{ g}_{\text{CO}_2} \text{ g}_{\text{sorbent}}^{-1}$), however, its CO_2 uptake gradually decreased with cycle number and reached $0.29 \text{ g}_{\text{CO}_2} \text{ g}_{\text{sorbent}}^{-1}$ after 10 carbonation/calcination cycles. The decay in the CO_2 capacity of unsupported CaO is due to the sintering-induced loss in pore volume owing to the low T_T of CaCO_3 of 533 °C.²⁵ We observed that the addition of Na_2CO_3 to CaO ($\text{Ca}/x\text{Na}$, with $x = 1, 3, 6, 10$ and 20) led to a dramatic drop in the CO_2 uptake of the sorbents (Figure 3.1b)

when compared to pure CaO (Ca/0Na). For instance, the maximum CO₂ uptake of Ca/1Na in the 1st cycle was only 0.21 g_{CO₂} g_{sorbent}⁻¹, a value that is ca. three times lower compared to Ca/0Na (0.65 g_{CO₂} g_{sorbent}⁻¹). After the 10th cycle, Ca/1Na showed a CO₂ uptake of 0.05 g_{CO₂} g_{sorbent}⁻¹, a value that is ca. six times lower compared to Ca/0Na. Increasing the Na₂CO₃ content deteriorated further the CO₂ uptake of the sorbents; for example, Ca/20Na showed CO₂ uptakes of 0.14 g_{CO₂} g_{sorbent}⁻¹ and 0.04 g_{CO₂} g_{sorbent}⁻¹ in the 1st and 10th cycle, respectively.

Analysis of the temporally-resolved CO₂ uptake curves (Figure B.6) revealed an irreversible mass gain Δm after the calcination step (900 °C, CO₂-rich atmosphere) for the Na₂CO₃-modified sorbents. The observed weight gain Δm indicates the incomplete regeneration of CaCO₃ to CaO in the calcination step. On the other hand, the CO₂ uptake curve of Ca/0Na showed no weight difference when calcined at 900 °C in a CO₂-rich atmosphere (and in the initial calcination at 800 °C in N₂). Moreover, the values of Δm determined are proportional to the Na content in the materials (Figure B.6). This observation suggests the formation of a phase (i.e. a Ca-Na mixed phase) that does neither capture nor release CO₂ under the conditions investigated. Further details about the presence and the nature of this phase is provided by SEM and Na K-edge XANES analyses (*vide infra*).

Additionally, temperature-programmed carbonation/calcination experiments (TPC, 150 cm³ min⁻¹, 20 vol.% CO₂ in N₂, 50 to 1000 °C, 10 °C min⁻¹) of Ca/0Na, Ca/1Na and Ca/20Na as well as the reference Na₂CO₃ were performed in a TGA (Figure B.7). As expected, pure Na₂CO₃ showed no weight increase over the entire temperature range probed. At temperatures above 850 °C, i.e. temperatures exceeding the melting temperature of Na₂CO₃ (melting temperature, $T_M = 851$ °C) a gradual weight loss was detected. This weight loss was due to the slow decomposition of Na₂CO₃ into Na₂O and CO₂, in agreement with previous observations.²⁰⁸ Turning to Ca/0Na, the TPC experiment showed a broad peak of weight gain with a maximum at ca. 570 °C due to the carbonation of CaO. The weight increase was followed by a rapid weight loss due to the decomposition of CaCO₃ starting at 800 °C. Interestingly, the addition of Na₂CO₃ to CaO changed dramatically the sorbent's TPC curve profile. The Na₂CO₃-modified sorbents showed a lower CO₂ uptake at intermediate temperatures ($T < 700$ °C), while the onset temperature for carbonation was not affected by the addition of Na₂CO₃ (Figure B.7). The broad shoulder at intermediate temperatures was

followed first by a narrow, sharp peak at $T \approx 750$ °C, and secondly by a weight loss corresponding to the decomposition of CaCO_3 . Increasing the Na_2CO_3 content shifted the maximum of the carbonation peak towards higher temperatures, i.e. 770 °C for Ca/1Na and 785 °C for Ca/20Na (Figure B.7). In contrast to pure Na_2CO_3 , the Na_2CO_3 -modified sorbents showed no weight loss at high temperatures, indicating the absence of Na_2CO_3 decomposition. We hypothesize that this was due to the formation of a stable Ca-Na mixed phase in CO_2 -containing atmospheres (*vide infra*).

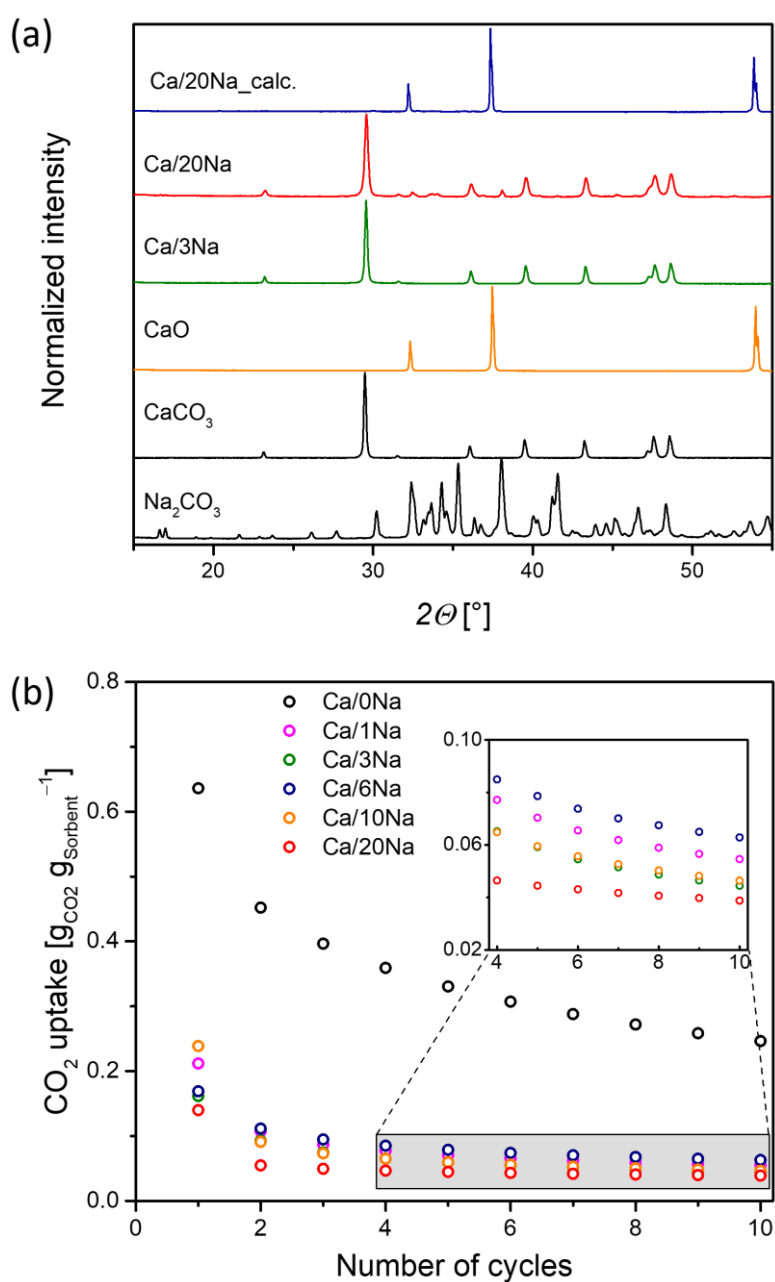


Figure 3.1. a) XRD patterns of CaO-based sorbent as prepared and calcined; and Na_2CO_3 and CaCO_3 references; b) Cyclic CO_2 capture of ball-milled Ca/xNa (calcination at 900 °C in CO_2 -rich atmosphere; carbonation at 650 °C in 20 vol.% CO_2).

3.4.3. Morphological characterization of the calcined sorbents

To understand the effect of the addition of Na_2CO_3 on the sorbents' microstructure and sintering characteristics, XRD, SEM and N_2 -physisorption experiments were performed on the calcined materials (initial calcination at $800\text{ }^\circ\text{C}$ in N_2). After calcination in N_2 at $800\text{ }^\circ\text{C}$, the average particle size remained largely unchanged ($0.4 \pm 0.1\text{ }\mu\text{m}$, Figure 3.2a,b) in Ca/0Na. We also observed an increase in the surface area and pore volume of Ca/0Na to, respectively, $16\text{ m}^2\text{ g}^{-1}$ and $0.13\text{ cm}^3\text{ g}^{-1}$, (compared to $9\text{ m}^2\text{ g}^{-1}$ and $0.04\text{ cm}^3\text{ g}^{-1}$, before calcination), which can be explained by the release of CO_2 during the decomposition of CaCO_3 to CaO (XRD, Figure 3.1a).³³ Different to Ca/0Na, we observed a considerable increase in particle size due to particle coalescence for the Na_2CO_3 -modified sorbents (Figure 3.2a,c). For example, the particle size of Ca/1Na increased from 350 nm to ca. $1.3\text{ }\mu\text{m}$, accompanied by a drastic decrease in surface area (from 10 to $2\text{ m}^2\text{ g}^{-1}$) and pore volume (from 0.06 to $0.01\text{ cm}^3\text{ g}^{-1}$). These measurements hint to a dramatic collapse of the sorbents' microstructure (Figure B.5).

The temperature dependence of the particle size of the sorbents was investigated in more detail and is shown in Figure 3.2a and Figure B.8. Sintering of the Na_2CO_3 -modified sorbents started at $500\text{ }^\circ\text{C}$ and was likely promoted by the addition of Na_2CO_3 ($T_M = 851\text{ }^\circ\text{C}$, $T_T = 290\text{ }^\circ\text{C}$) that covered the surface of CaCO_3 and/or CaO particles (Figure 3.2f), thus, accelerating inter-particle coalescence. The XRD analysis of the calcined, Na_2CO_3 -modified sorbents showed only Bragg peaks due to CaO (Figure 3.1a, Ca/20Na_calc.), possibly due to the amorphous nature of the Na-containing phase.

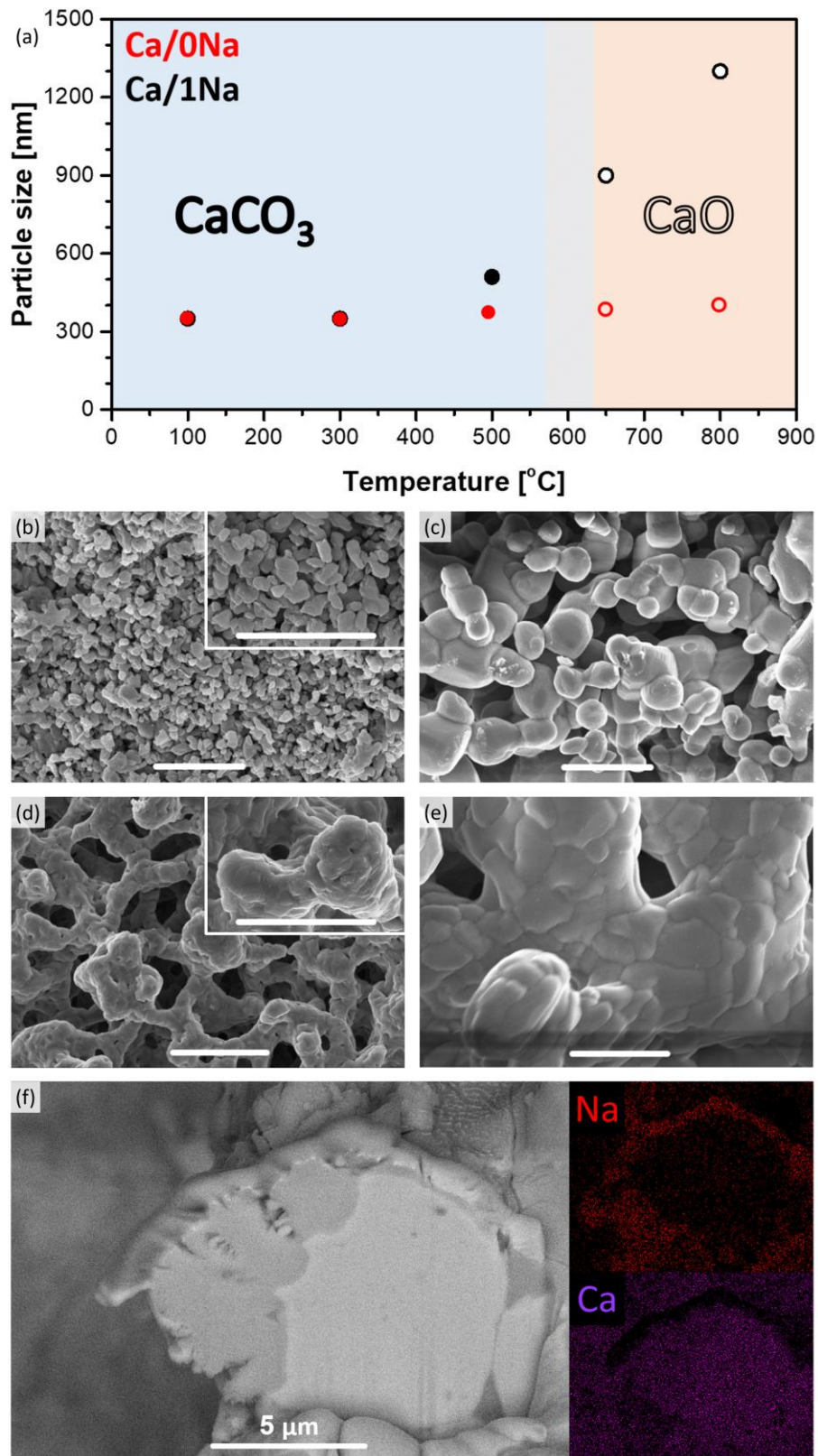


Figure 3.2. a) The evolution of the particle size of Ca/0Na and Ca/1Na during the initial calcination step in N₂ as determined by SEM, as a function of temperature; SEM images of b) Ca/0Na and c) Ca/1Na after the first calcination step; and d) Ca/0Na and e) Ca/1Na after the 10th carbonation step (the scale bar is equal to 2 μm); f) cross sectional HR-SEM and EDX elemental mapping of Ca/20Na after the 10th carbonation step.

3.4.4. The effect of sintering on the CO₂ uptake of the pure CaO sorbent

To determine whether sintering (induced by the addition of Na₂CO₃) was the only reason for the appreciably decreased CO₂ uptake performance of the Na₂CO₃-modified sorbents, we performed a series of control experiments. A set of pure CaCO₃ sorbents was sintered by annealing them in a CO₂ atmosphere at 750 °C for varying durations. The SEM micrographs as well as the surface area and pore volume measurements of the respective materials are presented in Figure B.9 and B.10, respectively, revealing highly sintered materials with specific surface areas and pore volumes below 2 m² g⁻¹ and 0.02 m³ g⁻¹, respectively (carbonated samples). However, similar to the as-prepared Ca/ONa and contrary to the Na₂CO₃-modified sorbents, calcination in N₂ yielded a significant increase in both the surface area and pore volume (Figure B.10). Additionally, we performed cyclic CO₂ uptake measurements for the sintered sorbents and compared the performance to that of pure and Na₂CO₃-modified CaO (Figure B.11). The sintered sorbents exhibited a worse CO₂ uptake performance when compared to Ca/ONa, but they exceeded substantially the CO₂ uptake performance of the Na₂CO₃-modified sorbents. Specifically, the most sintered, but Na₂CO₃-free sorbent that was annealed for 12 h had a CO₂ uptake of 0.15 g_{CO2} g_{sorbent}⁻¹ in the 10th cycle compared to 0.05 g_{CO2} g_{sorbent}⁻¹ for Ca/1Na. These results indicate that sintering was one contributor explaining the poor CO₂ uptake of Na₂CO₃-modified CaO, but not the only factor.

3.4.5. Structure and morphology of the cycled sorbents

XRD analysis of cycled Ca/20Na (collected after the carbonation step) revealed that CaO was the major phase with only traces of CaCO₃ present. This was in good agreement with the TGA-based CO₂ uptake experiments, where a CO₂ uptake of only 0.04 g_{CO2} g_{sorbent}⁻¹ was observed in the 10th cycle, corresponding to a CaO conversion of ca. 5 %. Additional low-intensity peaks appeared in the diffraction pattern, which are tentatively attributed to the Ca-Na double carbonate Na₂Ca(CO₃)₂ phase (in correlation with Na K-edge XAS, *vide infra*). SEM analysis of Ca/1Na after the 10th carbonation cycle (Figure 3.2e) revealed an even higher degree of sintering compared to Ca/1Na after the initial calcination and cycled Ca/ONa (Figure 3.2c and Figure 3.2d, respectively). Despite the drastic, sintering-induced morphological changes, the low magnification SEM/EDX elemental mapping showed no indication of agglomeration of Na-containing phases (i.e. the Na maps still revealed a high dispersion of Na over the CaO/CaCO₃ particles, Figure B.12). To obtain a more detailed insight

in the morphology of the material, a cross section of a Ca/20Na particle after the 10th carbonation step was prepared by FIB cutting and analyzed *via* high-resolution SEM/EDX. We observed that the CaO(CaCO₃) particles were covered by a shell of a Na-rich phase (Figure 3.2f), while the inner part of the particle was almost free of Na (Figure 3.2f).

3.4.6. XAS analysis: the nature of the Na containing phases in the cycled materials

To determine in more detail the nature of the Na-rich phase in the sorbents during the different steps of the CO₂ capture process, Na K-edge XANES data were acquired. After the initial calcination step (800 °C, N₂), the Na K-edge spectra of the sorbents matched perfectly the reference spectra of Na₂CO₃ (Figure B.14). This observation, combined with Ca K-edge XAS results (*vide infra*, Figure B.13), confirmed that all of the Na₂CO₃-modified sorbents consisted of a mixture of CaO and Na₂CO₃ after the initial calcination step and no Ca-Na mixed phase was present. The Na K-edge XANES spectra of all of the sorbents collected after the 10th carbonation step had a similar profile with a very characteristic shape of the XANES spectrum that was different from the XANES spectrum of pure Na₂CO₃ (Figure 3.3). Specifically, all spectra possessed a pre-edge peak at ca. 1073.2 eV (-1.5 eV with respect to the absorption edge, feature A, Figure 3.3), while Na₂CO₃ possessed a pre-edge feature at ca. 1073.5 eV (-1.2 eV with respect to the absorption edge). Additionally, contrary to the spectrum of Na₂CO₃ with a white line maximum at 1078.5 eV, the white line region of the Na₂CO₃-modified sorbents consisted of three defined features, i.e. B (ca. 1076.3 eV), C (ca. 1078 eV) and D (ca. 1080.6 eV, maximum intensity of the spectra) (Figure 3.3). Notably, the obtained Na K-edge spectra of the Na₂CO₃-modified sorbents did not correspond to any previously reported XANES spectrum of Na-based materials. On the other hand, the spectra matched perfectly the Na₂Ca(CO₃)₂ reference (P2₁ca space group,²⁰⁹ see XRD of the synthesized reference in Figure B.15). The Na K-edge XAS spectrum of Na₂Ca(CO₃)₂ is shown in Figure 3.3 and, to the best of our knowledge, is reported here for the first time. A perfect match between the spectrum of Na₂Ca(CO₃)₂ and the spectra of the cycled Na₂CO₃-modified sorbents (collected after the carbonation step) revealed the formation of the Ca-Na double carbonate (Na₂Ca(CO₃)₂) under carbonation conditions (Figure 3.3). Hence, the Na-rich phase that was observed by cross-sectional FIB-SEM (Figure 3.2f) to cover the surface of CaO/CaCO₃ particles was Na₂Ca(CO₃)₂. Figure 3.3 demonstrates that Na K-edge XANES can be used as a fingerprint

to distinguish between Na in Na_2CO_3 or $\text{Na}_2\text{Ca}(\text{CO}_3)_2$ environments. Being an element selective technique, XANES allowed us to study the Na environment in the materials, even when using relatively low Na contents (i.e. < 10 wt.% Na_2CO_3); a composition for which XRD failed to provide sufficient information on the Na containing phases.

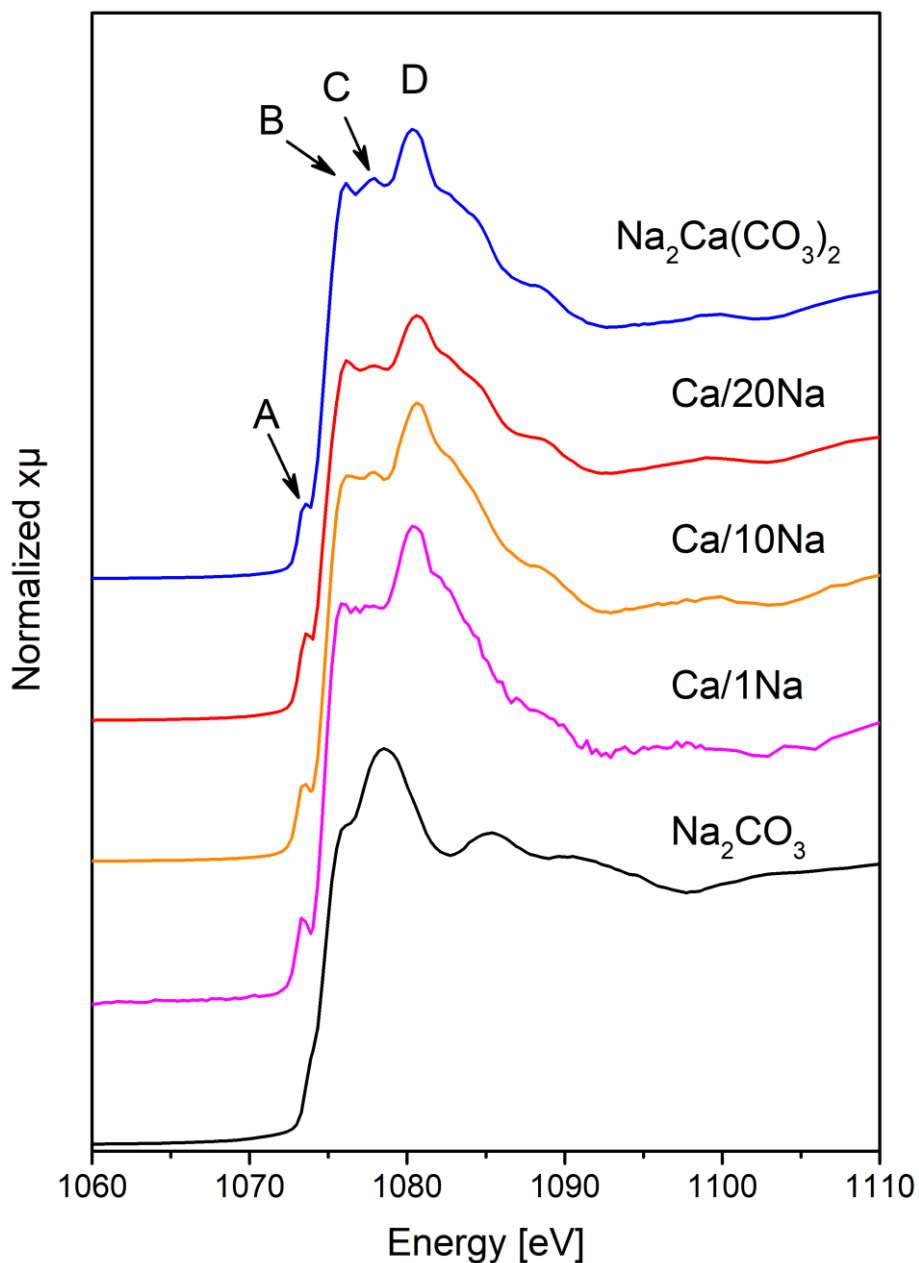


Figure 3.3. Na K-edge XANES spectra of Ca/1Na, Ca/10Na and Ca/20Na after 10th carbonation, as well as the references Na_2CO_3 and $\text{Na}_2\text{Ca}(\text{CO}_3)_2$.

Na K-edge XAS data were complemented by Ca K-edge XAS of the materials (Figure B.13). The spectra of the as-prepared materials matched the reference calcite (CaCO_3), revealing that no phase transformation (e.g. formation of aragonite CaCO_3 polymorph)²⁰⁵

occurred during the ball-milling process (Figure B.13). The spectra of the sorbents after the initial calcination step (800 °C, N₂) matched the reference CaO. For the sample collected after the 10th carbonation cycle, and in line with XRD, the Ca K-edge spectra showed that the Ca was mainly in a CaO environment. Nonetheless, some features corresponding to CaCO₃ could also be distinguished. These observations are in line with the TGA CO₂ uptake experiments revealing a CO₂ uptake below 0.05 g_{CO₂} g_{sorbent}⁻¹ after 10 cycles. Since the majority of the Ca atoms was present in a CaO phase, the Ca K-edge spectra could not distinguish well between the different types of carbonate phases (i.e. CaCO₃ and Na₂Ca(CO₃)₂).

3.4.7. Discussion

After elucidation of the nature of the Ca-Na mixed phase, we carried out a control experiment to evaluate the performance of pure Na₂Ca(CO₃)₂ under cyclic carbonation-calcination conditions (Figure B.16). It was found that in the initial calcination in pure N₂ Na₂Ca(CO₃)₂ decomposed into CaO and Na₂CO₃ (at ca. 600 °C, as determined from the weight loss). In the following carbonation step a rapid weight gain was observed. No weight change was detected during the subsequent calcination step, confirming the stability of Na₂Ca(CO₃)₂ during calcination at 900 °C in a CO₂-rich atmosphere (Figure B.16). This observation correlates well with the cyclic carbonation-calcination experiments of Ca/xNa as described above. In particular, the observed weight gain Δm by TGA under CO₂ rich atmosphere with respect to the initial calcination step in N₂ (Figure B.6) can be explained by the formation of a Na₂Ca(CO₃)₂ phase as revealed by XAS that was stable under both carbonation and calcination (in CO₂ rich atmosphere) conditions. Such a weight increase was due to the reaction between CaO, Na₂CO₃ and CO₂ forming Na₂Ca(CO₃)₂. The melting point of Na₂Ca(CO₃)₂ has been reported as $T_m = 817$ °C,²¹⁰ which is significantly lower than the calcination temperature used here (900 °C). Therefore, during calcination (performed in a CO₂-rich atmosphere) the Na₂CO₃-modified sorbent consisted of solid CaO covered by a molten Na₂Ca(CO₃)₂ layer. Therefore, the presence of a molten salt layer promoted the sintering of the material.

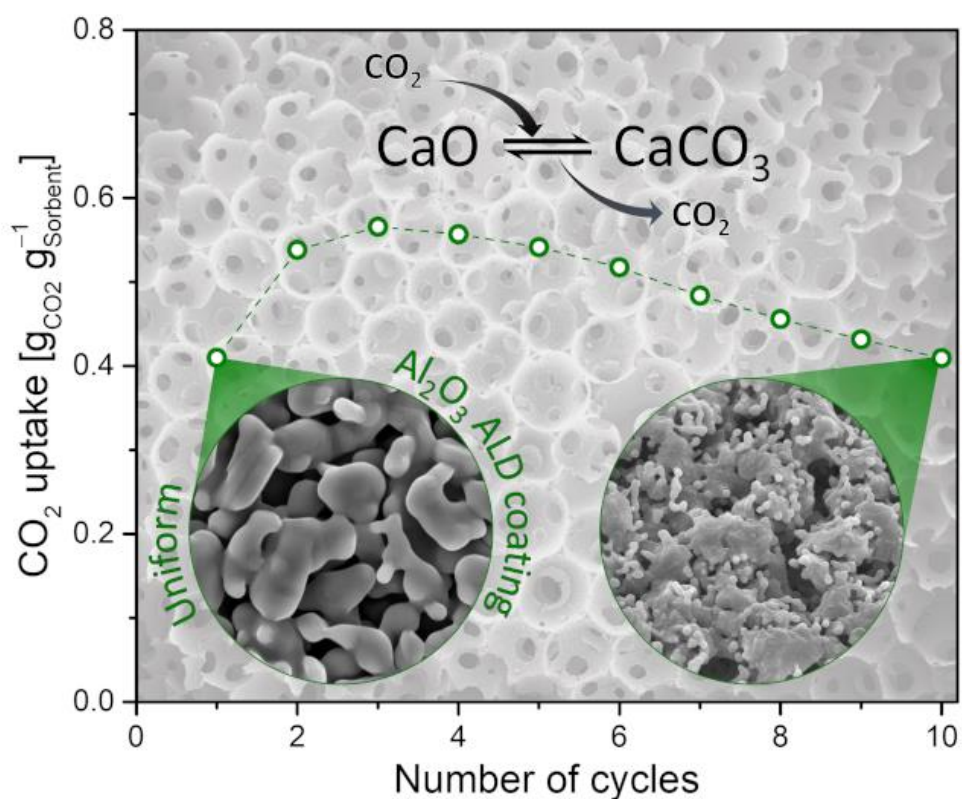
Overall, based on the results obtained here, the formation of Na₂Ca(CO₃)₂ resulted in a dramatic reduction of the CO₂ uptake performance of Na₂CO₃-modified CaO. This negative effect was attributed to (i) the formation of a molten Na₂Ca(CO₃)₂ layer during calcination in CO₂ rich atmosphere that promoted sintering, and (ii) the solidification of Na₂Ca(CO₃)₂ during carbonation that resulted in a dense layer covering the unreacted (or partially reacted) CaO

particles, thus hindering the further carbonation of CaO. Additionally, due to its low Tammann temperature ($T_T \approx 270$ °C), $\text{Na}_2\text{Ca}(\text{CO}_3)_2$ further promoted the sintering of the CaO/CaCO₃ particles.

3.5. Conclusions

To conclude, we demonstrated that the addition of 1 to 20 wt.% Na_2CO_3 to CaO reduces dramatically the CO₂ uptake performance of CaO from ca. $0.3 \text{ g}_{\text{CO}_2} \text{ g}_{\text{sorbent}}^{-1}$ for pure CaO to $0.05 \text{ g}_{\text{CO}_2} \text{ g}_{\text{sorbent}}^{-1}$ for Na_2CO_3 modified CaO after ten carbonation cycles. Combining TGA, XAS and FIB-SEM analyses allowed us to assign the formation of $\text{Na}_2\text{Ca}(\text{CO}_3)_2$ as a key factor to explain the poor CO₂ capture performance of Na_2CO_3 -modified CaO. The poor CO₂ capture performance of these materials is attributed to the presence of the low Tammann temperature phase $\text{Na}_2\text{Ca}(\text{CO}_3)_2$ that is molten during the calcination step, thereby promoting sintering. During carbonation, a solid, dense layer of $\text{Na}_2\text{Ca}(\text{CO}_3)_2$ covers the unreacted CaO particles, thus preventing its carbonation to CaCO₃.

Chapter 4: CaO-based CO₂ sorbents with a hierarchical porous structure made *via* microfluidic droplet templating



The results of this chapter are published as:

A. Kurlov, A. Armutlulu, F. Donat, A. R. Studart, C. R. Müller, CaO-Based CO₂ Sorbents with a Hierarchical Porous Structure Made *via* Microfluidic Droplet Templating, *Ind. Eng. Chem. Res.*, **2020**, 59, 7182-7188

4.1. Abstract

Calcium looping, a CO₂ capture technique based on the cyclic carbonation and calcination of CaO, is a promising short- to midterm solution to reduce CO₂ emissions. However, CaO suffers from sintering under industrially relevant operating conditions, which reduces rapidly its cyclic CO₂ uptake capacity. Here, we report the design and manufacture of a hierarchical, porous (HP) CaO-based CO₂ sorbent. The hierarchically porous sorbent is created through the assembly of calcium carbonate nanoparticles and monodisperse oil droplets generated *via* microfluidic emulsification. The structure of the sorbent is stabilized by an Al₂O₃ coating *via* atomic layer deposition (ALD). The sorbent outperformed the CO₂ uptake of the reference limestone by ca. 140 %. The improved CO₂ uptake capacity is attributed to (i) the stabilization of the micro- and mesoporous structure of the material by the formation of Ca–Al mixed oxides, that is, Ca₁₂Al₁₄O₃₃ and Ca₃Al₂O₆, and (ii) an improved mass transport within the sorbent particles owing to the HP structure of the material.

4.2. Introduction

CO₂ capture and storage (CCS) is expected to contribute appreciably to the reduction of anthropogenic CO₂ emissions that are linked directly to global warming.^{164-166,211} One of the most promising carbon capture technologies is calcium looping that relies on CaO for CO₂ capture, forming CaCO₃ in a reversible, cyclic fashion. Sorbents based on CaO are relatively cheap, naturally abundant and pure CaO has a high theoretical CO₂ uptake capacity (0.78 g_{CO₂} g_{sorbent}⁻¹).^{25-26,212-213} However, CaO-based sorbents undergo a rapid decay in their CO₂ uptake upon repeated carbonation/calcination cycles, which has been attributed largely to the sintering of the CaCO₃ phase.³⁰⁻³² That is because the operational temperatures of the calcium looping process range between 650-950 °C, which is considerably higher than the Tammann temperature of CaCO₃ ($T_T = 533$ °C).²⁵ To mitigate the sintering-induced deactivation of CaO-based sorbents, several concepts have been implemented such as high temperature activation,²¹⁴⁻²¹⁵ steam treatment²¹⁶⁻²¹⁷ and the stabilization of CaO with high- T_T materials such as Al₂O₃, MgO, TiO₂, or ZrO₂.^{25,38,42,56-57,204-205} Among these approaches, the introduction of a thermal stabilizer tends to improve significantly the cyclic CO₂ uptake stability of CaO. Besides sintering, breakage and attrition of sorbent particles are further challenges encountered in the calcium looping process. When operated in a (circulating)

fluidized bed, fine particles can entrain from the bed and leave the reactor system. As a consequence, an additional make-up stream of fresh material is required, increasing the operational cost of the process.²¹⁸⁻²²⁰ If the calcium looping process is employed for CO₂ capture, the most likely reactor will be (circulating) fluidized beds to handle the large volumetric flow rates of gas.^{177,221} Synthetic sorbents with a high surface area and large pore volume will most likely not be suitable for such reactor systems, owing to their lack of mechanical strength.

Calcium looping has been used also for sorption-enhanced reaction schemes, e.g. the sorption-enhanced reforming of CH₄ to produce high purity H₂.²²² For sorbent-enhanced reactions, fixed bed reactors are employed commonly, thus reducing the requirements on the mechanical stability of the sorbent to some extent.²²³⁻²²⁵ Previous works have demonstrated the general feasibility of the processes using a mixture of a dry reforming catalyst, e.g. Ni supported in Al₂O₃ and a CaO-based sorbent.^{161,226} In these sorption-enhanced processes the deactivation of the CaO-based sorbent is also a key limitation, as it reduces process performance, i.e. the time during which H₂ of high purity can be generated.¹⁶¹ The stability of the reforming catalyst has been less of a concern. When used in a packed bed configuration, (internal) mass transfer limitations in a material have to be considered, in addition to resistance to sintering. One strategy to reduce mass transfer limitations is the design of materials of high porosity. In this context, materials that contain a hierarchical porosity (HP), allowing fast mass transfer even if sintering occurs, are an attractive choice.²²⁷⁻²²⁸ Such HP materials have been applied in a variety of applications including catalysis,^{227,229} and, particularly, sorption-based techniques.^{56,230} Commonly adopted protocols to prepare HP structures include sacrificial templating,²³¹⁻²³³ freeze drying,²³⁴ and sol-gel techniques.²³⁵

In this work, we report on a microfluidic approach to prepare HP-CaCO₃ structures using an oil-in-water emulsion as sacrificial template (Figure 4.1).²³⁶⁻²³⁷ To stabilize the HP structure of the sorbent at high temperatures, the CaCO₃ particles are covered with a uniform coating of Al₂O₃ through atomic layer deposition (ALD). We first study the effect of the Al₂O₃ layer thickness on the stability and on the CO₂ capture efficiency of the structure by performing cyclic carbonation-regeneration experiments. Electron microscopy and X-ray diffraction are used to characterize the sorbents and shed light on the mechanisms underlying the stability and performance of the hierarchical porous structures.

4.3. Experimental section

4.3.1. Materials

Commercial CaCO₃ (Fischer Chemicals, analytical reagent grade, 10±5 μm particle size, Figure C.1) was modified through ball-milling (48 h milling at 500 rpm) to decrease its particle size following a reported method.²⁰⁵ The calcite nanoparticles obtained had a monomodal particle size distribution with an average size of 350 nm (Figure C.2) and BET surface area and BJH pore volume values of 16 m² g⁻¹ and 0.13 cm³ g⁻¹, respectively. Hierarchical porous structures were prepared by a sacrificial template method. A sacrificial emulsion template was produced *via* a microfluidic technique in a microcapillary reactor (Figure 4.1a and b). Here, a 2 wt.% PVA (Sigma-Aldrich, MW = 31000-50000) aqueous solution was used as the outer phase and 1,2-dichlorobenzene (DCB) (Sigma-Aldrich, 99 %) as the inner oil phase. The flow rates of the water and oil phase were controlled by syringe pumps (PHD 2000, Harvard Apparatus). Once a desired volume of DCB oil droplets had been collected (Figure 4.1c), the oil droplets were mixed with the freshly sonicated suspension of 40 vol.% CaCO₃ in a 2 wt.% PVA aqueous solution and left to settle to the bottom of a beaker. Once all oil droplets had settled, excess water was removed and the emulsion was left to dry at room temperature for 48 h. To remove the PVA coating of the CaCO₃ particles, the material was calcined in air at 500 °C for 2 h. The calcined material was sieved to 300-1180 μm for assessing the cyclic performance. Commercial limestone (*Rheinkalk limestone* pit, Germany), was used as a reference material.

4.3.2. Atomic layer deposition (ALD) of Al₂O₃

A commercial ALD system (Sunale R-150B, Picosun) was used to deposit Al₂O₃ films onto HP-CaCO₃ porous structures. Prior to deposition, the ALD chamber was flushed three times with nitrogen. Nitrogen served as both the purge and carrier gas for the precursors. Throughout the deposition process, the temperature of the reaction chamber was maintained at 300 °C, and the sample therein was exposed to pulse injections of electronic grade trimethylaluminium (TMA, Pegasus Chemicals) and deionized (DI) water in an alternating fashion. In a typical synthesis, the pulse and purge times of the precursors were set to 1 s and 10 s, respectively. According to reference experiments performed on Si wafers, the deposition rate of Al₂O₃ was ca. 0.9 nm/cycle as determined by spectroscopic ellipsometry (Sentech SE850 Ellipsometer).

4.3.3. Characterization

X-ray diffraction (XRD): The crystallinity and phase composition of the sorbents was analyzed by XRD (Bruker, AXS D8 Advance). The X-ray diffractometer was equipped with a Lynxeye superspeed detector and operated at 40 mA and 40 kV. All samples were scanned within the 2θ range of $5 - 90^\circ$ using a step size of 0.025° . A qualitative phase analysis was performed using the Eva software package (Bruker Corporation).

Electron microscopy: Scanning electron microscopy (SEM) was performed on a LEO Gemini 1530 (Zeiss, Germany). Prior to imaging all samples were sputtered with a thin (ca. 3 nm) layer of Pt. Scanning micrographs were obtained at 5 kV while cross sectional back scattered electron micrographs and EDX mapping were obtained at 20 kV. Prior to cross sectional imaging the sample was embedded into a matrix of an acrylic resin (SpeciFast, Struers) and polished first using sandpaper (from 300 to 1200 grade) and, finally, a $1 \mu\text{m}$ diamond paste (M106, Reishauer). Scanning transmission electron microscopy (STEM) was performed on a FEI Talos F200X operated at 200 kV and equipped with a SuperX EDX consisting of four SDD detectors. The probe size for STEM was approximately $0.8 \text{ nm} \times 0.8 \text{ nm}$. A 3-pixel smoothing filter was applied for visualization purposes.

4.3.4. CO₂ capture tests

The materials synthesized were investigated under realistic capture conditions using a thermogravimetric analyzer (TGA, Mettler Toledo TGA/DSC 3). The calcination reaction was performed in a CO₂-rich atmosphere at 900°C . Prior to the cyclic CO₂ uptake experiments, all samples were calcined at 800°C for 2 h in air. In a typical TGA experiment 2.5-3 mg of sample was placed in a $70 \mu\text{L}$ alumina crucible. The carbonation reaction was performed for 20 min in 20 vol.% CO₂ in N₂ (total flow rate: $150 \text{ cm}^3 \text{ min}^{-1}$, measured at ambient temperature and pressure) at 650°C . Subsequently, the materials were calcined for 10 min in a CO₂-rich atmosphere at 900°C (total flow rate: $55 \text{ cm}^3 \text{ min}^{-1}$). Flow rates include a N₂ purge flow of $25 \text{ cm}^3 \text{ min}^{-1}$ over the microbalance. All heating and cooling steps were performed at a rate of $50^\circ\text{C min}^{-1}$ in pure CO₂ and 20 vol.% CO₂, respectively. The cyclic carbonation-calcination experiments were repeated 10 times. The cyclic CO₂ uptake, expressed in $\text{g}_{\text{CO}_2} \text{ g}_{\text{sorbent}}^{-1}$, was calculated from the measured weight change as:

$$\text{CO}_2 \text{ uptake} = \frac{m_{\text{carb}} - m_{\text{calc}}}{m_{\text{calc}}} \quad (\text{Eq. 4.1})$$

where m_{carb} is the sample mass measured at the end of the carbonation stage and m_{calc} is the sample mass measured at the end of the calcination stage. Replacing m_{carb} with $m(t)$, the sample mass measured during the carbonation reaction, gives the CO₂ uptake as a function of time.

4.4. Results and discussion

4.4.1. Sorbent synthesis

Electron micrographs of the HP-CaCO₃ structure obtained by the microfluidic approach capture the unique hierarchical architecture of the sorbent (Figure 4.1d). The low magnification image reveals the formation of an open, macroporous structure with a macropore size of ca. 150-200 μm. This open porosity ensures a rapid access of the gaseous reactants to the sorbent particles. The image at a higher magnification (inset of Figure 4.1d) depicts the predominantly submicron-sized grains that serve as the building blocks of the backbone of the hierarchical structure. The open windows between the macropores in the dried structure correspond to the contact points between the oil droplets of the initial emulsion template. As observed in earlier work,²³⁶ particles present in the aqueous continuous phase of the emulsion are depleted from the contact point between droplets during the assembly process. This occurs when the particles are well wetted by the continuous phase and thus do not adsorb at the oil-water interface of the templating emulsions. It is worth mentioning that while the microfluidic device utilized in this study delivers emulsion quantities that are sufficient for preparing lab-scale samples, the fabrication of larger porous structures would require a higher emulsification throughput. Recent developments in microfluidic emulsification technologies have shown that the production of monodisperse droplets at high throughput rates is possible by combining a step emulsification mechanism with extensive parallelization of droplet-making fluidic channels.²³⁸

Coating of the material with Al₂O₃ x ALD, shown in Figure 4.1e, did not cause a notable change in the material's macrostructure, suggesting that the operating conditions of the ALD process have no detrimental impact on the morphology. In the given example, 100 ALD cycles were employed to generate an Al₂O₃ layer of 9 nm thickness. The high-magnification SEM image, shown in Figure 4.1e, reveals that the surface morphology of the building blocks became smoother after ALD coating. XRD analysis of the ALD-coated materials (Figure 4.2a)

shows the presence of CaCO_3 (calcite) only, indicating that the as-synthesized Al_2O_3 coating was amorphous.

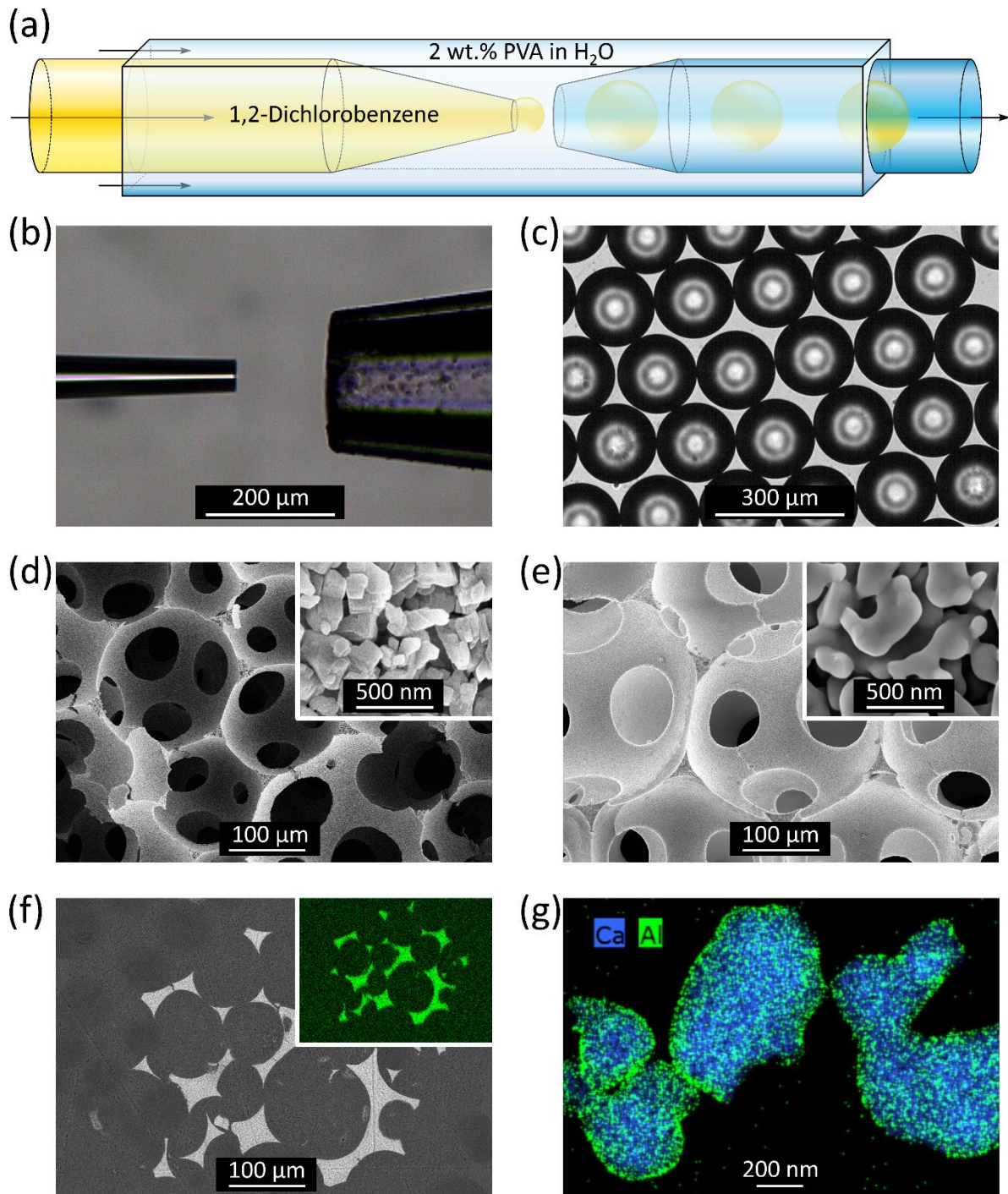


Figure 4.1. a) Schematic illustration of the preparation of the templating emulsion in a double microcapillary device, b) high-magnification light microscopy image of the microfluidic device, and c) example image of the droplets of 1,2-dichlorobenzene formed in the microcapillary device. SEM images of the hierarchical, porous CaCO_3 structure (d) as-prepared and (e) after 100 Al_2O_3 ALD cycles. f) Cross-sectional SEM image of as-prepared HP- CaCO_3 after exposure to 100 Al_2O_3 ALD cycles. The inset shows EDX map the distribution of aluminium in the structure. g) STEM-EDX maps of the CaCO_3 particles comprising the backbone of the HP- CaCO_3 structure after exposure to 100 Al_2O_3 ALD cycles.

To probe the homogeneity of the ALD-grown Al_2O_3 film within the CaCO_3 structure, EDX was performed on cross-sections. An EDX mapping confirms the homogeneous distribution of aluminium within the sorbent structure (Figure 4.1f). Furthermore, STEM/EDX maps of Ca and Al (in blue and green, respectively in Figure 4.1g) indicate a conformal coating of Al_2O_3 onto the submicron-sized CaCO_3 particles comprising the backbone of the HP structure.

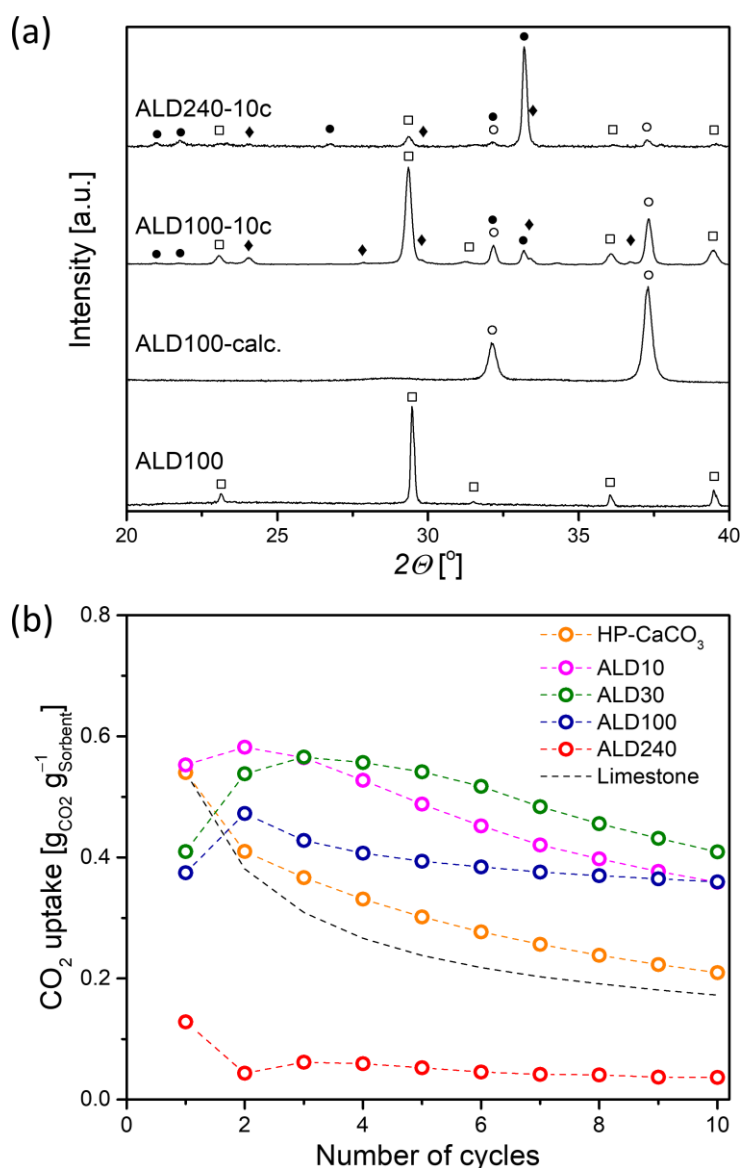


Figure 4.2. a) XRD patterns of HP- CaCO_3 -based, Al_2O_3 -coated CO_2 sorbents at different reaction stages, i.e. as-prepared (ALD100), calcined (ALD100-calc) and after 10 carbonation/calcination cycles (carbonated state, ALD100-10c and ALD240-10c). Samples ALD100-10c and ALD240-10c were previously prepared using 100 and 240 Al_2O_3 deposition cycles during the ALD coating process. Crystalline (\square) calcite, CaCO_3 ; (\circ) lime, CaO ; (\blacklozenge) mayenite, $\text{Ca}_{12}\text{Al}_{14}\text{O}_{33}$; (\bullet) tricalcium aluminate, $\text{Ca}_3\text{Al}_2\text{O}_6$ phase are indicated directly in the XRD pattern. b) Cyclic CO_2 uptake of HP-based CO_2 sorbents as a function of cycle number and number of ALD cycles. The benchmark limestone is also included.

4.4.2. CO₂ capture performance

The cyclic CO₂ uptake performance of the HP-based sorbents was assessed in a TGA and compared to that of the benchmark limestone (Figure 4.2b). The HP-structured material without Al₂O₃ showed only a marginal improvement over the benchmark sorbent limestone. The minor improvement can be explained by the introduction of extra macroporosity as well as the smaller initial grain size in HP-CaCO₃ compared to the limestone. Calcite nanoparticles in the HP-CaCO₃ structure have a diameter of ca. 350 nm, whereas those in the reference limestone exhibit ca. 2 μm (Figure C.3). Nonetheless, both sorbents were prone to sintering under the harsh operating conditions, as visualized by SEM (Figure 4.3a and Figure C.4).

Al₂O₃-stabilized sorbents with a film thickness as low as 1 nm (10 ALD cycles, Ca : Al ~ 50) outperformed their counterparts from the second calcination/carbonation cycle onward and exhibited a remarkable cyclic stability. The incorporation of higher amounts of Al₂O₃ to reach coating thicknesses of 2.7 and 9 nm (30 and 100 ALD cycles and Ca : Al atomic ratios of 5 and 3, respectively) resulted in a further improvement in the cyclic stability of the sorbents, albeit at the cost of an overall reduced CO₂ uptake. The decrease in the overall CO₂ uptake can be explained by the formation of mixed oxides in the CaO - Al₂O₃ system (i.e. mayenite and/or tricalcium aluminate),^{58,239} which is not active for CO₂ uptake at the conditions studied. After 10 carbonation/calcination cycles, the CO₂ uptake of the sorbents that had been stabilized with Al₂O₃ coatings of a thickness of 2.7 or 9 nm, was 0.41 and 0.36 g_{CO₂} g_{sorbent}⁻¹, respectively. These values exceeded the performance of the reference limestone by ca. 110 % and 140 %, respectively. A substantial further increase of the thickness of the Al₂O₃ coating to ca. 20 nm (240 ALD cycles, Ca : Al atomic ratio of ca. 1.6) reduced the CO₂ uptake capacity of the sorbent to negligible quantities, i.e. 0.04 g_{CO₂} g_{sorbent}⁻¹ after 10 carbonation/calcination cycles.

The carbonation profiles shown in Figure C.5 revealed a much slower carbonation rate in the first carbonation for the Al₂O₃ coated (i.e. HP-CaCO₃ coated with 30 ALD cycles) sorbent compared to pure HP-CaCO₃, which was probably due the amorphous Al₂O₃ layer hampering CO₂ access to CaO. For higher cycle numbers, i.e. 5 and 10, the carbonation rates of both pure and Al₂O₃ coated HP-CaCO₃ were very similar. As is also evident from the XRD pattern in Figure 4.2a, the amorphous Al₂O₃ transformed into crystalline calcium aluminate during

cycling and thus impaired the integrity of the Al_2O_3 coating, providing a better access of CO_2 to unreacted CaO and stabilizing the structure.

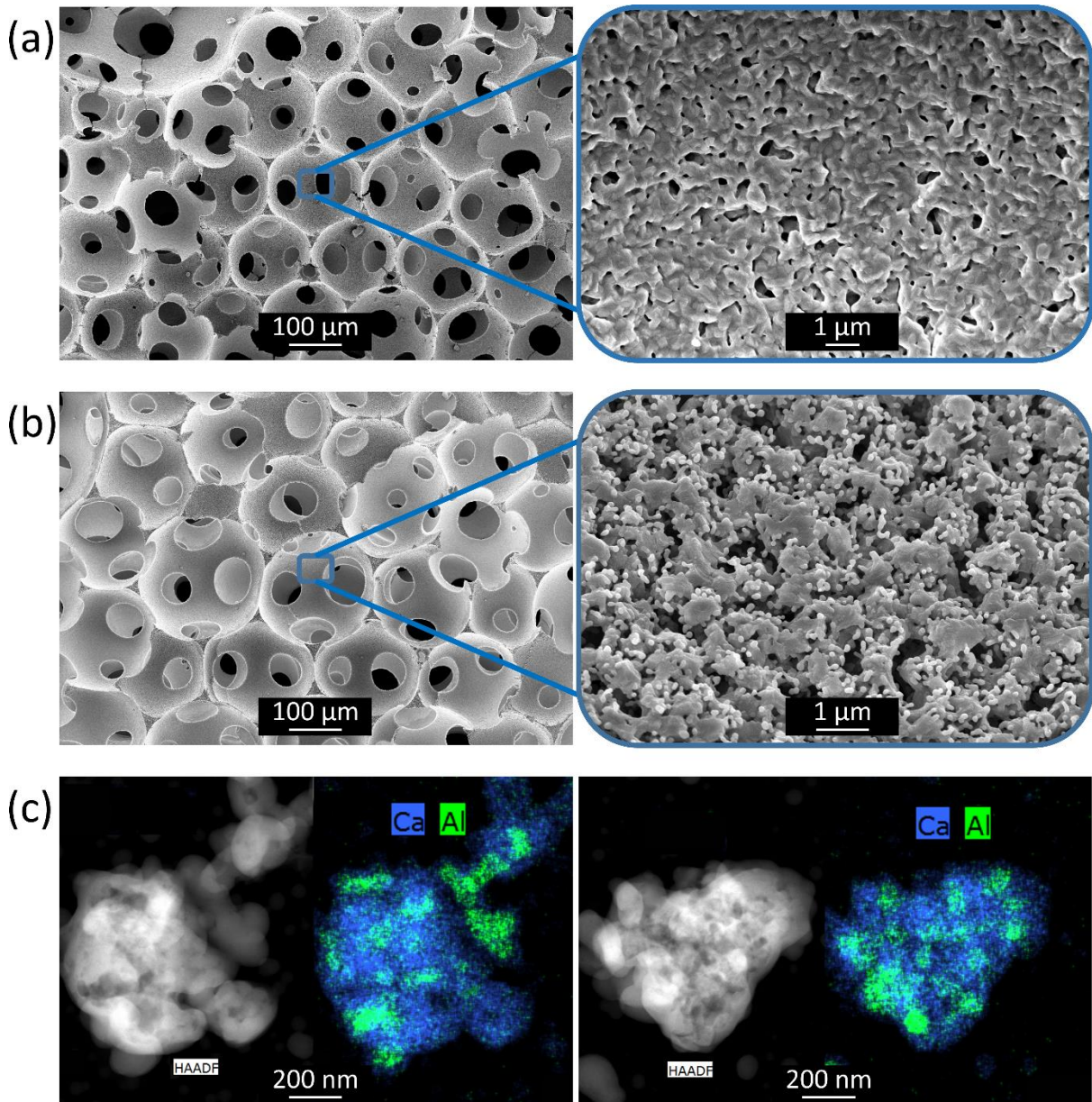


Figure 4.3. SEM micrographs of HP- CaCO_3 after 10 carbonation/calcination cycles in the (a) absence and (b) presence of an ALD-grown Al_2O_3 coating (c) HAADF and STEM-EDX maps of agglomerates of CaCO_3 backbone particles in HP- CaCO_3 exposed to 100 Al_2O_3 ALD cycles after 10 carbonation/calcination cycles.

4.4.3. Characterization of reacted sorbents

XRD analysis of the sorbents after 10 carbonation/calcination cycles (carbonated state) was performed to probe the interaction between Al_2O_3 and CaO and link this interaction to material stabilization or deactivation. HP- CaCO_3 containing a 1 nm thick coating of alumina showed no reflections due to aluminium-containing phases (Figure C.6), probably

because the relative quantity of the Ca-Al mixed oxide was too small (the atomic ratio Ca : Al in this material was 50 : 1). XRD analysis of the sorbents that contained an Al₂O₃ coating of thickness 2.7 or 9 nm revealed the presence of a mayenite (Ca₁₂Al₁₄O₃₃) phase (Figure 4.2a), which has been associated with the stabilization of CaO-based sorbents against sintering.^{42,239} In addition, XRD analysis of the sorbent with a 9nm-thick alumina coating shows ca. 8 wt.% of the Ca-rich tri-calcium-aluminate (Ca₃Al₂O₆) phase.

On the contrary, the sorbent with the thickest Al₂O₃ coating, i.e. ca. 20 nm (240 ALD cycles), is almost phase pure Ca₃Al₂O₆, containing only small quantities of mayenite (2 wt.%), calcite (5 wt.%) and lime (<1 wt.%) (Figure 4.2a). This observation explains the dramatically reduced CO₂ uptake capacity of this sorbent (Figure 4.2b). The very low amount of active CaO in this sample is insufficient for effective CO₂ capture. The predominant presence of Ca₃Al₂O₆ in the HP-CaCO₃ sample coated with a 20 nm thick layer of alumina is also in agreement with the atomic ratio of Ca : Al ~ 1.6 in this material as determined by EDX. Interestingly, only the Al₂O₃-stabilized sorbents showed some activation during the initial cycles. Such a behaviour has been observed previously in Al₂O₃-stabilized CaO-based sorbents⁵⁷ and was explained by phase changes in the Ca-Al mixed oxides.⁵⁸

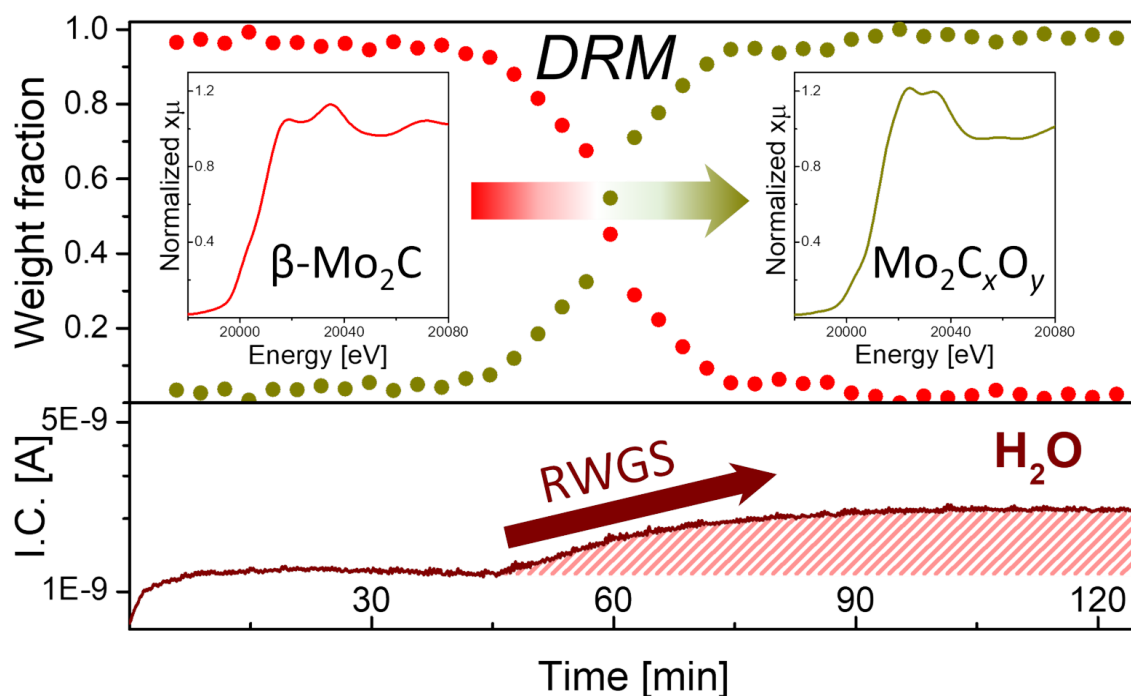
Finally, we probed the morphology of the cycled sorbents by electron microscopy (Figure 4.3a and b) aiming to link changes in the sorbents' morphology to changes in the carbonation profile of the materials (Figure C.5). Although pure HP-CaCO₃ lacked a structural stabilizer (Al₂O₃), the sorbent maintained its HP macro-structure over the cyclic experiments. Only at the micro- and meso-porosity level, a significant degree of sintering was observed (Figure 4.3a). The loss in micro- and meso-porosity caused the appreciable reduction in the CO₂ uptake of the material (Figure 4.2b). Owing to the large volumetric expansion of the material during carbonation (the ratio of the molar volume of CaCO₃ to CaO is ca. 2 : 1) and the low diffusion coefficient of CO₂ in CaCO₃ (ca. 100 times lower than the diffusion coefficient of CO₂ in CaO), a high micro- and meso-porosity is required to yield high CO₂ uptakes.²⁴⁰ The carbonation profile of HP-CaCO₃ (Figure C.5) shows a very rapid transition from the kinetically-controlled to the diffusion-controlled regime, suggesting the blockage of micro- and small meso-pores such that some pore volume was inaccessible for carbonation. By contrast, Al₂O₃-stabilized sorbents did not only maintain their macro-structure but also preserved the porosity on the meso- and, most probably, micro-level to a large extent

(Figure 4.3b). This structural stability was reflected by a relatively stable cyclic CO₂ uptake of these sorbents. Indeed, comparing the carbonation profiles of unstabilized HP-CaCO₃ and HP-CaCO₃ coated with 30 ALD cycles of Al₂O₃ reveals a major difference in the diffusion-limited regime. The smooth transition from the kinetically- to the diffusion-controlled regime for alumina-stabilized sorbents indicates that mesoporosity was largely preserved over 10 carbonation/calcination cycles. Additional high-resolution SEM images reveal the formation of dispersed nanoparticles upon cycling. Probing these areas by STEM/EDX (Figure 4.3c) confirmed that these nanoparticles were composed of Al-containing phases, i.e. mayenite and/or Ca₃Al₂O₆, acting as spacers between neighbouring grains of CaCO₃ and thus, providing stability to the sorbent against thermal sintering.

4.5. Conclusions

In summary, hierarchical porous CaO-based CO₂ sorbents were prepared *via* a sacrificial templating method and stabilized by an ALD-derived Al₂O₃ coating. The macrostructure of the sorbents was preserved throughout cyclic CO₂ capture and release reactions. Sorbents that were stabilized by an ALD-grown coating of Al₂O₃ showed also a high stability of the meso- and micro-scale structural features due to a significant reduction of sintering. Cyclic CO₂ uptake experiments revealed that after 10 carbonation/calcination cycles the best sorbent possessed a CO₂ uptake capacity of 0.41 g_{CO₂} g_{sorbent}⁻¹, exceeding the capacity of the benchmark limestone by ca. 140 %.

Chapter 5: Molybdenum carbide and oxycarbide from carbon-supported MoO₃ nanosheets: phase evolution and DRM catalytic activity assessed by TEM and *in situ* XANES/XRD methods



The results of this chapter are published as:

A. Kurlov, X. Huang, E. B. Deeva, P. M. Abdala, A. Fedorov, C. R. Müller, Molybdenum Carbide and Oxycarbide from Carbon-Supported MoO₃ Nanosheets: Phase Evolution and DRM Catalytic Activity Assessed by TEM and *in situ* XANES/XRD Methods, *Nanoscale*, **2020**, 12, 13086-13094

5.1. Abstract

Molybdenum carbide (β -Mo₂C) supported on carbon spheres was prepared *via* a carbothermal hydrogen reduction (CHR) method from delaminated nanosheets of molybdenum (VI) oxide (*d*-MoO₃/C). The carburization process was followed by combined *in situ* XANES/XRD analysis revealing the formation of molybdenum oxycarbide Mo₂C_xO_y as an intermediate phase during the transformation of *d*-MoO₃/C to β -Mo₂C/C. It was found that Mo₂C_xO_y could not be completely carburized to β -Mo₂C under a He atmosphere at 750 °C, instead a reduction in H₂ is required. The β -Mo₂C/C obtained showed activity and stability for the dry reforming of methane at 800 °C and 8 bar. *In situ* XANES/XRD evaluation of the catalyst under DRM reaction conditions combined with high resolution TEM analysis revealed the evolution of β -Mo₂C/C to Mo₂C_xO_y/C. Notably, the gradual oxidation of β -Mo₂C/C to Mo₂C_xO_y/C correlates directly with the increased activity of the competing reverse water gas shift reaction.

5.2. Introduction

Since the 1970s reports on the noble-metal-like catalytic activity of Mo₂C⁸⁴ and WC⁸⁵, transition metal carbides have remained in the focus of the catalysis community.²⁴¹⁻²⁴⁹ For instance, molybdenum carbide has been studied as a catalyst for various heterogeneous reactions including methane reforming,^{97,100} methane dehydroaromatization,²⁵⁰⁻²⁵¹ water gas shift,^{86,122,252} and deoxygenation reactions.²⁵³⁻²⁵⁶ The dry reforming of methane (DRM, Eq. 5.1) is a particularly relevant reaction because it allows producing synthesis gas from the two main greenhouse gases, CH₄ and CO₂, although it requires high temperatures for reaching high conversions (typically, 800 °C and above).⁷¹ However, Mo₂C catalyzes also the reverse water gas shift reaction (RWGS, Eq. 5.2),^{95-96,257} which can occur in parallel with the DRM reaction consuming the hydrogen produced, resulting in a decreased H₂/CO ratio of the produced syngas and the formation of steam.^{71,78,258} Currently, it remains unclear if the active sites for DRM and RWGS in Mo₂C catalyst are identical.



The oxophilicity of Mo₂C and, ultimately, its instability against oxidation to MoO₂^{97,102,259} in CO₂-rich feeds at high operating temperatures make the DRM challenging for Mo₂C-based catalysts.^{97,100,105,259-261} To attenuate this oxidative deactivation, DRM is often conducted at elevated pressure (2-10 bar) and/or with CH₄-rich feeds.^{97,101-102,260} Those reports have indicated that a pristine Mo₂C surface evolves to a molybdenum oxycarbide surface layer or a phase (MoO_xC_y), which plays a key role in both the DRM and RWGS reactions. It is also known that the oxygen coverage of the molybdenum carbide surface influences substantially its activity and selectivity, for instance in CO₂-assisted propane dehydrogenation.¹¹⁵

Supported Mo₂C-based catalysts are usually prepared by a so-called temperature programmed reduction (TPR) method, i.e. a gas-solid reduction of molybdenum oxide (or ammonia molybdate precursor) by a mixture of H₂ and a carbonaceous gas such as CH₄ or C₂H₆.^{95,97,254-255,262} However, this procedure may also deposit passivating carbon on the catalytically active carbide surface.²⁶² Alternatively, a carbothermal hydrogen reduction (CHR) method involving a reaction between solid carbon (or a carbon containing material) and molybdenum oxide under reducing (H₂) or inert atmosphere can be exploited.²⁶³⁻²⁶⁵ The relatively low carburization temperatures (typically, < 800 °C) and the absence of carbonaceous gases favor the production of high surface area nanostructured Mo₂C, which is beneficial for catalytic applications.

Here, we studied the CHR reaction of two dimensional delaminated MoO₃ nanosheets (*d*-MoO₃) supported on carbon spheres, which served as carbon source for carburization and also provided a suitable morphological and phase contrast for transmission electron microscopy. Combination of *in situ* XANES/XRD analysis^{69,122,266} and high resolution TEM revealed that Mo₂C_xO_y is an intermediate phase during the carbothermal CHR reaction of *d*-MoO₃/C to β-Mo₂C/C. Additionally, we demonstrate that under DRM conditions, β-Mo₂C/C evolves into Mo₂C_xO_y/C, which is found in active catalyst. Detection of the H₂O produced during the *in situ* XANES/XRD (DRM conditions) experiments allowed us to link the oxidation of β-Mo₂C/C to the emergence of the competing RWGS reaction. High resolution TEM of the active catalyst demonstrates two different morphologies, i.e. aggregates of nanoplatelets and nanorods, corresponding to β-Mo₂C and Mo₂C_xO_y structures, respectively.

5.3. Experimental section

5.3.1. Materials

The orthorhombic α - MoO_3 nanobelts were synthesized by a reported hydrothermal method using ammonium heptamolybdate tetrahydrate (AHM, Sigma-Aldrich, 99.98 % trace metals basis) and nitric acid (70 %, Sigma-Aldrich, ACS reagent grade).²⁶⁷ In a standard experiment, the pH of AHM (1 g) solution in deionized (DI) water (20 mL) was adjusted to 1 by the dropwise addition of HNO_3 (ca. 5 mL). The reaction mixture was then kept at 180 °C for 24 h in a Teflon-lined autoclave (45 mL). The obtained material was washed with DI water until a pH of ca. 7 was reached and subsequently dried at 100 °C.

d- MoO_3 nanosheets were synthesized according to a reported method.²⁶⁸ The orthorhombic α - MoO_3 (1 g) was ground in an agate mortar with acetonitrile (0.2 mL, Sigma-Aldrich, ACS reagent, ≥ 99.5 % purity) and the resulting material was dispersed by sonication in 50 % aqueous ethanol (15 mL) for 2 h. After sonication, the suspension was centrifuged (8000 rpm, 30 min) and the supernatant containing the dissolved *d*- MoO_3 nanosheets was collected and used for impregnation onto carbon spheres.

Carbon spheres were synthesized *via* a hydrothermal method from xylose (Sigma-Aldrich, ≥ 99 % purity) in water.^{49,269} Xylose (6 g) was dissolved in DI water (15 mL) and the mixture was kept at 180 °C for 20 h in a Teflon-lined autoclave (45 mL).

d- MoO_3/C material was obtained *via* wet impregnation of the supernatant solution of *d*- MoO_3 (ca. 1.5 mg mL⁻¹ by the thermogravimetric analysis) onto carbon spheres. The following treatment was applied: annealing of *d*- MoO_3/C in N_2 (800 °C, 1.5 h, 5 °C min⁻¹) followed by annealing in 10 vol.% H_2 in N_2 (30 min, 800 °C) giving ultimately β - $\text{Mo}_2\text{C}/\text{C}$.

5.3.2. Characterization

Ex situ X-ray powder diffraction (XRD) data were collected on a PANalytical Empyrean X-ray diffractometer equipped with a Bragg–Brentano HD mirror and operated at 45 kV and 40 mA using $\text{CuK}\alpha$ radiation ($\lambda = 1.5418$ nm). The materials were examined within the 2θ range of 5–90° using a step size of 0.0167°. The scan time per step was 3 s. Thermogravimetric analysis (TGA) experiments were performed in a Mettler Toledo TGA/DSC 3 instrument. Typically, 750 μL of a colloidal solution of *d*- MoO_3 was placed in a sapphire crucible (900 μL) that was heated to 80 °C (5 °C min⁻¹) and kept for 1 h. Inductively coupled plasma atomic

emission spectroscopy (ICP-AES) analysis was performed by the Mikroanalytisches Labor Pascher (Remagen, Germany). Scanning electron microscopy (SEM) was performed on a Zeiss LEO Gemini 1530 microscope. All electron microscopy images were taken at an acceleration voltage of 5 kV. Prior to imaging the materials were coated with a ca. 2 nm conductive layer of platinum.

Transmission electron microscopy (TEM) samples were prepared by dry-deposition of the sample powders onto Cu TEM grids covered with a thin holey carbon layer. TEM, high resolution TEM (HR-TEM) and high angle annular dark field scanning TEM (HAADF-STEM) images of the samples were taken by an aberration-corrected JEOL JEM-ARM 300F GrandARM transmission electron microscope operated at 300 kV. The energy-dispersive X-ray spectroscopy (EDX) elemental mapping was performed using dual silicon drift EDX detectors with a total detection area of 200 mm². The electron energy loss (EELS) spectra were recorded in dual EELS mode by a GIF Quantum ER System (Model 965) that is attached to the TEM.

Combined X-ray absorption spectroscopy (XAS) and powder diffraction (XRD) experiments were performed at the Swiss-Norwegian Beamlines (SNBL, BM31) at the European Synchrotron Radiation Facility (ESRF, Grenoble, France). XAS spectra were collected at the Mo K-edge using a double-crystal Si (111) monochromator with continuous scanning in transmission mode. XRD data were collected using a DEXELA-Perkin Elmer 2923 CMOS pixel detector²⁷⁰ and a Si (111) channel-cut monochromator set at a wavelength of $\lambda = 0.5 \text{ \AA}$. The *in situ* dry reforming of methane (DRM) experiment was performed in a quartz capillary reactor.²⁷¹ Calibration of the XAS data was based on Mo foil set at 20000.0 eV. In a typical XAS experiment ca. 2 mg of *d*-MoO₃/C was placed between two quartz wool plugs in a capillary reactor (outer diameter 1.5 mm, wall thickness 0.1 mm). The carburization step was performed in pure He in the temperature range from 50 to 750 °C (5 mL min⁻¹, ca. 4.5 °C min⁻¹); a final annealing was performed in 50 vol.% H₂ in He (750 °C, 10 mL min⁻¹, ca. 20 min). DRM tests were performed at 8 bar (CH₄ : CO₂ He = 4 : 3 : 3) with the total flow rate varying in the range 1.75 - 3.5 mL min⁻¹ (space velocity (SV) of ca. 3500 - 7000 L g_{Mo}⁻¹ h⁻¹; catalyst weight/volume flow rate (W/F) ratio of ca. 0.5 - 1 ms g_{Mo} mL⁻¹) at 730 °C. The composition of the outlet gases was followed online by a mass spectrometer (MS). *Ex situ* XAS data were collected from pellets of reference materials with an optimized amount of sample mixed with cellulose. Activated materials were handled in a N₂-filled glove box to prepare

specimen for XAS analysis in air-tight sealed Al bags. XAS data were processed using the Athena software (Demeter 0.9.25 software package)²⁰⁶. *In situ* time resolved XANES data were analyzed using a Multivariate Curve Resolution - Alternating Least Squares (MCR-ALS) method.⁶⁹ MCR-ALS analysis was performed with a MATLAB software package using the multivariate curve resolution toolbox.²⁷² The experimental spectra were analyzed in the 19950-20100 eV energy range. The number of components characterizing the whole XANES spectra dataset was determined using principal component analysis (PCA). Non-negative constraints for both the phase concentration and spectra profiles as well as cumulative concentration profile closure to 1 were applied in the analysis.²⁷³ The MCR-ALS routine was regarded successful when the convergence criterion fell below 0.1 %.

5.3.3. Catalytic Testing

The laboratory DRM tests were carried out in a metal fixed-bed reactor (Hastelloy X, 8 mm inner diameter) at 8 bar. In a typical experiment, 75 mg of *d*-MoO₃/C was placed in between two quartz wool plugs. Prior to the catalytic tests, *d*-MoO₃/C was transformed *in situ* into Mo₂C/C by thermal treatment in 1) N₂ (800 °C, 1.5 h, 20 mL min⁻¹, 5 °C min⁻¹) followed by 2) 10 vol.% H₂ in N₂ (800 °C, 30 min, 20 mL min⁻¹) at atmospheric pressure. After this pretreatment, the pressure was increased to 8 bar (N₂) and the DRM feed was introduced (CH₄ : CO₂ : N₂ = 4 : 3 : 3, a total flow rate was 10 mL min⁻¹, SV ca. 550 L g_{Mo}⁻¹ h⁻¹, W/F ca. 6.5 ms g_{Mo} mL⁻¹, 800 °C, 8 bar). The composition of the off-gas was analyzed *via* a gas chromatograph (GC, PerkinElmer Clarus 580) equipped with a thermal conductivity detector (TCD).

5.4. Results and discussion

Orthorhombic α -MoO₃ nanobelts were synthesized *via* a reported route.²⁶⁷ The nanobelt morphology of α -MoO₃ was confirmed by scanning electron microscopy (SEM, Figure D.1) and phase purity by X-ray powder diffraction (XRD) analysis (space group *Pbnm*, Figure D.2). Note that increasing the Mo concentration in the hydrothermal synthesis from 0.56 to 2 mol L⁻¹ yields a hexagonal polymorph *h*-MoO₃ (space group *P6₃/m*, Figure D.3). Sonication of grinded α -MoO₃ and its dispersion in 50 % aqueous ethanol yielded, after centrifugation, a transparent colloidal solution of delaminated MoO₃ films (*d*-MoO₃). Transmission electron microscopy (TEM) imaging of a dried aliquot of this solution revealed a

few-layer-thin nanosheets of *d*-MoO₃ (Figure D.4). High resolution TEM (HR-TEM) images show lattice fringes separated by 3.72 Å, which is characteristic for the distance of the (1 1 0) planes in α -MoO₃ (Figure D.4). The wet impregnation of carbon spheres (Figure D.5) with the colloidal solution of *d*-MoO₃ nanosheets (ca. 1.5 mg mL⁻¹ by thermogravimetric analysis, Figure D.6) yielded, after drying at 100 °C, *d*-MoO₃/C (1.49 wt.% Mo by elemental analysis, Figure 5.1a). High angle annular dark field scanning TEM (HAADF-STEM) imaging of *d*-MoO₃/C shows carbon spheres (light contrast) covered by a Mo- rich phase (heavier contrast) that segregates as poorly crystalline halo-like patterns around the carbon spheres (Figure 5.1b-d and Figure D.7). We also observed small poorly ordered crystalline clusters imbedded in the amorphous matrix of carbon spheres, as shown in Figure 5.1d and Figure D.7. Energy-dispersive X-ray spectroscopy (EDX) mapping indicates that the Mo-rich phase contains both Mo and O, consistent with *d*-MoO₃, as well as C from, possibly, bound acetonitrile/ethanol solvent molecules (Figure D.8). In agreement with EDX, electron energy loss spectroscopy (EELS) analysis indicates that the material contains C, O, and Mo (Figure D.9). According to the shape and energy position of the O K-edge peak (ca. 530 eV), Mo atoms have an oxidation state between +4 and +6 (Figure D.10).²⁷⁴⁻²⁷⁵ The partial reduction of Mo +6 states is likely due to the electron beam reduction during the acquisition of EELS data, consistent with the previous data.²⁷⁴

Annealing of *d*-MoO₃/C at 800 °C in N₂ (1.5 h) followed by an additional annealing step in 10 vol.% H₂ (800 °C, 30 min) gave Mo₂C/C. STEM imaging of this material, after exposure of the specimen to air during sample transfer, reveals crystalline nanorods of ca. 100-500 nm in length decorating the surface of carbon spheres (Figure 5.1f). Additionally, poorly crystalline agglomerates (Figure 5.1g,h) and core/shell nanoparticles (Figure 5.1i) were found on the surface of the carbon spheres. HAADF-STEM images uncover that the core/shell structures have a crystalline core and an amorphous shell (Figure 5.1i). EELS analysis performed on all observed morphologies demonstrates a shift of the Mo M_{2,3} edge to a lower energy when compared to *d*-MoO₃/C, which indicates a more reduced Mo. However, the position of the Mo M_{2,3} edge is close to that of Mo⁴⁺ (Figure D.11). However, the oxidization state of Mo is between +2 to +4 (Figure D.11). Furthermore, EDX mapping confirms the oxidized state of Mo, revealing that all structures contain Mo, C and O (Figure 5.1e). These results indicate that an oxidation of molybdenum carbide took place when exposing the activated **reduced material** to

ambient air during sample transfer, consistent with the high reactivity of the activated, highly oxophilic Mo_2C surface.²⁷⁶

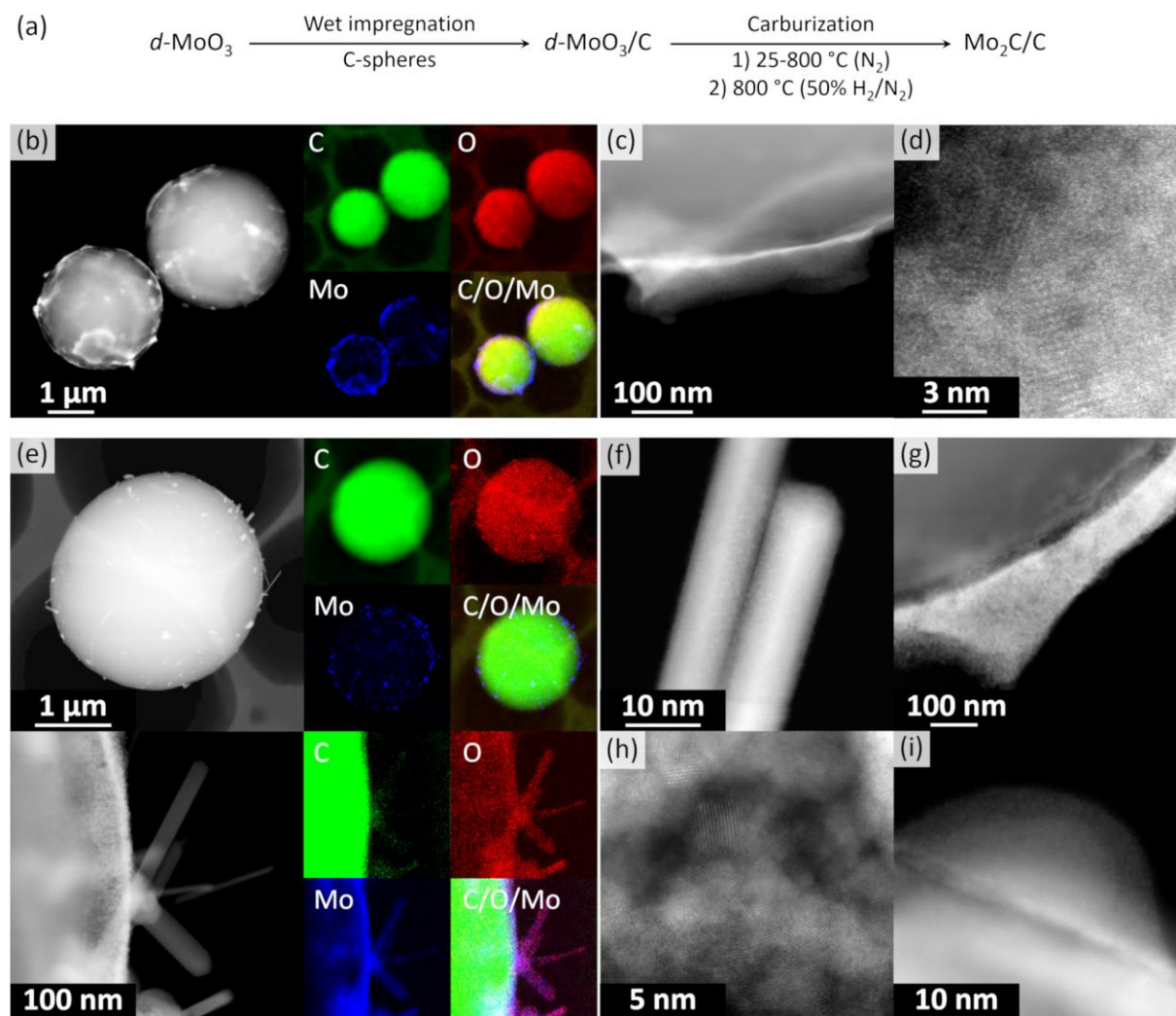


Figure 5.1. a) Synthesis of $\beta\text{-Mo}_2\text{C}/\text{C}$ from delaminated MoO_3 films; b) HAADF-STEM images and EDX maps of $d\text{-MoO}_3/\text{C}$; c)-d) HR-STEM images of $d\text{-MoO}_3/\text{C}$; e) HAADF-STEM images and EDX maps of $\text{Mo}_2\text{C}/\text{C}$; and f)-i) HR-STEM images of different morphologies decorating the surface of carbon spheres in $\beta\text{-Mo}_2\text{C}/\text{C}$.

To obtain information about the state of the annealed material at the specific temperatures and gas atmospheres, we turned to *in situ* experimentation and followed the CHR process ($d\text{-MoO}_3/\text{C} \rightarrow \beta\text{-Mo}_2\text{C}/\text{C}$) by a combined *in situ* XANES/XRD experiment.^{69,122,266} The XANES spectra were collected at the Mo K-edge during annealing of $d\text{-MoO}_3/\text{C}$ from 50 to 750 °C (highest attainable temperature of the set up) under He and 50% H_2/He at 750 °C (total flow rates of 5 and 10 mL min^{-1} , respectively), while XRD patterns were collected at 50, 400 and 750 °C during the same experiment. For the latter temperature, data were collected under a flow of pure helium or 50 % H_2/He . The XRD pattern collected at 50 °C contains no

Bragg peaks and shows a dominant amorphous halo due to the C phase, confirming the low crystallinity of the $d\text{-MoO}_3/\text{C}$ material as observed by TEM (Figure 5.2a and Figure 5.1d). At 400 °C, Bragg peaks corresponding to the MoO_2 phase (distorted rutile type structure, space group $P2_1/c$) appear, indicating a reduction of $d\text{-MoO}_3$ to MoO_2 by the carbon spheres (reducing agent), accompanied by the crystallization of MoO_2 (Figure 5.2a). Interestingly, while at 750 °C under a He atmosphere only reflections of MoO_2 are present, flowing H_2 through the specimen immediately reduced it to $\beta\text{-Mo}_2\text{C}$ (Figure 5.2a). Our *in situ* XRD results agree well with previous studies that have identified MoO_2 as an intermediate phase during the carburization of MoO_3 to Mo_2C , both *via* TPR^{257,277} and CHR^{265,278-279} routes. In addition, it was also reported that annealing of carbon-supported AHM in pure He at 800 °C for 2 h does not lead to its complete carburization, giving a mixture of MoO_2 and $\beta\text{-Mo}_2\text{C}$.²⁷⁹

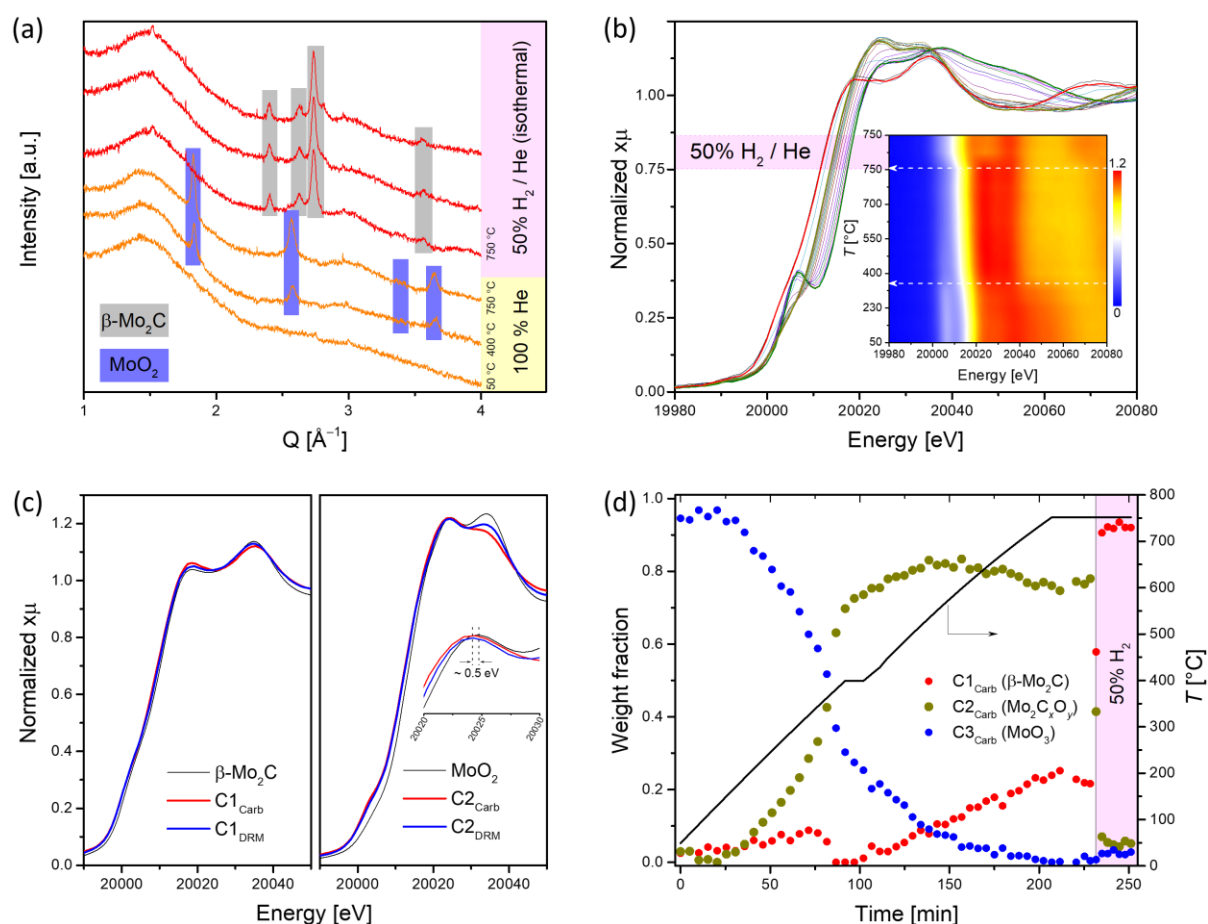


Figure 5.2. *In situ* carburization of $d\text{-MoO}_3/\text{C}$ under He and H_2 as followed by a) XRD ($Q = 4\pi\sin(\theta)/\lambda$) and b) Mo K-edge XANES; the inset shows the evolution of the pre-edge and edge features with increasing temperature. c) Comparison of the extracted C1 and C2 components spectra from the MCR-ALS analysis performed during the carburization of $d\text{-MoO}_3/\text{C}$ (labelled Carb) to $\beta\text{-Mo}_2\text{C}/\text{C}$ and during the dry reforming of methane (labelled DRM, *vide infra*) along with the references $\beta\text{-Mo}_2\text{C}$ and MoO_2 . d) Phase evolution during the carburization process according to MCR-ALS of the XANES data.

The *in situ* XANES data collected during annealing of *d*-MoO₃/C indicates clearly a gradual reduction of Mo⁺⁶ to Mo⁺⁴ when heating under He to 750 °C and the formation of β-Mo₂C, upon switching to 50 vol.% H₂/He, as confirmed by a shift of the Mo K edge energies from 20016.3 (at room temperature) to, respectively 20011.6 and 20000.6 eV (without and with co-feed H₂ at 750 °C; Figure 5.2b).¹²² Two notable changes are observed in the *in situ* XANES spectra. The first change occurs at ca. 360 °C and is associated with the disappearance of the characteristic pre-edge feature, typical for molybdenum in a non-centrosymmetric environment (Figure 5.2b, inset),²⁸⁰⁻²⁸¹ that can be explained by the reduction/transformation of *d*-MoO₃ to MoO₂. From 360 °C up to 750 °C (heating up in He) a slight shift of the Mo K-edge position towards lower energies is observed, consistent with a partial reduction. The second change occurs immediately after introducing H₂ at 750 °C and is associated with a prominent shift of the Mo K-edge position from 20011.6 to 20000.6 eV, highlighting a further reduction of the Mo phase. In agreement with the *in situ* XRD data, the XANES spectrum of the final phase corresponds to the reference spectrum of β-Mo₂C.

Further analysis of the *in situ* XANES data *via* principal component analysis (PCA) indicates the presence of three components during the annealing of *d*-MoO₃/C (Figure D.12). Using the information of the presence of three phases, MCR-ALS analysis was performed to extract the three components spectra that reproduce the full data set (Figure D.13). Comparison of the obtained spectra with the available references revealed that the spectrum of the component C1_{Carb} is identical to that of β-Mo₂C (Figure 5.2c). The spectrum of component C2_{Carb} resembles that of MoO₂ except that the edge and the white line feature are shifted to a lower energy (and the shape of the white line is slightly different), indicating overall a reduced Mo oxidation state compared to Mo⁺⁴, i.e. an oxidation state between MoO₂ and Mo₂C (Figure 5.2c). This finding suggests assigning the C2_{Carb} component to molybdenum oxycarbide (Mo₂C_xO_y). Combining this new insight with XRD analysis, we speculate that the Mo₂C_xO_y phase may be formed due to the incorporation of C into the MoO₂ lattice or surface layers during annealing, thus retaining the bulk structure of MoO₂ (distorted rutile type structure, space group P2₁/c). The formation of such a MoO₂/Mo₂C_xO_y phase is in a good agreement with a previous report indicating that MoO₂ can coexist with oxycarbide phases.²⁸² For brevity, we will refer to the MoO₂/Mo₂C_xO_y phase below as Mo₂C_xO_y. Notably, the shape of the obtained XANES spectra of the C2_{Carb} component resembles a recently reported

molybdenum oxycarbide $\text{Mo}_2\text{C}_x\text{O}_y$, although here, the Mo K-edge is shifted to lower energies indicating a more reduced Mo state, probably due to the higher C content in the oxycarbide.²⁸³ Lastly, the edge position and the oscillation profile of component C3_{Carb} is similar to that of MoO_3 , which allows ascribing C3_{Carb} to MoO_3 . The changes of weight fractions of the C1_{Carb} - C3_{Carb} components with annealing is presented in Figure 5.2d. $\text{Mo}_2\text{C}_x\text{O}_y$ that is formed *via* the reduction of MoO_3 by the carbon of the spheres, starts to appear at ca. 200 °C and reaches an asymptotic level of ca. 75-80 % at 400 °C (Figure 5.2d). Surprisingly, MCR indicates that the molybdenum carbide phase appears already at ca. 400 °C. This has not been observed in previous carburization studies of supported Mo oxides and is explained by the use of a carbon support as the carburizing agent in place of the traditionally used CH_4/H_2 carburizing gas mixture and thin sheets of *d*- MoO_3 . The fraction of MoO_3 reduces continuously from ca. 170 °C until it disappears at 750 °C. At this stage $\text{Mo}_2\text{C}_x\text{O}_y$ and Mo_2C coexist in a fraction of 75% and 25%, respectively (Figure 5.2d). However, as discussed above, a complete carburization by the internal carbon source could not be accomplished at 750 °C in He. To attain the complete conversion of the remaining $\text{Mo}_2\text{C}_x\text{O}_y$ to β - Mo_2C , a gas containing 50 vol.% H_2 in He was passed through the reactor at 750 °C. Under such conditions the remaining $\text{Mo}_2\text{C}_x\text{O}_y$ was immediately carburized to β - Mo_2C according to MCR analysis (Figure 5.2d).

To summarize, although MCR-ALS analysis reveals a coexistence of $\text{Mo}_2\text{C}_x\text{O}_y$ and β - Mo_2C at 750 °C in He, *in situ* XRD data showed only peaks corresponding to distorted rutile type MoO_2 . This observation can be explained by i) the amorphous nature of the molybdenum oxycarbide phase and/ or ii) the incorporation of variable amounts of carbon into the MoO_2 phase, forming effectively the $\text{Mo}_2\text{C}_x\text{O}_y$ phase with a reduced Mo oxidation state (and the corresponding Mo K-edge position), yet maintaining the same crystal structure as MoO_2 .

Next, we optimized the DRM conditions to obtain a stable catalytic performance of β - $\text{Mo}_2\text{C}/\text{C}$. The condition identified is a pressure of 8 bar at 800 °C and a CH_4 -rich feed, i.e. $\text{CH}_4 : \text{CO}_2 : \text{N}_2 = 4 : 3 : 3$ (Figure 5.3a). In particular, under this condition no considerable deactivation was observed over 8 h. The space time yield (STY) of CO was $0.22 \text{ mol}(\text{CO}) \text{ mol}(\text{Mo})^{-1} \text{ s}^{-1}$ while the methane conversion rate was $0.11 \text{ mol}(\text{CH}_4) \text{ mol}(\text{Mo})^{-1} \text{ s}^{-1}$ ($X(\text{CH}_4)$ was ca. 45 %, Figure 5.3b). However, the obtained

H₂ / CO ratio was ca. 0.7, which indicates that the RWGS and DRM reactions compete under these conditions.

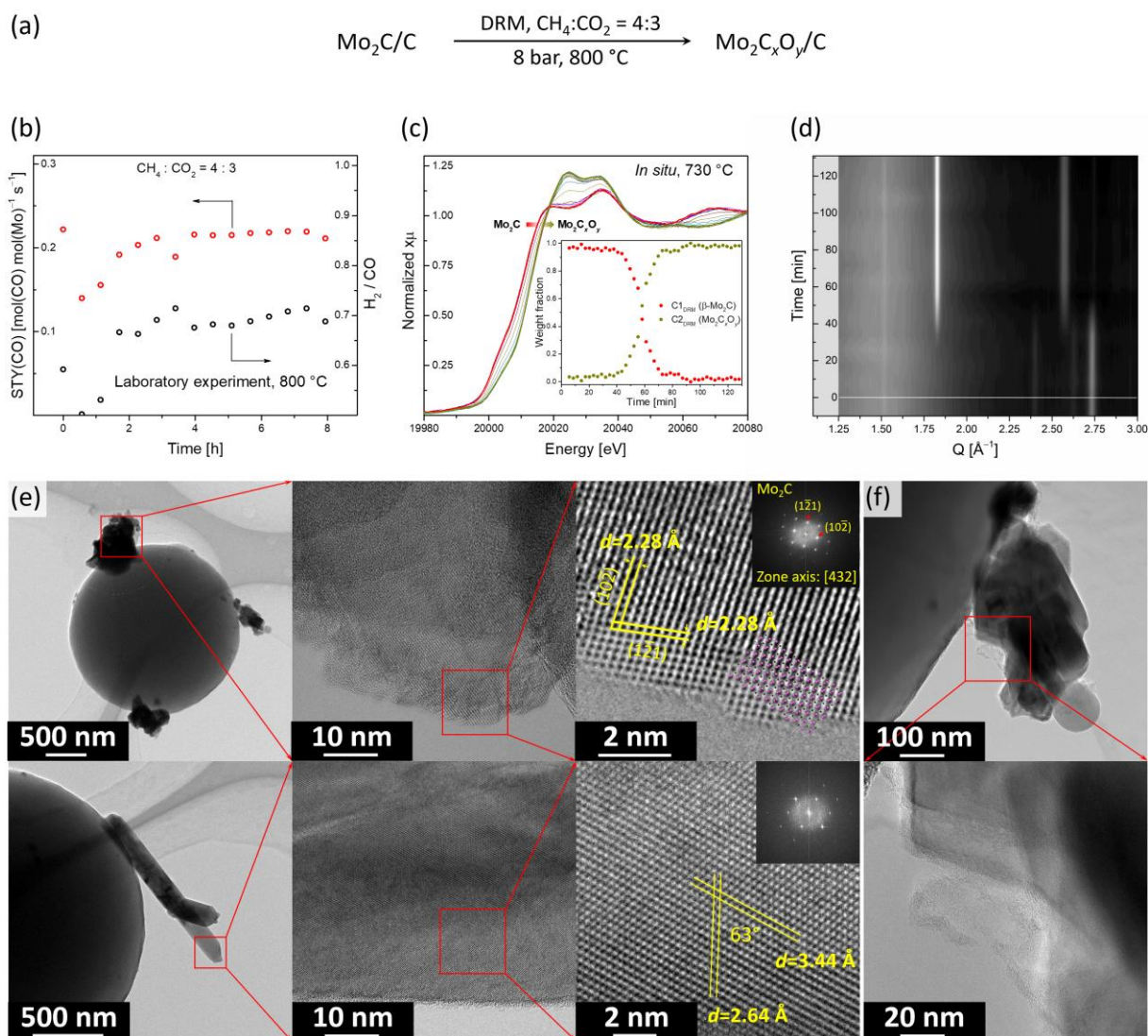


Figure 5.3. a) Schematic of the experimental conditions during the DRM experiment; b) catalytic performance of β -Mo₂C/C in DRM (laboratory scale reactor, 800 °C, 8 bar, SV= 550 L g_{Mo}⁻¹ h⁻¹); DRM experiment followed by c) Mo K-edge XANES, where the inset shows the phase evolution according to MCR-ALS, and d) XRD ($Q = 4\pi\sin(\theta)/\lambda$) (capillary reactor, 730 °C, 8 bar, SV= 3500 L g_{Mo}⁻¹ h⁻¹); e) TEM and HR-TEM images of the spent Mo₂C_xO_y/C catalyst revealing two different morphologies, i.e. aggregates of nanoplates (top) and nanorods (bottom); f) TEM images of amorphous carbon deposited on the active Mo₂C_xO_y/C catalyst.

To identify the active state and to follow the structural evolution of the β -Mo₂C/C catalyst under DRM conditions, an *in situ* XANES/XRD experiment was carried out in a capillary reactor. After the carburization pre-treatment, the feed was switched to DRM conditions (CH₄ : CO₂ = 4 : 3 at 8 bar and 730 °C) while analyzing the composition of the outlet gas by MS. Note that due to the heater limitation, the actual temperature in our catalytic *in situ*

XANES/XRD experiment was 730 °C, instead of 800°C as in the laboratory experiment, yet qualitatively similar results can be expected at those temperatures (Figure 5.3c,d). Laboratory and capillary synchrotron DRM experiments differ also in catalyst weight/volume flow rate (W/F) ratio, which were $W/F = 6.5$ and $1 \text{ ms g}_{\text{Mo}} \text{ mL}^{-1}$, respectively. PCA analysis indicates that two components are necessary to account for changes of XANES spectra with time on stream (TOS, Figure D.12). MCR-ALS analysis of the *in situ* XANES data yielded the XANES spectra for these two components, i.e. $C1_{\text{DRM}}$ and $C2_{\text{DRM}}$ (Figure D.13). Comparison of the calculated spectra with references and the components obtained in the carburization MCR-ALS analysis, identified them as $\beta\text{-Mo}_2\text{C}$ and $\text{Mo}_2\text{C}_x\text{O}_y$, respectively (Figure 5.2c and Figure D.13). Notably, the spectrum of the component $C1_{\text{DRM}}$, identified as $\beta\text{-Mo}_2\text{C}$, is identical to the spectrum of the component $C1_{\text{Carb}}$ obtained for the carburization process (Figure 5.2c). Interestingly, while the shape and edge position of the spectrum of $C2_{\text{DRM}}$ ($\text{Mo}_2\text{C}_x\text{O}_y$) is very similar to $C2_{\text{Carb}}$, it bears a notable difference in the intensities of the white line features (Figure 5.2c). This can probably be explained by the different C content and/ or C distribution within the oxycarbide, formed by incorporation of oxygen atoms into $\beta\text{-Mo}_2\text{C}$ (DRM conditions) or by incorporation of carbon atoms into MoO_2 (CHR conditions). No changes in XANES spectra and XRD data of $\beta\text{-Mo}_2\text{C}$ occur during the first 30-40 min TOS (Figure 5.3c,d). Note that the products CO and H_2 of the DRM reaction are detected by MS during the entire experiment (Figure D.14). After this initial period, a shift of the Mo K-edge position to higher energies sets in, indicating the gradual oxidation of $\beta\text{-Mo}_2\text{C}$. After ca. 1 h of TOS, $\beta\text{-Mo}_2\text{C}$ was transformed to $\text{Mo}_2\text{C}_x\text{O}_y$ according to the concentration profiles obtained by MCR analysis (Figure 5.3c). Consistent with XANES data, the XRD peaks corresponding to MoO_2 (or $\text{Mo}_2\text{C}_x\text{O}_y$) appear after ca. 40 min of TOS with a simultaneous reduction of the intensities of the peaks due to $\beta\text{-Mo}_2\text{C}$ (Figure 5.3d). After 50 min TOS, the MoO_2 peaks reach their maximal intensities and only a low intensity (1 2 1) peak of $\beta\text{-Mo}_2\text{C}$ ($Q = 2.74 \text{ \AA}^{-1}$) could be detected at this time. Interestingly, the MS data reveal an increase of the H_2O signal starting from TOS = 45 min, arising from the competing RWGS reaction. The increase in the MS H_2O signal coincides with the beginning of the oxidation of $\beta\text{-Mo}_2\text{C}$ observed by XANES and XRD (Figure D.14). This result suggests that the RWGS reaction is favored on a more oxygen-rich $\text{Mo}_2\text{C}_x\text{O}_y$ phase.

Flowing pure CH₄ for 1 h through the reacted catalyst after 130 min TOS does not lead to a re-carburization, leaving the catalyst composition unchanged according to the XANES data (Figure D.15).

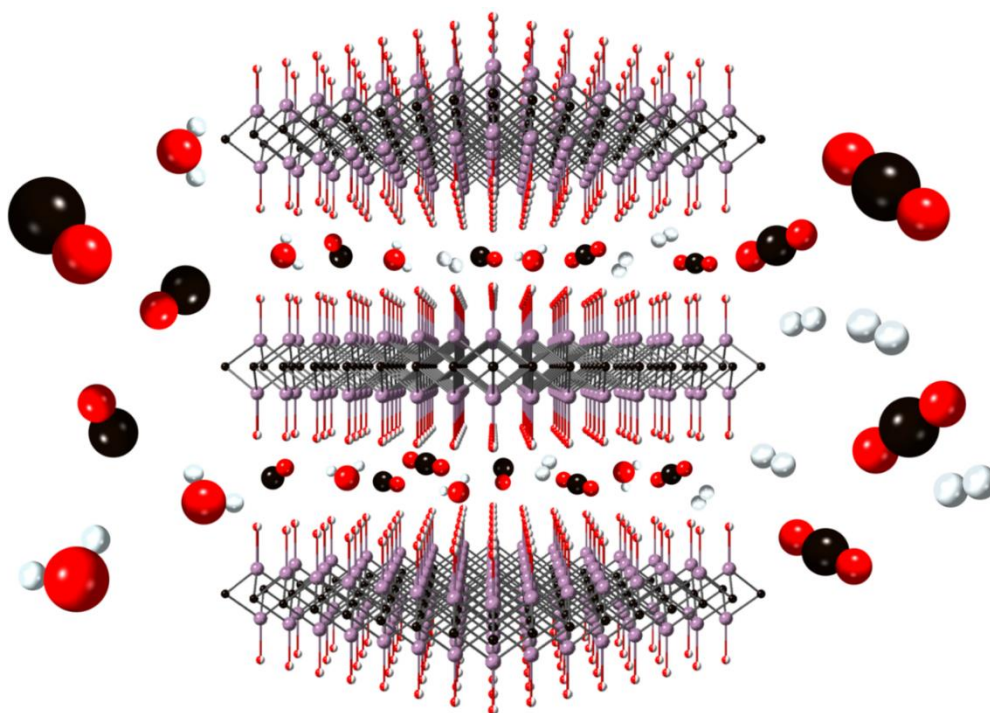
We have also investigated by TEM the active state of the Mo₂C/C catalyst, i.e. the material recovered after cooling down the working catalyst to room temperature in N₂ after 480 min TOS (Mo₂C/C_{TOS480}) at the stable performance stage (Figure 5.3d). The specimen was transferred in ambient air before the TEM analysis. Mo₂C/C_{TOS480} features aggregates of nanoplates and nanorods as the two main morphologies (Figure 5.3d and Figure D.16). We observe that the crystallinity of the material surface layer (for both morphologies) is lower compared to the crystallinity of the bulk structure (Figure D.17). Based on the EELS data, the Mo M_{2,3} edges position shows that the molybdenum oxidation state is below +4. Interestingly, the maximum of the Mo M₃ edge of Mo₂C/C_{TOS480} is found at a lower energy compared to that of Mo₂C/C (395.5 eV and 397.5 eV, respectively, Figure D.11), although both materials were exposed to ambient air during the transfer. This difference might be owing to the oxidation of β-Mo₂C during the DRM reaction, which enriches the catalyst surface layers with O, thereby preventing a further oxidation in air at room temperature. For both morphologies, the EDX mapping shows the presence of Mo, C and O elements, however, a higher oxygen to molybdenum ratio is observed in the nanorods compared to the nanoparticles (Figure D.18). Additionally, a higher oxygen content is observed in the surface layer compared to the bulk structure for both morphologies (Figure D.19), in line with the presence of an oxycarbide layer. The structural analysis of a plate-like nanoparticle by HR-TEM reveals that its crystal structure matches that of the orthorhombic Mo₂C (Figure 5.3e, top). In particular, the observed structure fits perfectly the [4 3 2] zone axis of β-Mo₂C (Pbcn). In contrast, the nanorod structure does not correspond to β-Mo₂C and it fits neither to MoO₃ or MoO₂ with a distorted rutile structure (Figure D.20). This observation combined with a high O content, in addition to the simultaneous presence of Mo and C elements in the EDX maps, allows us to attribute the nanorods to a crystalline oxycarbide phase Mo₂C_xO_y. Additionally, amorphous carbon was found attached to the surface of Mo₂C/C_{TOS480} (Figure 5.3e). The origin of the carbon observed can be either the partial degradation of the carbon spheres support or catalyst coking under reaction conditions. However the latter is unlikely due to the low coking rate of carbide based catalysts.⁹⁷ Noteworthy, the TEM analysis of Mo₂C/C_{TOS480} reveals no

presence of MoO₂ proving the high stability of Mo₂C_xO_y towards oxidation under operating conditions.

5.5. Conclusions

We have shown that delaminated MoO₃ nanosheets dispersed on carbon spheres, are carburized only partially by annealing in an inert gas and require H₂ to form β-Mo₂C/C quantitatively. The carburized material shows a stable performance in the DRM reaction at an elevated pressure of 8 bar. The combination of advanced *in situ* XANES/XRD analysis and TEM characterization allowed us to attribute a combination of β-Mo₂C and Mo₂C_xO_y to the active state of the catalyst. In addition, the higher oxidation states of β-Mo₂C/Mo₂C_xO_y catalyst correlate with higher rates of the competing, undesired RWGS reaction.

Chapter 6: *In Situ* XANES/XRD study of the structural stability of two-dimensional molybdenum carbide Mo_2CT_x : implications for the catalytic activity in the water-gas shift reaction



The results of this chapter are published as:

E.B. Deeva*, A. Kurlov*, P.M. Abdala, D. Lebedev, S.M. Kim, C.P. Gordon, A. Tsoukalou, A. Fedorov, C.R. Müller, *In Situ* XANES/XRD Study of the Structural Stability of Two-Dimensional Molybdenum Carbide Mo_2CT_x : Implications for the Catalytic Activity in the Water–Gas Shift Reaction, *Chem. Mater.*, **2019**, 31, 4505-4513

* E.B.D. and A.K. contributed equally

6.1. Abstract

MXenes, a recently discovered family of two-dimensional (2D) materials, are promising catalysts and supports for applications in heterogeneous catalysis, however, the thermal stability of MXenes and their surface chemistry are not fully explored. Here we report that 2D molybdenum carbide Mo_2CT_x remains stable and shows no appreciable phase transformation up to ca. 550-600 °C in reducing environment, as assessed by a combined *in situ* X-ray absorption near edge spectroscopy (XANES) and powder X-ray diffraction (XRD) study during a temperature programmed reduction (TPR) experiment. At higher temperatures, the passivating oxo, hydroxy and fluoro groups de-functionalize the molybdenum-terminated surface, inducing a transformation to bulk β - Mo_2C that is complete at ca. 730 °C. We demonstrate that Mo_2CT_x is a highly stable and active catalyst for the water gas shift (WGS) reaction with a selectivity > 99 % toward CO_2 and H_2 at 500°C. The conversion of carbon monoxide on Mo_2CT_x starts to decline at temperatures that are associated with the decrease of the interlayer distance between the carbide sheets, as determined by the XRD-probed TPR, indicative of increasing mass transfer limitations at these conditions. Our results provide an insight on the thermal stability and reducibility of Mo_2CT_x and serve as a guideline for its future catalytic applications.

6.2. Introduction

MXenes is a new family of well-defined two-dimensional (2D) carbides, nitrides and carbonitrides¹¹⁶⁻¹¹⁷ of a general formula $M_{n+1}X_nT_x$ (M is an early transition metal, $n = 1, 2, 3$, X is C and/or N and T_x are surface oxo, hydroxy and/or fluoro groups)^{116,118} with applications ranging from Li-ion batteries¹²⁶⁻¹²⁷ and supercapacitors,^{124,129-130} to electro-¹³⁵⁻¹³⁷ and heterogeneous catalysis.^{138-139,284} Synthetically, MXenes are prepared by the selective etching of an A (group IIIA or IVA) element from a respective ternary layered MAX phase (M and X as defined above);¹²⁰ this treatment typically uses aqueous HF and thereby installs the mentioned T_x groups on the surface of MXenes.¹¹⁶ Applications of MXenes as supports in traditional heterogeneous catalysis are currently gaining momentum because late transition metals, such as Pt, provide reactive metal-support interactions (RMSIs) with these materials.¹³⁸⁻¹³⁹ In addition, MXenes can efficiently stabilize single atom catalysts.^{137,140} However, a wider exploitation of catalysts based on MXenes is limited by the degradation of

these 2D carbides to oxides already under mild oxidizing conditions, especially in the presence of water.¹⁴²⁻¹⁴⁵ In addition, the stability of MXenes against sintering in reducing conditions as well as possible surface chemical reactions at high temperatures²⁸⁵ and the impact of the T_x groups on the catalytic processes are currently not well understood. That said, dependence of the supercapacitive performance of Ti_2CT_x on the post treatment was linked to the surface fluorine content²⁸⁶ and it has also been reported that the surface terminations of the Ti_2CT_x material affect its Li-ion storage capacity.¹²⁶ The density of states of the Fermi level (and therefore adsorption energies of catalytic intermediates) of MXenes depends on the surface terminations according to DFT calculations.²⁸⁷ Overall, these results suggest that controlling the surface functional groups is an important factor to consider when designing catalysts derived from MXenes.

Materials based on Mo and W carbides catalyze a number of industrially important reactions, including methane reforming,^{97,100} Fischer-Tropsch,⁹²⁻⁹³ and water-gas shift (WGS) reactions.^{86,88-89} Interestingly, the catalytic activity displayed by mentioned carbides is characteristic for noble metals,⁸⁵ providing an additional motivation to harness the potential of Mo_2CT_x for heterogeneous catalysis. In this work, we report the thermal stability of the multi-layer Mo_2CT_x material under reducing conditions by utilizing combined *in situ* X-ray diffraction – X-ray absorption experiments.^{82,288-289} We observe that no phase transition of two-dimensional Mo_2CT_x sheets into a bulk carbide phase occurs up to ca. 550-600 °C, although under these conditions the interlayer spacing of Mo_2CT_x decreases due to a de-functionalization of the surface and removal of the intercalated water. These results allow rationalizing the performances of as prepared and partially reduced Mo_2CT_x catalysts in the model WGS reaction and highlight the importance of gas diffusion effects when using heterogeneous catalysts based on unsupported MXene materials.

6.3. Experimental section

6.3.1. Materials

Bulk Mo_2Ga_2C was synthesized following a reported method.²⁹⁰ β - Mo_2C powder (2 g, Sigma-Aldrich, 99.5 wt.% purity, $1.6\text{ m}^2\text{ g}^{-1}$ by N_2 adsorption) was homogeneously mixed with metallic Ga (5.5 g, Sigma-Aldrich, 99.9995 % trace metals basis, 1:8 molar ratio of Mo:Ga) using a mortar heated to 45 °C. The resulting gray paste was transferred to a quartz tube,

which was then evacuated on an ultrahigh vacuum line (UHV, ca. 10^{-5} mbar), flame-sealed under dynamic vacuum and annealed for 48 h at 850 °C (10 °C min^{-1}). To remove excess metallic Ga, the as-prepared material was stirred in aqueous HCl (20 mL, 12 M, Fisher Scientific, puriss. p.a. ACS reagent grade) for 48 h at room temperature, and then washed with DI water until a pH of ca. 6 was reached. Drying in air at 80 °C for 12 h gave $\text{Mo}_2\text{Ga}_2\text{C}$.

Mo_2CT_x was synthesized by etching out Ga from prepared $\text{Mo}_2\text{Ga}_2\text{C}$ using a modified literature procedure.²⁹¹ $\text{Mo}_2\text{Ga}_2\text{C}$ (ca. 100 mg) and 15 mL of HF (≥ 48 %, Sigma-Aldrich, puriss. p.a. ACS reagent grade) were stirred (300 rpm, magnetic stirring) at 140 °C for 4 days in a sealed Teflon lined stainless steel Parr autoclave using a sand bath on a hot plate. Note that experiments with 48 % HF at high temperatures used in this work require extra care and were conducted in an HF-dedicated fume hood at the specialized Toxlab of ETH Zürich. The resulting suspension was centrifuged at 5000 rpm for 2 min, the solid was re-suspended in DI water and washed until a pH of ca. 6 was reached (5-6 \times 30 ml washings). The obtained Mo_2CT_x powder was dried in air at 80 °C for 12 h. Partially reduced *ex situ* samples Mo_2CT_x -500 and Mo_2CT_x -800 were prepared by reducing Mo_2CT_x in a vertical quartz reactor in 20 vol.% H_2 in N_2 at, respectively, 500 °C and 800 °C, for 1 h. To avoid surface oxidation of the activated materials, Mo_2CT_x -500 and Mo_2CT_x -800 were transferred into a nitrogen-filled glovebox (H_2O and O_2 levels < 1.5 ppm) without exposing the samples to air.

^{13}C -labelled bulk Mo_2^{13}C was prepared from ammonium heptamolybdate tetrahydrate (AHM, Sigma-Aldrich, 99.98 % trace metals basis) and ^{13}C -labeled D-glucose (Apollo Scientific, ≥ 99 atom.% ^{13}C , ≥ 99 % purity) following a slightly modified literature method.²⁷⁸ AHM and D-glucose (molar ratio Mo : C = 1 : 2, 8 mmol scale) were dissolved in DI water with stirring (ca. 15 min) and then this solution was dried at 100 °C for 24 h. The residue was transferred to a vertical quartz reactor, heated to 800 °C (10 °C min^{-1}) under a constant helium flow (15 mL min^{-1}) and annealed for 30 min. Synthesis of $\text{Mo}_2\text{Ga}_2^{13}\text{C}$ and $\text{Mo}_2^{13}\text{CT}_x$ was performed as described above for the respective unlabeled materials.

6.3.2. Characterization

Ex situ X-ray powder diffraction (XRD) data were collected on a PANalytical Empyrean X-ray diffractometer equipped with a Bragg–Brentano HD mirror and operated at 45 kV and 40 mA using $\text{CuK}\alpha$ radiation ($\lambda = 1.5418$ nm). The materials were examined within the 2θ range of 5–90° using a step size of 0.0167°. The scan time per step was 3 s. Scanning electron

microscopy was performed on a Zeiss LEO Gemini 1530 microscope equipped with an EDX detector. All electron micrographs and elemental maps were taken at an acceleration voltage of 5 kV and 20 kV, respectively, and without coating with a conductive layer. X-ray photoelectron spectroscopy (XPS) measurements were conducted on a Sigma 2 instrument (Thermo Fisher Scientific) equipped with an UHV chamber (non-monochromatic 200 W Al K α source, a hemispherical analyzer, and a seven channel electron multiplier). The analyzer-to-source angle was 50°, while the emission angle was 0°. A pass energy of 50 eV and 25 eV was set for the survey and the narrow scans, respectively, and C 1 s peak of adventitious carbon was set at 284.8 eV to compensate for any charge induced shifts. For the reduced or spent materials, an air-tight cell allowing to transfer specimens between the glovebox and the XPS instrument was used.²⁹² XPS data were analyzed in CasaXPS Version 2.3.19PR1.0 software. The background subtraction was performed according to Shirley,²⁹³ and the atomic sensitivity factors (ASF) of Scofield were applied to estimate the atomic composition.²⁹⁴ The thermogravimetric analysis (TGA) was performed in the Mettler Toledo TGA/DSC 3 instrument using temperature programmed reduction (TPR) in a flow of H₂. In a typical TGA experiment, ca. 20 mg of a sample was placed in an alumina crucible (70 μ L). The H₂ and N₂ gas flows were set to 15 and 110 mL min⁻¹ respectively, and a constant N₂ purge (25 mL min⁻¹) was applied over the microbalance (overall, 10 vol.% H₂ in N₂). The sample was heated to 800 °C (10 °C min⁻¹) and kept at 800 °C for 1 h. The weight loss and heat flow curves were recorded. Solid-state NMR spectra were recorded under magic angle spinning on a Bruker Avance III 400 MHz spectrometer using a 4 mm double resonance probe. The magnetic field was externally referenced by setting the downfield ¹³C signal of adamantane to 38.4 ppm.

Combined X-ray absorption spectroscopy (XAS) and powder diffraction (XRD) experiments were performed at the Swiss-Norwegian Beamlines (SNBL, BM31) at the European Synchrotron Radiation Facility (ESRF, Grenoble, France). XAS spectra were collected at the Mo K-edge using a double-crystal Si (111) monochromator with continuous scanning in transmission mode. XRD data were collected using a DEXELA-Perkin Elmer 2923 CMOS pixel detector²⁷⁰ and a Si (111) channel-cut monochromator set at a wavelength of 0.5 Å. The *in situ* (temperature programmed) reduction experiment was performed in a quartz capillary reactor (Figure E.1).²⁷¹ The calibration of the XAS data was based on the Mo foil set at 20000 eV. Approximately 2 mg of Mo₂C_{T_x} was mixed with amorphous SiO₂ in order to

optimize the X-ray absorption of the sample, and placed between two quartz wool plugs in a capillary (outer diameter 1.5 mm, wall thickness 0.1 mm, ca. 200 LgMo₂CT_x⁻¹ h⁻¹ GHSV). Temperature programmed reduction was performed in 20 vol.% H₂ in N₂ with a total flow rate of 10 mL min⁻¹ in the temperature range from 50 to 730 °C (ca. 9 °C min⁻¹). Acquisition of 10 XANES spectra were followed by acquiring an XRD pattern; a total of 40 XANES spectra and 4 XRD patterns were collected (Figure E.2). *Ex situ* XAS data were collected from pellets of reference materials with an optimized amount of sample mixed with cellulose. XAS data processing was performed using the Athena software and EXAFS fittings were performed with the Artemis software (Demeter 0.9.25 software package)²⁰⁶ with data collected at room temperature. For the EXAFS data analysis, the spectra were converted to the photoelectron wave vector k (Å⁻¹). The resulting $\chi(k)$ functions were k^2 weighted and Fourier transformed over 3–16.5 Å⁻¹. The S_0^2 value was determined by fitting metal Mo foil spectra and it was fixed for all further specimen. Full-pattern refinement (Rietveld²⁹⁵ and Le Bail²⁹⁶) were performed using Fullprof software.²⁹⁷

6.3.3. Catalytic Testing

The water-gas shift reaction was carried out in a fixed-bed quartz reactor (12.6 mm of internal diameter and 400 mm of length) at atmospheric pressure. Mo₂CT_x (30 mg) was supported on a plug of quartz wool, approximately 5 mm high, that was placed in the middle of the reactor. The reduced catalyst Mo₂CT_x-500 was prepared *in situ* prior to the WGS test using 10 vol.% H₂ in N₂ (500 °C, 10 °C min⁻¹, 100 mL min⁻¹, 1 h). The reactor was then purged with N₂ (100 mL min⁻¹, 30 min) and cooled down to 200 °C. Subsequently, the WGS was performed using a total flow rate of the feed gas of 55 mL min⁻¹ (GHSV = 110 L g_{cat}⁻¹ h⁻¹, CO : H₂O : N₂ = 1 : 1 : 9) in the temperature range 200–950 °C (5 °C min⁻¹). The stability test was conducted at 500 °C for 10 h at ca. 20 % conversion of CO. The gas flow rate was controlled by mass-flow controllers (Bronkhorst, EL-FLOW). The steam was generated by evaporating water in a controlled evaporation mixer (Bronkhorst), whereby the flow rate of water was controlled by a liquid flow meter (Bronkhorst, μ -FLOW series). The composition of the off-gas after condensation of the unreacted steam was analyzed using a micro-GC (C2V-200, Thermo Scientific) equipped with a thermal conductivity detector (TCD) and molecular sieve 5A and U-plot column cartridges. After catalytic tests, materials were cooled down to

room temperature in nitrogen and were exposed to air prior to XRD, SEM, XPS and ^{13}C NMR analysis.

6.4. Results and discussion

First, we have prepared $\text{Mo}_2\text{Ga}_2\text{C}$ (Figure 6.1a) and, using Rietveld refinement, have determined that this material is almost phase pure and contains only minor amounts of Mo_2C and Ga_2O_3 (< 1 wt.%, Figure 6.1b, Table E.1), significantly lower than reported previously (ca. 18 wt.% of a remaining $\beta\text{-Mo}_2\text{C}$ phase was observed in $\text{Mo}_2\text{Ga}_2\text{C}$).²⁹⁰ This improvement may be due to the UHV conditions used in our work that allows for a more complete removal of oxygen. The crystal structure of $\text{Mo}_2\text{Ga}_2\text{C}$ is hexagonal (space group $P6_3/mmc$) with cell parameters $a = 3.03670(2)$ Å and $c = 18.0849(1)$ Å (Figure 6.1b). Next, we optimized the conditions for etching out Ga from $\text{Mo}_2\text{Ga}_2\text{C}$ and identified that stirring in concentrated HF at 140 °C completely removes Ga from $\text{Mo}_2\text{Ga}_2\text{C}$ after 96 h (according to EDX mapping and XPS data, Figure E.3 and Figure E.11 respectively), producing Mo_2CT_x (Figure 6.1a). The morphology of the synthesized multi-layer Mo_2CT_x is very similar to that of $\text{Mo}_2\text{Ga}_2\text{C}$ by SEM (Figure E.3 and Figure E.4). In addition, both the O and F peaks are significantly increased in Mo_2CT_x relative to $\text{Mo}_2\text{Ga}_2\text{C}$, consistent with the presence of T_x surface groups (Figure E.3 and Figure E.11). The XRD diffractogram of Mo_2CT_x shows no remaining peaks of $\text{Mo}_2\text{Ga}_2\text{C}$ (Figure 6.1c). While the Rietveld refinement of Mo_2CT_x is impeded by a very high anisotropy of Mo_2CT_x , the Le Bail fitting of the diffractogram reveals that all reflections could be assigned to two different phases, i.e. $\beta\text{-Mo}_2\text{C}$ and Mo_2CT_x , where the MXene phase belongs to the same space group as $\text{Mo}_2\text{Ga}_2\text{C}$ ($P6_3/mmc$), thus confirming that the removal of Ga does not affect the layer structure. Additionally, the removal of gallium (and the surface functionalization with T_x groups) reduces the cell parameter a to 2.8629(3) Å with a simultaneous increase of the cell parameter c to 20.515(3) Å. The refinement in the 2θ range of 5-30° including (002), (004) and (006) reflections allows determining with good accuracy the z coordinate of the Mo atom, i.e. 0.0737(1) (Figure E.5). Based on the determined c parameter and the coordinate z , the Mo–Mo distance of the individual Mo_2CT_x layer was calculated as $d = 2 * z * c \sim 3$ Å at room temperature.

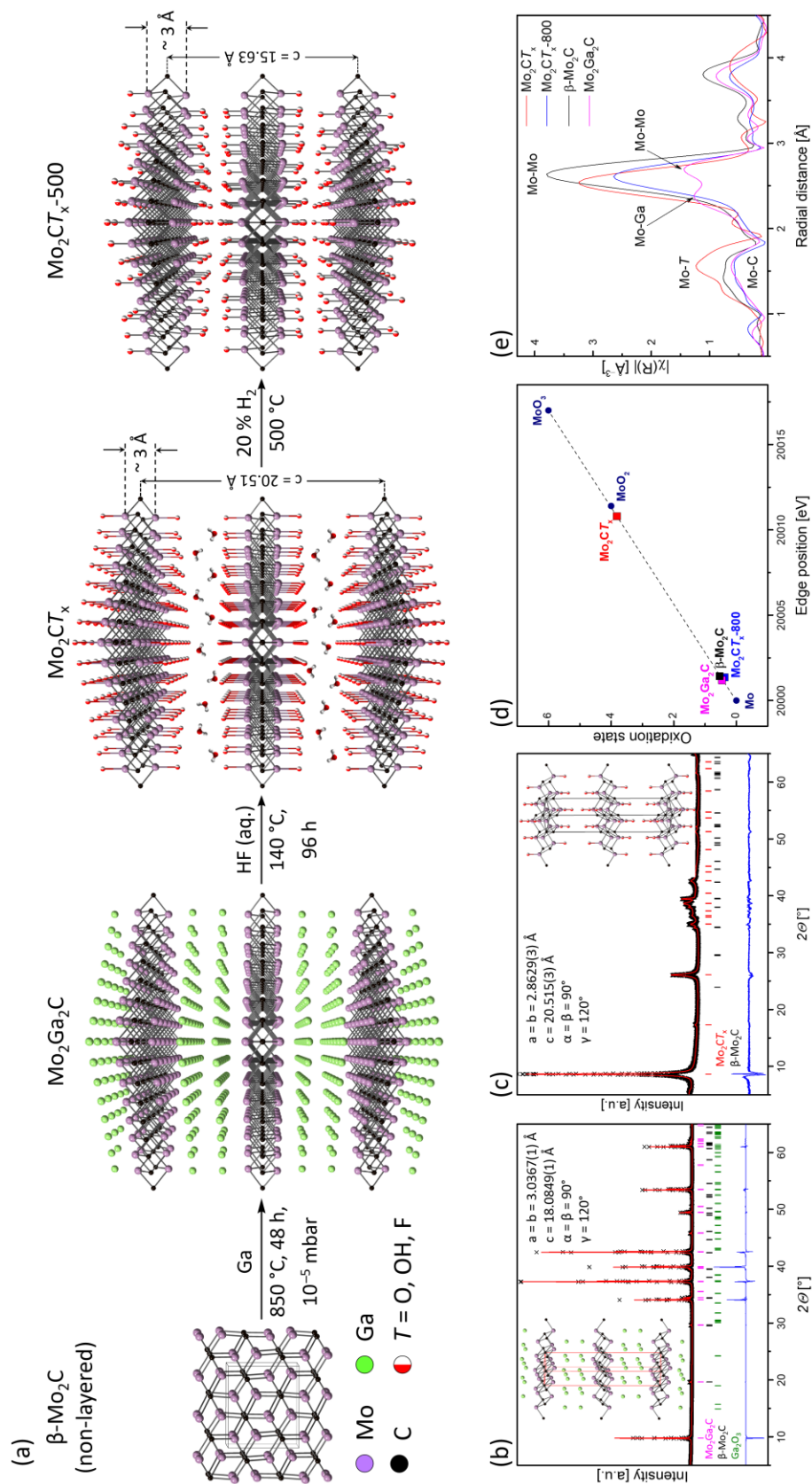


Figure 6.1. a) Synthesis of Mo_2CT_x , its thermal densification in a H_2 atmosphere, and selected structural parameters; b) Rietveld refinements of $\text{Mo}_2\text{Ga}_2\text{C}$; c) Le Bail fitting of Mo_2CT_x ; d) oxidation state of molybdenum in reference and synthesized materials determined from the edge position in XANES spectra; e) Fourier transformed EXAFS functions (uncorrected for the phase shift).

It was reported previously that the oxidation state of Mo could be determined from the edge position of Mo in K-edge XANES spectra (linear dependence).²⁹⁸⁻²⁹⁹ Using references of metallic Mo, MoO₂, and MoO₃ (edge positions 20000.0, 20011.4, and 20017.0 eV correspond to Mo oxidation states of 0, +4, and +6, respectively), we determined that the oxidation state of Mo in Mo₂Ga₂C and β-Mo₂C is close to metallic Mo (20001.0 and 20000.6 eV for Mo₂Ga₂C and β-Mo₂C, respectively, Figure 6.1d and Figure E.6). In a sharp contrast, the edge position of Mo₂CT_x is close to that of MoO₂ (20010.9 and 20011.4 eV, respectively), indicating that the average oxidation state of Mo in Mo₂CT_x is ca. +4. We explain this fact by the oxidation of surface Mo centers in the individual carbide layers by T_x groups during the HF treatment of Mo₂Ga₂C (140 °C, 4 days). Noteworthy, our results on Mo₂CT_x differ from the recent XANES analysis of Ti₃C₂T_x and Nb₂CT_x (at Ti and Nb K edges) that gave edge energies close to that of TiC and NbC, respectively,¹³⁹ but qualitatively agree, however, with the ca. + 2.3 average oxidation state of Ti in Ti₃C₂T_x determined in another report.³⁰⁰

The fitting of the experimental Fourier transformed EXAFS functions of β-Mo₂C and Mo₂Ga₂C demonstrates that the local structure around Mo is consistent with the respective crystallographic models (Figure 6.1e and Figure E.7). Specifically, both materials feature a coordination number (CN) of the first coordination sphere (i.e. Mo-C) that is equal to 3 (Table 6. 1). The Fourier transformed EXAFS functions of β-Mo₂C show only one broad peak corresponding to the Mo-Mo shell in the second coordination sphere. In agreement with the crystallographic model, it can be fitted with 3 different Mo-Mo interatomic distances, i.e. 2.91(1) Å, 2.96(1) Å, and 3.02(1) Å with a Mo–Mo CN equal to 4, 2, and 6, respectively. However, Mo₂Ga₂C exhibits two well-defined peaks in the second sphere (Table 6. 1). The first one of these two peaks has a fitted interatomic distance of 2.75(1) Å and corresponds to the Mo-Ga scattering path. The second peak can be fitted to the Mo–Mo shell at 3.05(1) Å and 3.23(2) Å (CN equal to 6 and 3, respectively). Fitting of the EXAFS functions for Mo₂CT_x yields a CN of 7(1) for the first coordination sphere, attributed to Mo-C and Mo-T_x shells (Table 6. 1). Note that without the T_x groups on the carbide surface, a theoretical CN value of 3 for the first Mo shell is expected from the crystal structure of Mo₂CT_x (P6₃/mmc). Therefore, the fitted CN = 7(1) for Mo₂CT_x clearly reveals the presence of scattering paths from the T_x groups that are not found in β-Mo₂C or Mo₂Ga₂C (Table 6. 1, distinguishing individual contributions from C, O and F scatters is not possible due to the close atomic number of these atoms). The

broad peak corresponding to the second coordination sphere, i.e. Mo–Mo, was fitted with two Mo–Mo scattering paths with interatomic distances of 2.87(1) Å and 3.20(1) Å and with CN of 3.8(2) and 1.9(2), respectively.

Table 6.1. Results of EXAFS best fits for β -Mo₂C, Mo₂Ga₂C, Mo₂CT_x and Mo₂CT_x-800.

Material	Shell	CN	σ^2 , Å ²	ΔE , V	R , Å	R factor
β -Mo ₂ C	Mo-C1	3	0.002(1)	5.9(5)	2.09(1)	0.013
	Mo-Mo1	4	0.003(1)		2.91(1)	
	Mo-Mo2	2	0.003(1)		2.96(1)	
	Mo-Mo3	6	0.003(1)		3.02(1)	
Mo ₂ Ga ₂ C	Mo-C1	3.3(4)*	0.003(1)	6.2(7)	2.12(1)	0.005
	Mo-Ga1	3	0.005(1)		2.75(1)	
	Mo-Mo1	3	0.008(1)		3.23(1)	
	Mo-Mo2	6	0.006(1)		3.05(1)	
Mo ₂ CT _x	Mo-C1/T _x	7(1)*	0.004(2)	9(1)	2.10(1)	0.017
	Mo-Mo1	1.9(2)*	0.002(1)		3.20(1)	
	Mo-Mo2	3.8(2)*	0.002(1)		2.87(1)	
Mo ₂ CT _x -800	Mo-C1	3	0.003(1)	8(1)	2.09(1)	0.011
	Mo-Mo1	4	0.006(1)		2.92(1)	
	Mo-Mo2	2	0.006(1)		3.04(3)	
	Mo-Mo3	6	0.006(1)		2.98(2)	

* fitted CN; $S_0 = 1$ was determined from fitting of Mo foil and fixed for all other samples.

β -Mo₂C and Mo₂Ga₂C materials feature the characteristic, sharp, isotropic signals in the ¹³C solid state NMR spectra of carbide peaks at 273 ppm and 178 ppm, respectively (Figure E.8). The observed chemical shift of β -Mo₂C is in excellent agreement with the previously reported data (273 ppm).³⁰¹⁻³⁰² Two reports compare changes in the ¹³C chemical shift that occur when etching an A metal from a MAX phase. Removing Al from Ti₃AlC₂ with HF leads to a large chemical shielding of the carbidic carbon, from 566 ppm in Ti₃AlC₂ to 382 ppm in Ti₃C₂T_x, and the latter peak is broad, indicating a distribution of carbidic environments in Ti₃C₂T_x.³⁰³ In contrast, carbidic carbon in V₂CT_x is more deshielded than in V₂AlC (ca. 260 ppm vs 208 ppm, respectively).³⁰⁴ In our case, etching out Ga from Mo₂Ga₂C barely changes the ¹³C chemical shift of the carbidic carbon as it is found in Mo₂CT_x at 175 ppm, however with a shoulder at ca. 125 ppm (Figure E.8). We tentatively attribute the latter peak to the oxycarbide carbon, that is the carbon next to the Mo=O sites, as its chemical shift is close to the previously reported molybdenum oxycarbide (MoO_xC_y, 113 ppm) obtained by the partial carburization of MoO₃.³⁰¹ Therefore, intercalation of Ga into β -Mo₂C shields the carbon by ca. 100 ppm, while the Ga etching and the concomitant Mo surface oxidation does not affect the chemical shift in Mo₂CT_x relative to Mo₂Ga₂C, except when T_x is oxo; in this case

the carbidic carbon is further shielded by ca. 50 ppm. A small peak at ca. 275 ppm is observed in the as prepared Mo_2CT_x and is due to the minor amount of $\beta\text{-Mo}_2\text{C}$.

To determine the reducibility of T_x surface groups in Mo_2CT_x , an *in situ* TGA temperature programmed reduction (TPR) experiment was performed. We observe a continuous weight loss in the temperature range 50 to 800 °C when flowing 10 vol.% H_2 in N_2 over Mo_2CT_x (Figure 6.2a). The results of four TPR TGA experiments give an average weight loss of 19 ± 2 wt.%. The derivative of the weight loss features three major, well-defined steps. We speculate that below ca. 350 °C, the residues of the solvent, i.e. water, trapped in between the carbide layers, are desorbed, while at higher temperatures, and specifically at ca. 500 and 600 °C, the surface T_x groups are de-functionalized from the surface.

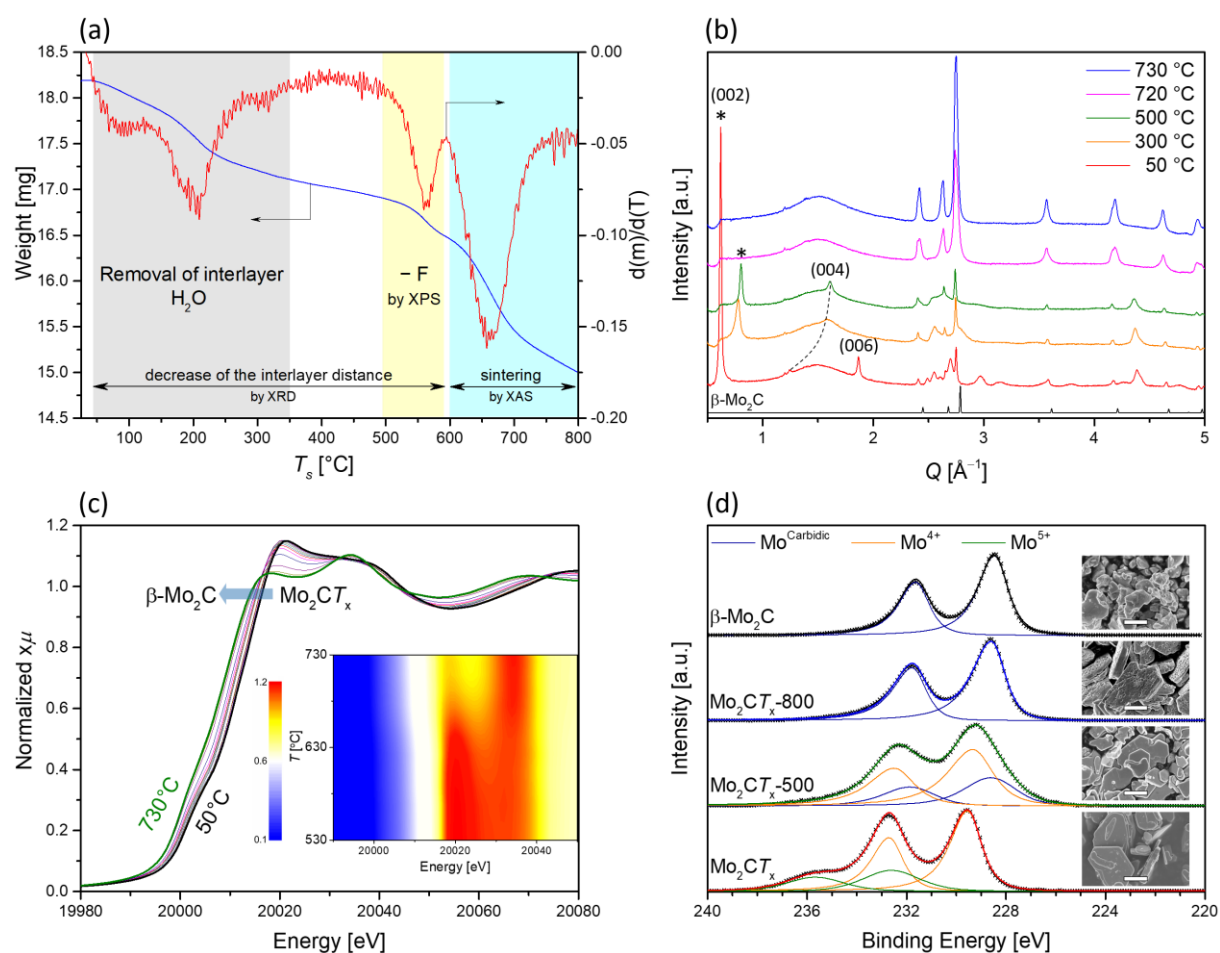


Figure 6.2. *In situ* structural stability H_2 -TPR study of Mo_2CT_x as followed by a) TGA, and b,c) XRD-XANES ($Q = 4\pi\sin(\theta)/\lambda$), and d) deconvolution of *ex situ* XPS data of the Mo 3d core levels of partially reduced Mo_2CT_x and reference materials with their respective SEM images (the scale bar is 2 μm , see Figure E.4 for details).

To probe further the behavior of Mo_2CT_x under reductive environments, we performed an *in situ* XANES-XRD experiment under H_2 -TPR conditions. During the TPR experiment, alternating XANES spectra and XRD patterns (40 and 5, respectively) were collected, the latter at 50, 300, 500, 720 and 730 °C (Figure 6.2b). The layered structure of Mo_2CT_x remains unchanged at least up to 500 °C, however, a dramatic shift of the (00 l) peaks to higher Q values as well as a significant reduction of the intensity ratio of the (002) to (004) peaks are observed. The shift of the peak positions reveals a decrease in the c cell parameter with increasing temperature, from $c = 20.26$ Å at 50 °C to $c = 15.63$ Å at 500 °C (Figure E.9), explained by the gradual release of the interlayer solvent and de-functionalization of the T_x surface groups from carbide layers, also observed by TGA, leading to a decrease of the interlayer distance. The change of the intensity ratio of the (002) to (004) peaks is related to an alteration of the coordinates of the Mo atoms, i.e. the z coordinate in the unit cell. Calculating dimensions of the Mo–C–Mo layer reveals that despite the contraction of the Mo_2CT_x unit cell, the individual Mo_2C layers retain the same thickness of ca. 3 Å. The XRD pattern acquired at 720 °C indicates that the reduction of surface T_x groups is followed by a phase transformation, leading to a bulk carbide structure, i.e. Mo_2CT_x is not present anymore at 720 °C. The XRD pattern at 730 °C (acquired after ca. 30 min annealing at 730 °C) reveals the formation of $\beta\text{-Mo}_2\text{C}$ ($Pbcn$).

In the same *in situ* experiment, the release of the T_x groups was also followed by XANES at the Mo K-edge. Simultaneously with a decrease of the c cell parameter observed by XRD, the edge position of Mo XANES spectra shifts continuously to lower energies, indicating a gradual decrease of the oxidation state of Mo (Figure 6.2c). Around 600 °C, a fast transformation of Mo_2CT_x to a new phase was observed (Figure 6.2c, insert). The XANES spectrum of the new phase corresponds to the reference spectrum of $\beta\text{-Mo}_2\text{C}$ (Figure E.6). Based on the information obtained by XRD analysis, the EXAFS data of $\text{Mo}_2\text{CT}_x\text{-800}$ were fitted using a $\beta\text{-Mo}_2\text{C}$ crystallographic model. Fitting of the EXAFS data revealed the absence of T_x groups and a $\text{CN}_{\text{Mo-C}} = 3$. The second coordination sphere (Mo–Mo peak) was fitted with 3 Mo–Mo distances, i.e. 2.92(1) Å, 3.04(3) Å, and 2.98(2) Å, values in a good agreement with the reference $\beta\text{-Mo}_2\text{C}$. Overall, the combination of *in situ* XRD-XANES results indicate that Mo_2CT_x preserves its layered structure in reducing conditions up to ca. 550-600 °C, followed by a reduction of the remaining T_x groups and fast collapse and densification ultimately forming

bulk β -Mo₂C phase beyond this temperature range. In contrast, according to XRD and SEM analysis, heating Mo₂CT_x to 800 °C in atmosphere of pure N₂ extrudes nanoparticles of MoO₂ onto the surface of the formed β -Mo₂C phase (Figure E.4 and Figure E.10).

Having established *in situ* the thermal stability and phase transitions of Mo₂CT_x in reductive environment, we turned to analysis of *ex situ* XPS data of reduced Mo₂CT_x-500 and Mo₂CT_x-800 that were handled in an air-tight XPS cell under inert atmosphere to prevent re-oxidation of the surface. The temperatures of 500 and 800 °C were chosen as representative of a partially reduced material still possessing a layered structure and a fully densified material, respectively. The deconvolved XPS Mo 3d spectra are presented in Figure 6.2d and the summary of the fitting is presented in Table E.2. The XPS spectra of Mo₂CT_x reveals that Mo is present in two different oxidation states, i.e. +4 and +5 (Mo 3d 5/2 binding energies of 229.6 and 232.6 eV, respectively). According to the fit, the proportion of the two Mo oxidation states is 72 % Mo⁴⁺ and 28 % Mo⁵⁺ (Table E.2). This observation is in a good agreement with our XAS results presented above. Additionally, O and F signals are present in the XPS survey spectrum indicative of the T_x surface groups (Figure E.11). A quantitative analysis, based on the areas of the F 1s and Mo 3d peaks, reveals a high concentration of surface F species with a F to Mo ratio of ca. 0.7. This observation is in a good agreement with the literature data indicating that F has the highest fraction of termination groups for as prepared MXenes (Ti, Nb).³⁰⁵ The Mo 3d spectrum of Mo₂CT_x-500 shows a partial reduction of Mo. The broad doublet reveals the presence of both carbidic (Mo 3d 5/2 at 228.5 eV) and oxidized Mo⁴⁺ (Mo 3d 5/2 at 229.3 eV) species (Mo^{Carbidic} : Mo⁴⁺ = 34 : 66). The quantitative analysis of the survey spectrum exposes a significantly smaller amount of F (F : Mo = 1 : 9) on the Mo₂CT_x-500 surface indicating that most of fluorine is reductively de-functionalized at temperatures below 500 °C (Figure E.13). This observation in combination with the TGA results (Figure 6.2a) allows us to propose that the first high temperature weight loss step on the TGA curve corresponds to the reductive de-functionalization of fluoride groups, while the final step corresponds to the reductive desorption of surface oxo groups. Finally, in a good agreement with XRD and XAS data, the Mo XPS spectrum of Mo₂CT_x-800 is similar to the spectrum of the reference β -Mo₂C and features a doublet with a Mo 3d 5/2 binding energy of 228.6 eV. The absence of F 1s peak is also consistent with the surface de-functionalization at 800 °C (Figure E.13).

Ex situ samples were further analyzed using scanning electron microscopy. SEM analysis of Mo₂CT_x-500 reveals no noticeable changes compared to initial Mo₂CT_x as its platelet morphology remains unchanged (Figure 6.2d and Figure E.4). However, although the platelet morphology remains also for Mo₂CT_x-800, this material contains pores of ca. 30-50 nm that likely originate from the recrystallization process specific to reductive densification, as material prepared by annealing Mo₂CT_x to 800 °C in N₂ is non-porous (Figure E.4).

Figure 6.3a plots the temperature dependence of the catalytic activity of Mo₂CT_x, Mo₂CT_x-500, and reference β-Mo₂C materials for the WGS reaction. Interestingly, Mo₂CT_x reveals the highest activity among all tested catalysts reaching the maximal activity at around 520 °C with a peak consumption rate of CO at ca. 100 μmol(CO) g(Mo)⁻¹ s⁻¹. This rate is comparable to that of the conventional high-temperature Fe-based catalyst, i.e. Fe/Ce/Co oxide, exhibiting CO consumption rate of ca. 60 μmol(CO) g(cat.)⁻¹ s⁻¹ at 500 °C.³⁰⁶ Additionally, the productivity of Mo₂CT_x (i.e. per gram of catalyst) at 500 °C is similar to the productivity of 3.9 wt.% Pt/Al₂O₃ (ca. 50 μmol(CO) g(cat.)⁻¹ s⁻¹)⁸⁹ at 400 °C. From 520 °C to ca. 600 °C, a slow decrease in the catalytic activity is observed. At higher temperatures the activity of Mo₂CT_x drops dramatically and reaches a plateau at ca. 720 °C. The observed loss of activity coincides with the densification of Mo₂CT_x at temperatures > 550 °C, as revealed by the *in situ* XANES-XRD study discussed above. Although the activity of Mo₂CT_x-500 is lower than that of Mo₂CT_x, the temperature profile of its reaction rate shows the same trend, i.e. reaching a maximum at 520 °C and decreasing after 600 °C. We speculate that the lower activity of Mo₂CT_x-500 is possibly linked to increased mass transport limitation within the layers of Mo₂CT_x-500, owing to the contraction of the interlayer distances as observed by XRD (from the crystal lattice parameter $c = 20.26 \text{ \AA}$ at 50 °C to $c = 15.63 \text{ \AA}$ at 500 °C). Note that β-Mo₂C, Mo₂CT_x and Mo₂CT_x-500 all have similar morphology by SEM (Figure E.4) and therefore similar limitations of inter-grain mass transport. In contrast to Mo₂CT_x, the reference bulk β-Mo₂C shows negligible activity at temperatures <600 °C with a slight improvement at higher temperatures.

XRD analysis of the spent catalysts, after having been exposed to WGS conditions up to 950 °C, reveals the presence of MoO₂ in all catalysts due to the oxidation of the carbide phases at high temperatures (Figure E.15). Overall, the results obtained indicate that the

partial removal of T_x surface groups does not improve the reaction rates likely because the partially reduced very oxophilic molybdenum carbide surface gets rapidly covered with oxygen under WGS reaction conditions.³⁰⁷

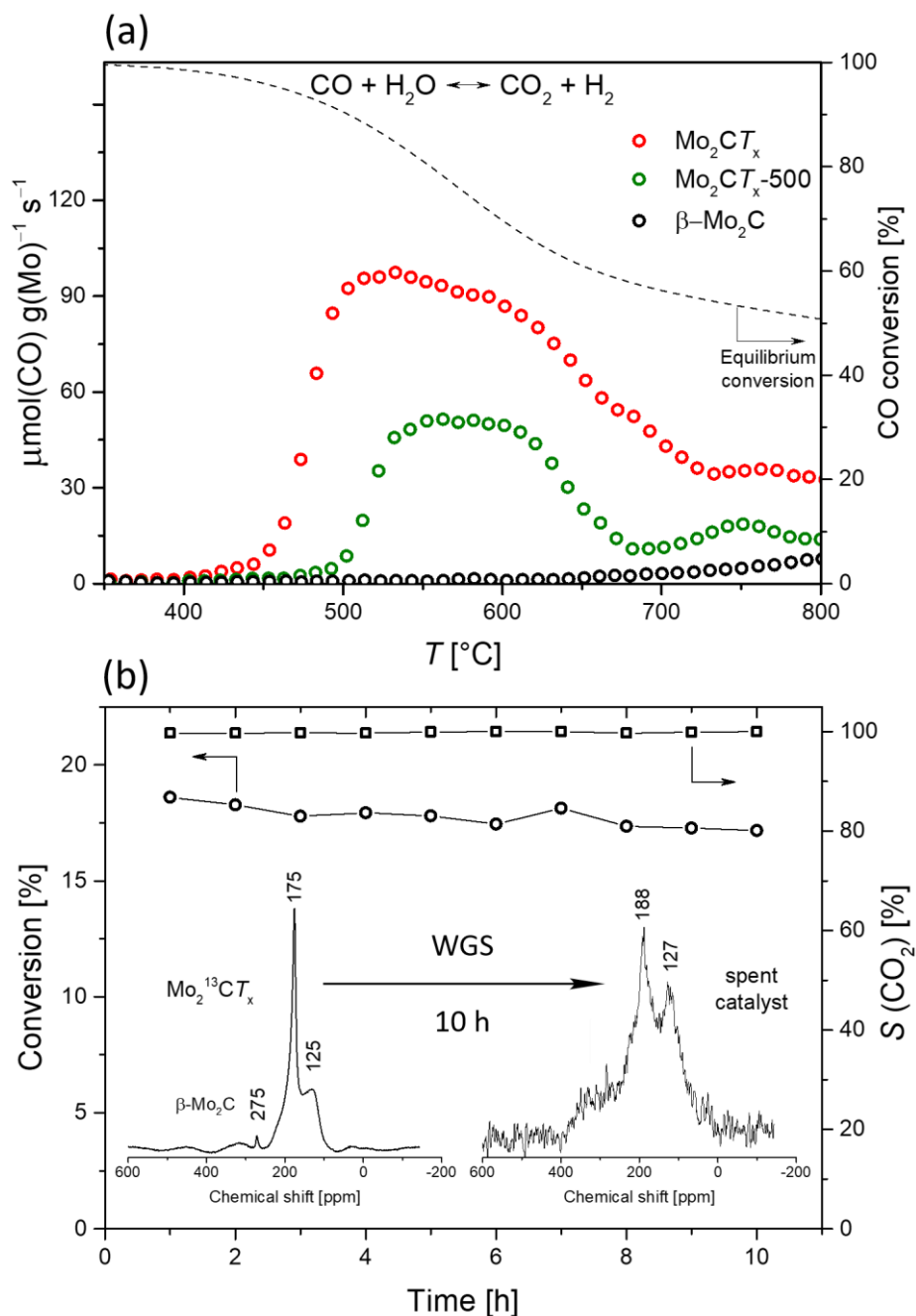


Figure 6.3. a) WGS catalytic activity of Mo_2CT_x , $\text{Mo}_2\text{CT}_x\text{-500}$, and a reference $\beta\text{-Mo}_2\text{C}$ and b) WGS stability test of $\text{Mo}_2^{13}\text{CT}_x$ at 500 °C and 13C MAS NMR (400 MHz, spinning rate 10 kHz) of $\text{Mo}_2^{13}\text{CT}_x$ before (1200 scans) and after (20000 scans) WGS catalytic test.

In addition, we have performed a stability test at 500 °C using Mo_2CT_x as the catalyst (Figure 6.3b). Only minor deactivation could be observed, i.e. 5 % reduction over 10 h on

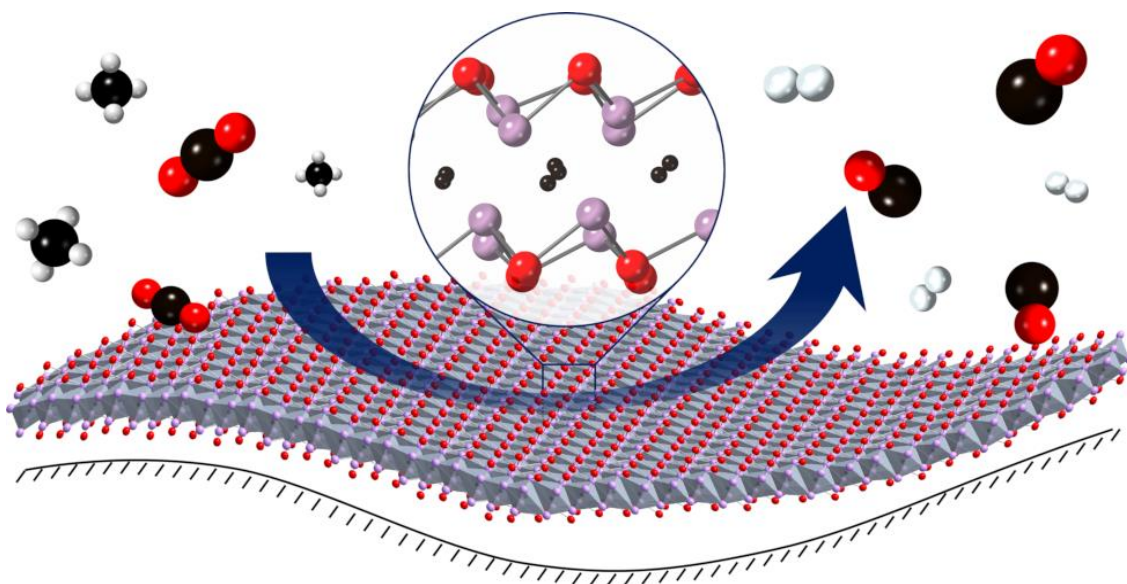
stream. Furthermore, CO and CO₂ were the only carbon-containing gases sampled in the off gas, revealing a selectivity exceeding 99 % toward CO₂. In comparison, the reference material β -Mo₂C is completely inactive for the WGS reaction under similar conditions. XRD analysis of spent Mo₂CT_x (Figure E.16) shows only trace amounts of MoO₃, underlying a remarkably high stability of Mo₂CT_x in oxygen-rich environments at high temperatures. The formation of MoO₃ is further confirmed by SEM imaging that reveals small nanoparticles decorating surfaces of Mo₂CT_x (Figure E.4). XPS analysis of spent Mo₂CT_x (Figure E.14) shows that, similar to initial Mo₂CT_x, molybdenum is present in +4 and +5 oxidation states (Mo 3d 5/2 binding energy of 229.6 eV and 232.4 eV, respectively), although with a slightly higher Mo⁺⁴ content (see Table E.2 for details). This observation proves stability of Mo₂CT_x under WGS conditions and indicates that the molybdenum oxycarbide is the most likely active phase for this reaction.²⁵² The ¹³C ssNMR spectrum of the spent catalyst (¹³C-labelled Mo₂CT_x with ≥ 99 atom.% enrichment was used) reveals significant changes compared to fresh Mo₂¹³CT_x (Figure 6.3b, insert). The main carbidic peak is shifted to 188 ppm and the contribution of the second peak at 127 ppm, attributed to an oxycarbide carbon, is increased noticeably compared to the fresh material. The change in the ratio between carbidic and oxycarbide signals indicates a further surface oxidation of the molybdenum layer and increase in the content of surface oxo groups during the WGS reaction, consistent with the oxophilic nature of the molybdenum carbide surface mentioned above. An additional shoulder at ca. 280-320 ppm can probably be attributed to the initial β -Mo₂C impurity phase and/or partial transformation of the catalyst to bulk β -Mo₂C. Interestingly, a dramatic decrease in the signal to noise ratio is likely due to an exchange of the carbide carbon during the WGS reaction, yielding a substitution of ¹³C by ¹²C from the feed. A similar participation of the carbide carbon was previously observed in CO hydrogenation,³⁰⁸ methane partial oxidation,²⁵⁹ and methane dry reforming³⁰⁹ reactions.

6.5. Conclusions

A phase pure Mo₂CT_x was synthesized and its structural stability was interrogated under heating in reducing atmospheres. The layered structure of Mo₂CT_x is preserved up to ca. 550 °C. At higher temperatures, Mo₂CT_x undergoes a transition to bulk β -Mo₂C as soon as the surface becomes de-functionalized from the T_x groups. Mo₂CT_x shows a remarkable activity and stability for the WGS reaction with a selectivity > 99 % toward CO₂ and H₂. Our observations indicate that catalytic applications in temperature regimes that partially reduce

MXenes and decrease their interlayer distance may become influenced by mass transport limitations, owing to a reduced distance between the carbide layers. Overall, the results obtained demonstrate that Mo_2CT_x is a robust catalyst for high temperature catalytic applications and that it is particularly stable against oxidation to MoO_2 .

Chapter 7: Two-dimensional silica-supported molybdenum oxycarbide $2\text{D-Mo}_2\text{CO}_x$: exploiting morphology to enable high activity and stability in the dry reforming of methane



The results of this chapter are published as:

A. Kurlov, E. B. Deeva, P. M. Abdala, D. Lebedev, A. Tsoukalou, A. Comas-Vives, A. Fedorov, C. R. Müller, Exploiting two-dimensional morphology of molybdenum oxycarbide to enable efficient catalytic dry reforming of methane, *Nat. Commun.*, **2020**, 11, 4920

7.1. Abstract

We report that silica-supported two-dimensional (2D) molybdenum oxycarbide, 2D-Mo₂CO_x/SiO₂, shows a remarkable activity in the dry reforming of methane (DRM) with a methane conversion rate up to 0.42 mol(CH₄) mol(Mo)⁻¹ s⁻¹ at 80 % CH₄ conversion (800 °C). This activity is 10-200 fold higher than the activities for other Mo₂C-based catalysts. The two-dimensional nanosheet morphology of the oxycarbide catalyst was found to be vital for imparting a high stability to the 2D-Mo₂CO_x/SiO₂ catalyst towards oxidation by CO₂ and maximizing metal utilization. Remarkably, 2D-Mo₂CO_x/SiO₂ does not deposit any coke in DRM experiments and while Mo₂C catalysts deactivate in a CO₂ atmosphere, 2D-Mo₂CO_x is activated by CO₂, which allows tuning the surface oxygen coverage for optimal catalytic performance. The most active 2D-Mo₂CO_x catalyst has a Mo oxidation state of ca. +4 according to Mo K-edge XANES and an oxygen coverage of approximately 0.7 monolayer, as determined by DFT calculations. According to the ab initio calculations, the dry reforming of methane proceeds on Mo sites of the oxycarbide nanosheet. Methane activation is the most energy demanding step, while the activation of CO₂ and the C–O coupling to form CO are low energy steps. The nanosheet morphology of 2D-Mo₂CO_x is retained after multiple catalysis – CO₂ regeneration cycles at 800 °C because the dispersion of the nanosheets on the silica support prevents their thermal sintering. The deactivation of 2D-Mo₂CO_x/SiO₂ under DRM conditions can be avoided by tuning the contact time, thereby preventing unfavorable too high or too low oxygen surface coverages of the active 2D-Mo₂CO_x phase. The results obtained indicate that supported 2D-Mo₂CO_x is a very active and robust oxycarbide-based catalyst that is remarkably resistant against oxidation at high temperatures.

7.2. Introduction

Since the early work by Sinfelt⁸⁴ and Boudart⁸⁵ demonstrated that Mo₂C and WC exhibit platinum-like catalytic activity in alkane hydrogenolysis and isomerization, a multitude of reports has appeared aiming to exploit molybdenum carbide for industrially-relevant reactions such as methane aromatization,⁹⁰⁻⁹¹ the water gas shift,⁸⁶⁻⁸⁷ and CO₂ hydrogenation reactions,⁹⁵⁻⁹⁶ to name just a few.²⁴² In contrast to middle-to-late transition metal-based catalysts that deactivate by the deposition of coke, sintering or poisoning,³¹⁰ carbide catalysts typically feature a low rate of coking,⁹⁷ are resistant to high temperature sintering as well as

to sulfur poisoning.⁹⁸⁻⁹⁹ However, the high oxophilicity of carbides fosters their evolution in reactions with oxygenate substrates, leading ultimately to deactivation *via* the formation of oxide phases; deactivated catalysts require regeneration by re-carburization with CH₄/H₂.⁹⁷ If such deactivation pathways are avoided while the metal utilization of carbides is maximized, for instance by developing catalysts with a high surface-to-bulk ratio and a high dispersion on supports, the replacement of traditional, more expensive middle-to-late transition metal catalysts by carbide-based catalysts will become viable.

The dry reforming of methane, (DRM, CH₄ + CO₂ ↔ 2CO + 2H₂) is an example of a particularly challenging reaction for Mo₂C-based catalysts because it combines a CO₂-rich feed with high operating temperatures (typically, 800 °C and above).^{97,100-102,105,259-261} Deactivation of Mo₂C in DRM conditions proceeds oxidatively according to Mo₂C + 5 CO₂ → 2 MoO₃ + 6 CO^{97,102,259} and in order to mitigate it, dry reforming of methane is often conducted at elevated pressures (2-10 bar).^{97,101-102,260} From a mechanistic standpoint, an ill-defined molybdenum oxycarbide phase (MoO_xC_y) has been reported to play a key role in DRM,²⁴⁷ as well as in the water gas shift,²⁵² deoxygenation,^{254,311} and CO₂-to-methanol⁹⁶ conversion processes, suggesting that the partial oxidation of Mo₂C is favorable for those reactions. In addition, recent reports on CO₂-propane dehydrogenation catalyzed by Mo₂C highlighted that control over the oxygen coverage of the surface oxycarbide layer allows tuning the catalytic activity and selectivity.^{115,255} Molybdenum oxycarbide species were also proposed as intermediates during the dehydroaromatization of methane on molybdenum-loaded zeolite ZSM-5.²⁵⁰ However, establishing the local structure and the nature of the active sites in such molybdenum oxycarbide phases has remained challenging, largely because well-defined oxycarbide catalysts, serving as references, are not available.

In this context, a recently discovered family of two-dimensional atomically-thin early transition metal carbides, nitrides and carbonitrides called MXenes¹¹⁹ could be exploited as an entry point to supported well-defined 2D carbides and oxycarbides. MXene films are nanocrystalline yet form stable colloidal solutions in protic solvents, and feature metal-terminated surfaces (*vide infra*) with a lateral size in the submicron scale, which yields highly uniform surface metal sites.³¹² The atomically thin nature of MXenes enables optimal metal utilization provided that these films are highly dispersed on a support. The 2D morphology is also advantageous for mechanistic studies since bulk metal sites in catalysts derived from

MXenes, are minimized. Therefore the characterization methods applied (even when not being inherently surface sensitive) will provide information mostly about the surface sites, which is instructive for structure-activity studies.

In what follows, we describe an approach to yield a supported two-dimensional (2D) model molybdenum oxycarbide material containing well-defined surface sites that are highly active in the dry reforming of methane. We prepared this catalyst from colloidal, delaminated thin films of the molybdenum carbide MXene phase, Mo_2CT_x , where T stands for OH, O, F surface termination groups. After supporting Mo_2CT_x on SiO_2 , these surface groups can be controllably removed (de-functionalized) by reduction in H_2 , giving $2\text{D-Mo}_2\text{C/SiO}_2$. The oxidation of $2\text{D-Mo}_2\text{C/SiO}_2$ by CO_2 at $800\text{ }^\circ\text{C}$ gives a 2D molybdenum oxycarbide $2\text{D-Mo}_2\text{CO}_x/\text{SiO}_2$ with a high oxygen surface coverage and an average Mo oxidation state of +5.5. Subjecting this material to DRM conditions reduces the oxygen coverage and forms a catalyst *in situ* with an average Mo oxidation state of +4. This material is highly active in DRM, in contrast to fully reduced $2\text{D-Mo}_2\text{C/SiO}_2$ and $2\text{D-Mo}_2\text{CO}_x/\text{SiO}_2$ material with highest oxygen coverage (confirmed by a Mo oxidation state of ca. +5) which are essentially inactive for the DRM. Our Mo K-edge XANES and XPS results verify that molybdenum oxycarbide is the active phase in Mo_2C -based DRM catalysts²⁸³ and DFT calculations identify that an oxygen coverage of ca. 0.7 monolayer provides a high activity of $2\text{D-Mo}_2\text{CO}_x/\text{SiO}_2$ in DRM. Reducing or increasing this optimal oxygen coverage decreases the reaction rate. $2\text{D-Mo}_2\text{CO}_x/\text{SiO}_2$ catalyst with reduced oxygen coverage is also less selective owing to a competing reverse water gas shift reaction. Hence, supported $2\text{D-Mo}_2\text{CO}_x$ catalyst with an initially high coverage of surface oxygen atoms activates first by reduction, that is the oxygen coverage is lowered until a maximum in DRM performance is reached at a Mo oxidation state of ca. +4. Reducing the Mo oxidation state further (i.e. lowering the oxygen coverage below ca. 0.7 monolayers) leads to catalyst deactivation. This observation is in sharp contrast to non-layered Mo_2C -based catalysts that readily deactivate by oxidation in a CO_2 atmosphere. It is therefore remarkable that deactivated $2\text{D-Mo}_2\text{CO}_x/\text{SiO}_2$ catalysts do not contain any deposited coke according to temperature-programmed oxidation (TPO) experiments and can be regenerated by oxidation in CO_2 , fully recovering their highest catalytic activity. Noteworthy, the deactivation of $2\text{D-Mo}_2\text{CO}_x/\text{SiO}_2$ under DRM conditions can be avoided by optimizing the contact time. Density functional theory calculations corroborate experimental observations and

demonstrate that the DRM pathway on an oxycarbide surface with a submonolayer oxygen coverage is energetically favored compared to the pathway occurring on a fully carbide surface. The fully oxygen-covered surface is unstable in DRM conditions and reduces *in situ* its oxygen coverage below 1 oxygen monolayer, also consistent with our experiments.

7.3. Experimental section

7.3.1. Materials

Multi-layered Mo_2CT_x material ($m\text{-Mo}_2\text{CT}_x$) was synthesized following a reported method.¹²² 2D- Mo_2CT_x nanosheets were delaminated from $m\text{-Mo}_2\text{CT}_x$ (50 mg) in ethanol (10 mL) using a pulse sonication (1.5 h, 85 W, 20 kHz) (Fisher Scientific, FB120). Resulting suspension was centrifuged (7000 rpm, 7 min) and the supernatant solution containing colloidal delaminated Mo_2CT_x nanosheets ($d\text{-Mo}_2\text{CT}_x$) was further used for the incipient wetness impregnation (IWI) onto SiO_2 support (150-300 μm particle size fraction of Aerosil 300 that had been calcined at 950 °C, 194 m^2g^{-1} surface area by nitrogen physisorption). The IWI procedure using ethanol colloidal solution of $d\text{-Mo}_2\text{CT}_x$ was repeated multiple times and after drying (100 °C, 12 h) yielded 2D- $\text{Mo}_2\text{CT}_x/\text{SiO}_2$ material with Mo loading of 0.48 wt.% (batch 1) and 0.35 wt.% (batch 2) according to elemental analysis (ICP-AES). 2D- $\text{Mo}_2\text{CT}_x/\text{SiO}_2$ was subsequently reduced in hydrogen (20 vol.% H_2/N_2 , 800 °C, 1.5 h, 50 mL min^{-1} , 10 °C min^{-1}) and oxidized in CO_2 (100 % CO_2 10 mL min^{-1} , 800 °C, 1.5 h) to give 2D- $\text{Mo}_2\text{C}/\text{SiO}_2$ and 2D- $\text{Mo}_2\text{CO}_x/\text{SiO}_2$ materials, respectively. To avoid surface modification of the activated materials, 2D- $\text{Mo}_2\text{C}/\text{SiO}_2$, 2D- $\text{Mo}_2\text{CO}_x/\text{SiO}_2$ and all activated catalysts were transferred into a nitrogen-filled glovebox (H_2O and O_2 levels < 0.5 ppm) and handled without exposure to air.

7.3.2. Characterization

Ex situ X-ray powder diffraction (XRD) data were collected on a PANalytical Empyrean X-ray diffractometer equipped with a Bragg–Brentano HD mirror and operated at 45 kV and 40 mA using $\text{CuK}\alpha$ radiation ($\lambda = 1.5418 \text{ nm}$). The materials were examined within the 2θ range of 5–90° using a step size of 0.0167°. The scan time per step was 3 s. Thermogravimetric analysis (TGA) was performed on Mettler Toledo TGA/DSC 3 instrument. The concentration of 2D- Mo_2CT_x flakes in the prepared colloidal solutions was determined by placing a 750 μL aliquot in a sapphire crucible (900 μL), that was kept at 80 °C for 1 h (5 °C min^{-1}). Temperature

programmed oxidation (TPO) was performed on Mettler Toledo TGA/DSC 1 instrument. Mo material (20 mg) was placed in a 70 μL alumina crucible and heated up to 800 $^{\circ}\text{C}$ (10 $^{\circ}\text{C min}^{-1}$) under air flow (125 mL min^{-1}). The H_2O and CO_2 content in the outlet gas was followed by a mass spectrometer MKS Cirrus 3. Inductively Coupled Plasma - Atomic Emission Spectroscopy (ICP-AES) analysis was performed by the Mikroanalytisches Labor Pascher (Remagen, Germany). X-ray photoelectron spectroscopy (XPS) measurements were conducted on a Sigma II instrument (Thermo Fisher Scientific) equipped with an UHV chamber (non-monochromatic 200 W Al $\text{K}\alpha$ source, a hemispherical analyzer, and a seven channel electron multiplier). The analyzer-to-source angle was 50 $^{\circ}$, while the emission angle was 0 $^{\circ}$. A pass energy of 50 eV and 25 eV was set for the survey and narrow scans, respectively, and C 1s peak of adventitious carbon was set at 284.8 eV to compensate for any charge induced shifts. An air-tight cell allowing to transfer specimens between the glovebox and the XPS instrument without exposure to air was used for reduced or spent materials.²⁹² XPS data were analyzed in CasaXPS Version 2.3.19PR1.0 software. The background subtraction was performed according to Shirley,²⁹³ and the atomic sensitivity factors (ASF) of Scofield were applied to estimate the atomic composition.²⁹⁴ HAADF STEM images were recorded using FEI Talos F200X with the accelerating voltage of 200 kV. All samples were prepared by shaking the holey carbon TEM grid with in the vial with the dry specimen powder. 2D-Mo₂C/SiO₂ and 2D-Mo₂CO_x/SiO₂ were deposited on TEM grids in the glove box and transferred to the microscope without ambient exposure by using the TEM vacuum transfer holder (Fischione, 2560). FTIR Spectroscopy was conducted using a 200 mL glass reactor with IR-transparent CaF₂ windows. A thin pellet of the sample was pressed in a glovebox and loaded to the reactor using a glass sample holder. A spectrum was recorded in an argon atmosphere in a transmission mode on a Nicolet 6700 FTIR spectrophotometer using 64 scans at a resolution of 2 cm^{-1} . CO chemisorption was performed using an AutoChem system (Micromeritics) with a thermal conductivity detector (TCD). Approximately 100 mg of the material was loaded in a U-shape reactor and reduced at 800 $^{\circ}\text{C}$ under 5 % H_2/Ar for 1.5 h (10 $^{\circ}\text{C min}^{-1}$, 50 mL min^{-1}). The sample was then cooled down under a He atmosphere to 450 $^{\circ}\text{C}$ and degassed for 2 h. The first CO adsorption isotherm was carried out at 50 $^{\circ}\text{C}$. The reactor was then purged with He for 30 min to remove weakly adsorbed species prior to performing the second CO isotherm, also at 50 $^{\circ}\text{C}$. The amount of strongly adsorbed CO was determined as a difference

between the first and the second adsorption isotherms, which provided the CO adsorption capacity. The surface area of the 2D-Mo₂C nanosheets in 2D-Mo₂C/SiO₂ was estimated based on the crystal structure of Mo₂CT_x.¹²² Considering the hexagonal ordering of the Mo atoms with a Mo-Mo distance of 2.8629 Å gave an area estimate of 7.098 Å² per Mo atom. Based on the Mo content in 2D-Mo₂CT_x/SiO₂, determined by ICP, and the mass of the 2D-Mo₂CT_x/SiO₂ specimen used for CO chemisorption, the amount of strongly chemisorbed CO was normalized per the surface area of the two-dimensional molybdenum nanosheets (Table F.4).

X-ray absorption spectroscopy (XAS) was performed at the Swiss-Norwegian Beamlines (SNBL, BM31)²⁷¹ at the European Synchrotron Radiation Facility (ESRF, Grenoble, France). XAS spectra were collected at the Mo K-edge using a double-crystal Si (111) monochromator with continuous scanning in transmission mode (unfocused beam, 1-2·10⁹ ph s⁻¹ mm⁻¹). The calibration of the XAS data was based on edge position of the Mo foil reference set at 20000 eV. The *operando* DRM experiment was performed in a quartz capillary reactor (Figure F.1).²⁷¹ Approximately 2 mg of 2D-Mo₂CT_x/SiO₂ was placed between two quartz wool plugs in a capillary cell (outer diameter 1.5 mm, wall thickness 0.1 mm). The reduction step was performed in 20 vol.% H₂ in N₂ using a total flow rate of 10 mL min⁻¹ in the temperature range from 50 to 750 °C (ca. 9 °C min⁻¹, 20 min holding time). The oxidation step was performed in pure CO₂ with a flow rate of 10 mL min⁻¹ at 730 °C for 2 h. DRM catalytic experiments was performed at 730 °C under a mixture of CH₄ and CO₂ of varied ratio diluted in N₂ with a total flow rate of 5 mL min⁻¹ (HSV of ca. 30000 L_{gMo}⁻¹ h⁻¹). The composition of the outlet gas was followed by a compact GC (Global Analyser Solutions) equipped with TCD and FID detectors. *Ex situ* XAS data were collected from pellets of reference materials with an optimized amount of specimen mixed with cellulose. All materials derived from reduced 2D-Mo₂C/SiO₂ were handled in a glovebox and their analysis performed in an air-tight sealed bags. XAS data processing was performed using the Athena software, and extended X-ray absorption fine structure (EXAFS) fittings were performed with Artemis software (Demeter 0.9.25 software package).²⁰⁶ The edge position for oxygen free materials, i.e. Mo and Mo₂C, was defined as the position of the first maximum in the first derivative curve. The second maximum of the first derivative curve was chosen as the edge position for oxide and oxycarbide materials.

7.3.3. Catalytic Testing.

The catalytic testing of freshly prepared materials in conditions of the dry reforming of methane was carried out in a fixed-bed quartz reactor at atmospheric pressure. In a typical experiment, 100 mg of freshly prepared 2D-Mo₂CT_x/SiO₂ material was used. Prior to the activity tests, 2D-Mo₂CT_x/SiO₂ was *in situ* reduced in 20 vol.% H₂/N₂ (800 °C, 1.5 h, 50 mL min⁻¹, 10 °C min⁻¹) and then oxidized in pure CO₂ (800 °C, 1.5 h, isothermal). The activity test was then performed at 800 °C with a variable total flow rate of the feed (10 to 50 ml min⁻¹, SV = 1200-6000 L g_{Mo}⁻¹ h⁻¹, 45 % CH₄, 45 % CO₂, and 10 % N₂). The composition of the off-gas was analyzed *via* a GC (PerkinElmer Clarus 580) equipped with a thermal conductivity TCD detector. The carbon balance during the catalytic tests was generally close to 100 %, maximal deviations noted were +/- 10 %, observed when switching gases.

We note that catalytic results reported were obtained with freshly-prepared 2D-Mo₂CT_x/SiO₂. When as prepared 2D-Mo₂CT_x/SiO₂ was left for a prolonged time (ca. 1 month) in air, a fragmentation of 2D-Mo₂CT_x nanosheets into nanoparticles had occurred according to TEM characterization (Figure F.7). The latter material is inactive in DRM, which emphasizes the importance of 2D nanosheets morphology for the high catalytic activity.

7.3.4. Computational Details

The periodic density functional theory (DFT) calculations were carried out with the Vienna Ab Initio Simulation Package (VASP) code³¹³⁻³¹⁵ and the projector-augmented-wave,³¹⁶ for which interactions between valence electrons and ion cores are described by pseudopotentials, and the electronic wave functions are expanded in terms of a discrete plane wave basis set. A plane-wave energy cutoff of 500 eV was used for all calculations. Electron exchange and correlation were treated with the generalized gradient approximation (GGA) including dispersion corrections by means of the BEEF-vdw density functional.³¹⁷

Brillouin zone sampling was performed using Monkhorst–Pack grids.³¹⁸ (3 × 3 × 1) for the Mo₂C surface. Electronic occupancies were determined according to a Gaussian Smearing with an energy smearing of 0.05 eV. Self-consistent field (SCF) calculations of the electronic structure were considered converged when the electronic energy change between two steps was below 10⁻⁵ eV. All geometries were fully optimized using an energy-based conjugate gradient algorithm until the forces acting on each atom were converged below 10⁻⁴ eV Å⁻¹. Dipole corrections were applied in the z-direction and placed in the center in the unit cell. The

energy of isolated molecules was determined by a Γ -point calculation placing each species in a box with dimensions $15 \times 15.5 \times 16 \text{ \AA}$. The climbing image nudged elastic band (CI-NEB) method with eight intermediate images was used to locate transition states (TS).³¹⁹ It was further confirmed that TS structures actually corresponded to saddle points by a frequency analysis. Normal vibration modes of adsorbed species were calculated by diagonalization of the Hessian matrix, obtained using a central finite difference approximation with displacements of 0.015 \AA in the direction of each Cartesian coordinate. All Mo and C atoms from the carbide were kept fixed during the frequency calculations of the adsorbed species. All the reported energy values in the main text correspond to Gibbs Energies at $800 \text{ }^\circ\text{C}$. The theoretical model of the (001) facet of 2D-Mo₂C was constructed as presented in Figure F.28. The experimental bulk structure of Mo₂Ga₂C was taken as a starting point. Then, the Ga atoms (in green) were removed from this structure to generate the bulk Mo₂C structure. Next, an ideal 2D-facet model for Mo₂C was obtained by selecting the inner fragment of the cell in the 001 direction (Figure F.28). This was followed by the full geometry optimization of the resulting structure. The Mo₂C (001) surface slab were taken with dimensions equal to 3×3 , using two Mo layers on the top and the bottom of the slab and one middle carbon layer. 15 \AA of vacuum were added in the direction perpendicular to the surface.

7.4. Results and discussion

7.4.1. Synthesis and characterization of silica-supported 2D-Mo₂CT_x, 2D-Mo₂C and 2D-Mo₂CO_x materials.

Multi-layered Mo₂CT_x¹²² (referred to as *m*-Mo₂CT_x) was sonicated in ethanol to yield, after centrifugation, a transparent purple colloidal solution of delaminated 2D-Mo₂CT_x flakes (Figure 7.1a and Figure F.2).²⁹¹ A dried aliquot of this solution was analyzed by transmission electron microscopy (TEM) revealing single and a few-layer thin flakes of Mo₂CT_x, the latter morphology is identified by the characteristic scrolling of edges of the few-layer thin MXene nanosheets (Figure F.3).³²⁰ The X-ray powder diffraction pattern of the dried delaminated material is typical of a layered Mo₂CT_x structure (Figure F.4).¹¹⁸ The colloidal solution of the Mo₂CT_x nanoflakes (ca. 0.15 mg mL^{-1} concentration determined by thermogravimetric analysis) was used for several consecutive incipient wetness impregnations of a SiO₂ support (Aerosil 300, calcined at $950 \text{ }^\circ\text{C}$, $194 \text{ m}^2 \text{ g}^{-1}$ surface area according to nitrogen physisorption), giving 2D-Mo₂CT_x/SiO₂ that, after drying at $100 \text{ }^\circ\text{C}$ in air, contained 0.48 wt.% Mo by elemental

analysis. TEM imaging of 2D-Mo₂CT_x/SiO₂ shows agglomerated amorphous silica grains that are homogeneously covered with thin Mo₂CT_x nanosheets (Figure 7.1b and Figure F.5). Consistent with an MXene structure, hexagonally ordered Mo atoms are observed by HR-TEM in 2D-Mo₂CT_x/SiO₂ (Figure F.5). The X-ray powder diffraction pattern of 2D-Mo₂CT_x/SiO₂ reveals only an amorphous halo corresponding to SiO₂ (Figure F.6). The absence of crystalline peaks of *m*-Mo₂CT_x confirms a high dispersion of individual delaminated Mo₂CT_x nanosheets on the support.

Next, we fitted the experimentally acquired Fourier-transformed Mo K-edge EXAFS functions of 2D-Mo₂CT_x/SiO₂ with two coordination spheres, i.e. Mo–C/O/OH and Mo–Mo. The fitting of the first coordination sphere of Mo gives two scattering paths with interatomic distances of 1.74(1) and 2.03(1) Å and coordination numbers (CN) of 1.0(2) and 1.2(3), respectively (Table 7.1, Figure F.12). The shorter scattering path is attributed to molybdenum oxo (Mo=O) surface sites since the fitted distance 1.74(1) Å is in good agreement with the reported Mo=O bond lengths of ca. 1.7 Å found in a molybdenum oxycarbide in a zeolite structure²⁸³ as well as in molecular Mo complexes³²¹⁻³²² (determined by EXAFS and X-Ray crystallography, respectively). The second scattering path of the first coordination shell with an interatomic distance of 2.03(1) Å is attributed to the Mo–C and Mo–O bonds where O belongs to a hydroxy surface termination site and C is the interlayer carbidic carbon, consistent with the 2.1 Å Mo–C distance in the parent *m*-Mo₂CT_x.¹²² The second Mo coordination sphere is fitted with three Mo–Mo scattering paths with interatomic distances of 2.63(1), 2.92(2) and 3.42(2) Å and with coordination numbers of 0.8(4), 1.4(5) and 1.1(4), respectively (Table 7.1, Figure F.12). The presence of three different Mo–Mo paths indicates a strong distortion of Mo sites in silica-supported Mo₂CT_x, deviating notably from the Mo coordination environment in parent *m*-Mo₂CT_x that features only two Mo–Mo paths at 2.9 Å and 3.2 Å with coordination numbers of 4 and 2, respectively (as determined by EXAFS).¹²² This deviation is likely owing to (i) the higher fraction of Mo=O sites in 2D-Mo₂CT_x/SiO₂ relative to the *m*-Mo₂CT_x, (ii) a disorder of 2D-Mo₂CT_x/SiO₂ caused by the geometrical curvature of the delaminated nanosheets supported on the silica grains and (iii) the interaction with the support. All these factors could contribute to the lower total CNs of Mo in 2D-Mo₂CT_x/SiO₂ as determined by EXAFS.

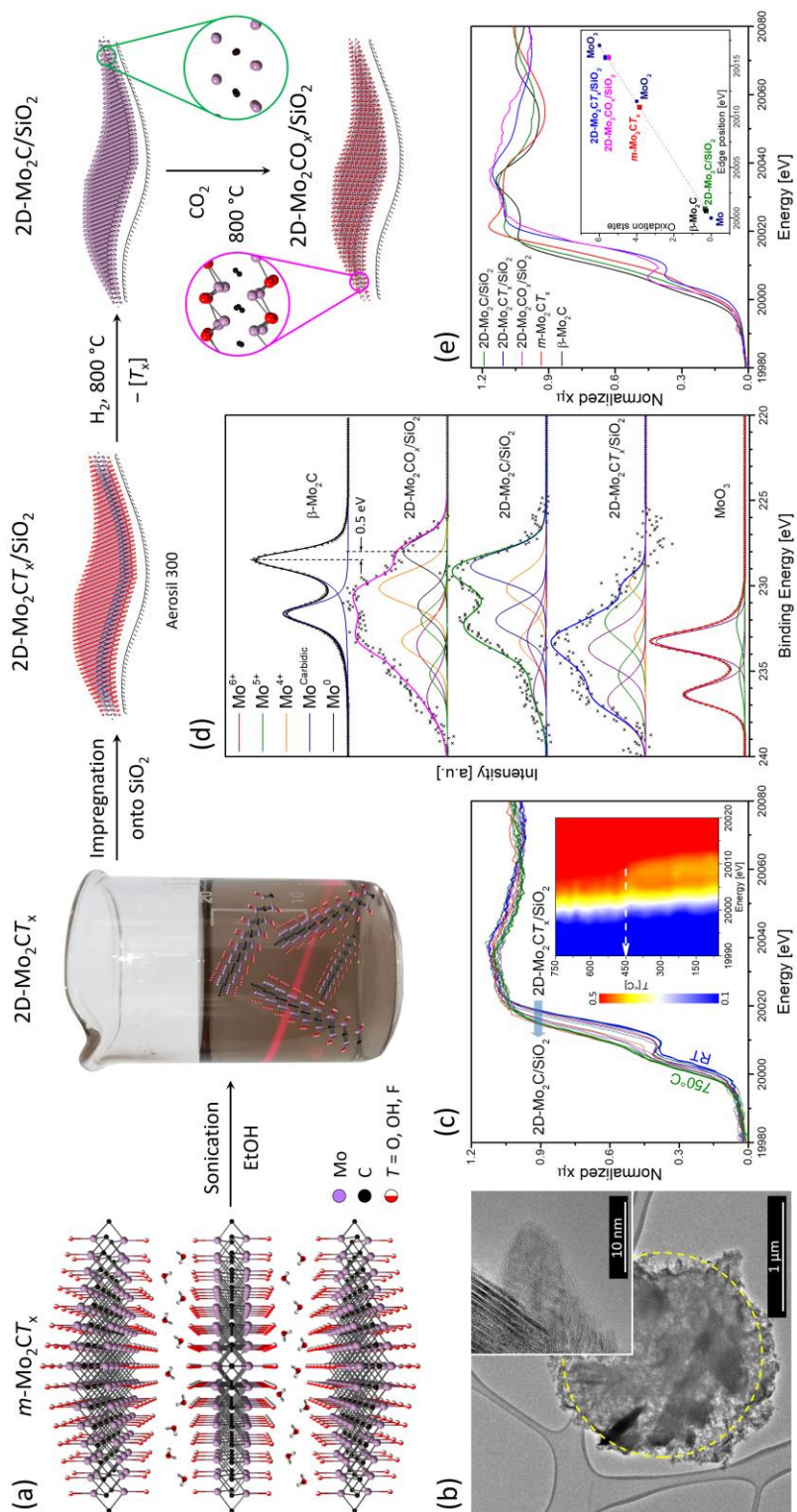


Figure 7.1. a) Synthesis of 2D-Mo₂CO_x/SiO₂ from delaminated Mo₂CT_x films *via* incipient wetness impregnation of their colloidal solution onto silica, followed by the reduction of the T_x groups under H₂ (giving 2D-Mo₂C/SiO₂) and the subsequent oxidation in CO₂ (giving 2D-Mo₂CO_x/SiO₂); b) TEM images of 2D-Mo₂CT_x/SiO₂; c) *in situ* reduction of 2D-Mo₂CT_x/SiO₂ under H₂ as followed by Mo K-edge XANES revealing an evolution of the pre-edge feature with temperature (shown in the inset as a contour plot); d) oxidation state of Mo in reference and synthesized materials determined from the deconvolution of *ex situ* XPS data of the Mo 3d core levels as well as from e) the edge position in XANES spectra.

Table 7.1. EXAFS fitting of 2D-Mo₂CT_x/SiO₂ (R factor 0.008)

Shell	CN	R (Å)	σ ² (Å ²)	ΔE (eV)
Mo–O1	1.0(2)	1.74(1)	0.005(2)	6(2)
Mo–C/O2	1.2(3)	2.03(1)		
Mo–Mo1	0.8(4)	2.63(1)	0.006(2)	
Mo–Mo2	1.4(5)	2.92(2)		
Mo–Mo3	1.1(4)	3.42(2)		

Subsequently, we explored the transformation of these silica-supported 2D-Mo₂CT_x sheets in reductive, oxidative and DRM conditions. Note that, unless specified otherwise, all these treated materials were characterized by avoiding exposure to air, using *in situ* experimentation, gloveboxes and air-tight transfers for characterization (XPS, IR, TEM and XANES). Reductive de-functionalization of 2D-Mo₂CT_x/SiO₂ from the passivating T_x surface groups was first studied in H₂ flow by *in situ* XANES (Mo K-edge, Figure 7.1c). Interestingly, in contrast to the bulk Mo₂CT_x,¹²² a well-defined pre-edge feature, typical for molybdenum in a non-centrosymmetric environment,²⁸⁰⁻²⁸¹ appears in the room temperature XANES spectrum of 2D-Mo₂CT_x/SiO₂ (Figure F.13). Under H₂ flow and with increasing temperature (*in situ* XANES experiment), the Mo K-edge in 2D-Mo₂CT_x/SiO₂ shifts to lower energies and this process continues up to ca. 450 °C (from 20015.8 to 20002.0 eV), indicating a gradual reduction of Mo due to the de-functionalization of the T_x groups (Figure 7.1c). Simultaneously, the intensity of the characteristic pre-edge feature of 2D-Mo₂CT_x/SiO₂ reduces until its disappearance at ca. 450 °C. Increasing the temperature further to 750 °C induces only a minor shift of the Mo K-edge position compared to 450 °C, that is from 20002.0 to 20000.8 eV, the latter value is very close to the edge position of β-Mo₂C (20000.7 eV). This suggests that H₂ treatment at 750 °C leads to a Mo terminated carbidic surface predominantly free from oxo, hydroxy and fluoro terminations, supporting the assignment of the aforementioned pre-edge feature to molybdenum sites in 2D-Mo₂CT_x/SiO₂ as opposed to MoO₂ or MoO₃ (conceivable oxidation products of 2D-Mo₂CT_x). Noteworthy, the temperature for the de-functionalization of most of the T_x groups in 2D-Mo₂CT_x/SiO₂ (according to XANES) is approximately 450 °C, which is 150 °C lower than that of *m*-Mo₂CT_x,¹²² probably owing to

the high dispersion of the 2D-Mo₂CT_x sheets on the silica surface that eliminates gas diffusion limitations in the pores of *m*-Mo₂CT_x.

Since the DRM reaction typically requires high temperatures to yield high equilibrium conversions (> 700 °C),⁷¹ 2D-Mo₂CT_x/SiO₂ was treated in a H₂ flow at 800 °C for 1 h to obtain 2D-Mo₂C/SiO₂. This high temperature, reductive treatment did not affect significantly the original morphology and high dispersion of the silica-supported nanosheets, as confirmed by TEM imaging (Figure F.8). That said, in few cases small nanoparticles (ca. 2-3 nm) decorating molybdenum carbide sheets could be discerned in TEM images (Figure F.8) possibly due to the partial sintering of 2D-Mo₂C sheets to Mo₂C nanoparticles at areas where nanosheets overlap. Overall, 2D-Mo₂CT_x/SiO₂ behaves very differently in reductive de-functionalization conditions when compared to *m*-Mo₂CT_x that sinters under these conditions forming a porous bulk β-Mo₂C phase.¹²² Similarly, a multi-layer *m*-V₂CT_x was reported to sinter around 600 °C, which appears to be a general temperature limitation of multi-layer MXenes.³²³ These results underline the importance of the dispersion of the nanosheets on a support to avoid sintering. Next, we prepared silica-supported model 2D molybdenum oxycarbide 2D-Mo₂CO_x/SiO₂ by treating 2D-Mo₂C/SiO₂ in a flow of CO₂ (800 °C, 1 h, Figure 7.1a). According to TEM, the CO₂ treatment of 2D-Mo₂C/SiO₂ does not alter the morphology or dispersion of the supported nanosheets (Figure F.9).

A comparison of the Mo 3d XPS spectra of the prepared silica-supported materials and β-Mo₂C and MoO₃ references is given in Figure 7.1d. The Mo 3d spectrum of 2D-Mo₂CT_x/SiO₂ was fitted with Mo⁴⁺, Mo⁵⁺ and Mo⁶⁺ components with the latter two being the dominating oxidation states (Table F.2). In contrast, the Mo 3d spectrum of *m*-Mo₂CT_x can be fitted using only Mo⁴⁺ and Mo⁵⁺ components (Table F.2)¹²² indicating that Mo sites are more oxidized in the silica-supported delaminated Mo₂CT_x nanosheets than in *m*-Mo₂CT_x. In contrast, the Mo 3d XPS spectrum of 2D-Mo₂C/SiO₂ is described by mostly carbidic Mo sites in addition to a smaller fraction of Mo⁴⁺ and Mo⁶⁺ sites (Table F.2). To understand better the nature of the Mo⁴⁺ and Mo⁶⁺ sites, observed by XPS of the reduced materials, 2D-Mo₂C/SiO₂ was analyzed by transmission IR spectroscopy revealing a low intensity band at ca. 2290 cm⁻¹ that is tentatively assigned to surface [≡Si-H] sites (Figure F.15). We speculate that the high temperature H₂ treatment of 2D-Mo₂CT_x/SiO₂ may give molybdenum hydrides (carbidic or oxycarbidic) that further react by opening the siloxane bridges of silica forming [Mo-O_s] and

[≡Si–H] bonds (Figure F.15, inset). Such reactivity has been observed previously for surface hydrides of tantalum that cleaved siloxane bridges of silica.³²⁴ Therefore Mo⁴⁺ sites in 2D-Mo₂C/SiO₂ are likely formed due to the grafting³²⁵ of the reduced nanosheets onto the silica surface.

Interestingly, the fitting of the 3d XPS spectrum of Mo in 2D-Mo₂CO_x/SiO₂ requires 4 components, namely Mo⁶⁺, Mo⁵⁺, Mo⁴⁺ and metallic Mo⁰ (Table F.2). Note that Mo⁰ is not observed in the XPS spectra of 2D-Mo₂C/SiO₂ and 2D-Mo₂CT_x/SiO₂. We rationalize this result by a partial removal of the carbidic carbon from the 2D-Mo₂C layer by CO₂ at 800 °C (forming 2 equiv of CO) and attribute the presence of the Mo⁶⁺ component in the fit to the oxygen-rich oxycarbide phase of 2D-Mo₂CO_x/SiO₂. In contrast, heating multi-layer *m*-Mo₂CT_x in a CO₂ flow transforms it into a mixture of β-Mo₂C and MoO₂ already at ca. 550 °C, according to our *in situ* XRD experiment (Figure F.16). This result underlines again that dispersion and isolation of MXene nanosheets on a support is a critical step, prior to high temperature treatments in both reducing and oxidizing conditions, to retain the nanosheet morphology of the (oxy)carbide phase. In a sharp contrast to the stability of 2D-Mo₂CO_x/SiO₂ in an atmosphere of pure CO₂ at 800 °C, other supported Mo₂C-based catalysts yield MoO₂ already in CO₂-rich DRM feeds, which is the main deactivation pathway of these catalysts.^{97,261}

Next, *ex situ* Mo K-edge XANES spectra of 2D-Mo₂CT_x/SiO₂, 2D-Mo₂C/SiO₂ and 2D-Mo₂CO_x/SiO₂ were compared (Figure 7.1e). Note that the edge position is defined as the first inflection point of the XANES spectra after the pre-edge feature (where the pre-edge corresponds to the forbidden 1s-4d transition).²⁸¹ In agreement with XPS results, 2D-Mo₂CT_x/SiO₂ features an edge position at 20015.8 eV that is notably higher than in *m*-Mo₂CT_x (20010.9 eV) indicating more oxidized Mo sites in supported Mo₂CT_x nanosheets.¹²² The observed Mo edge energy is consistent with an average oxidation state of 2D-Mo₂CT_x/SiO₂ of ca. +5.5 (Figure 7.1e, inset and Table F.1). The reduction of 2D-Mo₂CT_x/SiO₂ to 2D-Mo₂C/SiO₂ in H₂ leads to the disappearance of the pre-edge feature, as was also observed in the *in situ* XANES reduction experiment, and shifts the Mo edge positions significantly to lower energies, i.e. from 20015.8 to 20000.8 eV. While the Mo K-edge position confirms the carbidic nature of 2D-Mo₂C/SiO₂, the white line region of the XANES spectrum of 2D-Mo₂C/SiO₂ differs from the spectrum of bulk β-Mo₂C (Figure 7.1e) owing to the different morphologies of these two materials. This observation corroborates

the results of TEM analysis and confirms further that sintering to the bulk carbide phase did not occur during the reductive treatment of 2D-Mo₂CT_x/SiO₂. Consistent with XPS analysis, the XANES spectrum of 2D-Mo₂CO_x/SiO₂ reveals a significant shift of the Mo K-edge towards higher energies compared to 2D-Mo₂C/SiO₂ (i.e. 20015.7 vs 20000.7 eV), suggesting an average Mo oxidation state for 2D-Mo₂CO_x/SiO₂ between Mo⁵⁺ and Mo⁶⁺ (Figure 7.1e inset, Table F.1). The XANES spectrum of 2D-Mo₂CO_x/SiO₂ displays a characteristic pre-edge feature, similarly to 2D-Mo₂CT_x/SiO₂. We conclude that all available characterization data (XANES, XPS, TEM) are consistent with a predominantly nanosheet morphology and a carbidic and oxycarbidic nature of, respectively, 2D-Mo₂C/SiO₂ and 2D-Mo₂CO_x/SiO₂.

7.4.2. Correlating catalytic activity of 2D-Mo₂CO_x/SiO₂ in DRM to the oxygen coverage of its surface.

The catalytic activities of 2D-Mo₂C/SiO₂ and 2D-Mo₂CO_x/SiO₂ for the dry reforming of methane (800 °C, 1 bar, SV 1200 L g_{Mo}⁻¹ h⁻¹, W/F = 3 ms g_{Mo} mL⁻¹ contact time, 1 : 1 CO₂ : CH₄ ratio) are strikingly different (Figure 7.2a). While 2D-Mo₂C/SiO₂ shows negligible DRM activity, 2D-Mo₂CO_x/SiO₂ is highly active with methane conversion rates of 0.42 mol(CH₄) mol(Mo)⁻¹ s⁻¹ after 10 min on stream at 80 % CH₄ conversion (i.e. ca. 10 % below the thermodynamic equilibrium in those conditions, Figure 7.2a).⁷¹ Note that the 2D nature of our catalysts enables a very high utilization of Mo such that when normalized by weight of Mo, the initial methane consumption rate of 2D-Mo₂CO_x/SiO₂ is approximately 10-200 times higher than the rates that have been reported for other Mo₂C-based catalysts at similar conditions (Table F.3). The reference catalysts β-Mo₂C and *m*-Mo₂CT_x exhibit a significantly lower DRM activity in these conditions (ca. 0.0003 and 0.002 mol(CH₄) mol(Mo)⁻¹ s⁻¹ after ca. 5 min of time in stream, respectively), and deactivated entirely after 30 min of reaction (Figure F.17). The CO chemisorption capacity was determined for *in situ* reduced 2D-Mo₂CT_x/SiO₂ and the reference β-Mo₂C catalysts in order to establish if the superior catalytic performance of 2D-Mo₂CT_x/SiO₂ with respect to β-Mo₂C (normalized per mass of Mo) is due to the improved utilization of Mo atoms in the 2D-nanosheet catalyst, or due to a higher activity of the Mo sites in 2D-Mo₂CT_x/SiO₂ owing to their different structure and/or morphology, or a combination of these factors. Our results show that the estimated areal CO capacity in 2D-Mo₂CT_x/SiO₂ and the reference β-Mo₂C catalysts are nearly the same (ca. 0.2 and 0.25-0.5 μmol m⁻², respectively; see Table F.4 and ESI for details). However, the

measured methane conversion rate is ca. 3 orders of magnitude higher for 2D-Mo₂C_{T_x}/SiO₂ relative to the β-Mo₂C catalyst. These results provide strong evidence that the improved catalytic activity is due to the different nature of Mo sites in 2D-nanosheet catalyst.

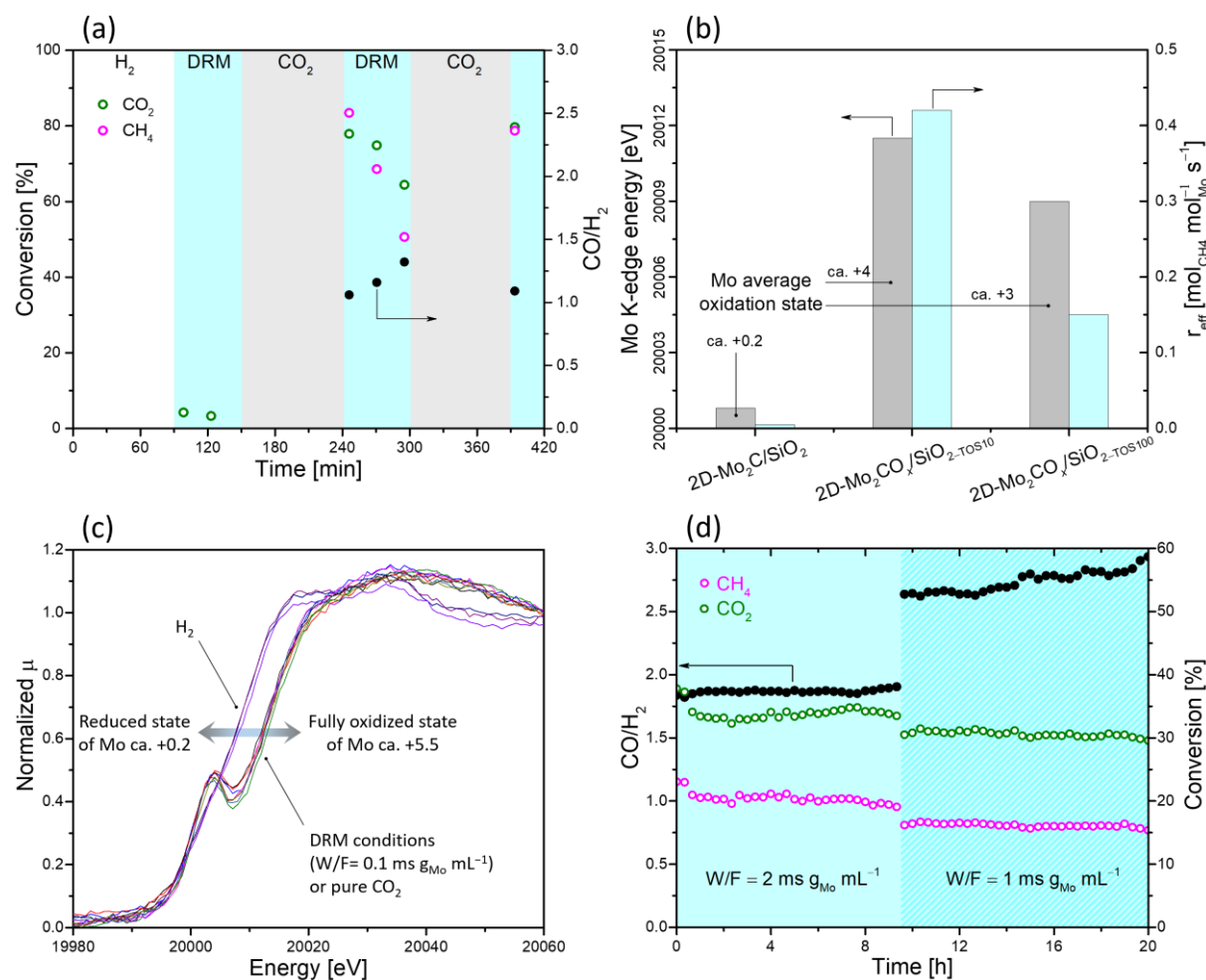


Figure 7.2. a) Catalytic performance of 2D-Mo₂C/SiO₂ (90 to 150 min) and 2D-Mo₂CO_x/SiO₂ (240 to 300 min and from 390 min after the CO₂ regeneration step) in DRM at a contact time (W/F) of 3 ms g_{Mo} mL⁻¹; b) correlation of the Mo oxidation state, determined by Mo K-edge XANES, and the catalytic activity of the material; c) Mo K-edge XANES spectra of 2D-Mo₂CO_x/SiO₂ when exposed to DRM (0.1 ms g_{Mo} mL⁻¹ contact time), reductive and oxidative conditions at 730 °C; d) stable performance of 2D-Mo₂CO_x/SiO₂ at contact times of 1 or 2 ms g_{Mo} mL⁻¹.

When using a CH₄ : CO₂ feed ratio of 1 : 1 and a contact time of 3 ms g_{cat} L⁻¹, 2D-Mo₂CO_x/SiO₂ continuously deactivates, with the methane consumption rate dropping within 100 min on stream by almost a factor of three to 0.15 mol(CH₄) mol(Mo)⁻¹ s⁻¹. At this point, the CH₄ conversion has declined from ca. 80 to 30 %. However, the initial activity can be fully regenerated by subjecting the catalyst, after 100 min time in stream (TOS), to a flow of pure CO₂ at 800 °C for 1 h. While carbide catalysts are generally not known for deactivation

by coking,¹⁰ we evaluated the possible deposition of carbon during the DRM catalytic test in a TPO-TGA experiment with a simultaneous detection of the off gas by MS (Figure F.19). Noteworthy, no increase in the intensity of the CO₂ peak was observed for the used 2D-Mo₂CO_x/SiO_{2-TOS10} and 2D-Mo₂CO_x/SiO_{2-TOS100} catalysts (note: these materials remained light grey before and after catalytic testing). Consistent with this, 2D-Mo₂CO_x/SiO_{2-TOS10} and 2D-Mo₂CO_x/SiO_{2-TOS100} did not lose any weight during the TPO experiment. Thus, TPO data provide strong evidence that no detectable carbon deposition occurred on 2D-Mo₂CO_x/SiO₂ under the experimental conditions of the DRM tests.

While the activation of metallic DRM catalysts by CO₂ treatment has been reported before,³²⁶ in particular through the removal of deposited carbon by gasification,³²⁷ the reactivation of carbide-based DRM catalysts by CO₂ is, to the best of our knowledge, unprecedented and remarkable given that Mo₂C-based catalysts for DRM are typically oxidized by CO₂ yielding inactive MoO₂.^{97,100} Note that the reference materials could not be reactivated in CO₂, which is explained by the formation of MoO₂ layer covering the active phase (Figure F.18). We hypothesized that the deactivation of 2D-Mo₂CO_x/SiO₂ with time on stream (Figure 7.2a) occurred due to a continuous depletion of the oxygen coverage of the CO₂-activated molybdenum oxycarbide surface. Therefore, to relate the decrease of the catalytic performance of our Mo oxycarbide catalyst to the oxidation state of Mo, 2D-Mo₂CO_x/SiO₂ that has been exposed for 10 or 100 min to DRM conditions was analyzed by XPS and XANES. The deconvolution of the Mo 3d spectrum of 2D-Mo₂CO_x/SiO_{2-TOS10} reveals Mo⁶⁺, Mo⁵⁺, Mo⁴⁺ and carbidic Mo states with Mo⁴⁺ being the main component at 41 % (Table F.2). Note that metallic Mo is absent in the fit of 2D-Mo₂CO_x/SiO_{2-TOS10} in contrast to 2D-Mo₂CO_x/SiO₂ discussed above. This might be due to the facile carburization of Mo⁰ with time on stream or the removal of volatile Mo carbonyl species. The deconvolution of the Mo 3d spectrum of 2D-Mo₂CO_x/SiO_{2-TOS100} reveals the same oxidation states as those found in 2D-Mo₂CO_x/SiO_{2-TOS10} (Mo⁶⁺, Mo⁵⁺, Mo⁴⁺ and carbidic states, Figure F.22). However, carbidic Mo is the main component in 2D-Mo₂CO_x/SiO_{2-TOS100} with a fitted fraction of 45 % (Table F.2). This comparison of 2D-Mo₂CO_x/SiO₂ after 10 or 100 min of TOS clearly points at a reduced surface oxygen coverage and therefore a higher fraction of carbidic Mo in the less active catalyst, namely 2D-Mo₂CO_x/SiO_{2-TOS100}. Noteworthy, similarly to the as prepared 2D-Mo₂CT_x/SiO₂, the XRD pattern of 2D-Mo₂CO_x/SiO_{2-TOS100} features no Bragg peaks thereby

further confirming that no sintering to crystalline molybdenum oxides or carbides had occurred after this time (Figure F.6).

XANES data agree well with the XPS results as the catalyst with the highest activity (2D-Mo₂CO_x/SiO_{2-TOS10}) features a Mo K-edge position at 20011.5 eV, which corresponds to an average oxidation state of Mo of +4 (Figure F.14 and Figure 7.2b). Note that the pre-edge feature in 2D-Mo₂CO_x/SiO₂ is well-defined, but poorly resolved in 2D-Mo₂CO_x/SiO_{2-TOS10}, suggesting a change in the geometry of the Mo sites due to the partial reduction during DRM conditions (Figure F.14). 2D-Mo₂CO_x/SiO_{2-TOS100} displays a Mo K-edge position at 20009.0 eV, corresponding to an average Mo oxidation state of ca. +3. This means that 2D-Mo₂CO_x/SiO₂ does not produce any measurable amount of coke when operated under a contact time of 3 ms g_{Mo} mL⁻¹ and deactivates by reduction, lowering the oxygen coverage with TOS compared to the as-CO₂-treated 2D-Mo₂CO_x/SiO₂ material. Subjecting 2D-Mo₂CO_x/SiO_{2-TOS100} to a CO₂ atmosphere (800 °C, 1 h) recovers the fully-oxidized 2D-Mo₂CO_x/SiO₂ characterized by a Mo oxidation state of ca. +5.5, that is the same as in the as-prepared 2D-Mo₂CO_x/SiO₂ material (Figure F.14). Likewise, the identical XANES spectra of 2D-Mo₂CO_x/SiO₂ prior to DRM testing and after a CO₂-based regeneration step are also in line with a fully recovered oxygen coverage after regeneration (Figure 7.2a and Figure F.14). TEM images of the regenerated material reveal that the 2D-Mo₂CO_x nanosheets have a similar morphology to the initial 2D-Mo₂CT_x nanosheets as the hexagonal ordering of the Mo atoms and the characteristic scrolling of the nanosheets at the edges are still observed (Figure F.10). Overall, these results highlight the remarkable structural stability of silica-supported 2D-Mo₂CO_x nanosheets under catalytic DRM environments as well as in an oxidative CO₂ atmosphere at 800 °C.

To further interrogate the relationship between the oxygen coverage of 2D-Mo₂CO_x/SiO₂ and the catalytic activity in DRM, an *in situ* XANES experiment was performed (BM31, ESRF)²⁷¹ in a capillary cell reactor wherein 2D-Mo₂CT_x/SiO₂ was first treated under H₂ (750 °C, 0.5 h) to prepare 2D-Mo₂C/SiO₂ followed by exposing the material to DRM conditions at 730 °C (CH₄ : CO₂ = 1 : 1, SV = 3 × 10⁴ L g_{Mo}⁻¹ h⁻¹, contact time of 0.1 ms g_{Mo} mL⁻¹). In those DRM conditions, an immediate oxidation of 2D-Mo₂C/SiO₂ to 2D-Mo₂CO_x/SiO₂ occurred as indicated by a change of the Mo oxidation state from ca. +0.2 to +5 (Mo edge positions of 20000.7 and 20014.4 eV, respectively), consistent with a high oxygen coverage of the material (Figure F.22). Monitoring the off-gas composition using a

compact GC⁶⁹ shows no catalytic activity at those high oxygen coverages of 2D-Mo₂CO_x. Hence, no reduction of 2D-Mo₂CO_x with TOS occurs at low contact times of the synchrotron experiment. The oxygen coverage of 2D-Mo₂CO_x/SiO₂ is high under those DRM conditions as a change to a CO₂ flow does not affect the XANES spectra significantly (Figure 7.2c and Figure F.23). Switching to a N₂ atmosphere and co-feeding ca. 5 % of H₂ instantly reduces Mo to the carbidic state, yielding XANES spectra similar to that of 2D-Mo₂C/SiO₂ (Figure 7.2c). However, introducing the DRM feed re-forms immediately 2D-Mo₂CO_x/SiO₂ with a Mo oxidation state of ca. +5, inactive for the DRM. The major difference between the laboratory (Figure 7.2a) and synchrotron experiments lies in the space velocity that is roughly 25 times higher in the synchrotron experiment. We conclude that while the *ex situ* XANES data associate the highest DRM activity of 2D-Mo₂CO_x/SiO₂ with an average Mo oxidation state of +4 and subsequent deactivation with TOS with the reduction of Mo, *in situ* Mo K-edge DRM experiment revealed that the oxycarbidic surface with a high oxygen coverage and an average oxidation state of +5 is inactive for DRM. The latter observation is consistent with the reduction of the average Mo oxidation state from +5.5 to +4 in 2D-Mo₂CO_x/SiO₂ within 10 min TOS in a laboratory DRM catalytic test (W/F = 3 ms g_{Mo} mL⁻¹). Note that no characteristic MoO₂ features were observed with both *ex* and *in situ* XANES spectra for the catalyst after DRM catalytic tests, indicating that 2D-Mo₂CO_x/SiO₂ does not oxidize to bulk Mo oxides in the presence of both CO₂ and H₂O (the latter, owing to the parallel RWGS reaction).

Next, we varied the contact time of the laboratory DRM experiment and found that for a contact time between 1-2 ms g_{Mo} mL⁻¹, the performance of 2D-Mo₂CO_x/SiO₂ in DRM is stable over 20 h TOS (Figure 7.2d). Note that the measured ratio of CO : H₂ of ca. 2 and 3 for, respectively, 2 and 1 ms g_{Mo} mL⁻¹, indicates that the reverse water-gas shift reaction (RWGS, CO₂ + H₂ ↔ CO + H₂O) takes place as a side reaction under these conditions. Noteworthy, the contact times associated with a stable catalytic performance are intermediate between the contact times used in the synchrotron experiment and laboratory experiments in which catalyst deactivation occurred (ca. 0.1 and 3 ms g_{Mo} mL⁻¹, respectively). This suggests that at short contact times, dissociation of CO₂ proceeds fast and yields a too high oxygen coverage of the Mo₂CO_x surface, while at high contact times CH₄ and/or DRM products (CO and H₂) deplete the surface coverage of Mo₂CO_x beyond the optimal value, leading to catalyst deactivation. Note that 2D-Mo₂CO_x/SiO₂ exhibits a high stability over 20 hours on stream at

W/F = 1-2 ms g_{Mo} mL⁻¹ despite the presence of steam produced by the competing RWGS reaction. However, while at these conditions the selectivity and catalytic activity are stable, both values are lower than the initial (viz. TOS = 10 min) activity and selectivity of 2D-Mo₂CO_x/SiO₂ at W/F = 3 ms g_{Mo} mL⁻¹ (Figure 7.2a and 7.2d). Our search for a stable catalytic performance with increased activity and selectivity as compared to conditions of W/F = 1-2 ms g_{Mo} mL⁻¹ uncovered that performing the catalytic test at a higher pressure (i.e. 8 bar instead of 1 bar) and keeping W/F = 3 ms g_{Mo} mL⁻¹ yields a CO : H₂ ratio close to 1.5 and only a slightly lower methane conversion rate as compared to that at 1 bar (0.42 vs 0.34 mol(CH₄) mol(Mo)⁻¹ s⁻¹). Thus, oxygen coverage higher than optimal (i.e. corresponding to an Mo oxidation state of +4) not only decreases the methane conversion rates, but also compromises the selectivity due to the competing RWGS reaction.

Finally, aiming to induce major structural changes in 2D-Mo₂CO_x/SiO₂, we subjected the material to three subsequent DRM-catalysis-CO₂-regeneration cycles with a total TOS of ca. 30 h using a contact time of 2 ms g_{Mo} mL⁻¹ for the DRM step (Figure F.20). Note, that the resulting material collected after the DRM step (labelled 2D-Mo₂CO_x/SiO_{2-spent}) was only partially deactivated, featuring a methane conversion rate of 0.08 mol(CH₄) mol(Mo)⁻¹ s⁻¹. Similarly to 2D-Mo₂CO_x/SiO_{2-TOS10}, deconvolution of the Mo 3d spectrum of the spent catalyst reveals Mo⁶⁺, Mo⁵⁺, Mo⁴⁺ and carbidic Mo components, with Mo⁴⁺ being the main component at 62 % (Figure F.22, Table F.2). TEM analysis of 2D-Mo₂CO_x/SiO_{2-spent} (exposed to air) reveals the presence of 2D nanosheets with a hexagonal ordering (Figure F.11) and overlapping signals of Mo, C and O in the EDX maps, confirming the oxycarbidic nature of the catalyst. Additionally, areas containing a bulk crystalline phase of MoO₂ with a distorted rutile structure were revealed by FT HR-TEM imaging (Figure F.11), in agreement with the high fraction of Mo⁴⁺ identified in the XPS fittings of this sample and its reduced activity relative to the most active 2D-Mo₂CO_x/SiO_{2-TOS10} catalyst. In agreement with TEM results, the XRD analysis of 2D-Mo₂CO_x/SiO_{2-spent} revealed very small but discernable peaks corresponding to MoO₂. That said, supported nanosheets remain the dominant morphology of the spent catalyst, underlining its remarkable stability.

7.4.3. Theoretical modelling of DRM reaction pathways on 2D-Mo₂CO_x/SiO₂.

Density functional theory (DFT) calculations provided further insight into the role of oxygen coverage for DRM activity and the energetically preferred structure of 2D-Mo₂C

nanosheets after CO₂ treatment and under DRM conditions. 2D-Mo₂C was modelled by three atomic layers, with two Mo layers exposed to reactants and a carbon layer in between these Mo layers (Figure 7.3 and Figure F.28). The stability of the orthorhombic Mo₂C and Mo₂CO_x phases have been previously evaluated by DFT calculations.^{282,328} Our evaluation of the thermodynamic stability of the different oxygen coverages of the 2D-Mo₂C slab at 800 °C under CO₂ reveals that a molybdenum oxycarbide phase with one oxygen monolayer (1 O ML) adsorbed on each of the Mo layers, i.e. 2D-Mo₂CO₂, is preferred thermodynamically (see the ESI for further details). 2D-Mo₂CO₂ is formed from 2D-Mo₂C and CO₂ that react yielding one oxygen atom chemisorbed on the carbide surface with a concomitant release of one gas-phase CO molecule. To reach this full oxygen surface coverage, 18 CO₂ molecules react per unit cell (9 CO₂ molecules per each side of the slab) in a highly exergonic reaction releasing Gibbs energy of -928 kJ mol⁻¹ per unit cell (ca. -52 kJ mol⁻¹ per CO₂ molecule). The reaction of an additional CO₂ molecule yields an overall Gibbs free energy of -903 kJ mol⁻¹, therefore this step is unfavorable and the most stable configuration corresponds to 1 O ML coverage (i.e. one oxygen atom per Mo atom on the 2D-Mo₂C surface), which is in agreement with the observed stability of 2D-Mo₂CO_x/SiO₂ in a CO₂ atmosphere at 800 °C. Under DRM conditions, the reaction of 2D-Mo₂C 1O ML with one methane molecule has favorable energetics for the formation of one CO and two H₂ gas-phase molecules, reducing thereby the surface oxygen coverage. Specifically, decreasing the oxygen coverage of 2D-Mo₂CO_x from a full coverage of 1 O ML to 0.89, 0.78 and 0.67 O ML proceeds with reaction energetics of -30, -18 and 0 kJ mol⁻¹, that is changing from exergonic to isoergonic energetics. This data confirm that the full coverage of the surface by 1 O ML is thermodynamically unstable under DRM conditions, as observed experimentally.

In the following, we selected 2D-Mo₂CO_x-0.67 O ML as a starting point to calculate the energy profile of the DRM reaction pathways since the oxygen coverage of this structure is consistent with the optimal oxygen coverage observed experimentally (characterized by an average Mo oxidation state of +4). This partial 0.67 O ML oxygen coverage allows for free reactive Mo sites on the surface. The energetic penalty to form 2D-Mo₂CO_x-0.67 O ML from 2D-Mo₂CO₂ is merely +30 kJ mol⁻¹ higher than forming the most stable oxygen coverage under the DRM conditions, i.e. 2D-Mo₂CO_x-0.88 O ML. The adsorption of CO₂ on 2D-Mo₂CO_x-0.67 O ML is endergonic by 143 kJ mol⁻¹, leading to a bent CO₂ on the Mo sites of

the oxycarbide surface. Dissociation of this bent CO_2 to adsorbed CO^* and O^* products requires 173 kJ mol^{-1} of Gibbs free energy, and is overall exergonic by 12 kJ mol^{-1} (Figure 7.3). This Gibbs energy barrier is even lower than the one obtained for a Ni(111) surface at $650 \text{ }^\circ\text{C}$ (209 kJ mol^{-1}).³²⁹ In terms of required electronic energy, CO_2 cleavage of the adsorbed, bent CO_2 intermediate has a very low energy barrier of $+31 \text{ kJ mol}^{-1}$. This bent CO_2 adsorbate was evaluated previously on several metal carbides³³⁰ and was suggested to enhance the reactivity of CO_2 on interfaces between a metal and a metal carbide³³¹ or a metal oxide.³³²⁻³³⁴ DFT calculations on the clean, Mo-terminated surface of $\delta\text{-Mo}_2\text{C}(001)$ showed that CO_2 activation on molybdenum carbides is also associated with a low activation barriers.³³⁵ In turn, the activation of CH_4 *via* C–H bond cleavage requires a higher Gibbs activation energy of 242 kJ mol^{-1} and the reaction occurs on Mo sites of the oxycarbide surface. The calculated energy barrier is comparable to the ones computed for Ni(111), Pd(111) and Pt(111) surfaces.³²⁹ Conversely, CH_4 activation on oxygen sites to form $^*\text{OCH}_3$ and $^*\text{OH}$ is endergonic by 105 kJ mol^{-1} , which is by 45 kJ mol^{-1} less favorable than CH_4 activation on the Mo sites of the same surface.

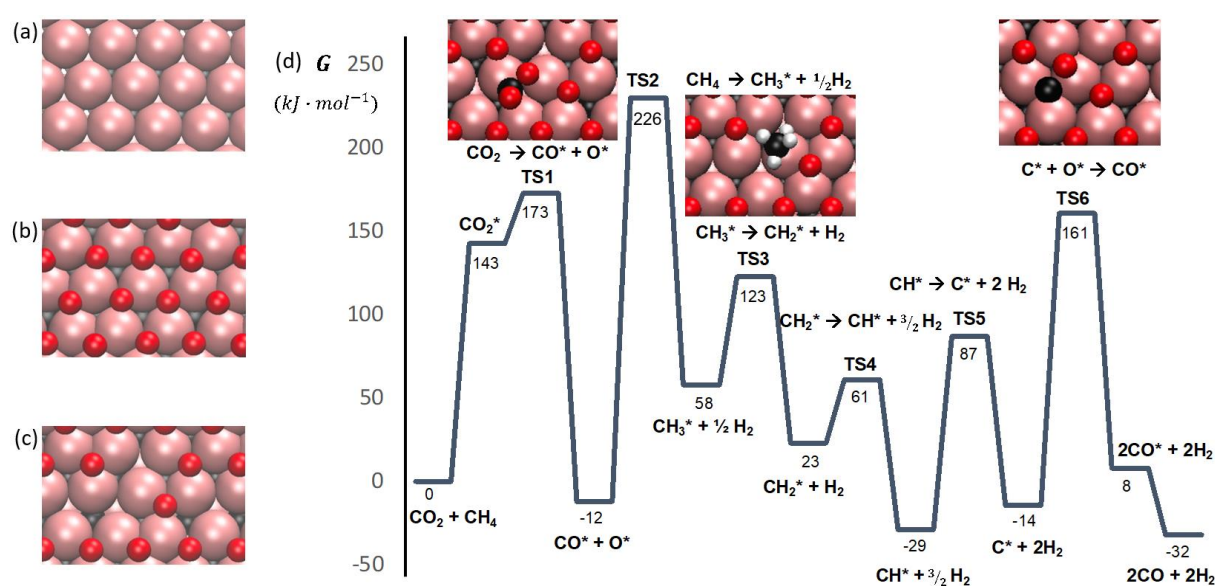


Figure 7.3. Top view of the a) clean 2D-Mo₂C, b) 2D-Mo₂C-1 O ML and c) 2D-Mo₂C-0.67 O ML surfaces. d) Gibbs free energy profile of the dry reforming of methane catalyzed by the 2D-Mo₂C-0.67 O ML surface. Gibbs energies are given with respect to initial reactants, CH₄ and CO₂, at $800 \text{ }^\circ\text{C}$ and under 1 bar pressure. For brevity, the reaction profile is presented without H–H coupling steps. The full profile is shown in Figure F.24.

Subsequent CH_3 and CH_2 activation steps to form CH_2^* and CH^* species are significantly less energy demanding than the initial C–H activation of CH_4 , with respective

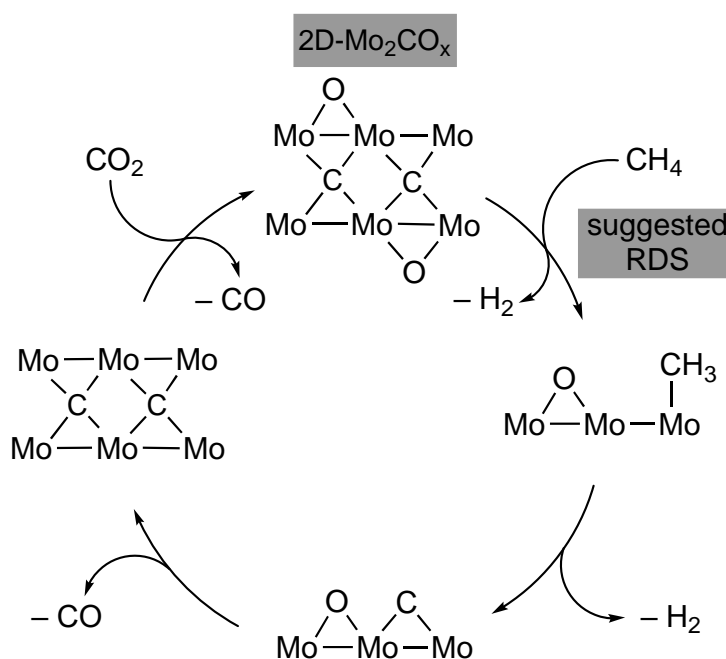
Gibbs energy barriers of 63 and 38 kJ mol⁻¹. However, the cleavage of the C–H bond in CH* to form adsorbed C and H has a high Gibbs energy barrier of 117 kJ mol⁻¹. Note that each successive C–H activation of methane generates an adsorbed hydrogen that can be released as an H₂ in a strongly entropically favored process, releasing 59 kcal mol⁻¹ at 800 °C per each desorbed H₂ molecule (Figure 7.3).

Besides the activation of CO₂ and CH₄, another key step in the dry reforming of methane is the oxidation of either CH* or C* species on the oxycarbide surface by adsorbed oxygen (O* or structural oxygen)³³⁶ ultimately producing adsorbed CO. In the case of 2D-Mo₂CO_x, and in contrast to metallic surfaces,³²⁹ the preferred mechanism is the direct oxidation of adsorbed C* by adsorbed O* to form CO*. This pathway has a Gibbs energy barrier of 175 kJ mol⁻¹, and it is endergonic by only 22 kJ mol⁻¹. The alternative pathway involving the coupling of CH* and O* to form adsorbed CHO*, followed by its decomposition to co-adsorbed CO* and H*, is less favorable (Figure F.25). Finally, desorption of CO is exergonic by 20 kJ mol⁻¹ per CO molecule. Overall, the calculated energy barriers of the proposed mechanism are feasible under the DRM conditions studied here (800 °C, CH₄ : CO₂ = 1 : 1) and are thermodynamically exergonic by 32 kJ mol⁻¹. The most energy demanding step is the initial methane activation step, which is associated with a significantly higher barrier than the direct CO₂ activation or the C–O coupling step forming CO. In addition, the relative rates for the formation and consumption of intermediate oxygen and carbon surface species, and, therefore their ratio on the 2D-oxycarbide surface, has to be similar in order to obtain a good catalytic performance. Our theoretical calculations suggest that the ratio of C* to O* is another possible factor (besides the oxidation state of Mo atoms on the surface) that can contribute to the significantly higher catalytic activity of the 2D-Mo₂C 0.67 O ML system in comparison to the clean 2D-Mo₂C surface.

We also evaluated the energy profile of the DRM reaction on a clean 2D-Mo₂C surface and found that the activation of CO₂ occurs on this surface easier than on 2D-Mo₂CO_x-0.67 O ML. The produced CO* and O* surface species are significantly more stabilized on 2D-Mo₂C compared to 2D-Mo₂CO_x-0.67 O ML, featuring a lower Gibbs energy barrier for CO₂ activation of 109 kJ mol⁻¹ (compare to 173 kJ mol⁻¹ for the 2D-Mo₂C-0.67 O ML surface). The resulting adsorbed CO* and O* species are located at -99 kJ mol⁻¹ for the clean 2D-Mo₂C surface, which is significantly lower than for the 2D-Mo₂C-0.67 O ML surface (-12 kJ mol⁻¹,

Figure F.26). That said, the free energy barrier for CH₄ activation is very similar for both surfaces (238 vs. 243 kJ mol⁻¹). Another difference with implications for the catalytic activity is the substantial stabilization of CH* and C* species on the 2D-Mo₂C surface with respect to the initial reactants. The high adsorption energy of C* and O* species lead to a significantly higher energy barrier for the C–O coupling step (+219 kJ mol⁻¹) on 2D-Mo₂C, in contrast to the respective barrier on the 2D-Mo₂CO_x-0.67 O ML surface (+175 kJ mol⁻¹). This overstabilization of CH* and C* and O* intermediates on a clean 2D-Mo₂C surface explains its lower activity for DRM. In contrast, the 2D-Mo₂CO_x-0.67 O ML surface does not bind intermediates too strongly. Scheme 7.1 summarizes our computational studies, which agree well with the experimental results discussed above.

Scheme 7.1. A Simplified Proposed Mechanism for the Dry Reforming of Methane on 2D-Mo₂CO_x.



7.5. Conclusions

We have shown that supporting and dispersing delaminated 2D-Mo₂CT_x nanosheets on silica prevents to a large extent their thermal sintering to bulk Mo₂C and MoO₂ phases, paving the way for the application of 2D Mo-carbides and oxycarbides for high temperature heterogeneous catalysis. XANES and XPS analysis indicate that oxycarbide 2D-Mo₂CO_x with an average Mo oxidation state of +4 is the active phase for DRM and oxidizing or reducing this state reduces the methane consumption rate. DFT calculations suggest that the rate-limiting

step in the DRM on 2D-Mo₂CO_x is CH₄ cleavage and that the oxygen coverage resulting from the initial CO₂ activation steps reduces the binding energy of C* and O* species and lowers in turn the energy barriers of the C–O coupling step. Importantly, when deactivation by reduction of the oxygen coverage has occurred, the catalyst can be reactivated to its initial activity by re-oxidation in a pure stream of CO₂. Noteworthy, the nanosheet morphology of 2D-Mo₂CO_x is maintained during catalysis and regeneration. In addition, we identified hydrodynamic conditions that ensured a stable performance over 20 h time on stream, owing to an *in situ* regeneration of the optimal oxygen coverage in those conditions. Overall, the results obtained indicate that supported 2D-Mo₂CO_x is a very active and robust catalyst for high temperature catalytic applications, exhibiting a remarkable stability in oxidative environments.

Chapter 8: Conclusions and Outlook

8.1. Conclusions

The work presented in this doctoral Thesis focused on the development of novel, highly effective sorbents for CO₂ capture, and catalysts for DRM. In what follows, the summary of the key conclusions of each chapter is presented.

In Chapter 2, it was demonstrated that a readily scalable wet mechanochemical activation *via* ball milling allows for the manufacture of highly effective CaO-based CO₂ sorbents. A thorough optimization of the ball-milling parameters, i.e. milling speed and duration, allowed to attain favorable particle characteristics and reduce the amount of inert stabilizer (MgO) to as little as 15 wt.%. Using electron microscopy, it was demonstrated that the effective stabilization of CaO/CaCO₃ particles against sintering was achieved by small MgO nanoparticles decorating the surface of larger CaO particles. After 30 cycles, the best CO₂ sorbent exceeded the CO₂ uptake of the reference limestone by 200 %.

In Chapter 3, it was demonstrated that the addition of an alkali-based salt, i.e. Na₂CO₃, reduces severely the CO₂ uptake performance of CaO-based CO₂ sorbents. The combination of TGA, XAS and FIB-SEM analysis allowed to attribute the degradation of the performance of Na-promoted CaO-based sorbents to the formation of Na₂Ca(CO₃)₂. During calcination, Na₂Ca(CO₃)₂ is in a molten state inducing strong sintering, which in turn results in the dramatic loss of porosity. In addition, the formation of a dense layer of Na₂Ca(CO₃)₂ covering CaO prevented its full carbonation to CaCO₃.

In Chapter 4, CaO-based CO₂ sorbents with a hierarchical porosity were prepared *via* a microfluidic emulsification technique. The sorbents were stabilized by an ALD-grown uniform Al₂O₃ coating. The materials obtained had a highly improved CO₂ uptake owing to the enhanced stability of the structural features at the meso- and micro-scale. The best-performing sorbent showed a CO₂ uptake of 0.41 g_{CO₂} g_{sorbent}⁻¹ and thus exceeded the CO₂ uptake capacity of the benchmark limestone by ca. 140 %. The high CO₂ sorption performance and the improved mass transport characteristics of the material make it a promising material for sorption-enhanced applications, e.g. to produce hydrogen.

Turning to the development of Mo₂C-based catalysts for methane reforming, a carbothermal hydrogen reduction method was utilized in Chapter 5 to produce β-Mo₂C supported on carbon spheres. The carburized material was found to be active and stable in the DRM reaction at an elevated pressure of 8 bar. The combination of advanced *in situ* XANES/XRD analysis and TEM characterization provided evidence that the catalyst in its active state contains a combination of β-Mo₂C and Mo₂C_xO_y phases. Additionally, a transformation of β-Mo₂C/C to Mo₂C_xO_y/C was found to correlate with higher rates of the competing (undesired) RWGS reaction.

In Chapter 6, a phase-pure, multi-layered Mo₂CT_x material of the MXene family was synthesized and its structural stability investigated under heating in reducing atmospheres. The layered Mo₂CT_x structure was found to be stable up to ca. 550-600 °C in a H₂ atmosphere. At higher temperatures, as soon as the surface became de-functionalized from the T_x groups, Mo₂CT_x sintered to form bulk β-Mo₂C. Mo₂CT_x showed a remarkable activity and stability for the WGS reaction with a selectivity > 99 % toward CO₂ and H₂ at 500 °C. Furthermore, at higher temperature (i.e. 500 °C), the catalytic performance of Mo₂CT_x was influenced by mass transport limitations due to the reduction of the Mo₂CT_x interlayer distance resulting from the partial de-functionalization of the surface from the T_x groups.

Finally, Chapter 7 demonstrated a strategy to exploit Mo₂CT_x at high temperature, i.e. 800 °C. It was demonstrated that the dispersion of exfoliated 2D Mo₂CT_x nanosheets on SiO₂ inhibited strongly the thermal sintering of Mo₂CT_x to bulk Mo₂C and MoO₂ phases. The combination of XANES and XPS analysis indicated that oxycarbide 2D-Mo₂CO_x with an average Mo oxidation state of +4 was the active phase for the DRM in this material. Contrary to the conventional Mo₂C-based catalysts that undergo an oxidative deactivation in CO₂-rich feeds at high temperatures, the transformation of 2D-Mo₂CO_x towards the carbide state was found to significantly reduce the methane consumption rate. However, this reductive deactivation could be reversed by re-oxidation in a stream of pure CO₂. Such oxidative treatment was found to reactivate the catalyst to its initial activity by adjusting the surface oxygen coverage while avoiding the formation of MoO₂. Moreover, the 2D (MXene) morphology of the catalyst was maintained during pretreatment, catalysis and regeneration stages, revealing a remarkable resistivity of the 2D Mo₂CO_x sheets against oxidation and sintering at high temperatures and harsh conditions.

8.2. Outlook

The results of this doctoral Thesis suggest several research questions that merit follow-up work. For instance, while Chapter 3 revealed a clear negative effect of the addition of Na_2CO_3 on the CO_2 uptake performance of CaO-based sorbent, it would be beneficial to assess further the influence of alternative Na-based salts, e.g. sodium halides, to generalize the effect of Na-doping. In particular, it would be interesting to identify counterions of Na salts that would avoid the formation of a $\text{Na}_2\text{Ca}(\text{CO}_3)_2$ phase during carbonation. Additionally, the effect of other alkali metal salts, i.e. those of Li, K, Rb and Cs, as well as their concentrations, has to be investigated systematically.

It is noteworthy that recent studies on the promotion of CaO with alkali metal salts were inspired by the positive promotion effect of molten alkali salts for MgO-based CO_2 sorbents. Therefore, it is important to mention that under the realistic carbonation conditions (i.e. $650\text{ }^\circ\text{C}$) studied in Chapter 3, Na_2CO_3 and $\text{Na}_2\text{Ca}(\text{CO}_3)_2$ are present in a solid state. In this context, it is worth exploring sorbents that are promoted with alkali metal salts that possess melting points below the carbonation temperature ($650\text{ }^\circ\text{C}$) and do not decompose up to the calcination temperature ($900\text{ }^\circ\text{C}$). Currently, it is also not clear how the presence of a molten phase during carbonation affects the performance of CaO-based CO_2 sorbents.

Finally, the high catalytic activity of $2\text{D-Mo}_2\text{CO}_x$ in the DRM and its stability in a pure CO_2 atmosphere makes such nanosheets promising materials for exploitation in the SE-SMR processes. Additionally, the high thermal stability of $2\text{D-Mo}_2\text{CO}_x$ could possibly allow the effective mitigation of sintering of CaO-based sorbents, provided that no mixed phase forms between $2\text{D-Mo}_2\text{CO}_x$ and CaO/ CaCO_3 . In this context, a combination of the most effective CaO-based sorbent obtained here and the highly active $2\text{D-Mo}_2\text{CO}_x$ catalyst could yield active and robust bi-functional materials for the SE-SMR process.

Appendices

A. Experimental setups and procedures

A.1. Ball milling

In this work, a Pulverisette 7 Premium line (Fritsch) planetary micro mill was used to prepare the CO₂ sorbents. A schematic, showing the equipment used and the operating principle of the mill are given in Figure A.1. During milling two jars rotate simultaneously with a programmable rotation speed in the range from 100 to 1100 rotations per minute. The jar and the support disc rotate in opposite directions.

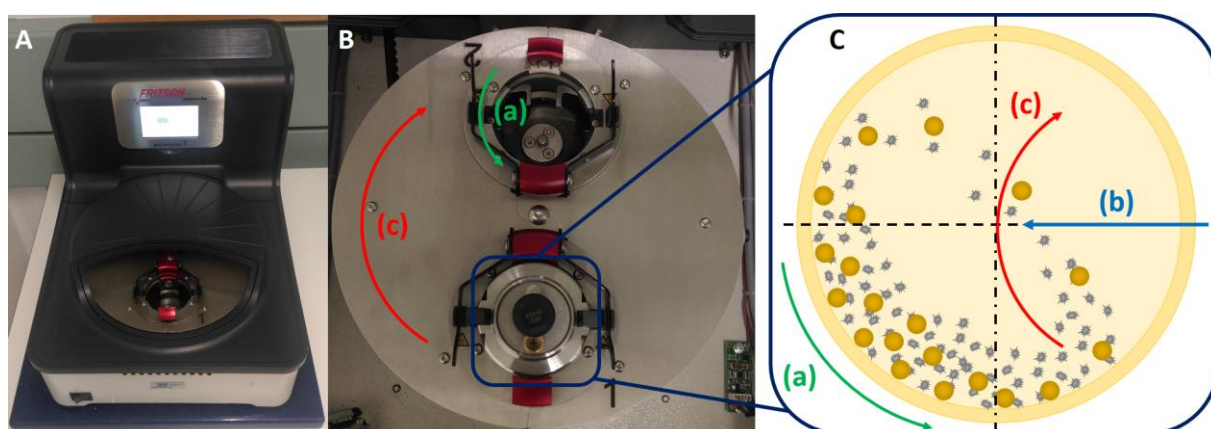


Figure A.1. (A) Pulverisette 7 Premium line planetary micro mill, (B) support disc and (C) schematic of the working principle: (a) rotation of the jar, (b) direction of the centrifugal force and (c) rotation of the support disc (adapted from the Fritsch operation manual).

In this work, 45 ml jars and 5 mm balls (both made of silicon nitride) were used. To produce fine powders each jar contained 110 balls. In all experiments, the jar was filled with 7 g of material and 10 ml of water, which is less than half of the working capacity.

A.2. Microfluidic setup

The microfluidic devices were made of glass capillaries. To build a substrate for the device, three glass slides (Micro slides, plain 75x50x1 mm, Corning) were glued together with epoxy glue (Automix 03 rapid, DELO). A squared capillary (outer diameter (OD) 1.5 mm, inner diameter (ID) 1 mm, length 150 mm, World Precision Instruments) was then glued on the substrate. Round capillaries with an outer diameter of 1 mm and an inner diameter of 580 μm (OD 1 mm, 0.5 mm, length 150 mm, World Precision Instruments) were used as inlet and collecting capillaries. The tip of the inlet capillary was produced by pulling the capillaries on a

micropipette puller (Flaming/Brown Micropipette puller P-97, Sutter Instrument Co.). The tip size was varied with a microforge (MF 830, Narishige) where the pulled tip was inserted in a molten glass ball and left to solidify. The tip was then broken in a controlled way by pulling the capillary away from the glass ball. Tip (inner) diameters in the range from 20 μm to 40 μm were used in the devices as inner inlet capillaries. The same type of capillary with a tip (inner) diameter ranging from 100 μm to 580 μm was used as a collecting one. The inlet and collecting capillaries were then aligned and glued in the squared capillary (Figure 4.1a,b). Blunt syringe tips (gauge 20, I and Peter Gonano) were glued as connectors.

Polyethylene tubes (LDPE tubing ID 0.86 mm, OD 1.32 mm, Scientific Commodities Inc.) were used to connect the syringes (1010TLL, Hamilton) containing the aqueous and the oil phase to the outer and inner inlet capillaries, respectively. Syringe pumps (PHD 2000, programmable, Harvard Apparatus) were used to achieve a precise flow rate control.

To control the droplet formation during experiment, the microfluidic device was viewed under an inverted microscope (DMI3000B, Leica) equipped with an ultrafast camera (Phantom V9.1, Vision Research Inc.). The as-produced droplets were collected at the end of the collecting capillary in vessels or on watch glasses.

A.3. X-ray diffraction

X-ray diffraction (XRD) is an important tool that is used to determine the crystal structure and phase analysis of a material. Using XRD technique qualitative and quantitative analysis of very fine-grained crystalline substances (such as minerals) can be determined on the basis of their characteristic diffraction pattern. This technique is mostly based on the interaction of the material with X-rays, which are electromagnetic radiation with very short wavelengths and high energy. In particular crystal lattice planes act as a diffraction grating for X-rays. Therefore, the X-rays interfere constructively with a given lattice plane, when Bragg's law (Eq. A.1) is satisfied,

$$n \lambda = 2d \sin\theta \quad (\text{Eq. A.1})$$

where d is the inter-planar spacing, θ - the angle between the incident X-ray and the lattice plane, n is the number describing the order of diffraction, and λ - the wavelength of the incident X-ray.

To obtain a high quality diffraction pattern, a careful sample preparation is required. First, to increase the number of particles and therefore enhances the particle statistics the analyzed powder should be grinded (ideally with ethanol). Ethanol should be used to ensure the better dispersing of the particles and to prevent the overheating of the system. In order to eliminate the peak position error and obtain sharp peaks the surface of the analyzed sample on the sample holder has to be flat. At the same time the powder should not be mechanically pressed in the sample holder as in this case a preferred orientation can be introduced.

If all the phases in a material are identified, the Rietveld refinement, a method invented by Hugo Rietveld in 1967,³³⁷ can be used to determine the composition of the material and to refine the crystal structure of the phases (e.g. lattice parameters and atomic positions). This method uses a least square approach to refine a calculated pattern until it matches the measured profile. The theoretical diffraction pattern is calculated based on crystal structures of the phases involved and instrumental parameters. Additionally, the Scherrer equation (Eq. A.2) can be applied to determine the average crystallite size (sub-micrometre) based on the broadening of a peak in a diffraction pattern.

$$\tau = \frac{K \lambda}{\beta \cos\theta} \quad (\text{Eq. A.2})$$

Where, τ is the crystallite size, K is the proportionality constant depending on the crystallite shape (with a typical value of ca. 0.9), λ is the X-ray wavelength, β is the full width at half maximum (FWHM) of the peak profile, and θ is the Bragg angle.

A.4. X-ray absorption spectroscopy

X-ray absorption spectroscopy (XAS) is a powerful analysis technique that allows to probe the electronic and structural properties of materials. In particular, it can provide information about the oxidation state, interatomic distances and the coordination number of a selected element. Importantly, XAS does not require long range periodicity and, therefore, can be applied to not only polycrystalline materials but amorphous materials, liquids and even gases. It is based on the Lambert–Beer law (Eq. A.3) describing the probability that X-rays will be absorbed while passing through the sample of thickness τ :

$$I = I_0 e^{-\mu(E)\tau} \quad (\text{Eq. A.3})$$

where I and I_0 are the intensities of the transmitted and incident X-rays, respectively and μ is the linear absorption coefficient, measured as a function of energy E . Besides the energy, absorption coefficient μ depends also on sample density the atomic number Z , and atomic mass of the element. Additionally, when the incident X-ray has an energy equal to that of the binding energy of a core-level electron, a sharp rise in absorption, referred to as absorption edge, is observed. Therefore, the fact that the energies corresponding to the absorption edge are related to the core-level energies of the atom makes XAS an element specific technique.

$$k = \sqrt{\frac{2m(E - E_0)}{\hbar^2}} \quad (\text{Eq. A.4})$$

Where, m is the electron mass, \hbar is the Planck's constant and E_0 is the binding energy of the photoelectron.

An ejected photoelectron, regarded as a spherical wave with a wave number k (Eq. A.4), propagate away from the "parent" atom and, if surrounded by neighbour atoms, can be partially scattered by each of the surrounding atoms. The interference between the outgoing wave and the back-scattered waves (one from each neighboring atom) produces the extended structure in the absorption coefficient known as EXAFS (Eq. A.5).³³⁸

$$\chi(E) = \frac{\mu(E) - \mu_0(E)}{\Delta\mu_0(E_0)} \quad (\text{Eq. A.5})$$

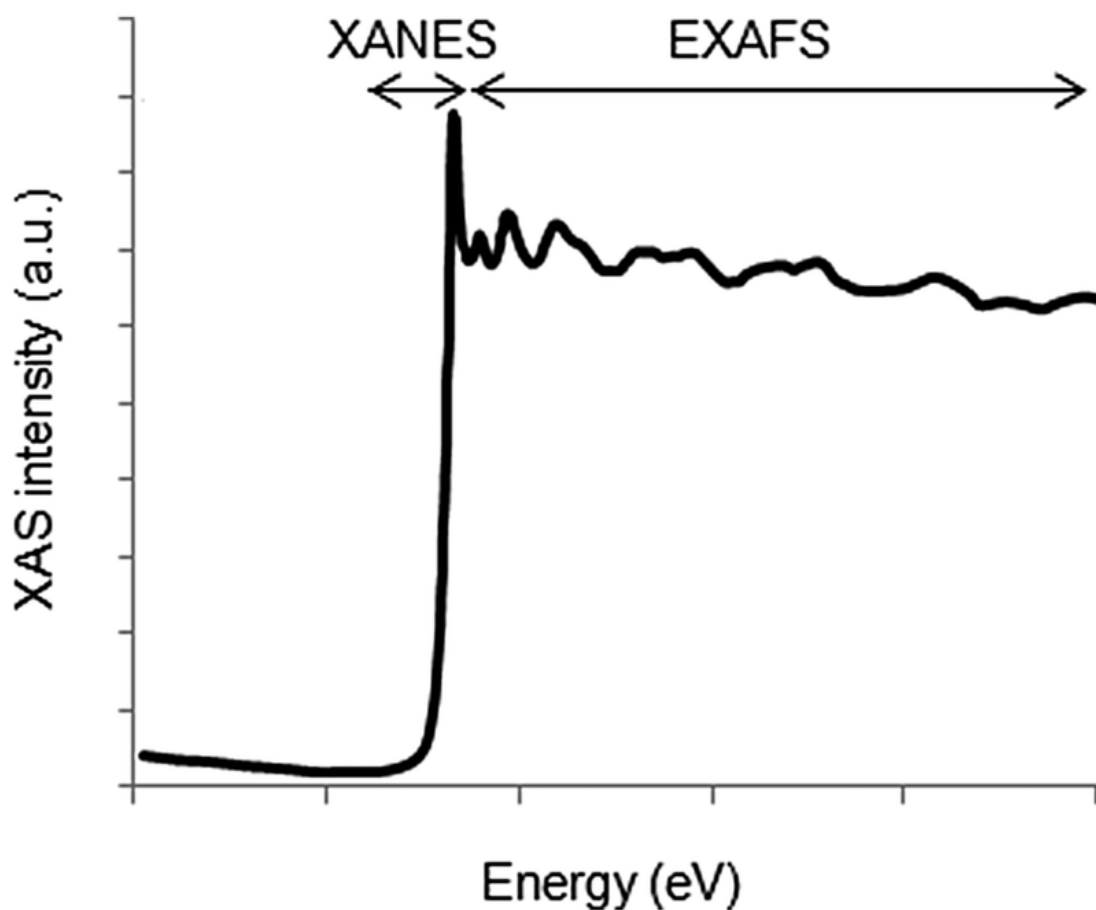


Figure A.2. XANES and EXAFS regions on a typical XAS spectrum. (Adopted from ref. ³³⁹)

Typically, the XAS spectrum is divided into two regions, i.e. X-ray absorption near edge structure (XANES) and extended X-ray absorption fine structure (EXAFS) (Figure A.2). The XANES region, describing the edge structure up to around 25 eV above the edge, provides information about the oxidation state and the site symmetry of the detecting atom. The EXAFS, in turn, describing the higher energies region, provides information regarding the absorbing atom coordination number and inter-atomic distances.

B. Supplementary information for Chapter 3

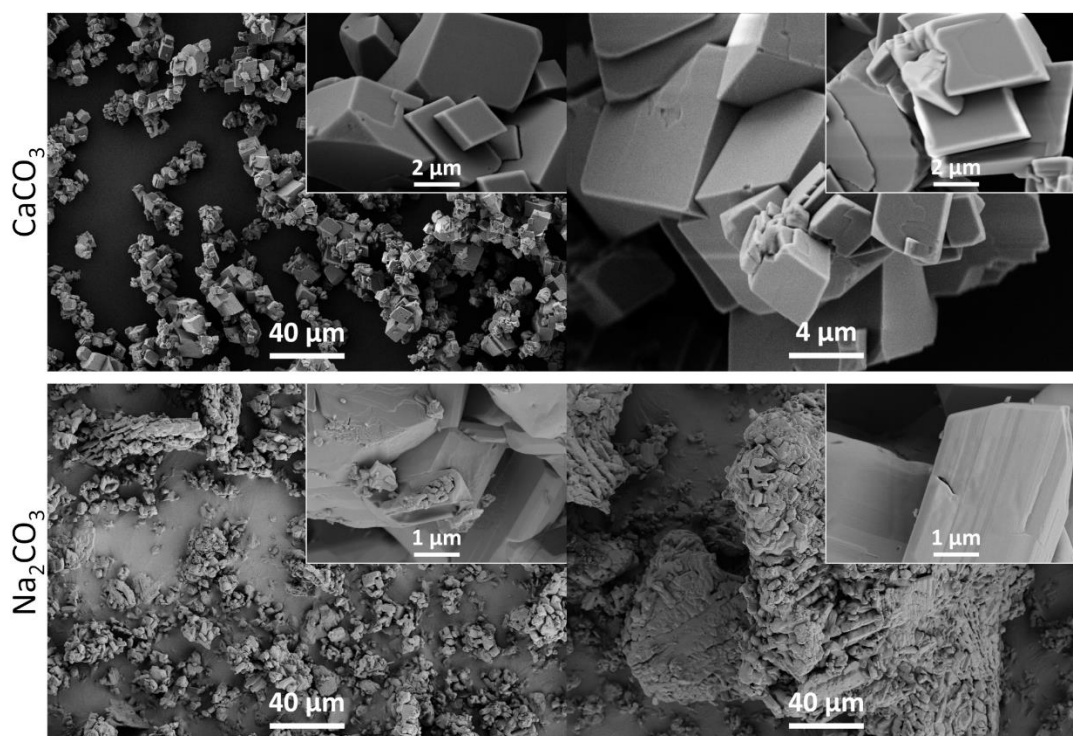


Figure B.1. SEM images of the CaCO_3 and Na_2CO_3 precursors.

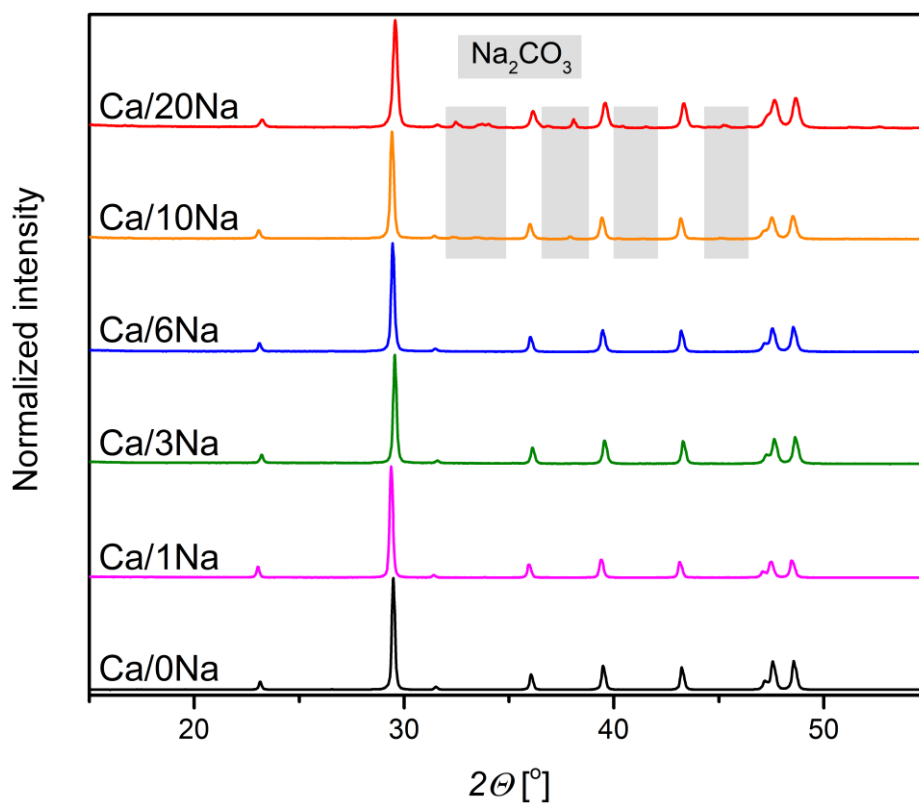


Figure B.2. XRD patterns of as prepared CaO-based sorbents.

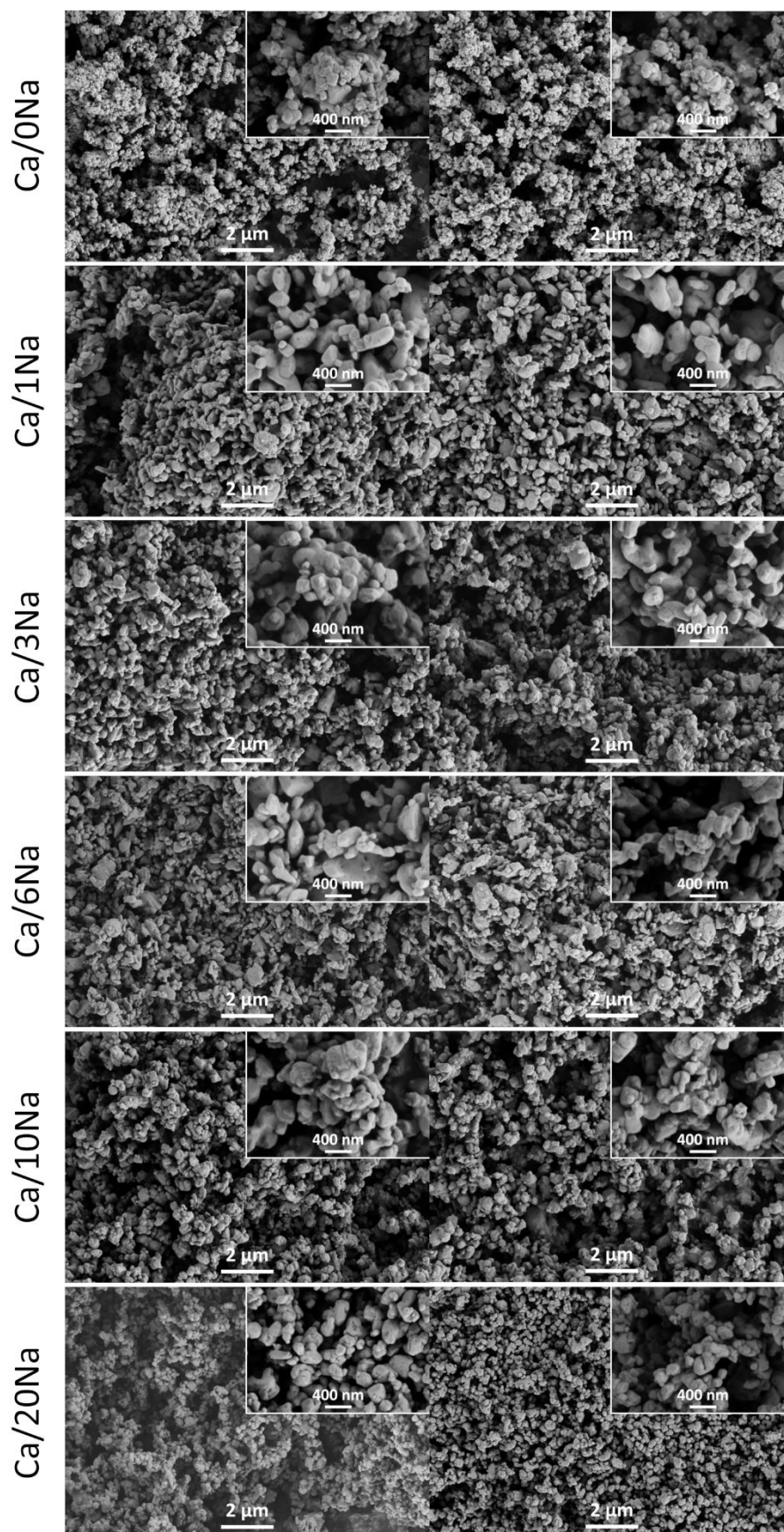


Figure B.3. SEM images of the as prepared sorbents, i.e. Ca/0Na, Ca/1Na, Ca/3Na, Ca/6Na, Ca/10Na, and Ca/20Na.

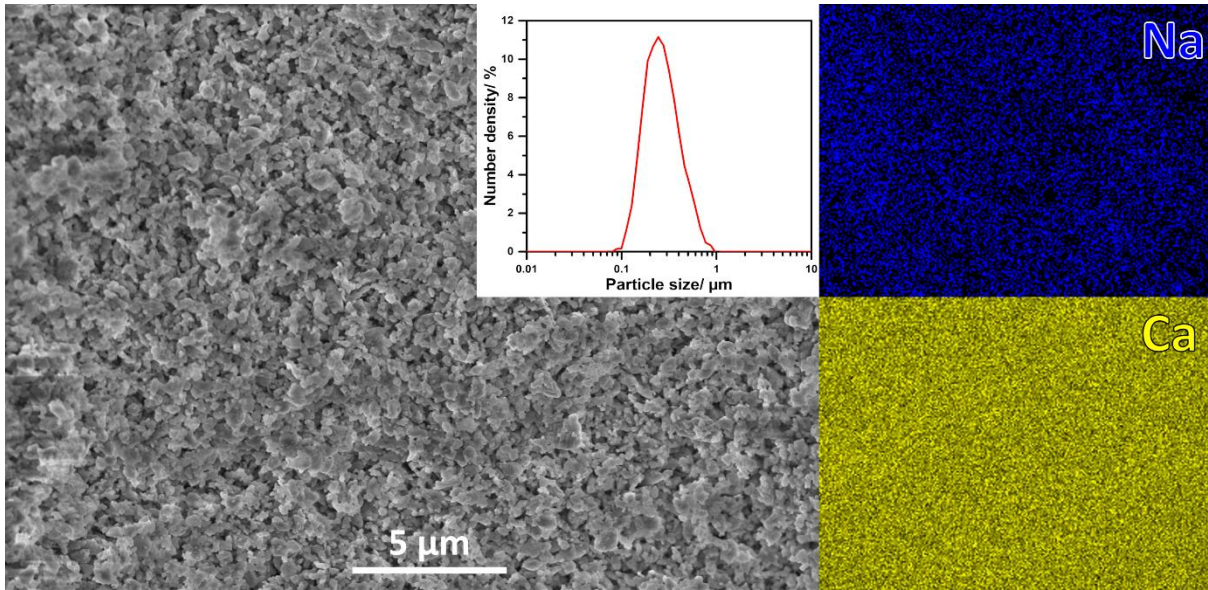


Figure B.4. SEM/EDX elemental mapping of Ca/3Na.

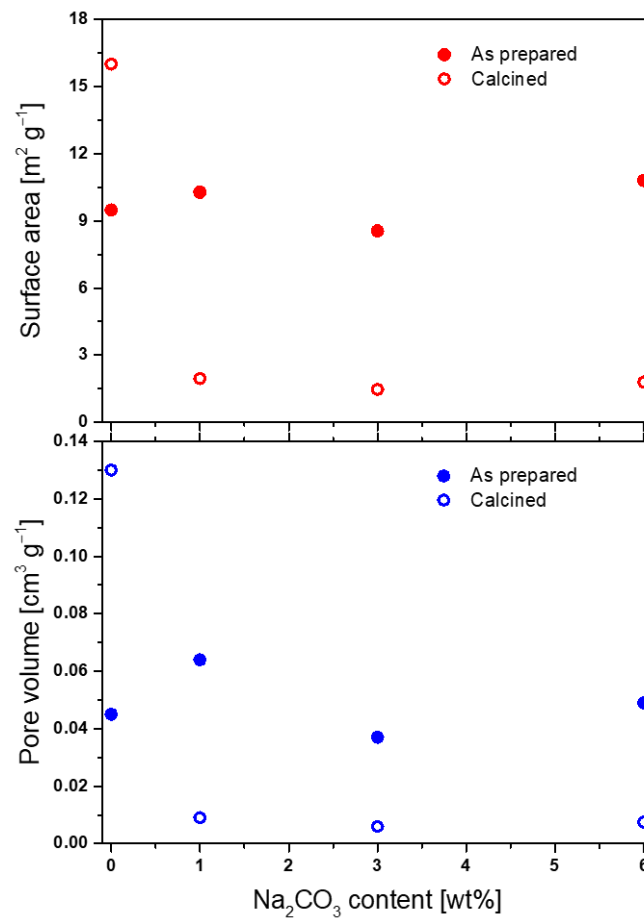


Figure B.5. BET surface area and BJH pore volume of CaO-based sorbents in the as-prepared (prior to the initial calcination) and calcined states as a function of the Na_2CO_3 content.

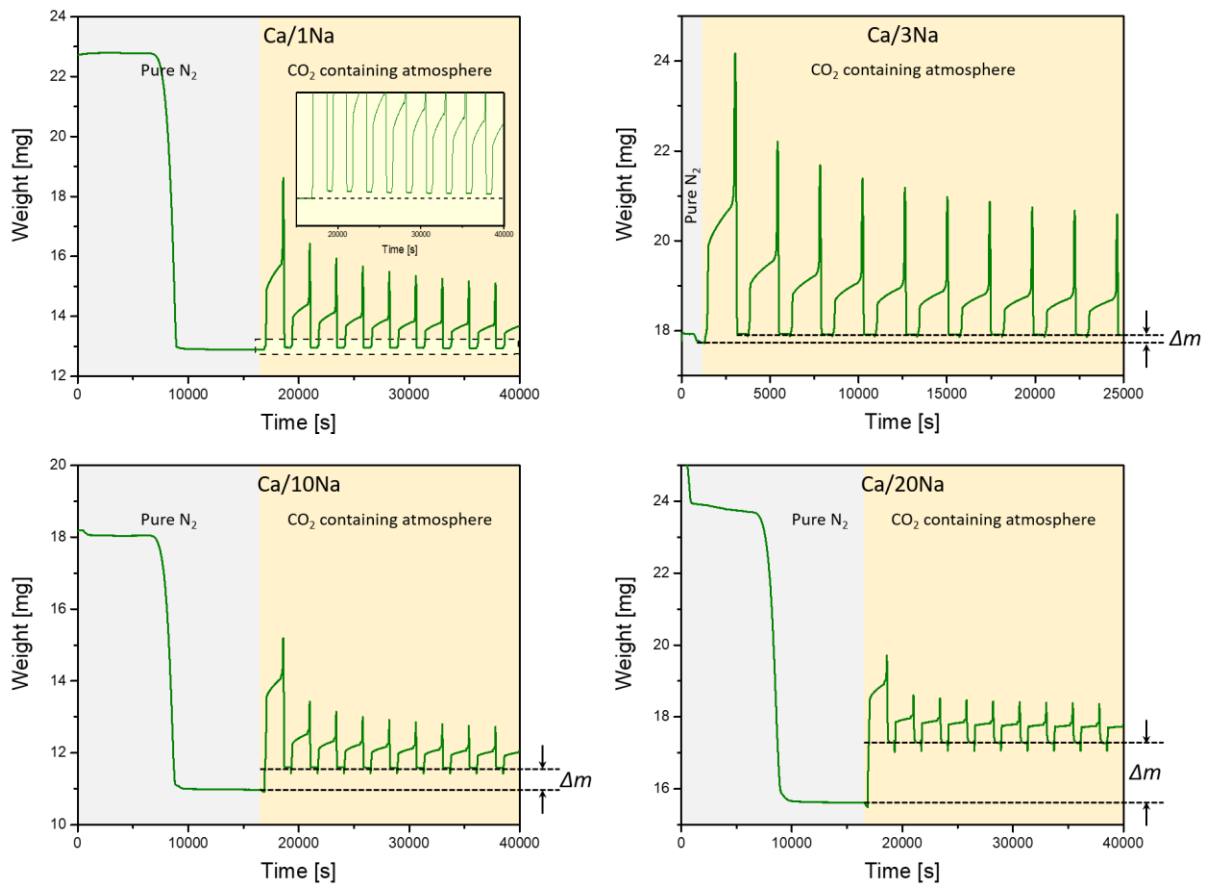


Figure B.6. CO₂ uptake profile of Ca/1Na, Ca/3Na, Ca/10Na, and Ca/20Na revealing a weight difference, Δm , when the sorbent is calcined in pure N₂ or a CO₂-rich atmosphere.

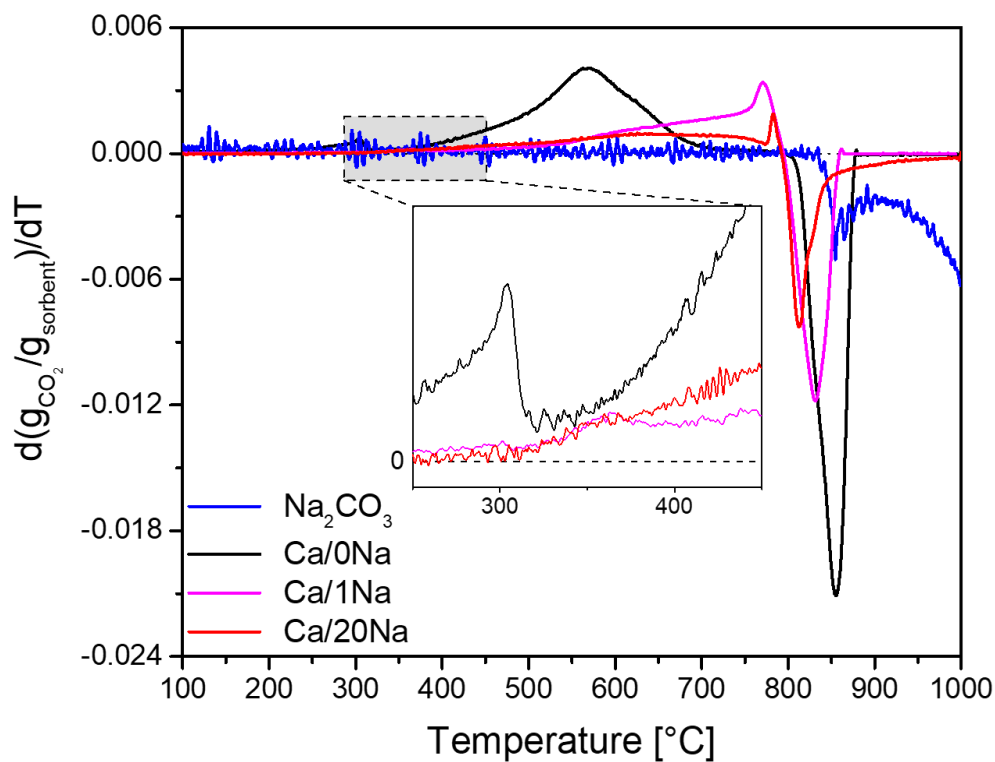


Figure B.7. TPC profiles of CaCO₃, Na₂CO₃, Ca/1Na and Ca/20Na.

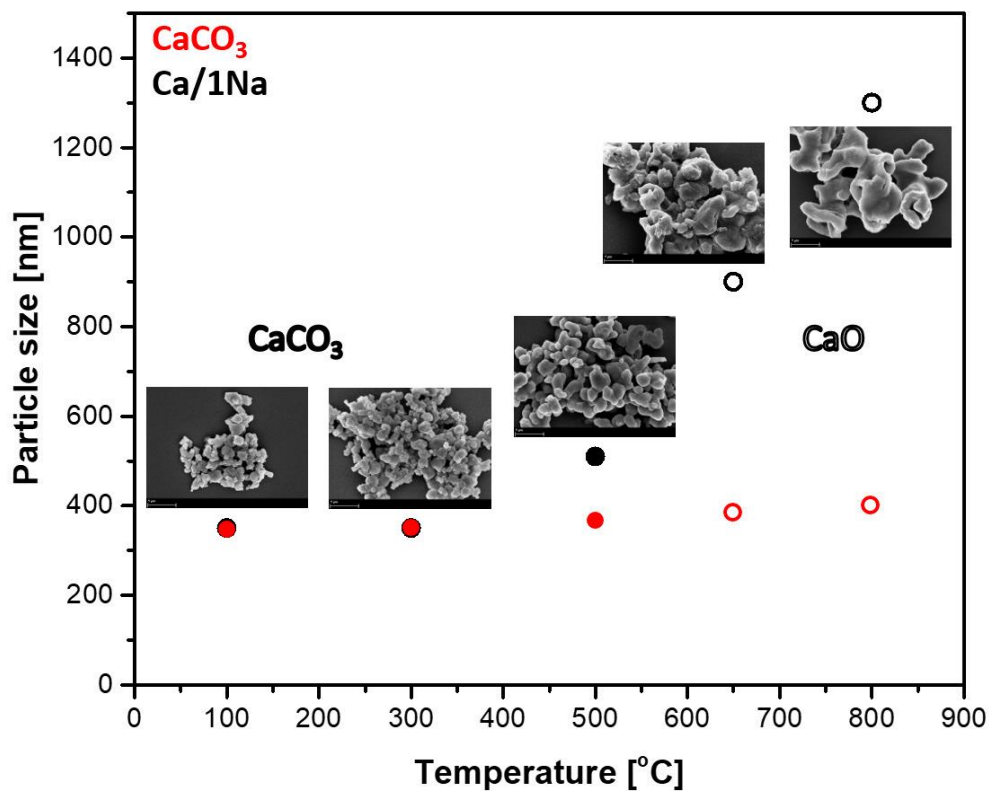


Figure B.8. Increase in particle size of CaCO₃ (red) and Ca/1Na (black) during the initial calcination step in N₂ as a function of the calcination temperature.

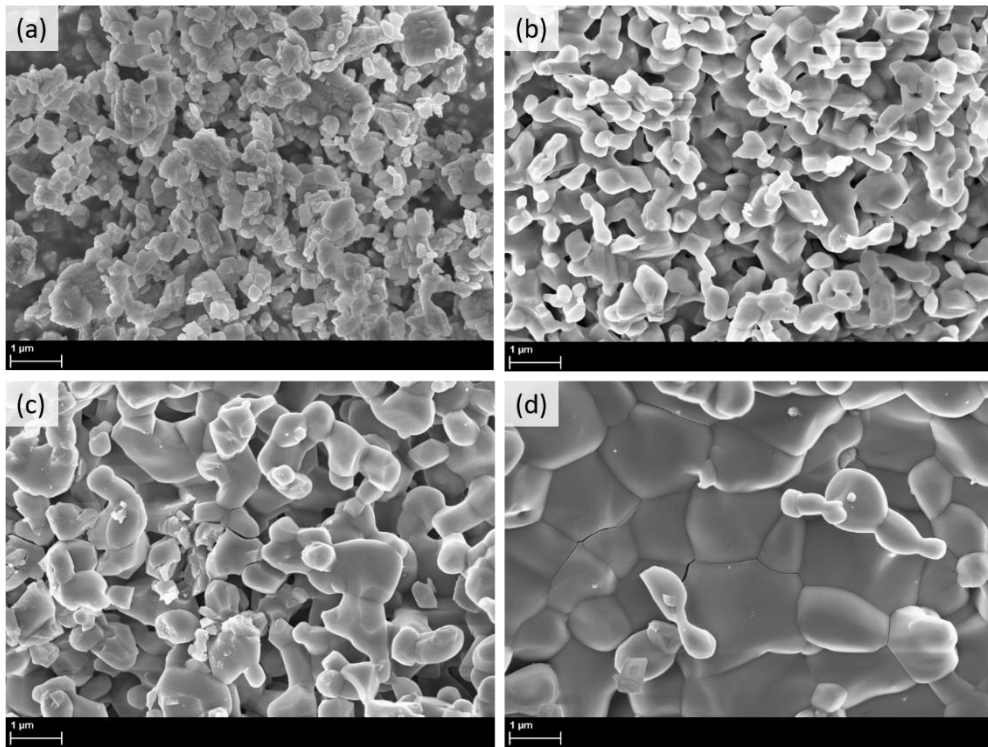


Figure B.9. SEM images of CaCO_3 annealed at 750°C in CO_2 for a) 0 h, b) 1 h, c) 5 h and d) 12 h

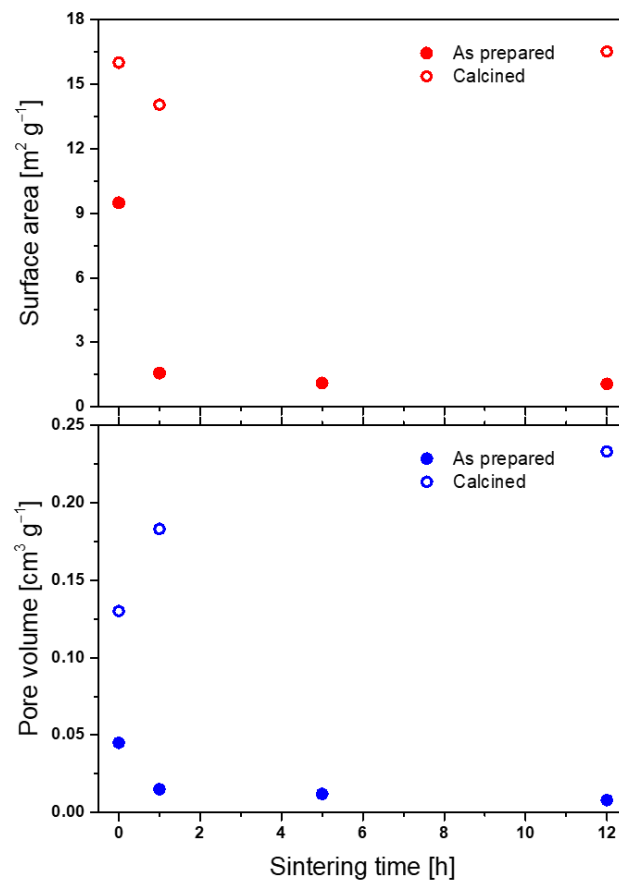


Figure B.10. Surface area and pore volume of CaCO_3 in the as-prepared (prior to the initial calcination) and calcined states as a function of sintering time.

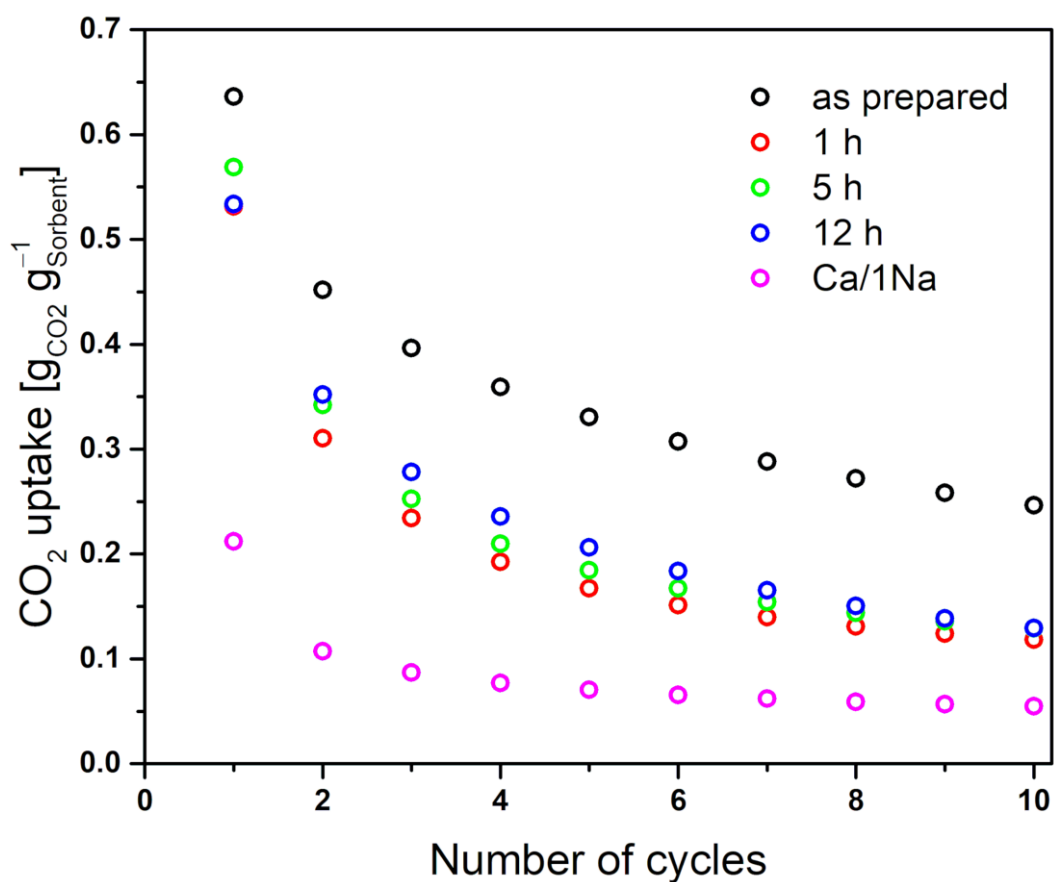


Figure B.11. Cyclic CO₂ uptake of ball-milled CaCO₃ that has been exposed prior to CO₂ uptake test to sintering conditions for varying durations (sintering temperature 750 °C in pure CO₂ atmosphere) under realistic CO₂ capture conditions (calcination at 900 °C in a CO₂-rich atmosphere; carbonation at 650 °C in 20 vol.% CO₂/N₂). Abbreviations 1 h, 5 h and 12 h in the legend correspond to the samples which have been annealed at 750 °C in CO₂ for 1 h, 5 h and 12 h, respectively (as described in Figures B.9 and B.10).

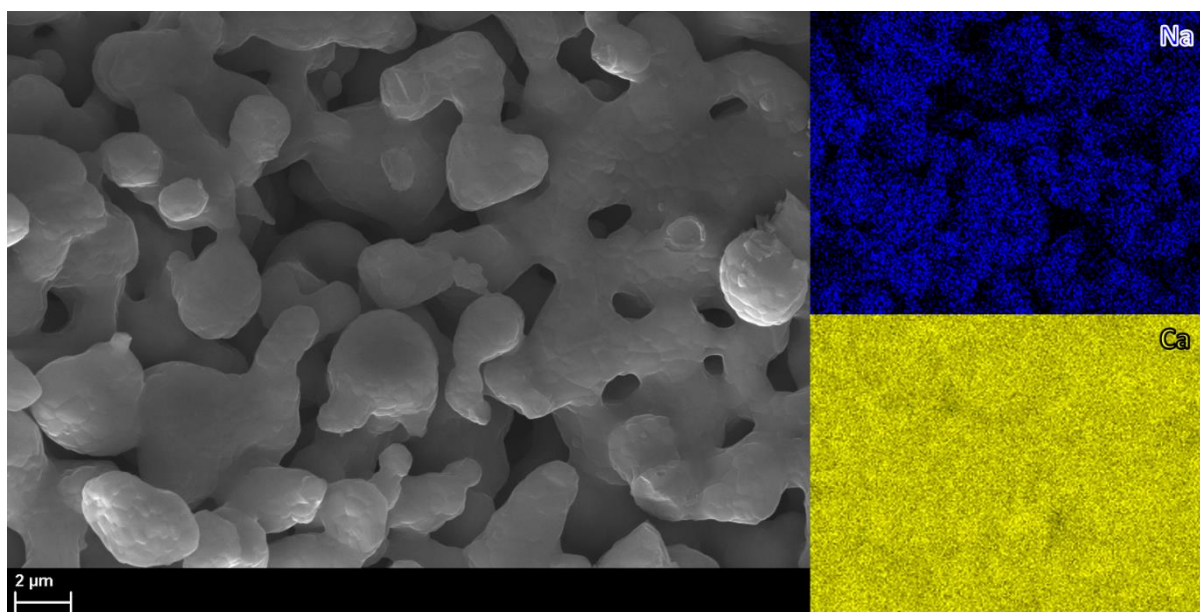


Figure B.12. SEM images and EDX elemental mapping of Ca/3Na after the 10th carbonation step.

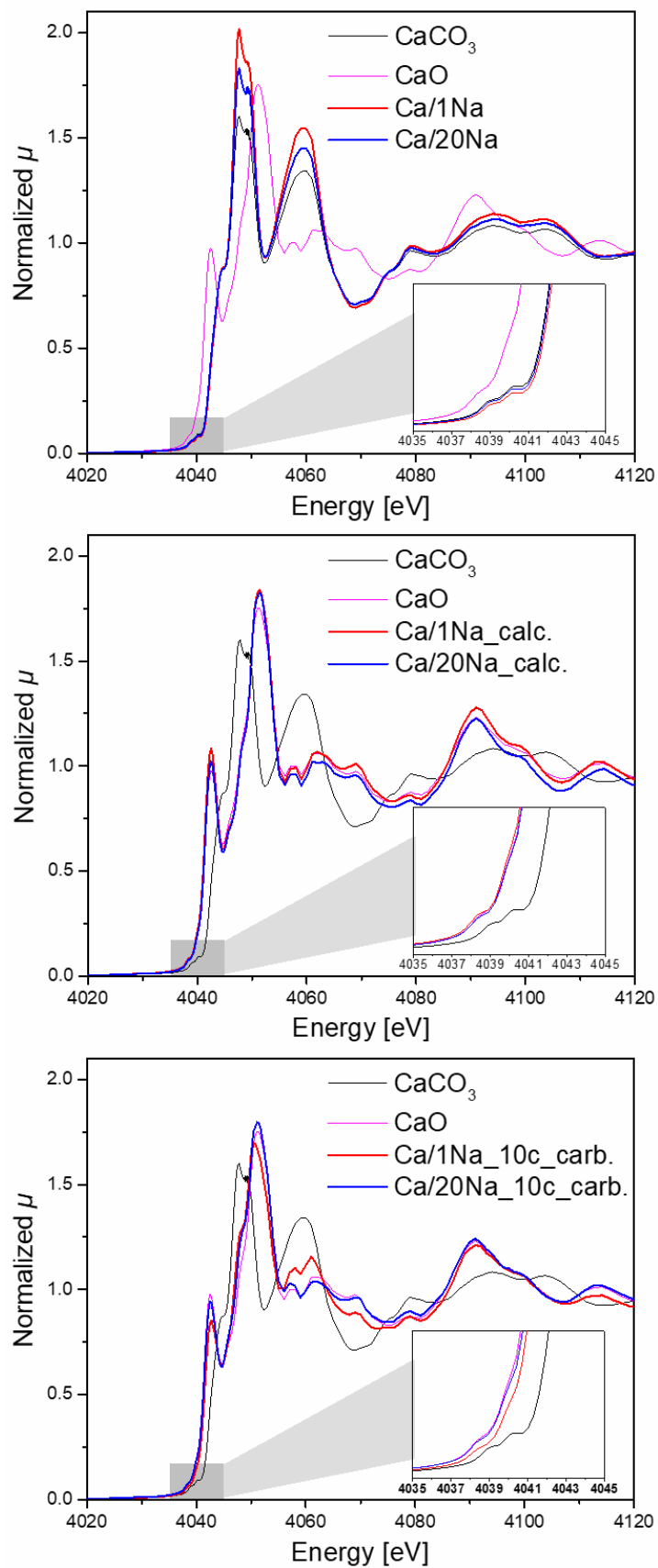


Figure B.13. Ca K-edge spectra of Ca/1Na and Ca/20Na at different states, i.e. as prepared, after the initial calcination (*_calc.*) and after the 10th carbonation step (*_10c_carb.*) compared to the reference spectra of CaO and CaCO₃.

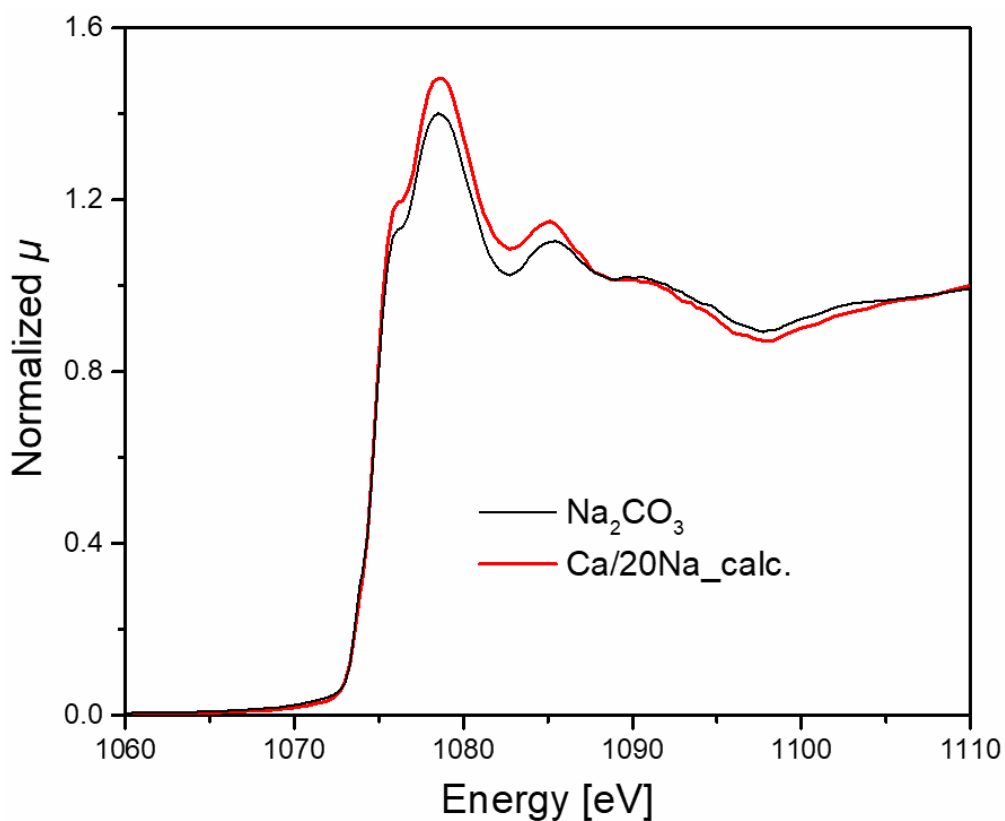


Figure B.14. Na K-edge spectra of Na_2CO_3 -modified CaO after initial calcination (800 °C, N_2) compared to the reference spectra of NaCO_3 .

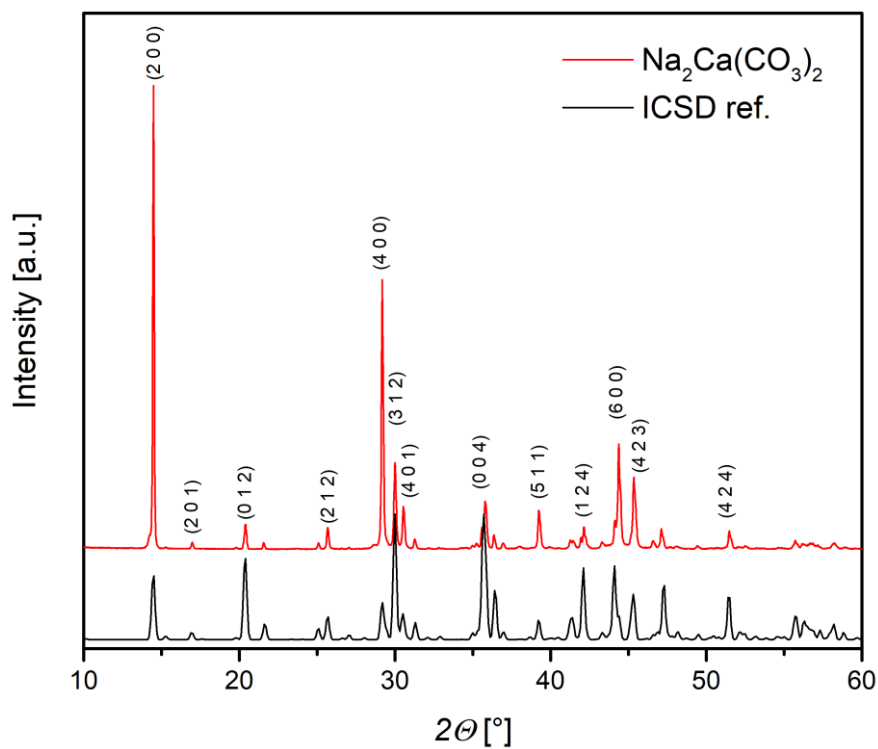


Figure B.15. XRD pattern of the $\text{Na}_2\text{Ca}(\text{CO}_3)_2$ reference and the simulated pattern according to the ICSD database, crystal structure reported in *Cryst. Growth Des.* 2016, 16, 1893–1902 ($\text{P2}_1\text{ca}$, $a = 10.0713 \text{ \AA}$, $b = 8.7220 \text{ \AA}$, $c = 12.2460 \text{ \AA}$).

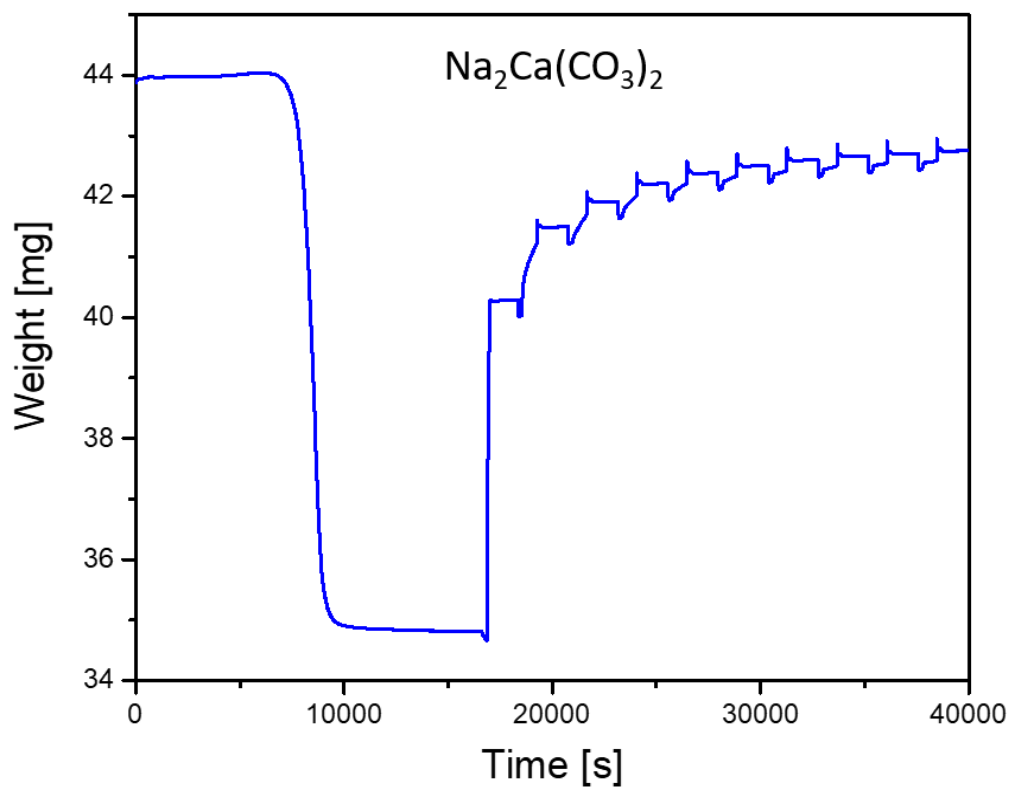


Figure B.16. TGA data when the reference $\text{Na}_2\text{Ca}(\text{CO}_3)_2$ is exposed to cyclic carbonation calcination conditions. $\text{Na}_2\text{Ca}(\text{CO}_3)_2$ does not decompose under the carbonation and calcination conditions studied (CO_2 , 650–900 °C).

Table B.1. Theoretical and ICP-determined Na_2CO_3 contents in the prepared sorbents.

Sample	Nominal Na_2CO_3 content wt.%	Na/Ca ratio	Determined Na_2CO_3 content wt.%
Ca/1Na	1	0.009	0.8
Ca/3Na	3	0.057	5
Ca/10Na	10	0.130	10.7
Ca/20Na	20	0.301	21.7

C. Supplementary information for Chapter 4

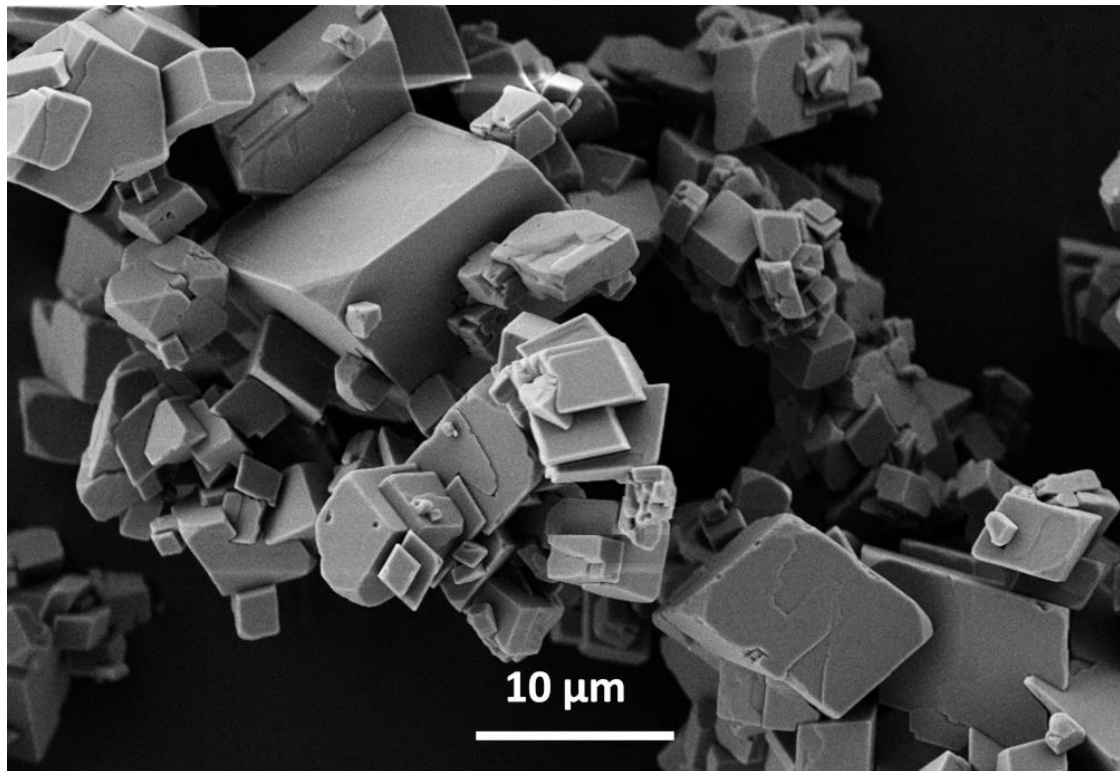


Figure C.1. SEM image of commercial CaCO₃.

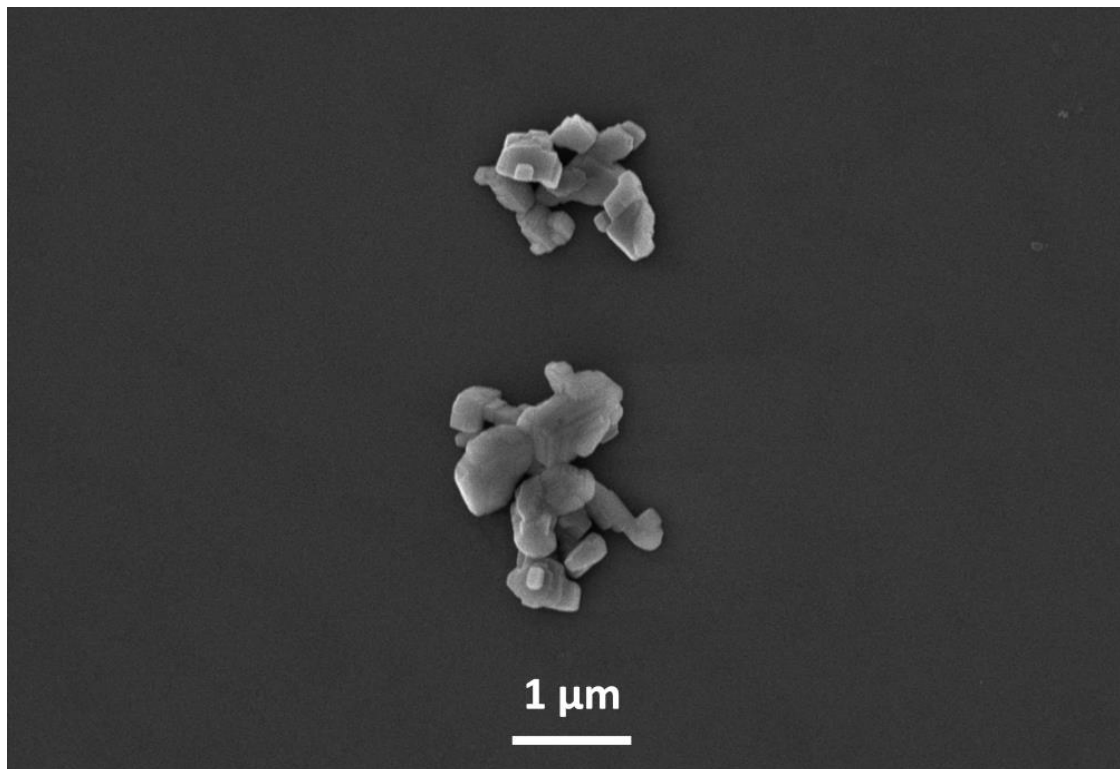


Figure C.2. SEM image of ball-milled CaCO₃.

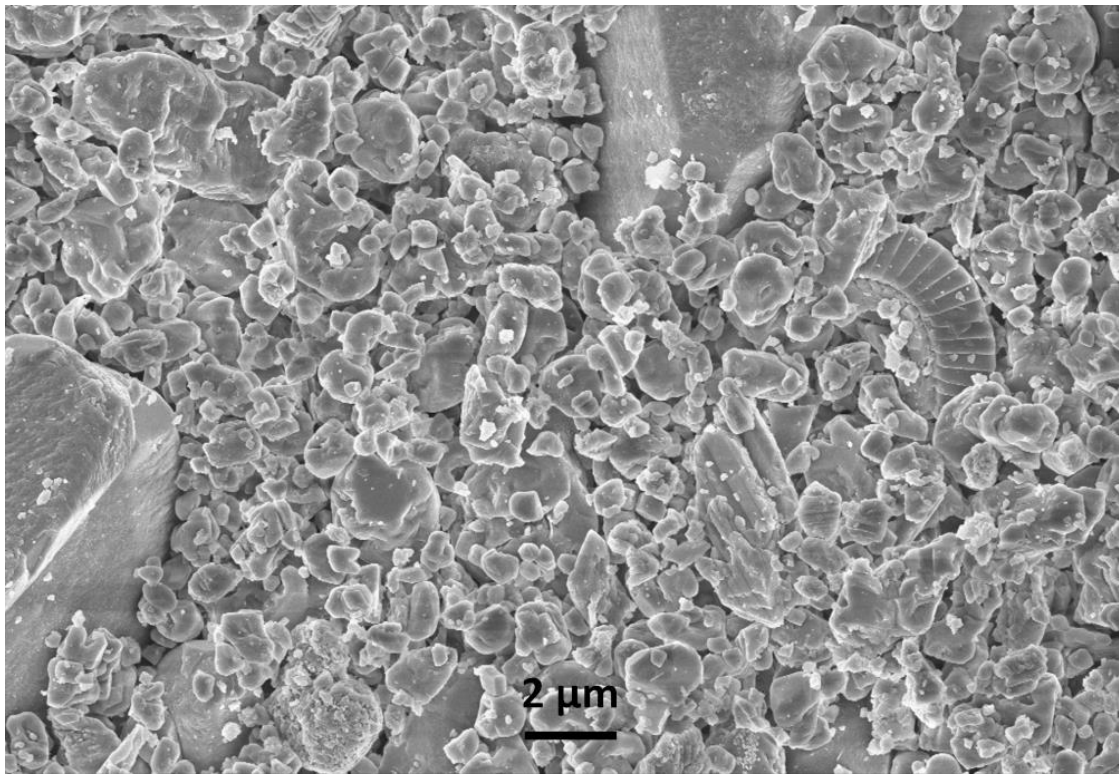


Figure C.3. SEM image of as received Rheinkalk limestone.

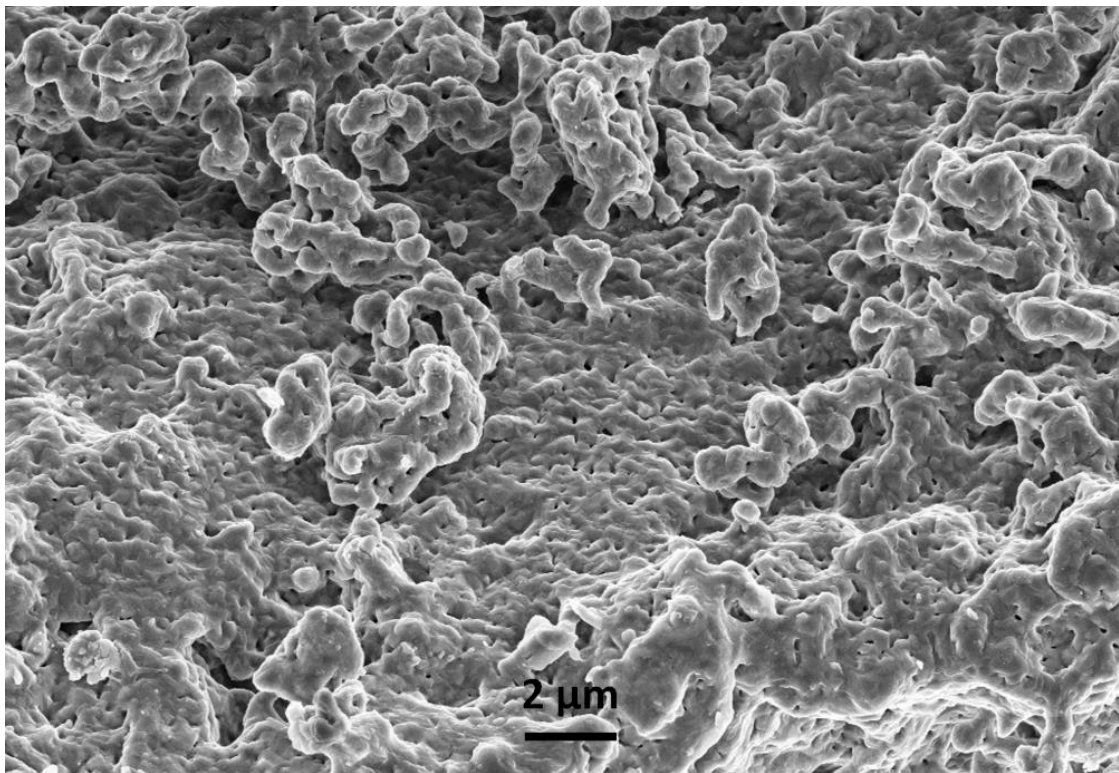


Figure C.4. SEM image of Rheinkalk limestone after 10 carbonation/calcination cycles.

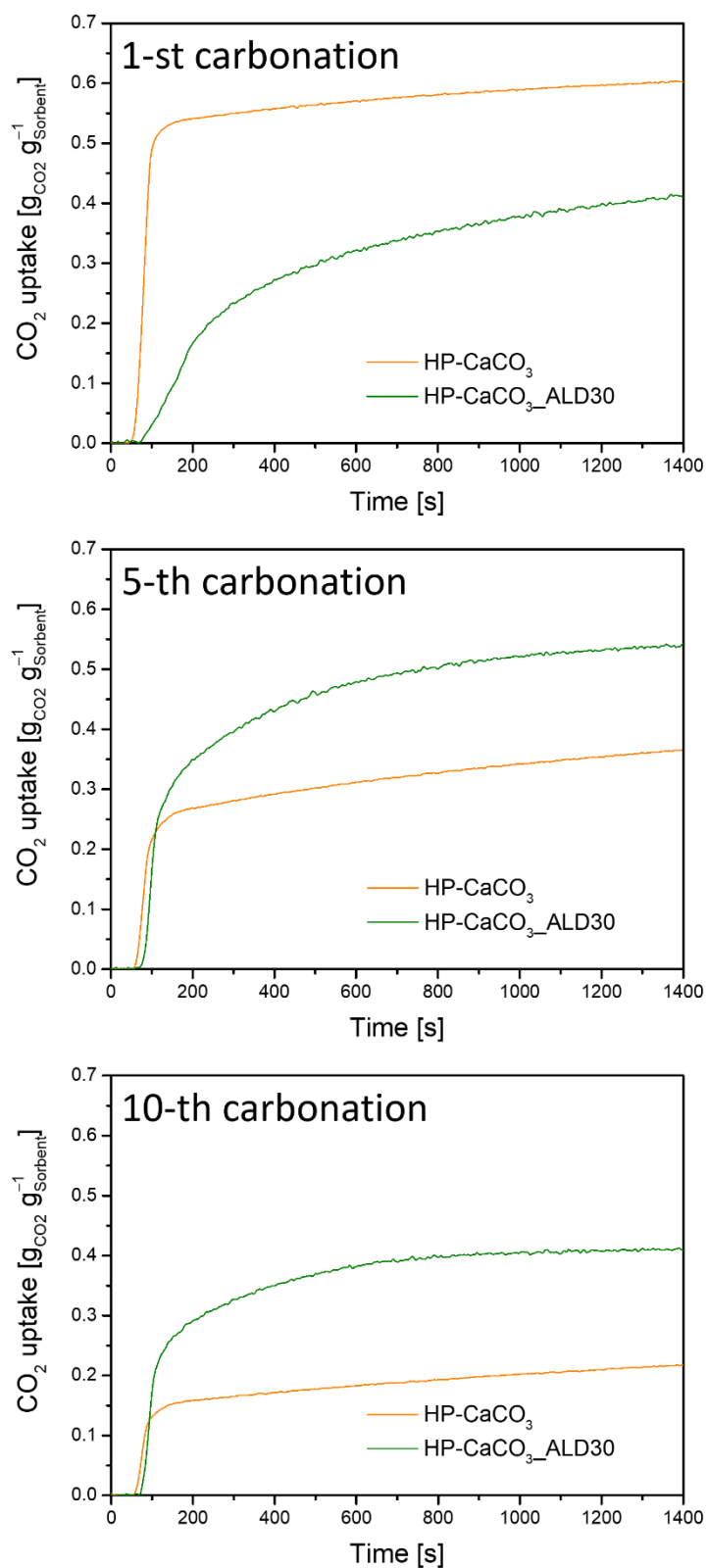


Figure C.5. Carbonation profiles of HP-CaCO₃ and HP-CaCO₃ coated with 30 Al₂O₃ ALD cycles during the 1-st, 5-th and 10-th carbonation cycle.

Note that the total time of carbonation exceeds 20 min because the actual carbonation reaction began during the cooling of the sample from 900 to 650 °C under 20 vol.% CO₂.

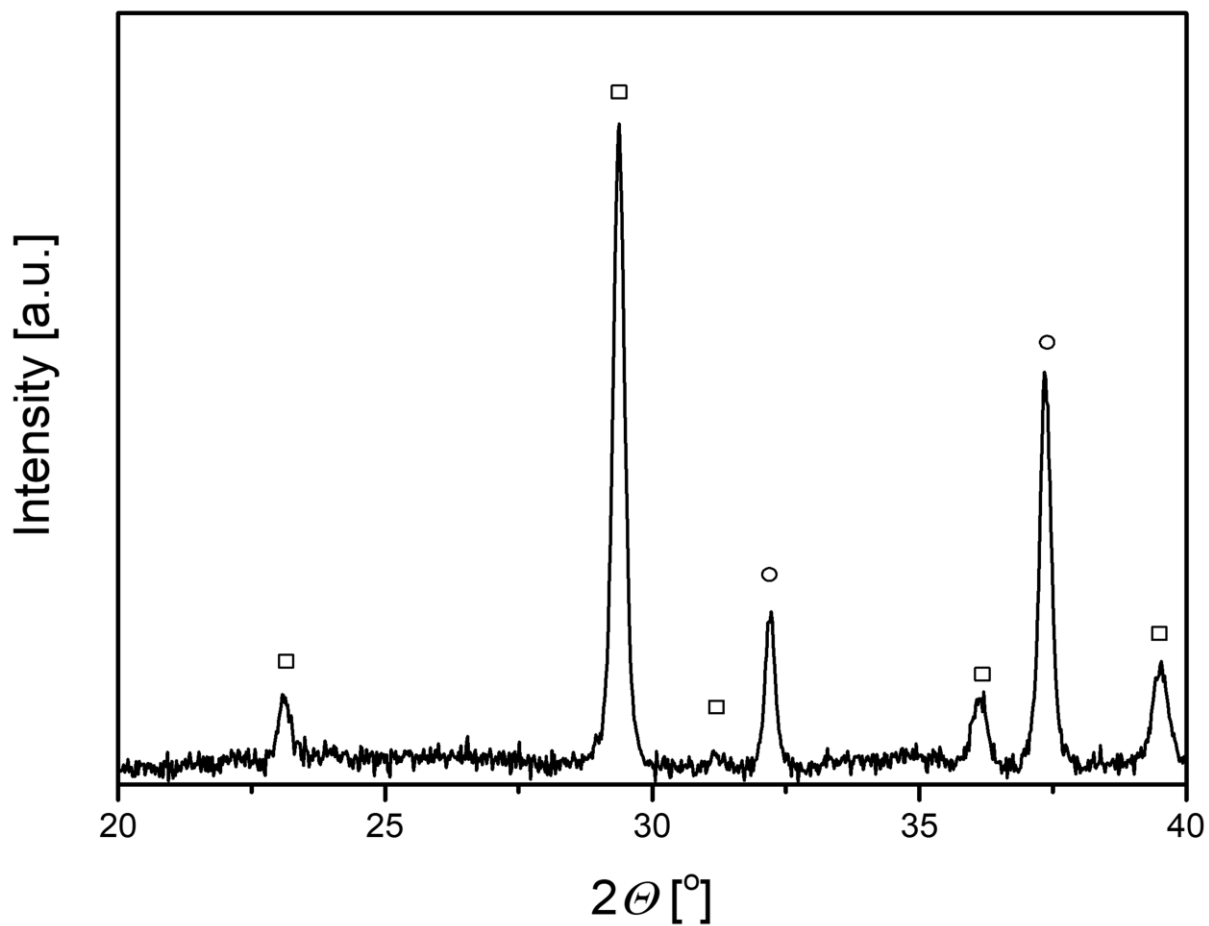


Figure C.6. XRD pattern of HP-CaCO₃ sorbent with 1 nm alumina coating (10 ALD cycles) after 10 carbonation/calcination cycles: (□) calcite, CaCO₃; (○) lime.

D. Supplementary information for Chapter 5

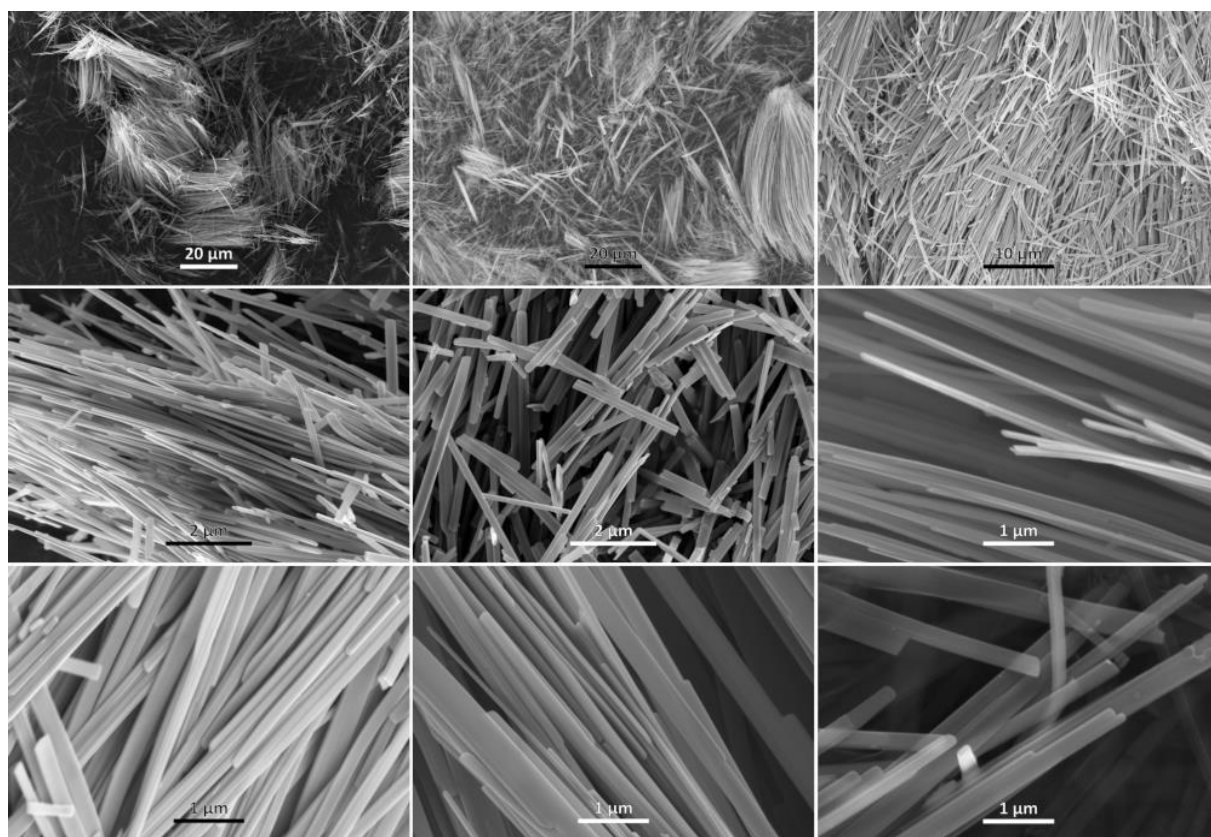


Figure D.1. SEM images of $\alpha\text{-MoO}_3$ nanobelts.

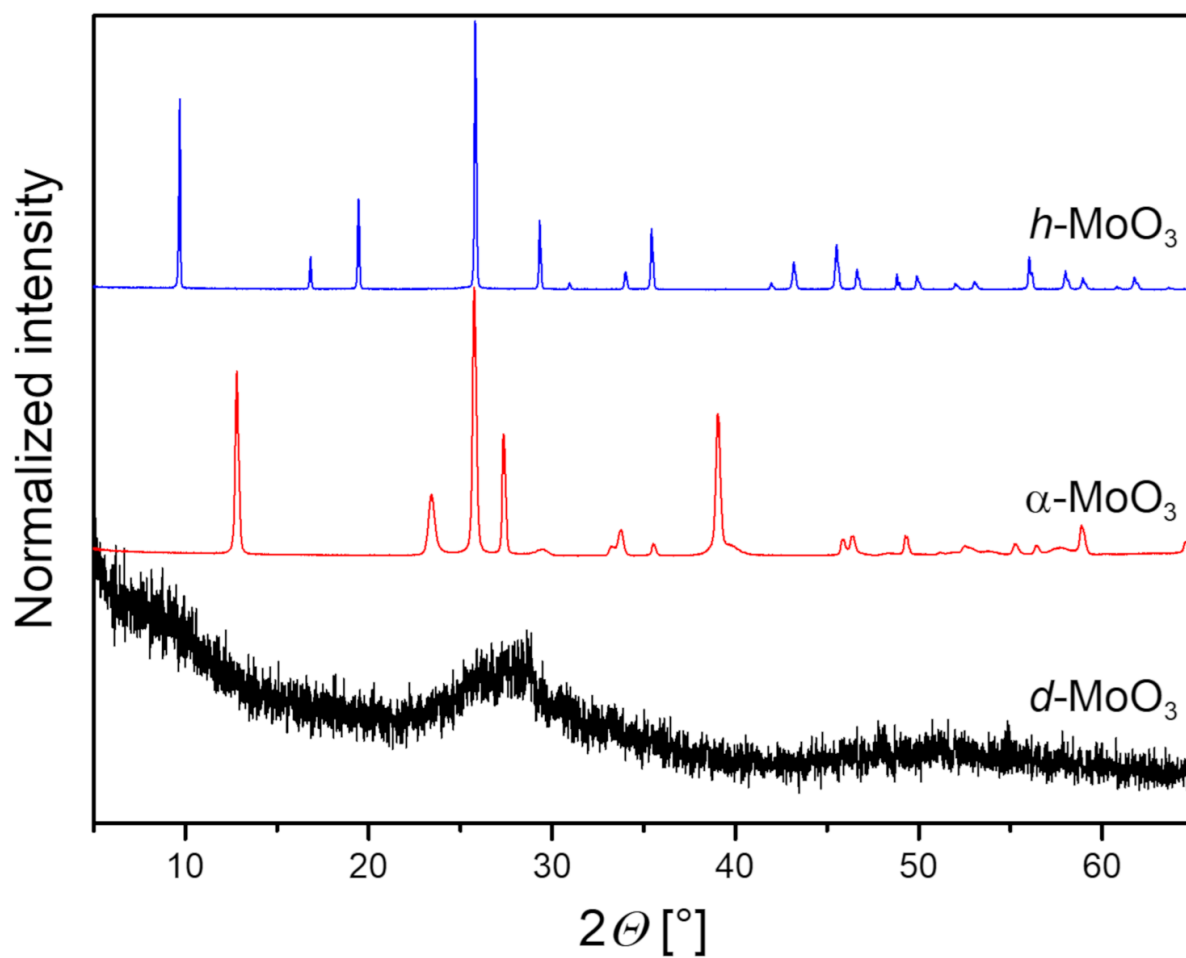


Figure D.2. XRD (laboratory based) patterns of $h\text{-MoO}_3$, $\alpha\text{-MoO}_3$ and $d\text{-MoO}_3$.

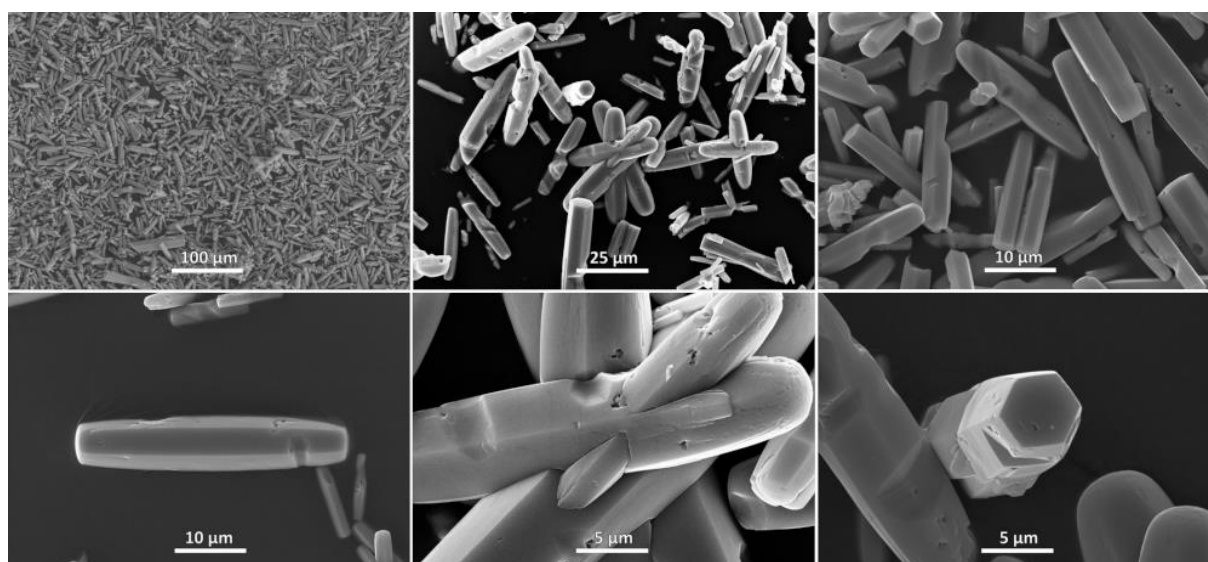


Figure D.3. SEM images of $h\text{-MoO}_3$.

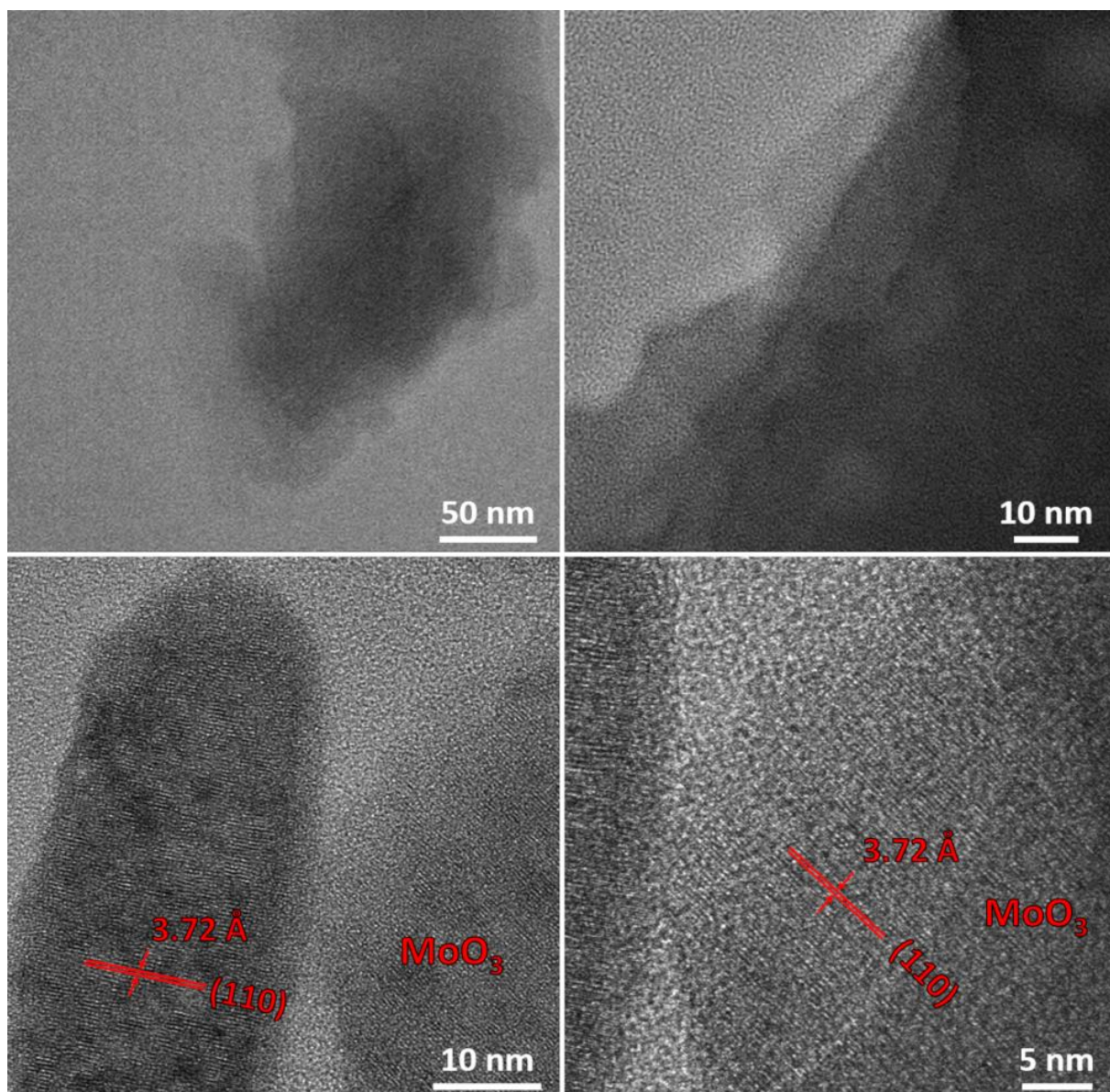


Figure D.4. TEM images of exfoliated $d\text{-MoO}_3$.

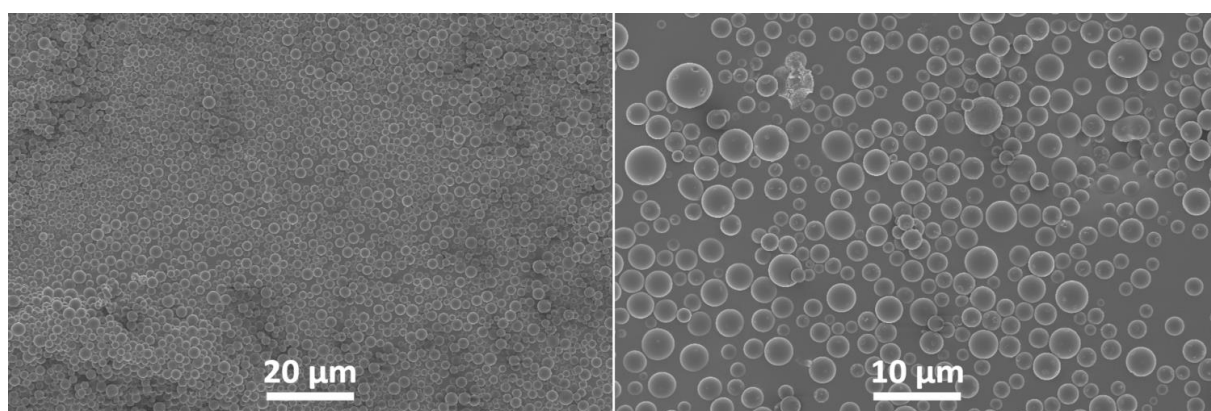


Figure D.5. SEM images of carbon spheres.

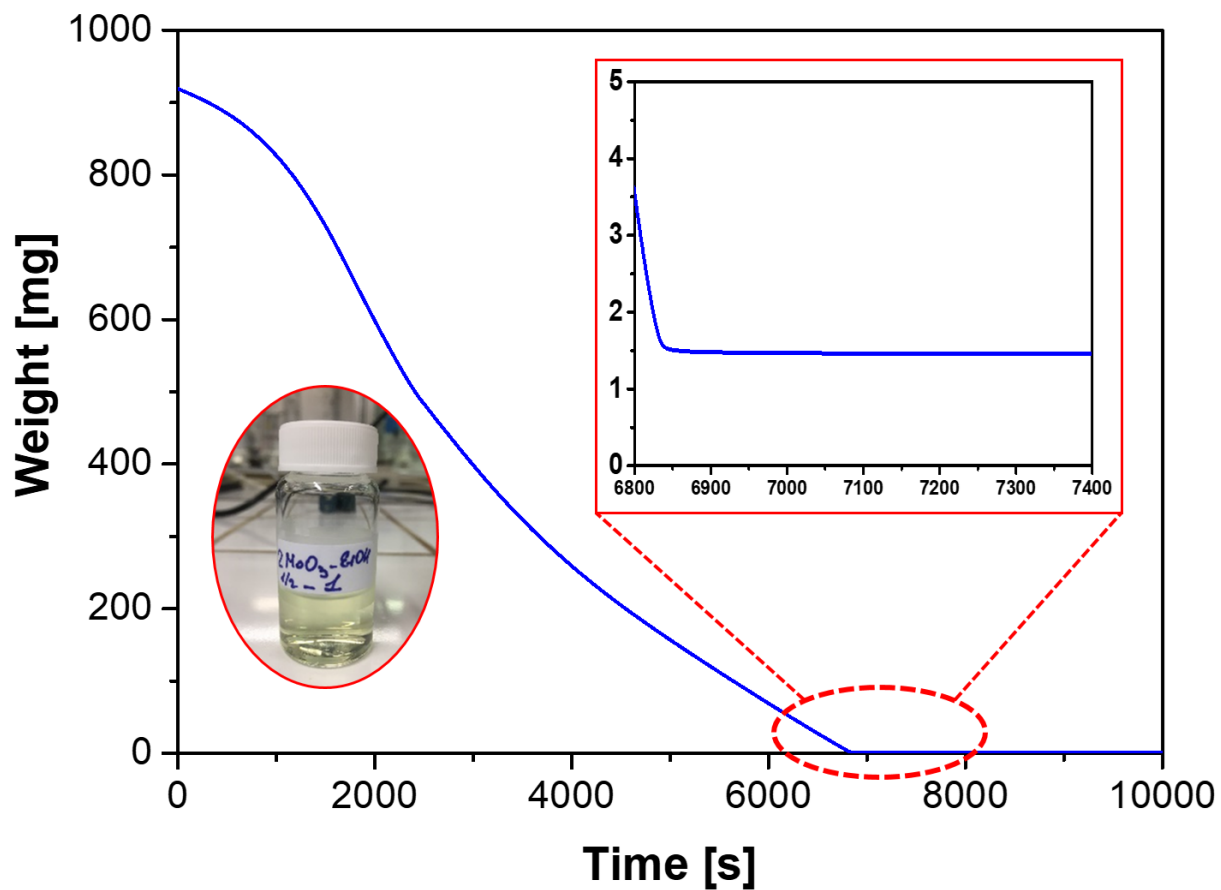


Figure D.6. TGA weight loss curve of the $d\text{-MoO}_3$ colloidal solution.

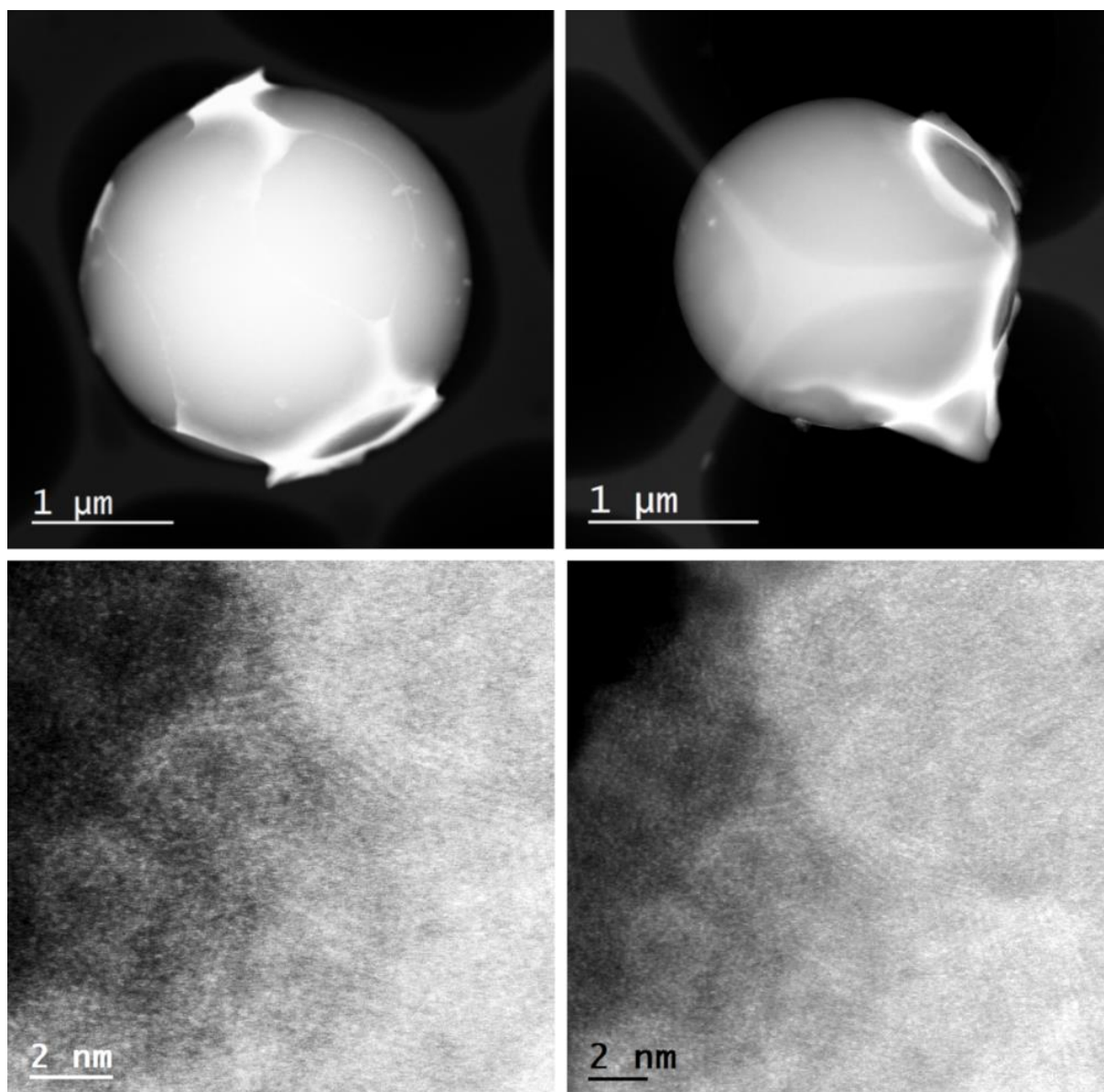


Figure D.7. HAADF-STEM (top) and HR-STEM (bottom) images of *d*-MoO₃/C.

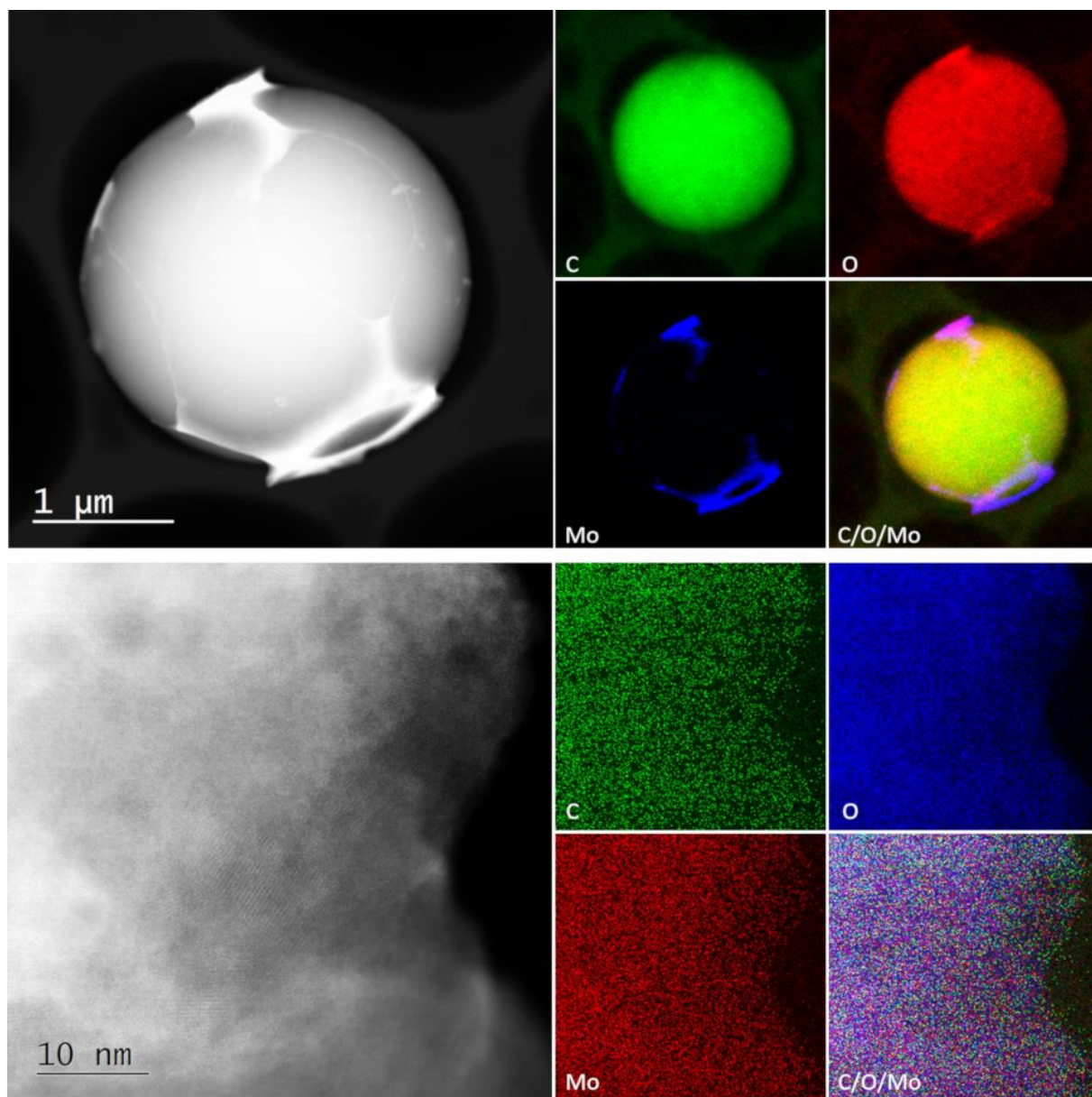


Figure D.8. STEM/EDX mapping of *d*-MoO₃/C.

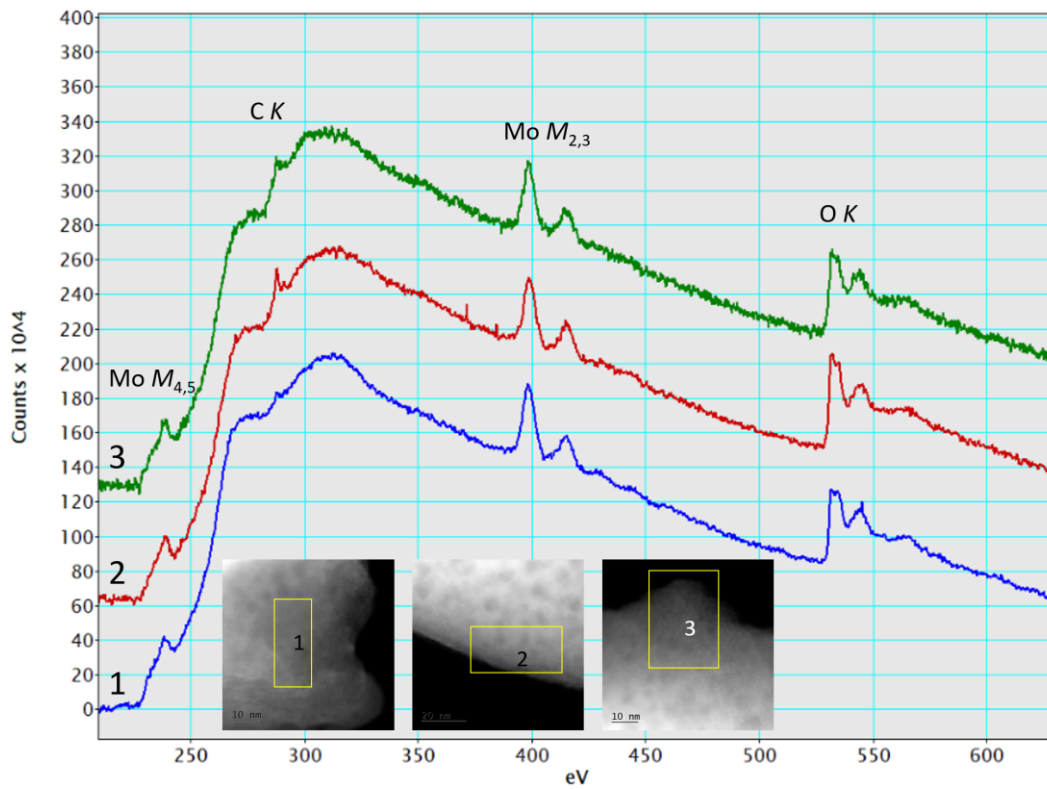


Figure D.9. EELS spectra of the Mo-rich phase of $d\text{-MoO}_3/\text{C}$.

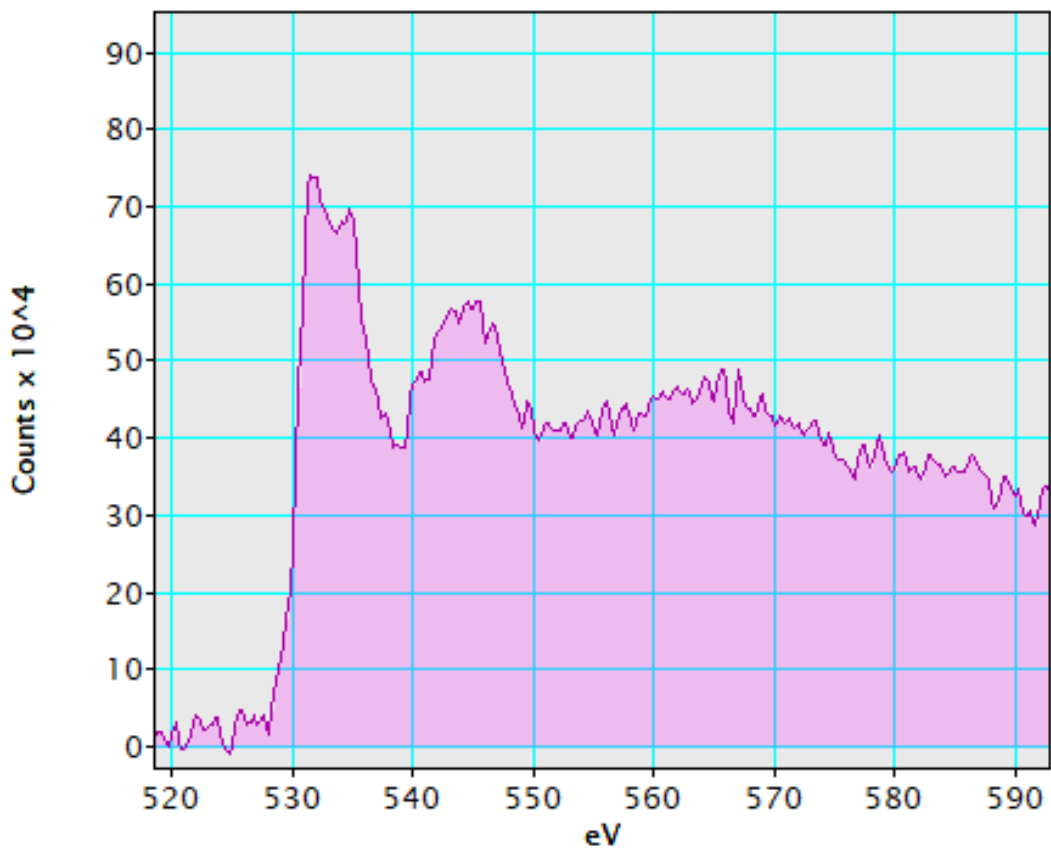


Figure D.10. O K-edge spectrum of $d\text{-MoO}_3/\text{C}$.

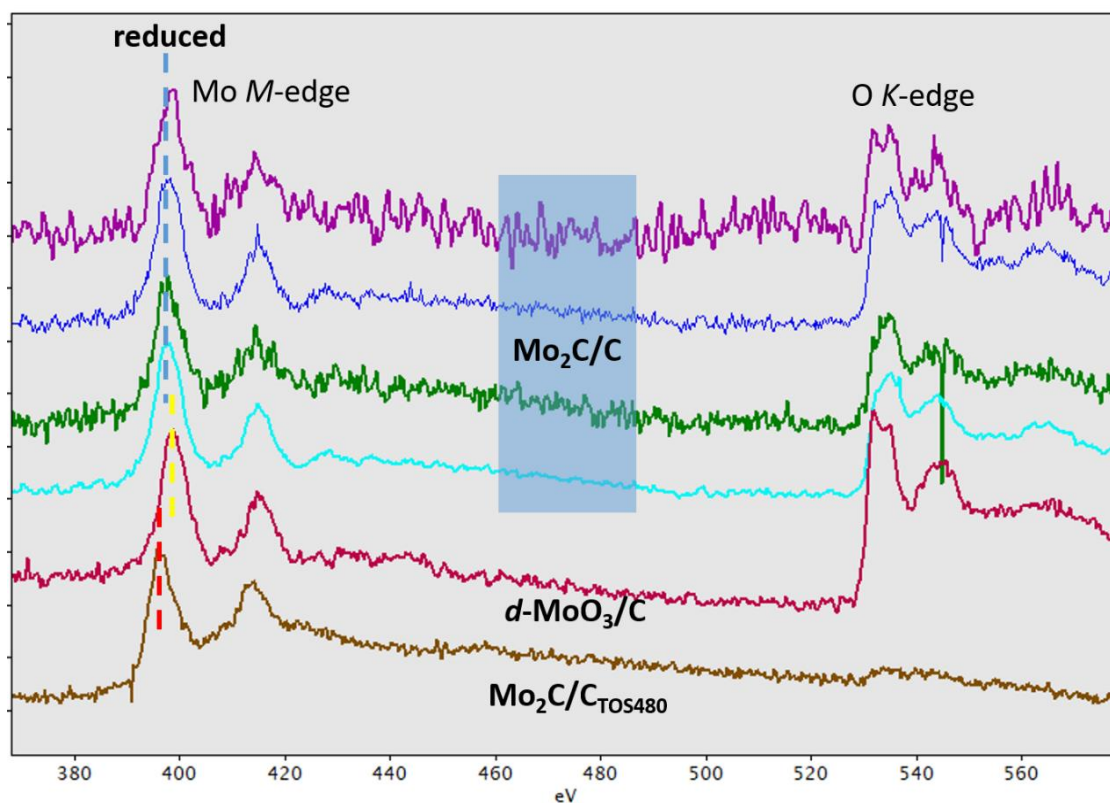


Figure D.11. Comparison of EELS Mo M_{2,3} edge and O K-edge of *d*-MoO₃/C, Mo₂C/C and Mo₂C/C_{TOS480}.

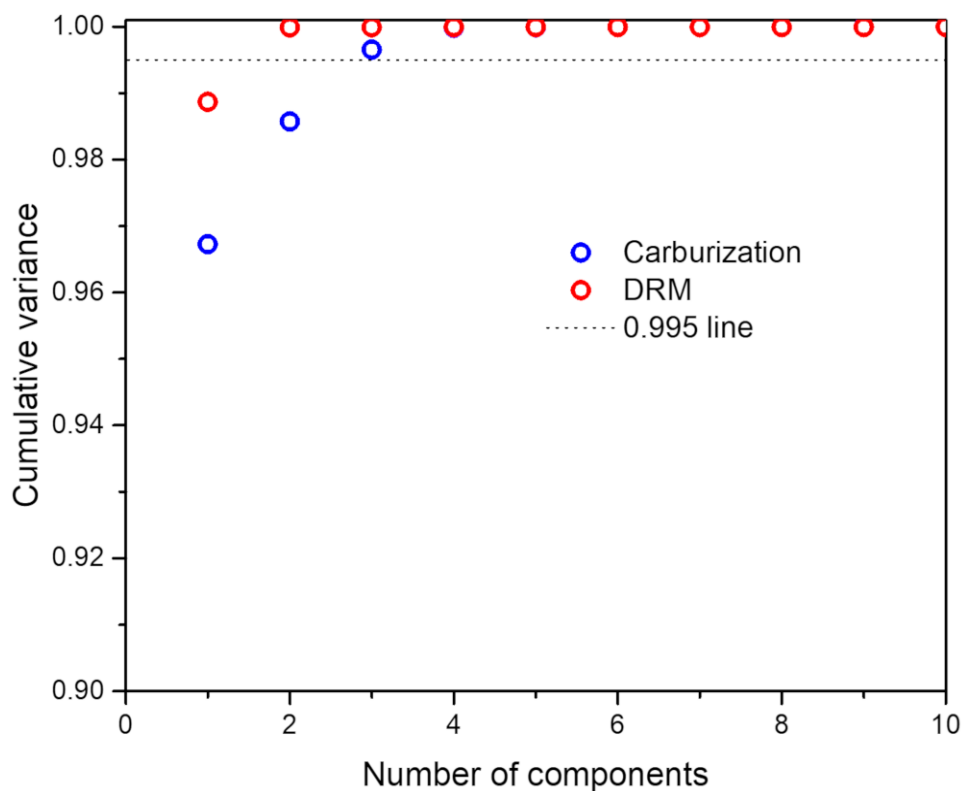


Figure D.12. Cumulative variance plots obtained by principal component analysis (PCA) of the *in situ* XANES data during carburization and DRM.

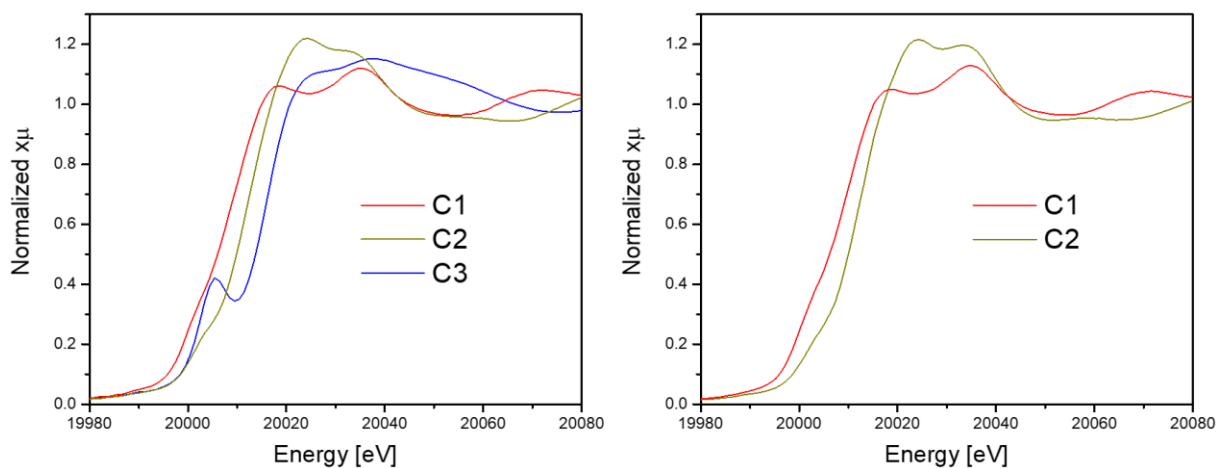


Figure D.13. XANES spectra of the components obtained by MCR-ALS analysis during carburization (left) and DRM (right).

Table D.1. Quality indicators of the MCR-ALS analysis of *in situ* XANES data obtained during the carburization and the DRM reaction.

Carburization	
Fitting error (lack of fit, LOF) in % (PCA)	1.4486×10^{-13}
Fitting error (lack of fit, LOF) in % (exp.)	0.45665
Percentage of variance explained at the optimum	99.9979
DRM	
Fitting error (lack of fit, LOF) in % (PCA)	1.9635×10^{-14}
Fitting error (lack of fit, LOF) in % (exp.)	0.35492
Percentage of variance explained at the optimum	99.9987

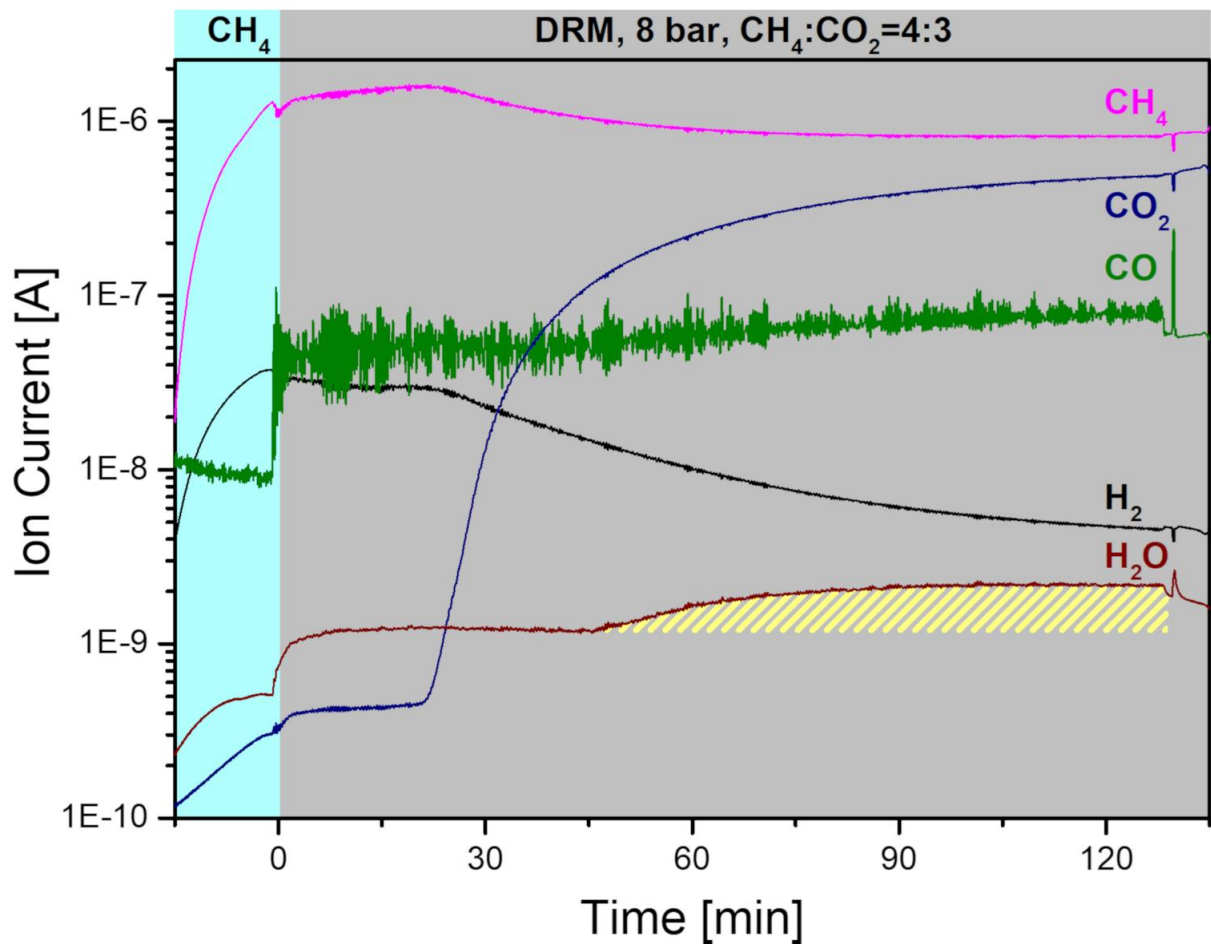


Figure D.14. Trends in the composition of the off gas during the *in situ* DRM experiments as determined by a mass spectrometer (MS).

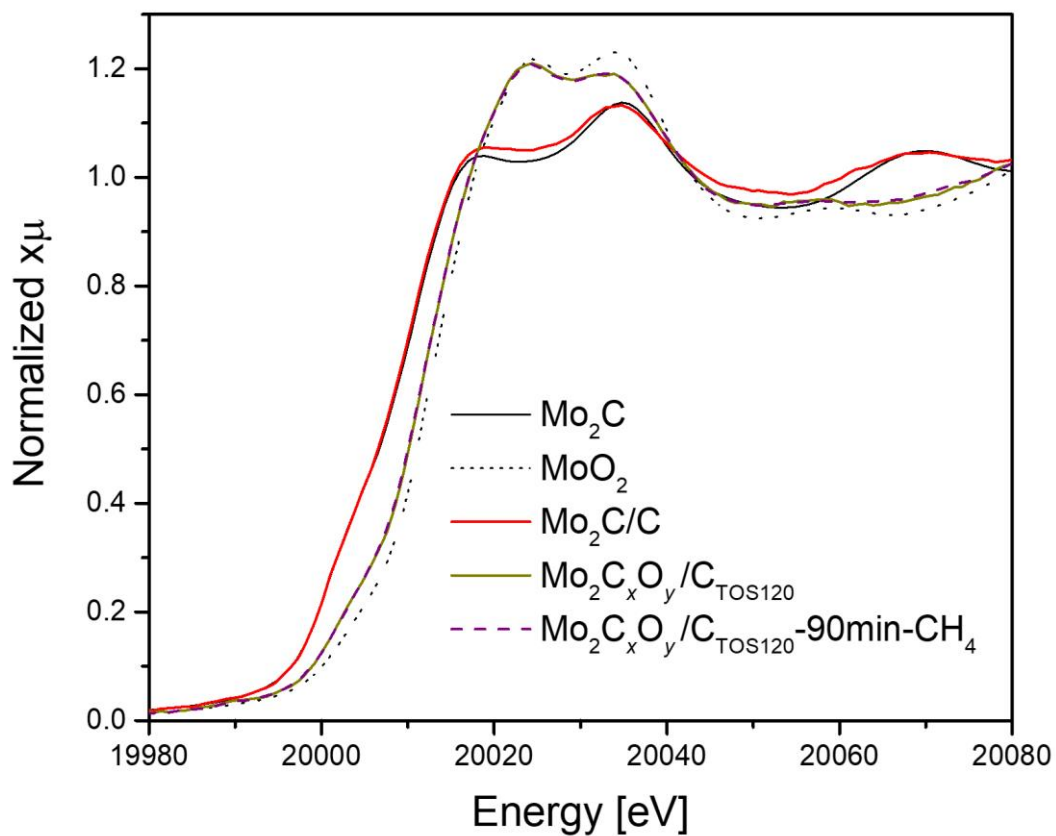


Figure D.15. Comparison of the XANES spectra of the catalyst $\text{Mo}_2\text{C}/\text{C}$ after having been exposed for 2 h under DRM conditions and after a re-carburization attempt in CH_4 for 90 min.

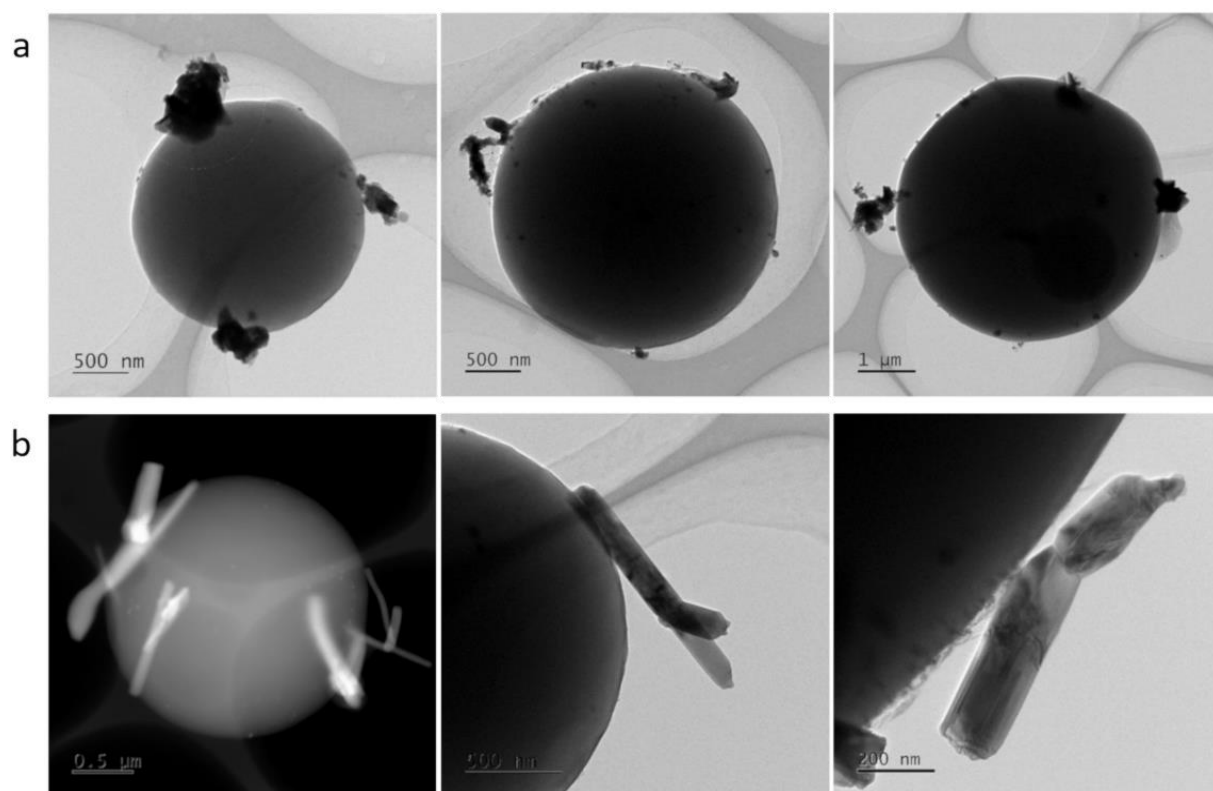


Figure D.16. (S)TEM images of reacted $\text{Mo}_2\text{C}_x\text{O}_y/\text{C}$ with platelet (a) and nanorod (b) structures.

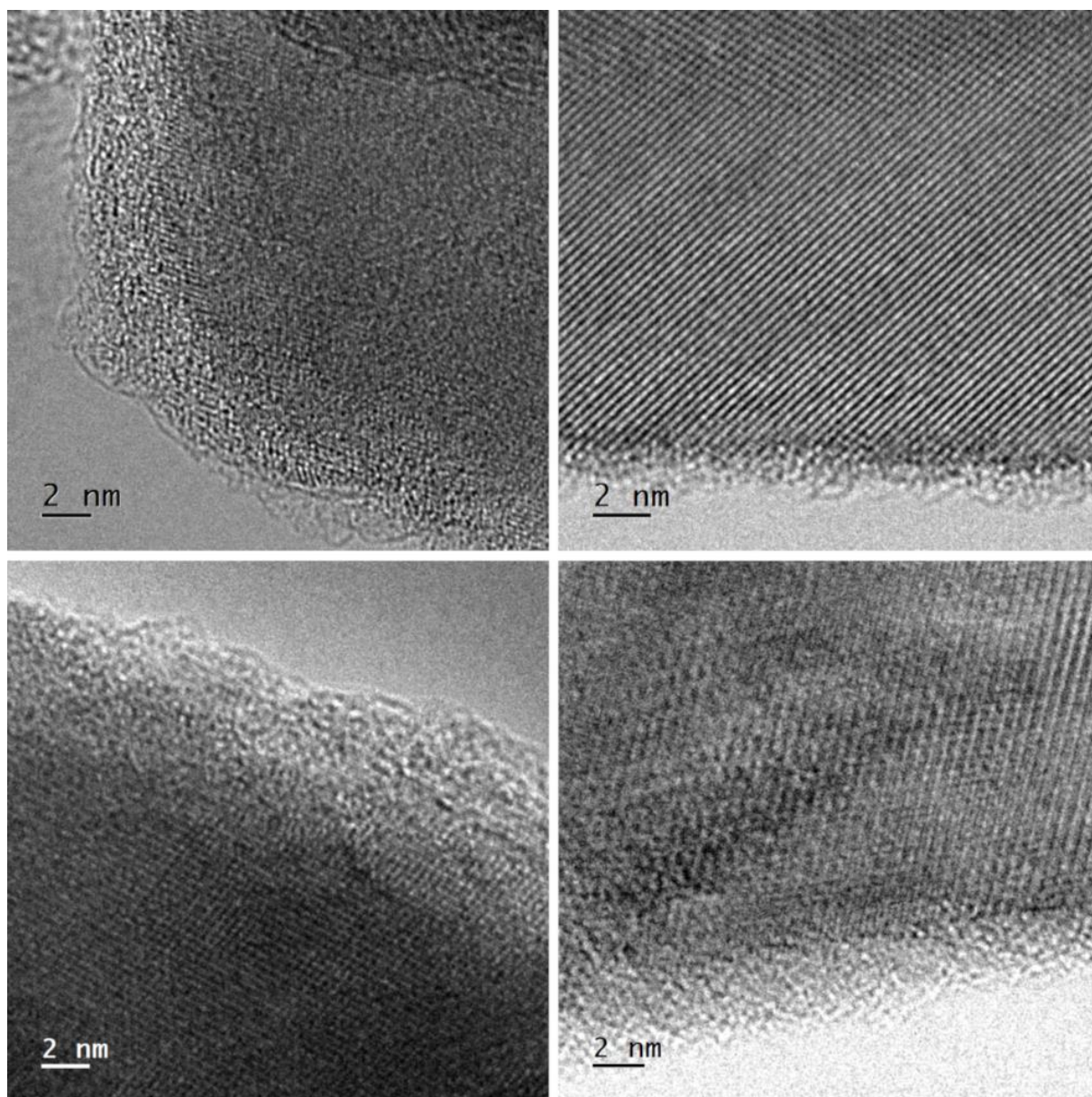


Figure D.17. TEM images of reacted $\text{Mo}_2\text{C}_x\text{O}_y/\text{C}$ indicating a surface layer with low crystallinity.

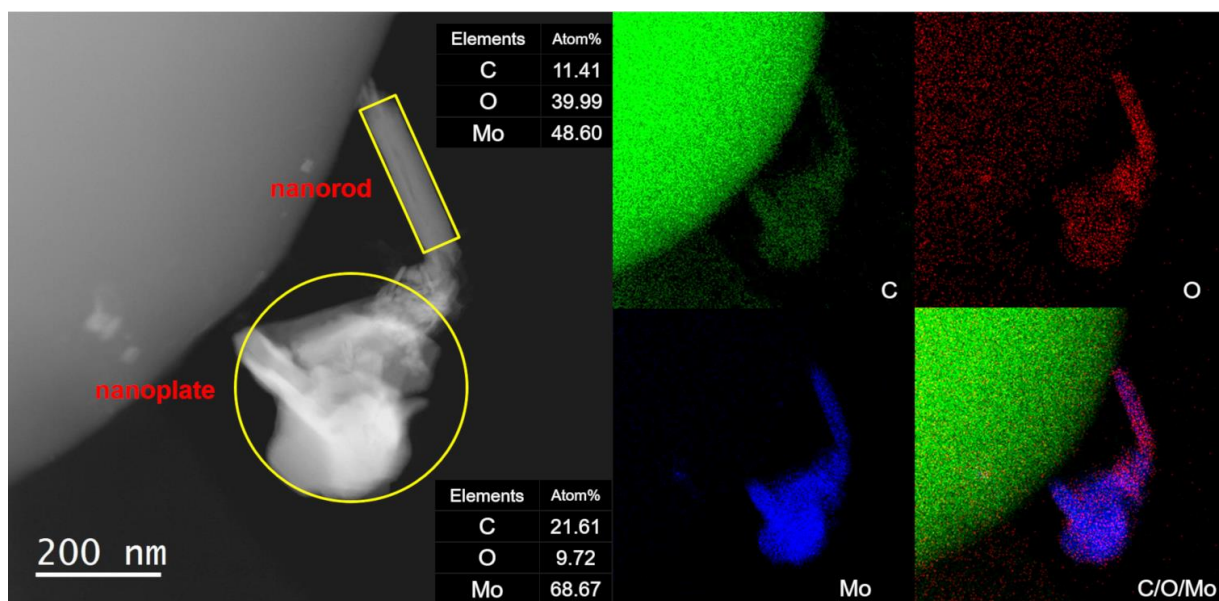


Figure D.18. STEM/EDX mapping of reacted $\text{Mo}_2\text{C}_x\text{O}_y/\text{C}$ indicating differences in the oxygen content in the various morphologies.

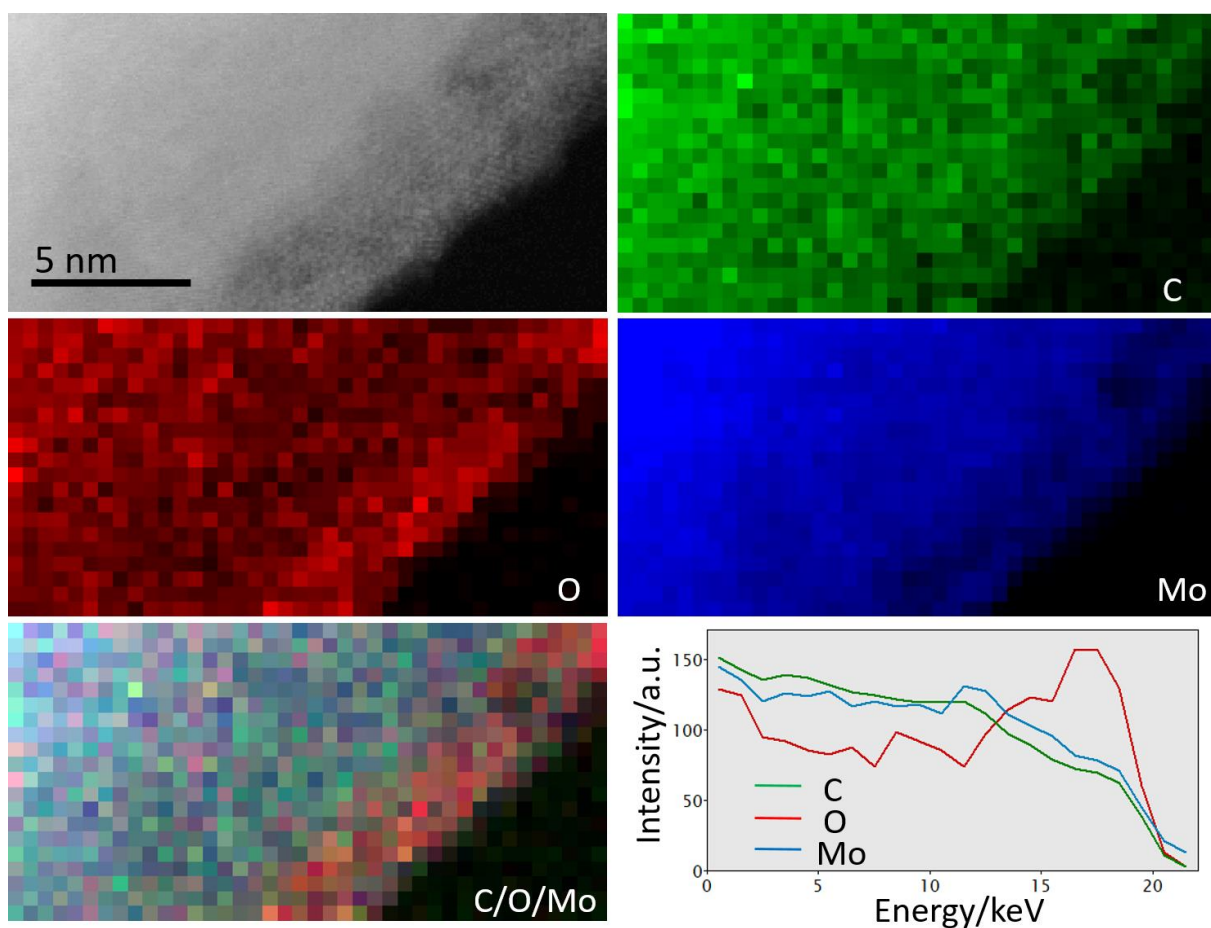


Figure D.19. STEM/EDX mapping and EDX line profile of $\text{Mo}_2\text{C}_x\text{O}_y/\text{C}$ indicating an O-rich surface layer.

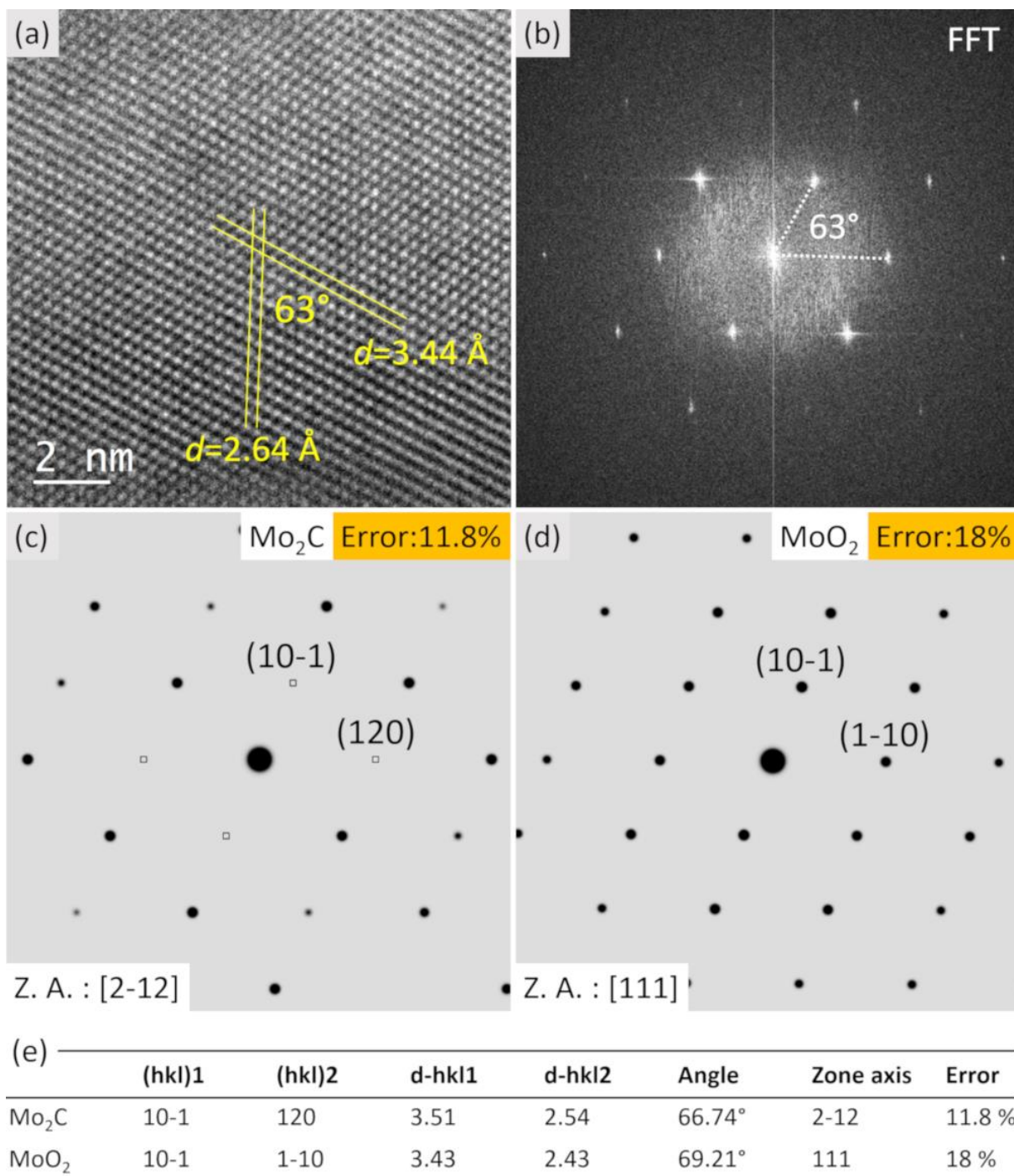


Figure D.20. a) HRTEM image of the $\text{Mo}_2\text{C}_x\text{O}_y$ nanorod in the spent catalyst and b) corresponding FFT; c), d) simulated electron diffraction along the most possible zone axis by referencing the standard Mo_2C and MoO_2 ; e) standard values calculated from the two reference structures; the errors are generated due to the misfit between our experimental data and the standard values.

E. Supplementary information for Chapter 6

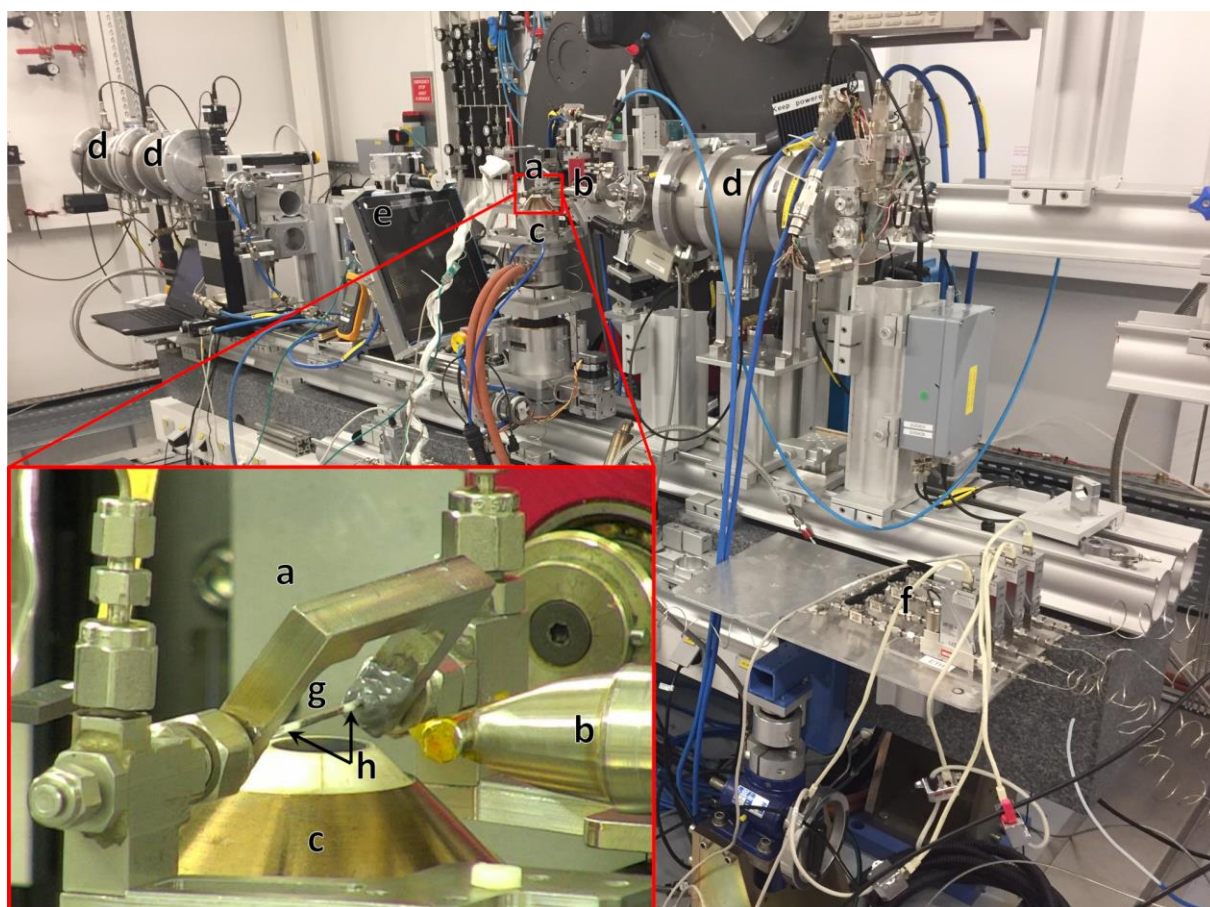


Figure E.1. Experiment setup for the *in situ* experiments performed at SNBL with magnified capillary cell. a) Capillary cell, b) incident beam, c) heating air gun, d) ion chambers, e) XRD detector, f) gas MFCs, g) sample, h) quartz wool plugs.

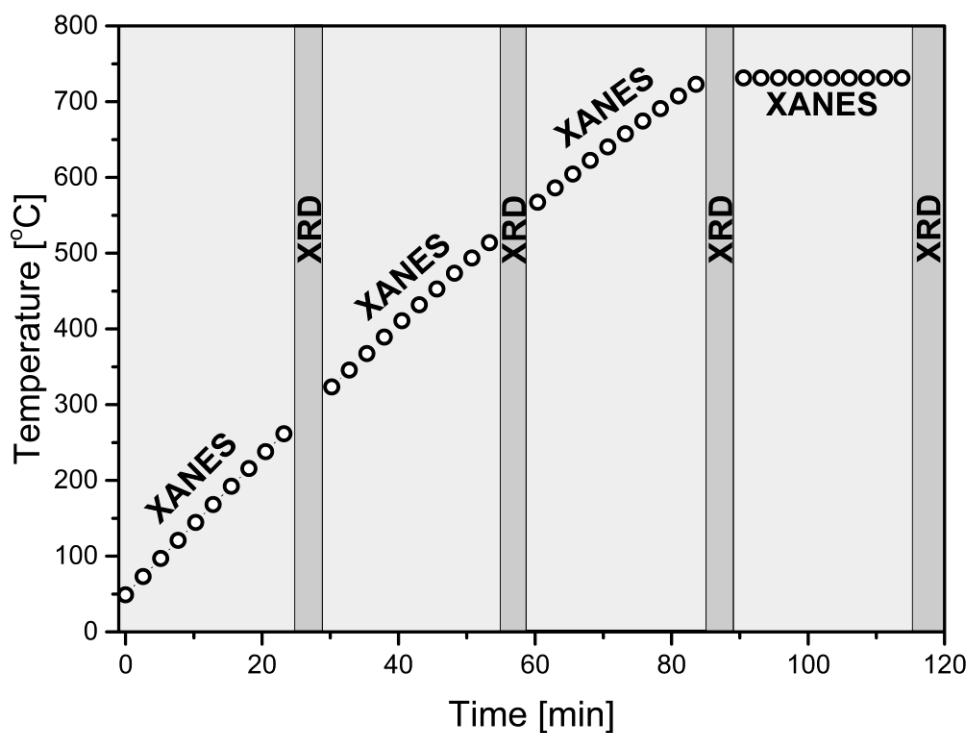


Figure E.2. The data collection program during the *in situ* synchrotron TPR experiment.

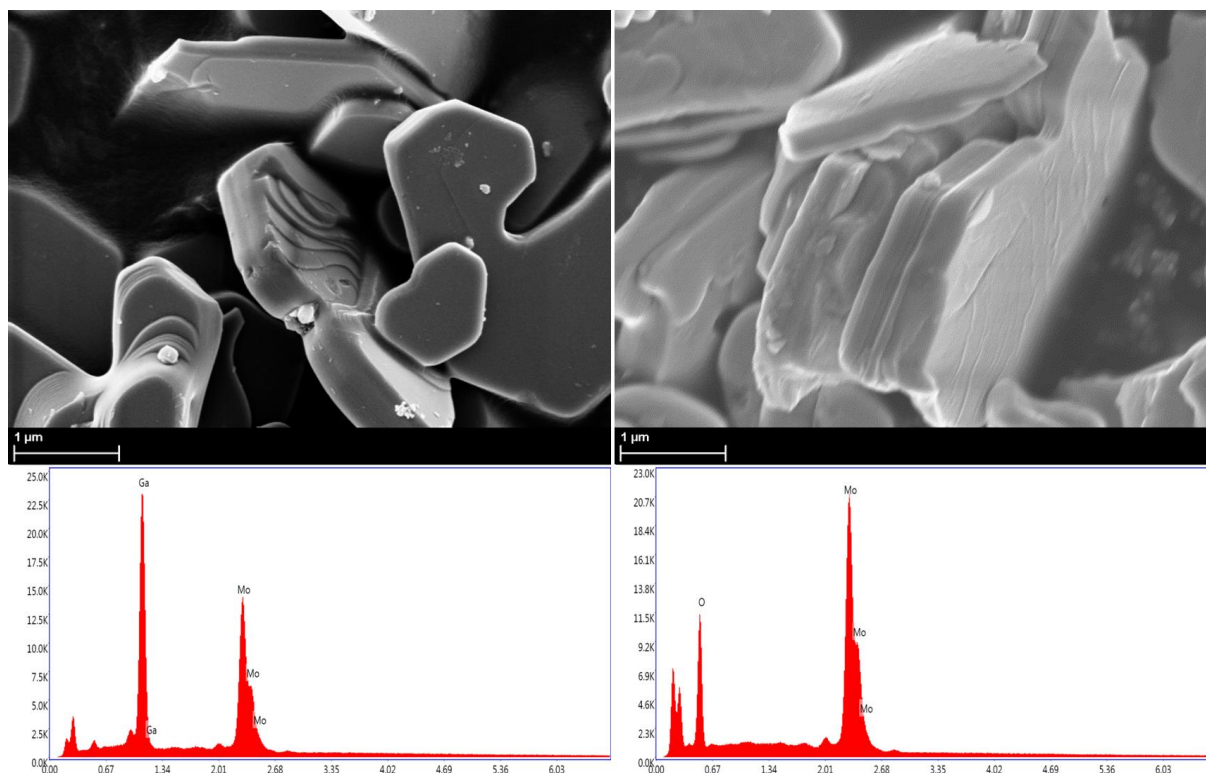


Figure E.3. SEM-EDX images of $\text{Mo}_2\text{Ga}_2\text{C}$ (left) and Mo_2CT_x (right).

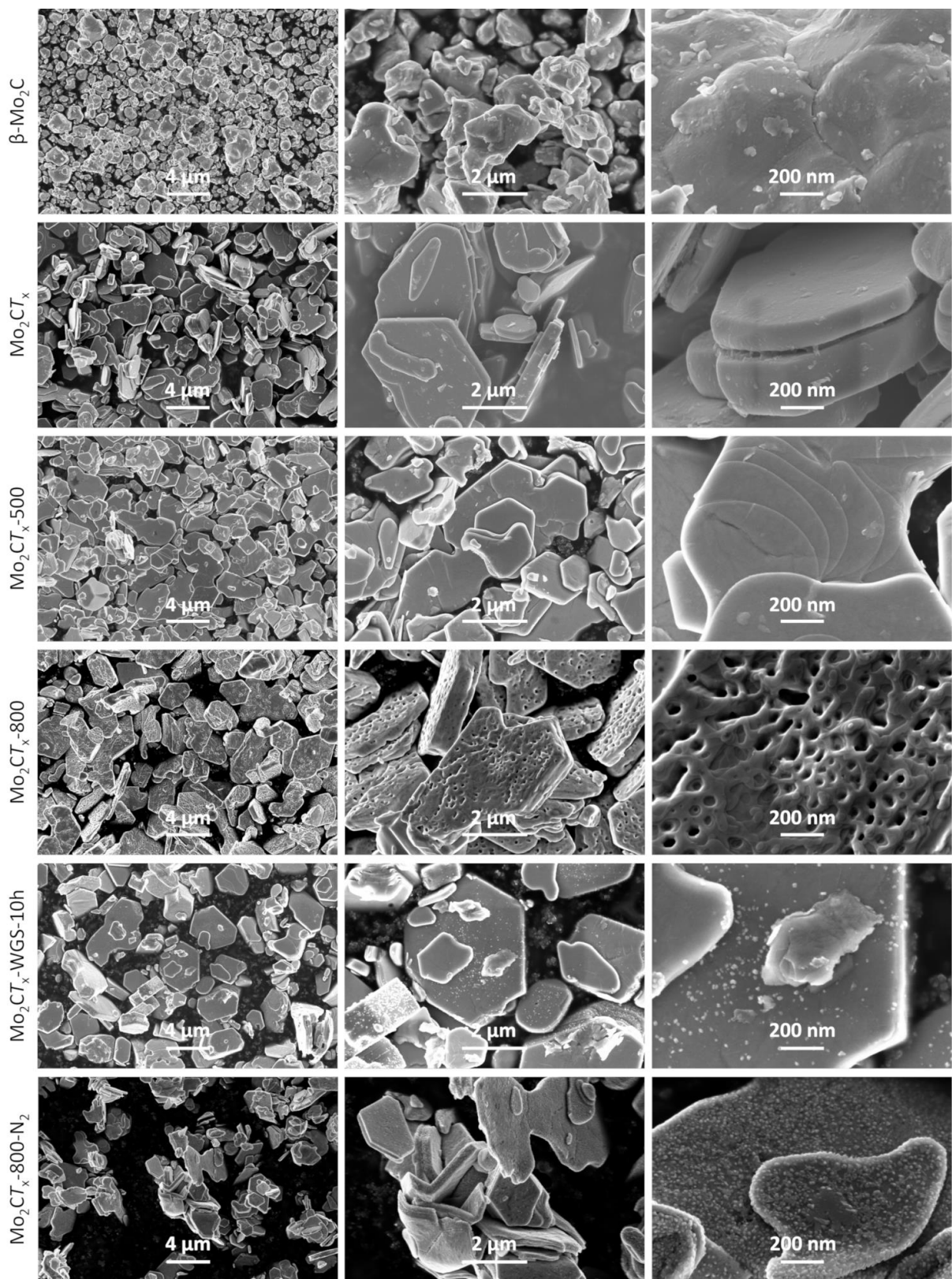


Figure E.4. SEM micrographs of β -Mo₂C, Mo₂CT_x, Mo₂CT_x-500, Mo₂CT_x-800, Mo₂CT_x-WGS-10 h and Mo₂CT_x-800-N₂.

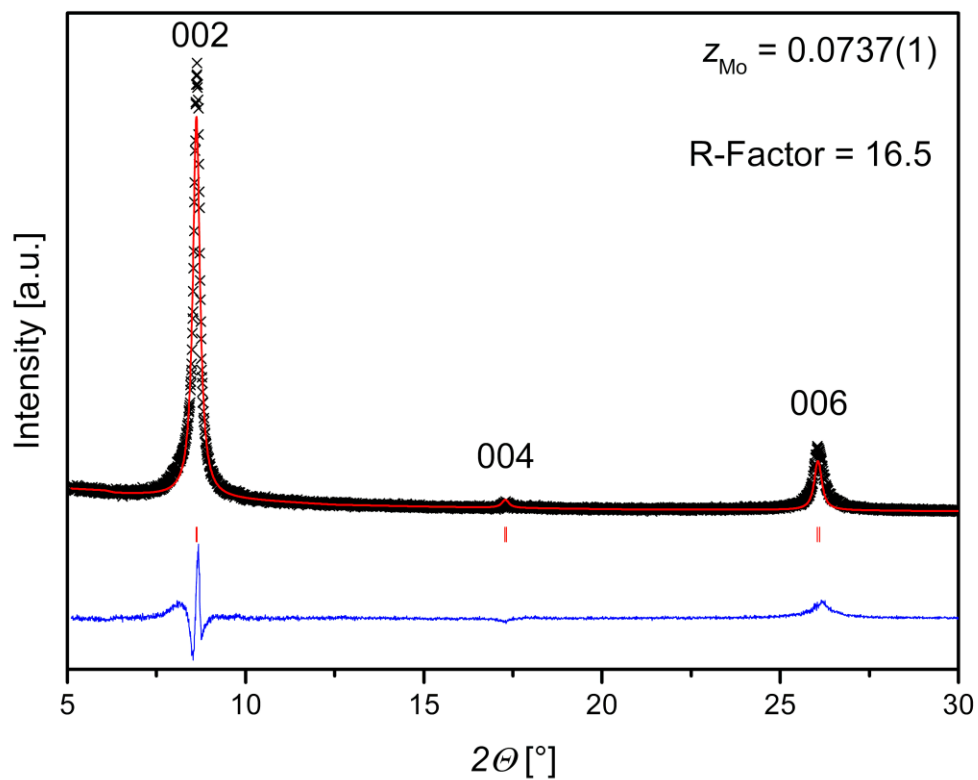


Figure E.5. Rietveld refinement of (0 0 l) family peaks of Mo_2CT_x to determine Mo z coordinate.

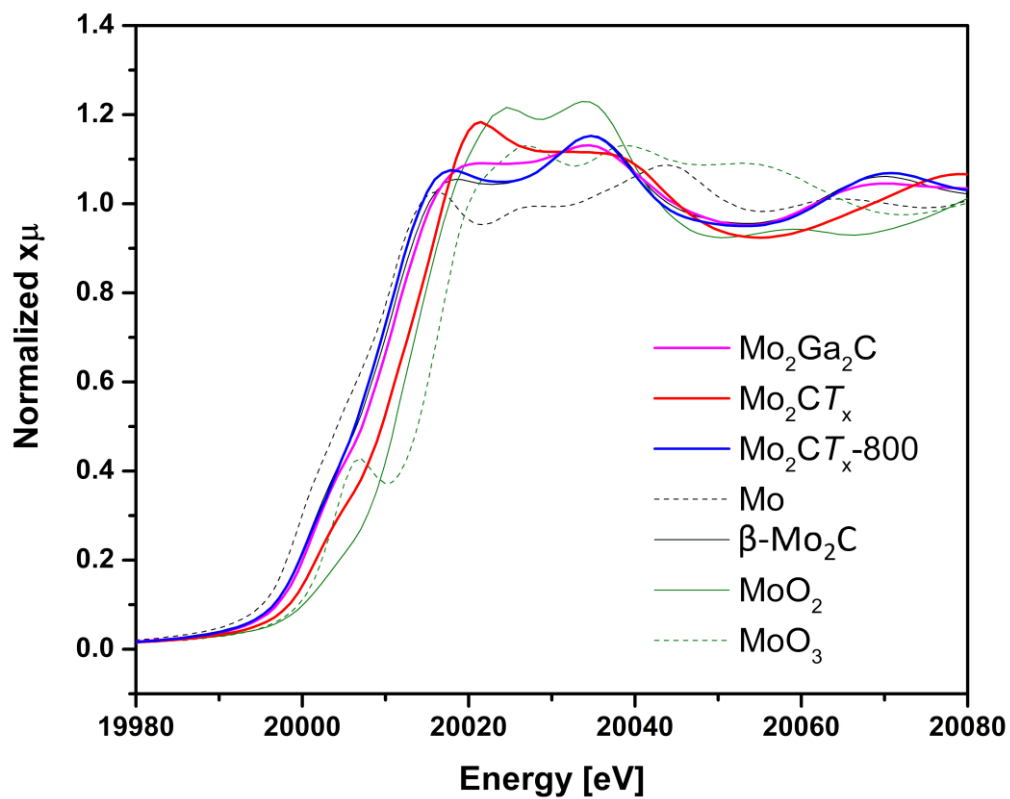


Figure E.6. XANES spectra of $\text{Mo}_2\text{Ga}_2\text{C}$, Mo_2CT_x , $\text{Mo}_2\text{CT}_x\text{-800}$, and reference materials (Mo, $\beta\text{-Mo}_2\text{C}$, MoO_2 , and MoO_3).

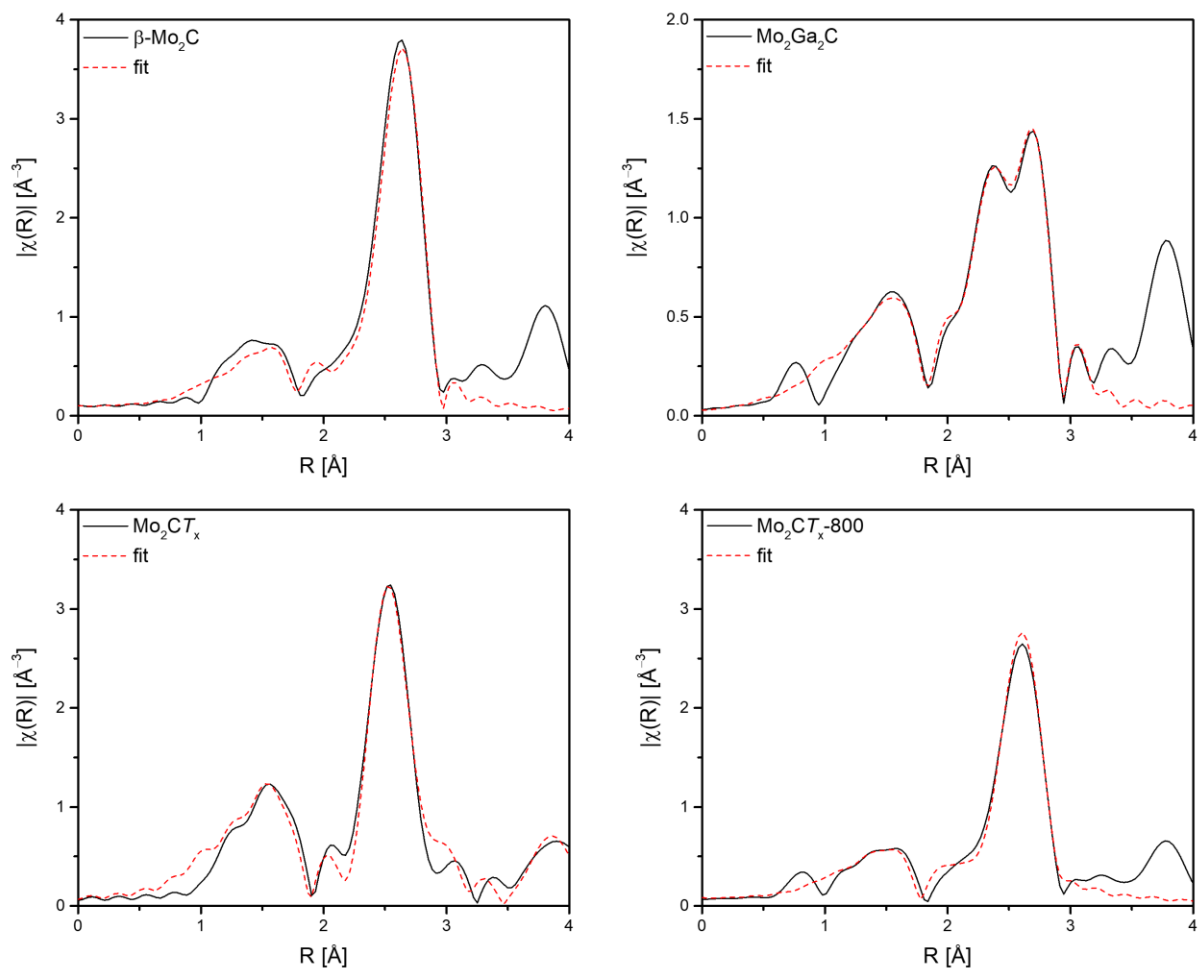


Figure E.7. EXAFS fittings of $\beta\text{-Mo}_2\text{C}$, $\text{Mo}_2\text{Ga}_2\text{C}$, Mo_2CT_x , and $\text{Mo}_2\text{CT}_x\text{-800}$.

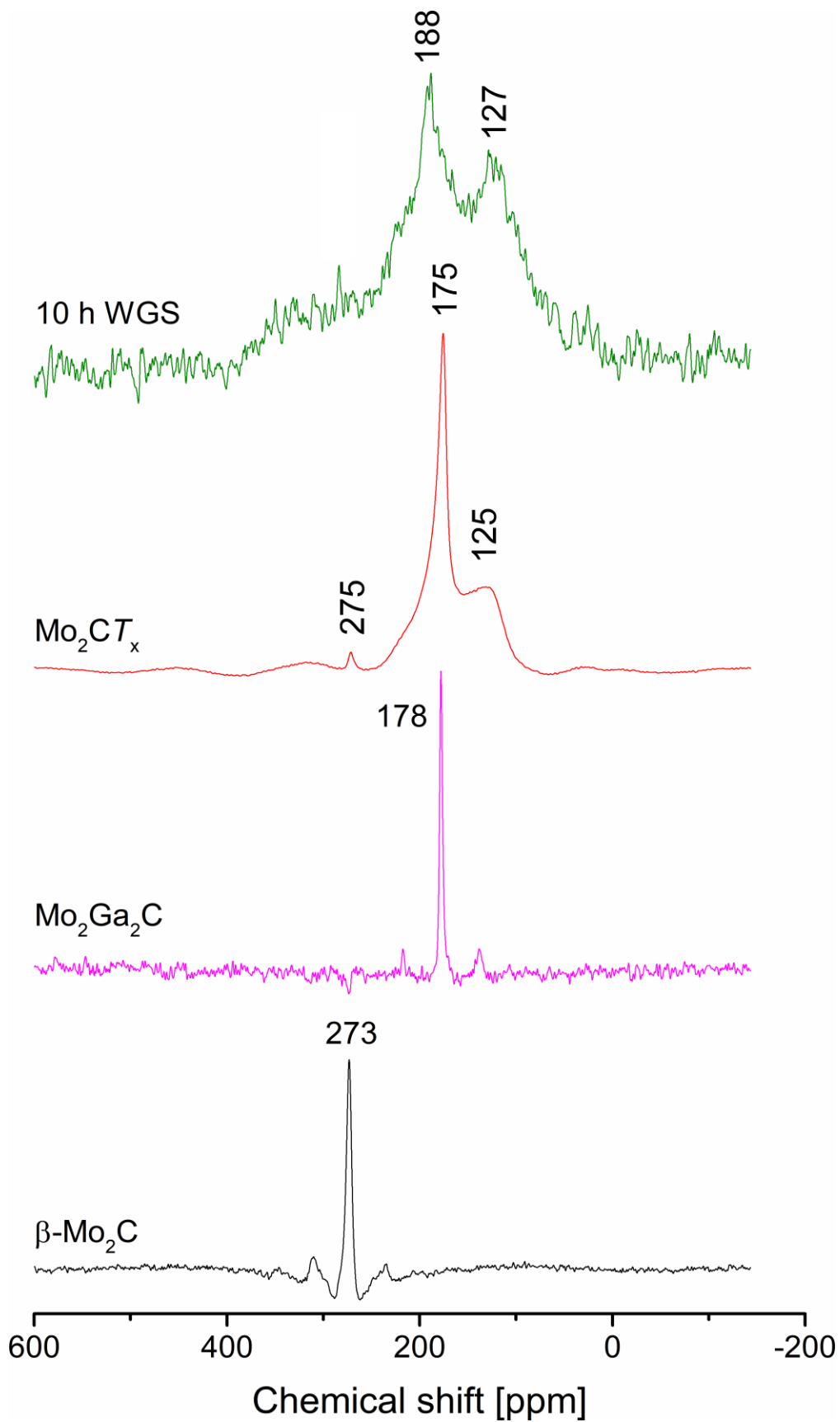


Figure E.8. ^{13}C NMR spectra of $\beta\text{-Mo}_2\text{C}$ and $\text{Mo}_2\text{Ga}_2\text{C}$ (400 MHz, spinning rate 4 kHz, 576 and 2848 scans, respectively), and Mo_2CT_x and Mo_2CT_x after 10 h under WGS reaction (400 MHz, spinning rate 10 kHz, 1200 and 20000 scans, respectively).

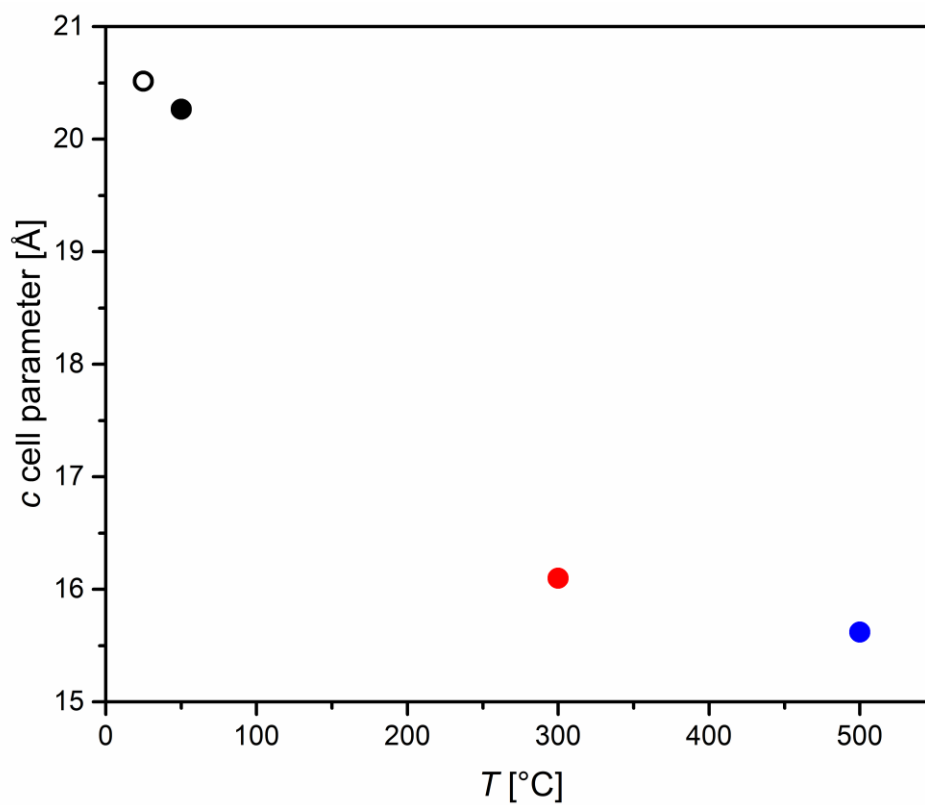


Figure E.9. Mo_2CT_x c cell parameter temperature dependence determined from *in situ* XRD.

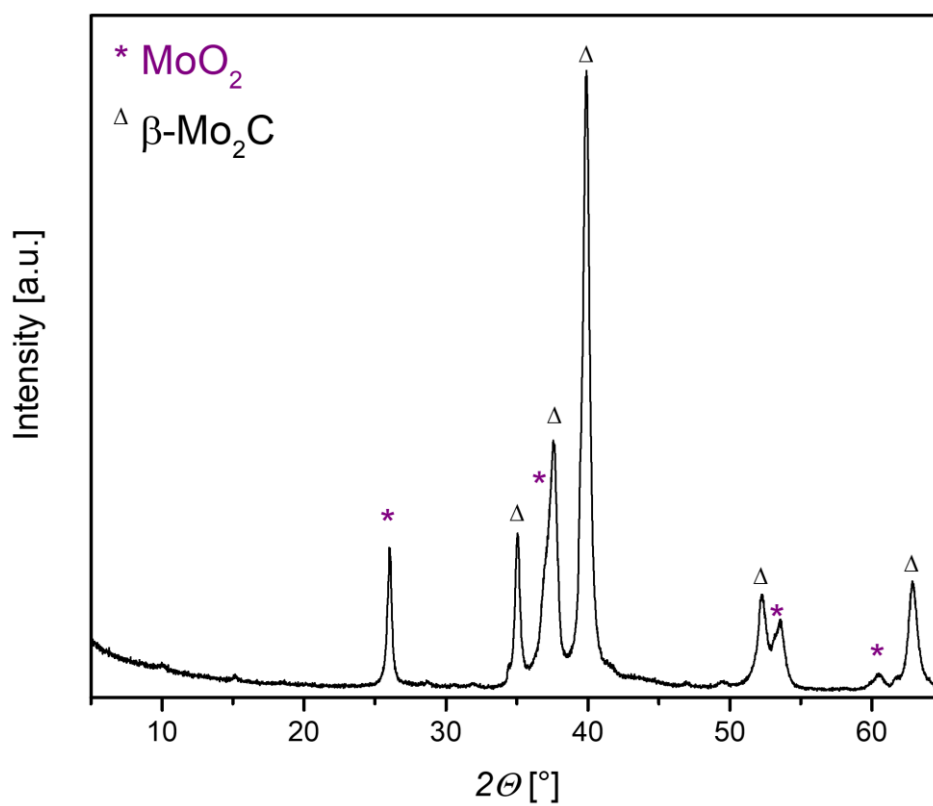


Figure E.10. XRD pattern of Mo_2CT_x annealed at 800 °C in pure N_2 .

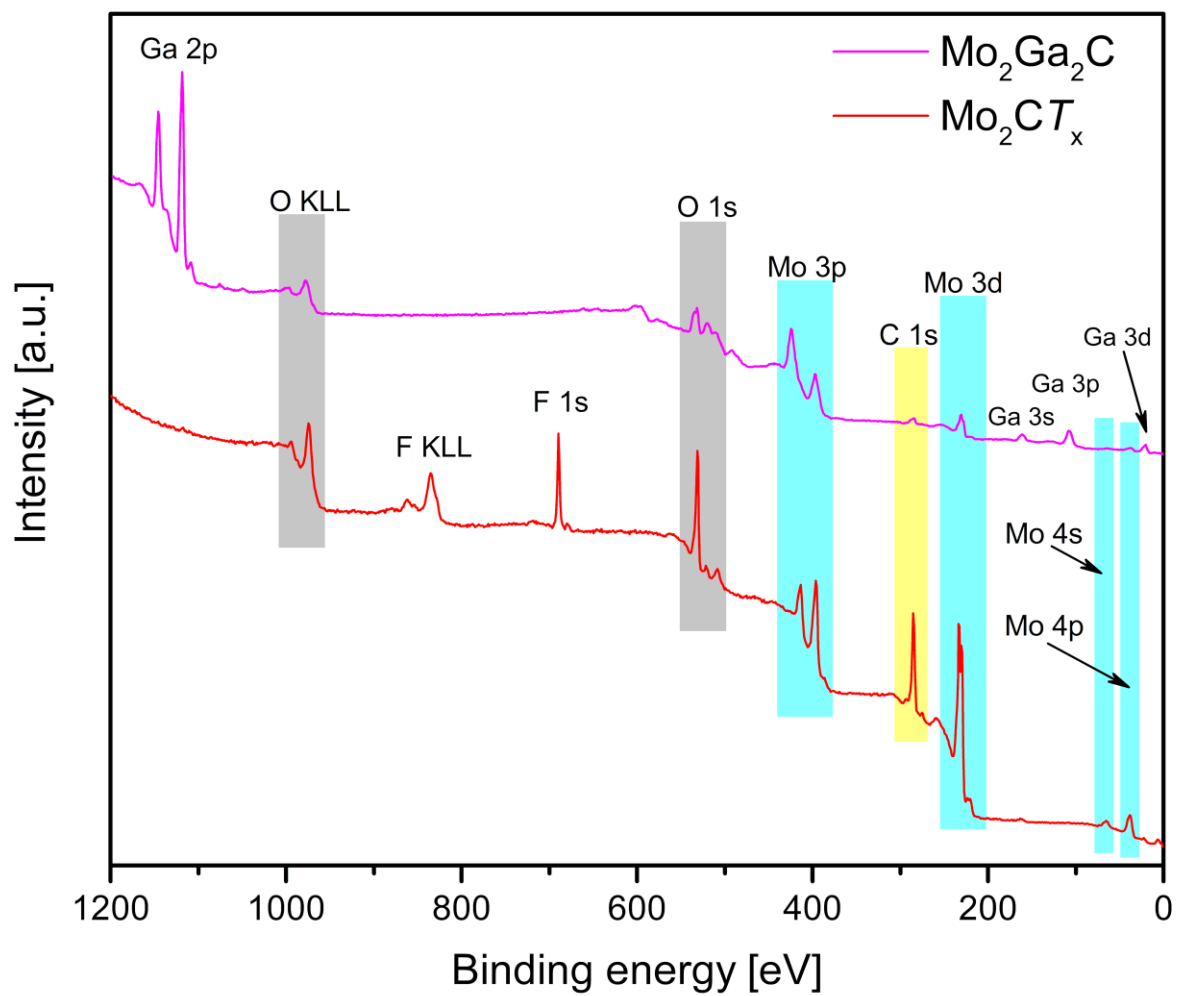


Figure E.11. XPS survey spectra of $\text{Mo}_2\text{Ga}_2\text{C}$ and Mo_2CT_x revealing a total removal of Ga during the etching step and presence of surface O and F.

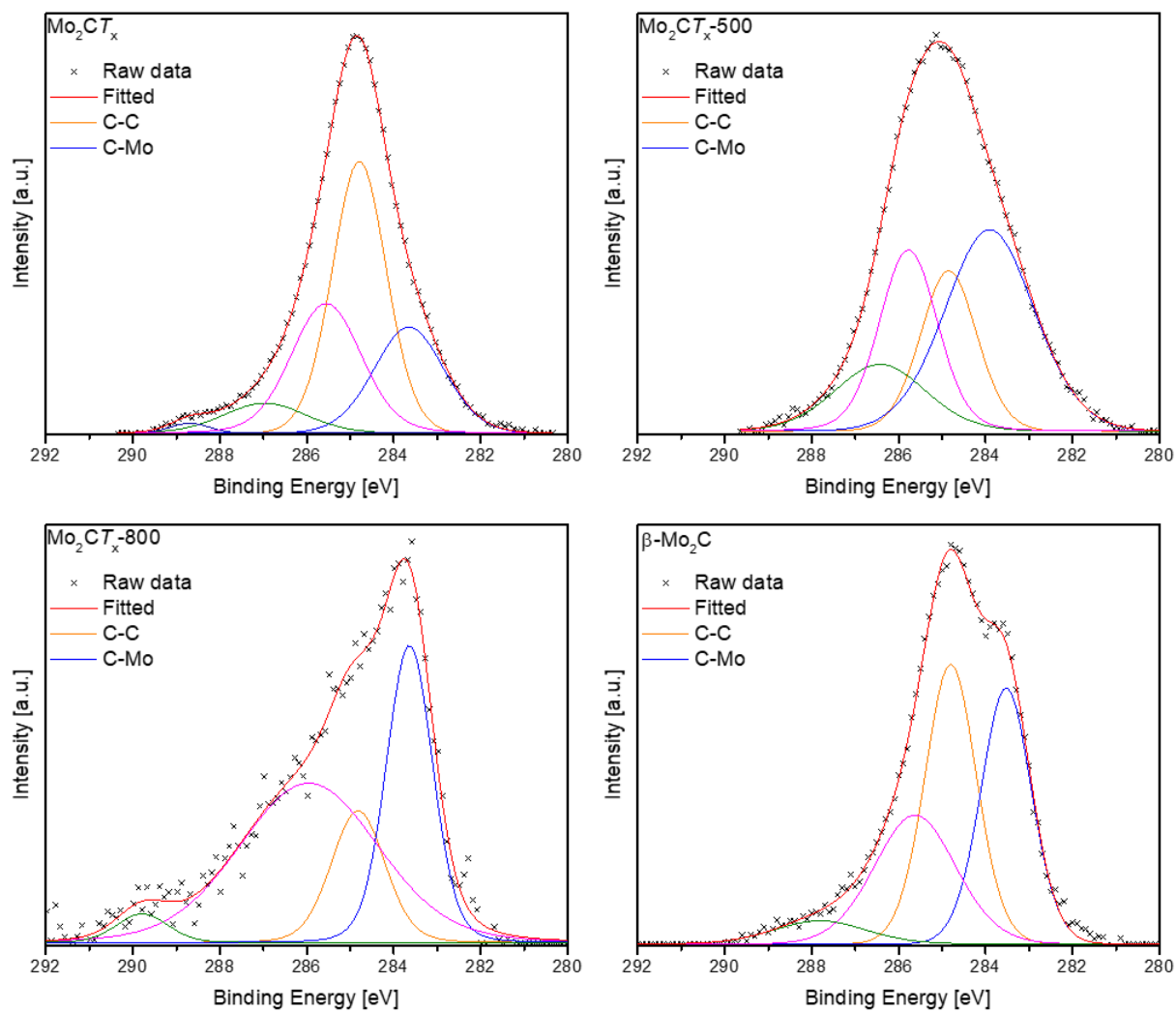


Figure E.12. Deconvolution of C 1s spectra of Mo_2CT_x , $\text{Mo}_2\text{CT}_{x-500}$, $\text{Mo}_2\text{CT}_{x-800}$, and $\beta\text{-Mo}_2\text{C}$.

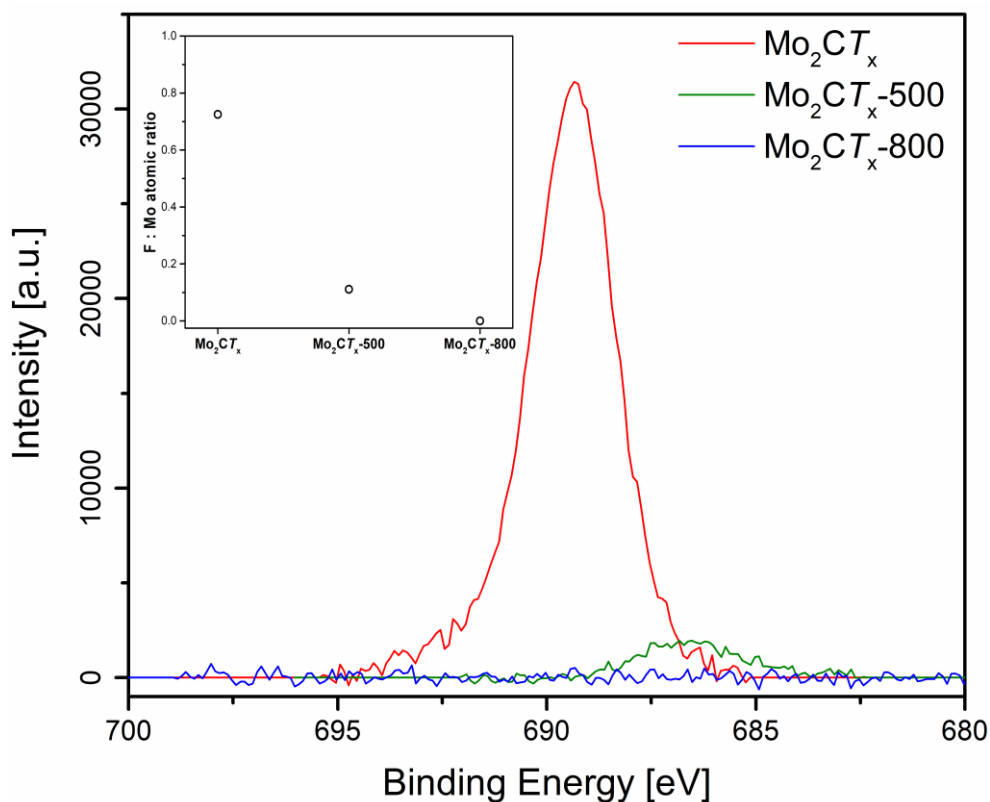


Figure E.13. F 1s XPS spectra of Mo_2CT_x , $\text{Mo}_2\text{CT}_x\text{-500}$, and $\text{Mo}_2\text{CT}_x\text{-800}$. F : Mo ratios are presented in the insert.

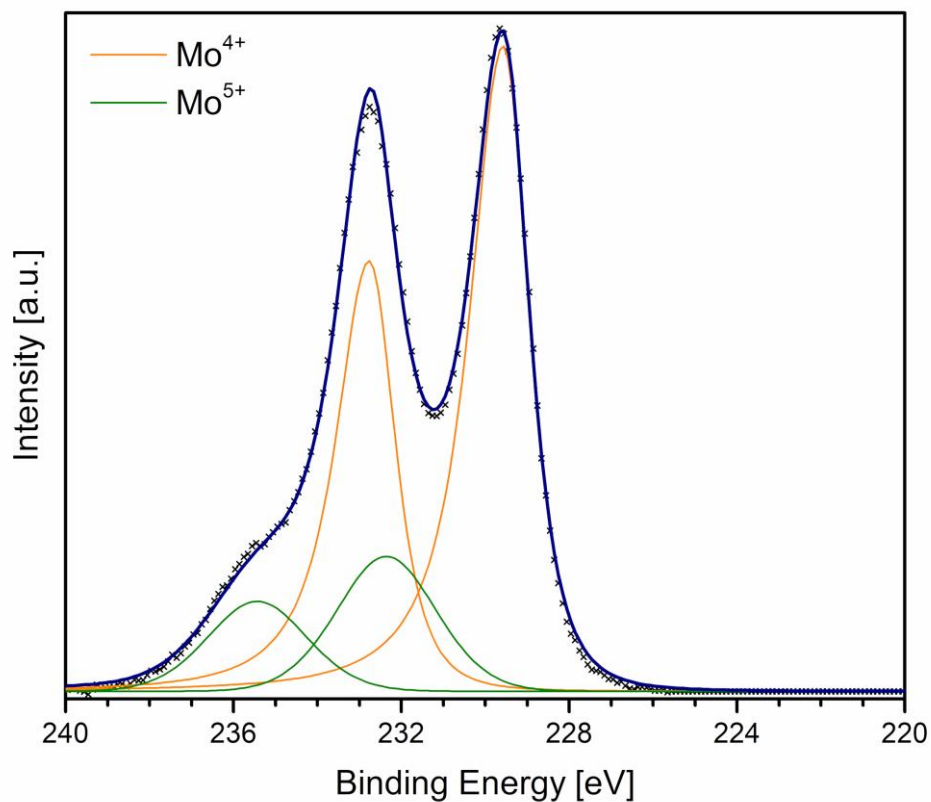


Figure E.14. Deconvolution of Mo 3d spectra of Mo_2CT_x after 10 h at WGS reaction conditions.

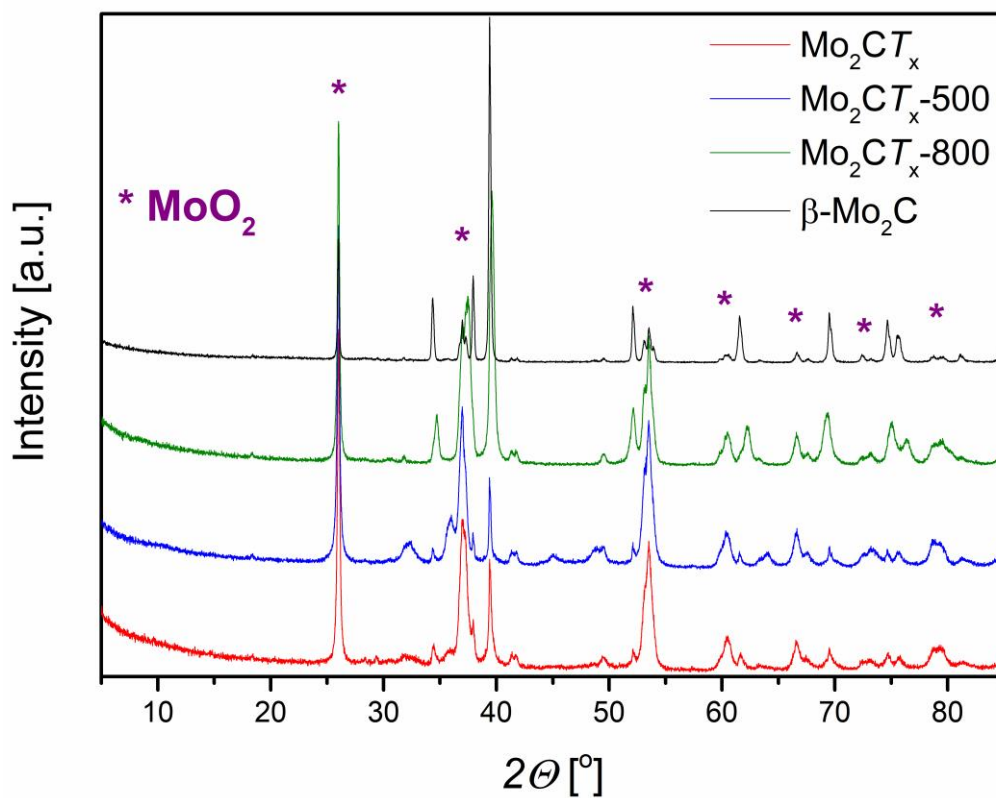


Figure E.15. XRD of samples after WGS testing experiments. Star indicates MoO_2 peaks.

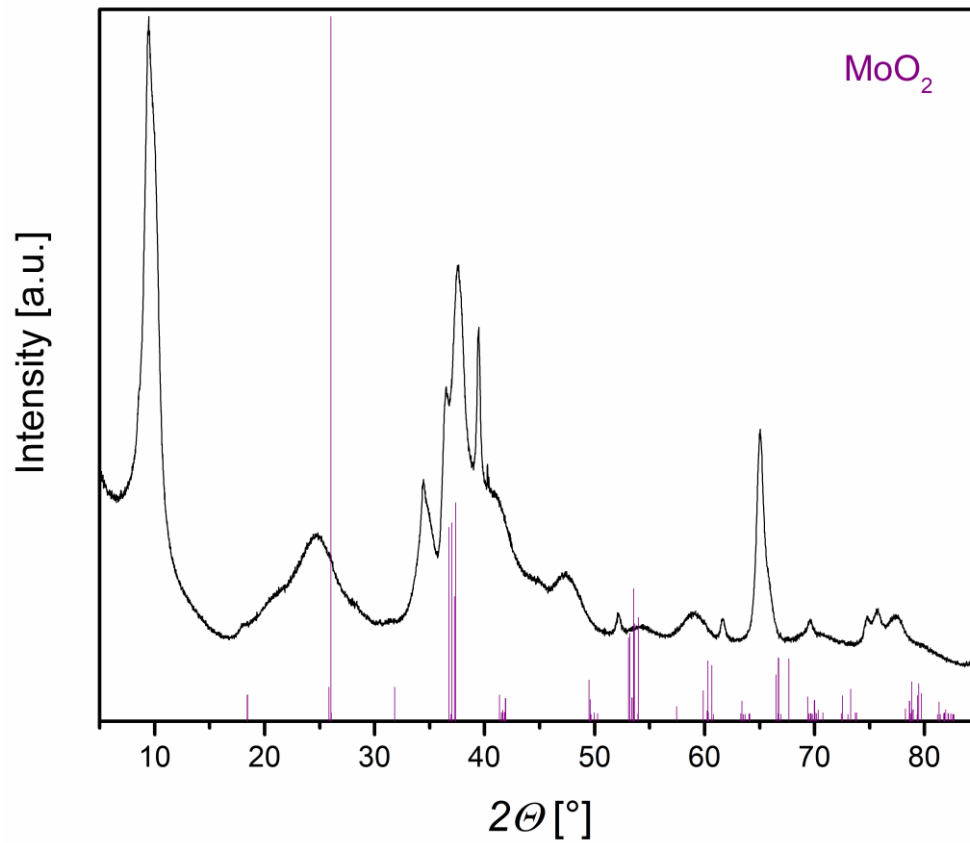


Figure E.16. XRD of Mo_2CT_x after 10 h of WGS testing.

Table E.1. Rietveld refinement parameters of Mo₂Ga₂C. Parameters given in bold were refined during the fitting.

Space group	P6 ₃ /mmc			
<i>a</i> = <i>b</i> , Å	3.03670(2)			
<i>c</i> , Å	18.0849(1)			
Atom parameters				
	<i>x</i>	<i>y</i>	<i>z</i>	<i>Occupancy</i>
Mo	1/3	2/3	0.06593(4)	1
Ga	1/3	2/3	0.68267(6)	1
C	0	0	0	0.5
β-Mo ₂ C content, wt.%	0.55(3)			
Ga ₂ O ₃ content, wt.%	0.22(4)			
R _w	13.6			
R _{wp}	16.5			
R _{exp}	1.93			
χ ²	73.15			

Table E.2. XPS fitting parameters for Mo₂CT_x, Mo₂CT_x-500, Mo₂CT_x-800, Mo₂CT_x-WGS-10h and β-Mo₂C.

State	Mo 3d 5/2 B.E. [eV]	ΔB.E. [eV]	FWHM [eV]	Peak shape	Amount [%]
Mo₂CT_x					
Mo ⁴⁺	229.6	3.15	1.31	LA*	72
Mo ⁵⁺	232.6	3.06	2.62	GL [#]	28
Mo₂CT_x-500					
Carbodic	228.5	3.26	2.31	LA	34
Mo ⁴⁺	229.3	3.17	1.89	LA	66
Mo₂CT_x-800					
Carbodic	228.6	3.18	1.29	LA	100
β-Mo₂C					
Carbodic	228.5	3.17	1.26	LA	100
Mo₂CT_x-WGS-10h					
Mo ⁴⁺	229.6	3.19	1.45	LA*	77.5
Mo ⁵⁺	232.4	3.07	2.77	GL [#]	22.5

* LA- Lorentzian Asymmetric line shape, [#] GL- Gaussian/Lorentzian line shape.

F. Supplementary information for Chapter 7

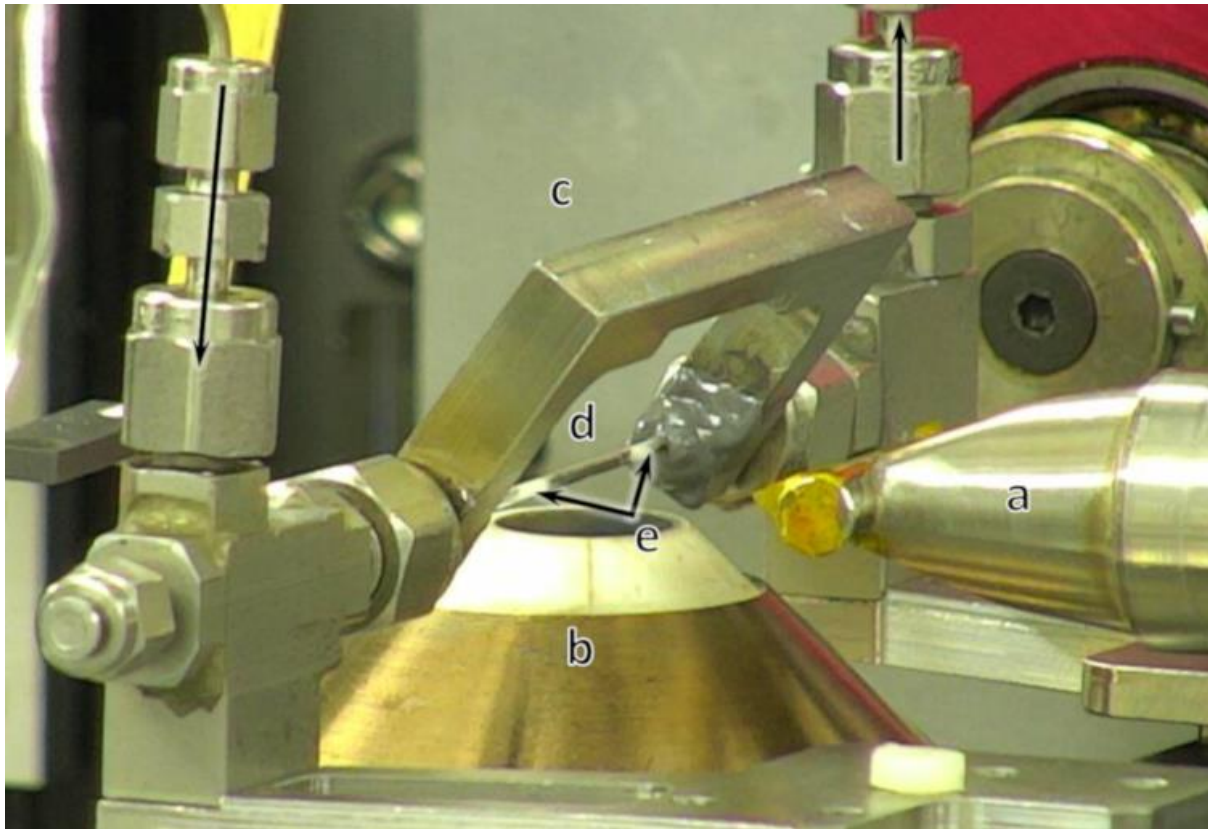


Figure F.1. Experiment setup for the *in situ* experiments performed at SNBL.

a) incident beam, b) heating air gun, c) capillary cell, d) sample, e) quartz wool plugs. Arrows indicate the direction of the gas flow.

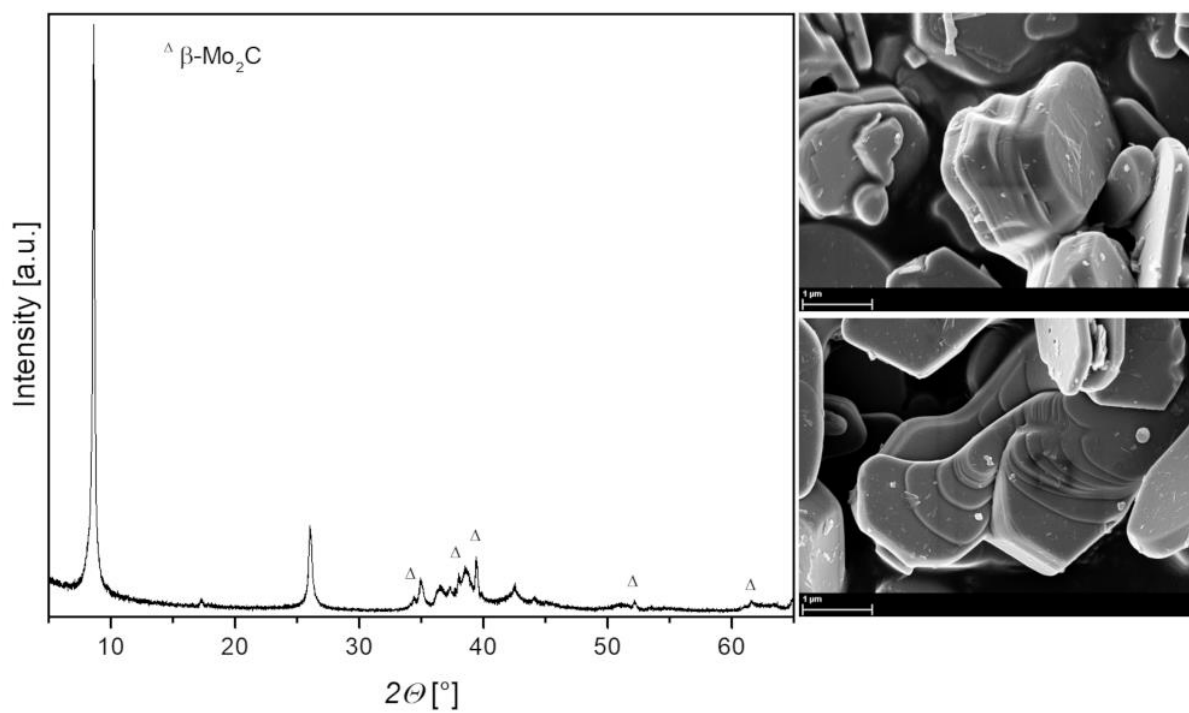


Figure F.2. XRD pattern and SEM images of synthesized $m\text{-Mo}_2\text{CT}_x$.

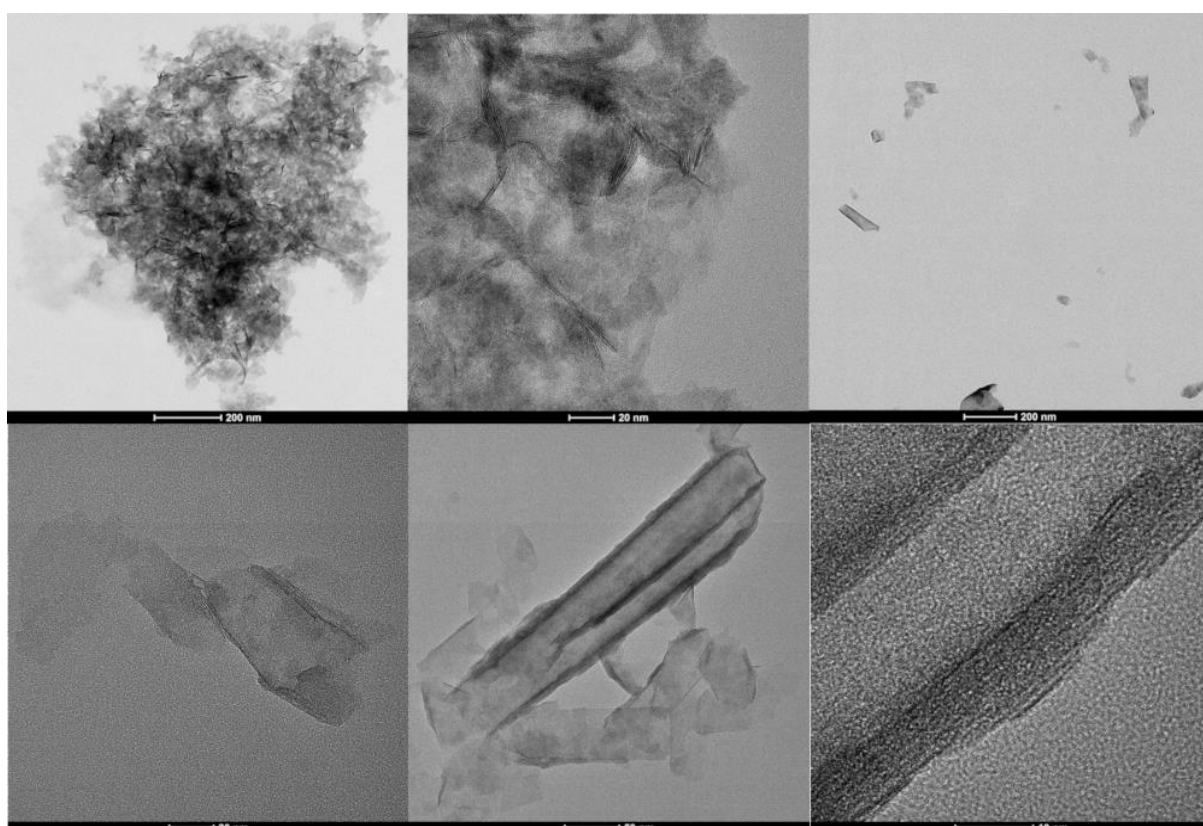


Figure F.3. TEM images of exfoliated $2\text{D-Mo}_2\text{CT}_x$.

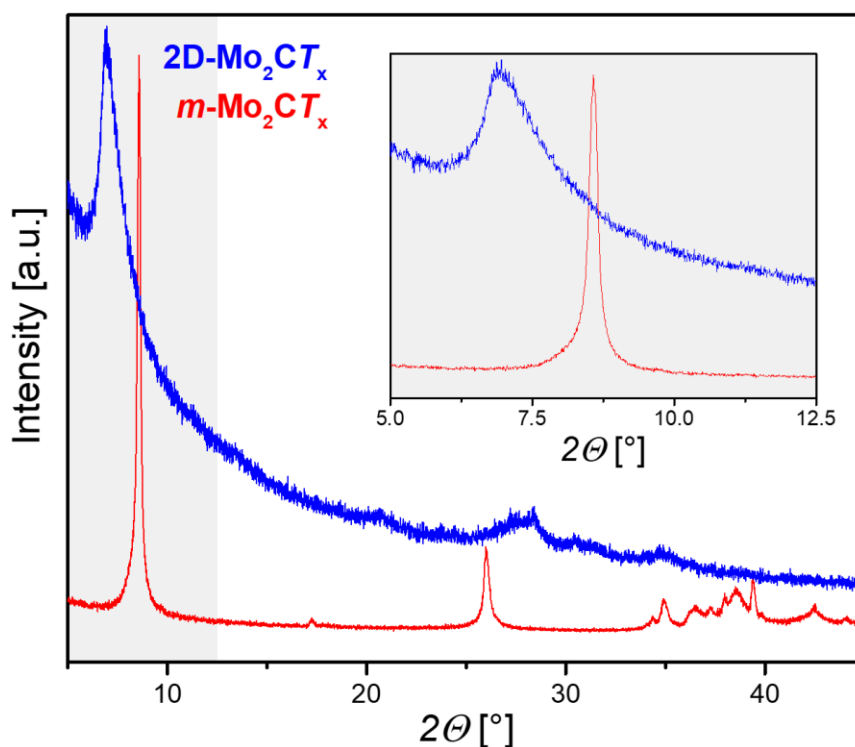


Figure F.4. XRD pattern of $m\text{-Mo}_2\text{CT}_x$ and delaminated $2\text{D-Mo}_2\text{CT}_x$.

X-Ray powder diffraction pattern of the dried delaminated Mo_2CT_x is similar to that of $m\text{-Mo}_2\text{CT}_x$ material, although with significantly broader peaks shifted towards smaller 2θ values relative to peaks of non-delaminated Mo_2CT_x (Figure F.4). The shift towards smaller 2θ values can be related to the increase of the interlayer distance from ca. 7 \AA in $m\text{-Mo}_2\text{CT}_x$ material to ca. 10 \AA in $d\text{-Mo}_2\text{CT}_x$, caused by the intercalation of ethanol molecules in between the individual $2\text{D-Mo}_2\text{CT}_x$ layers. The broadening of the peak at $2\theta = 7^\circ$ is explained by the loss of coherence (more disordered structure of the nanosheets) during delamination of individual $2\text{D-Mo}_2\text{CT}_x$ flakes and their non-regular re-stacking upon drying of the solution with $d\text{-Mo}_2\text{CT}_x$.

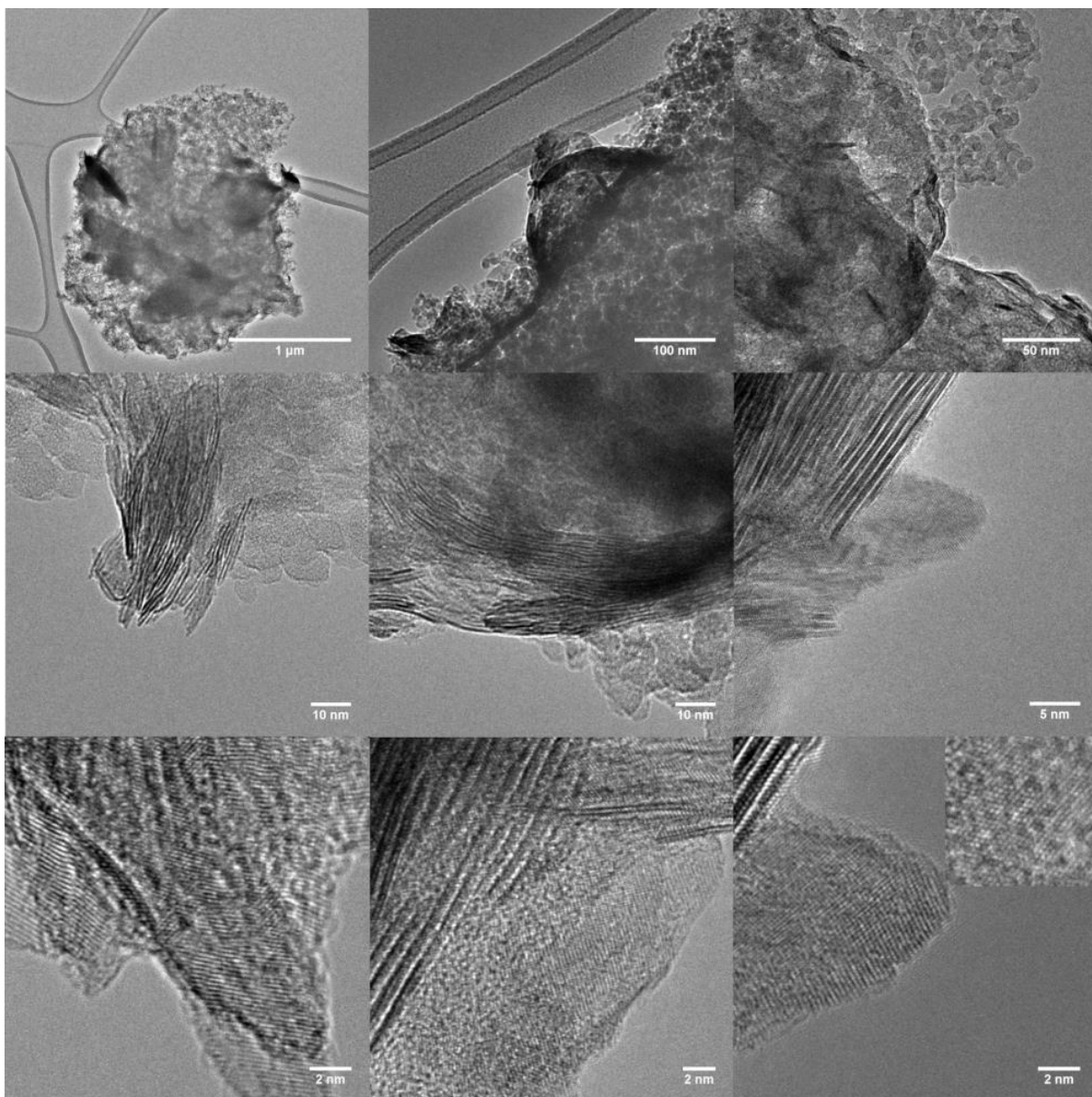


Figure F.5. TEM images of 2D-Mo₂CT_x/SiO₂.

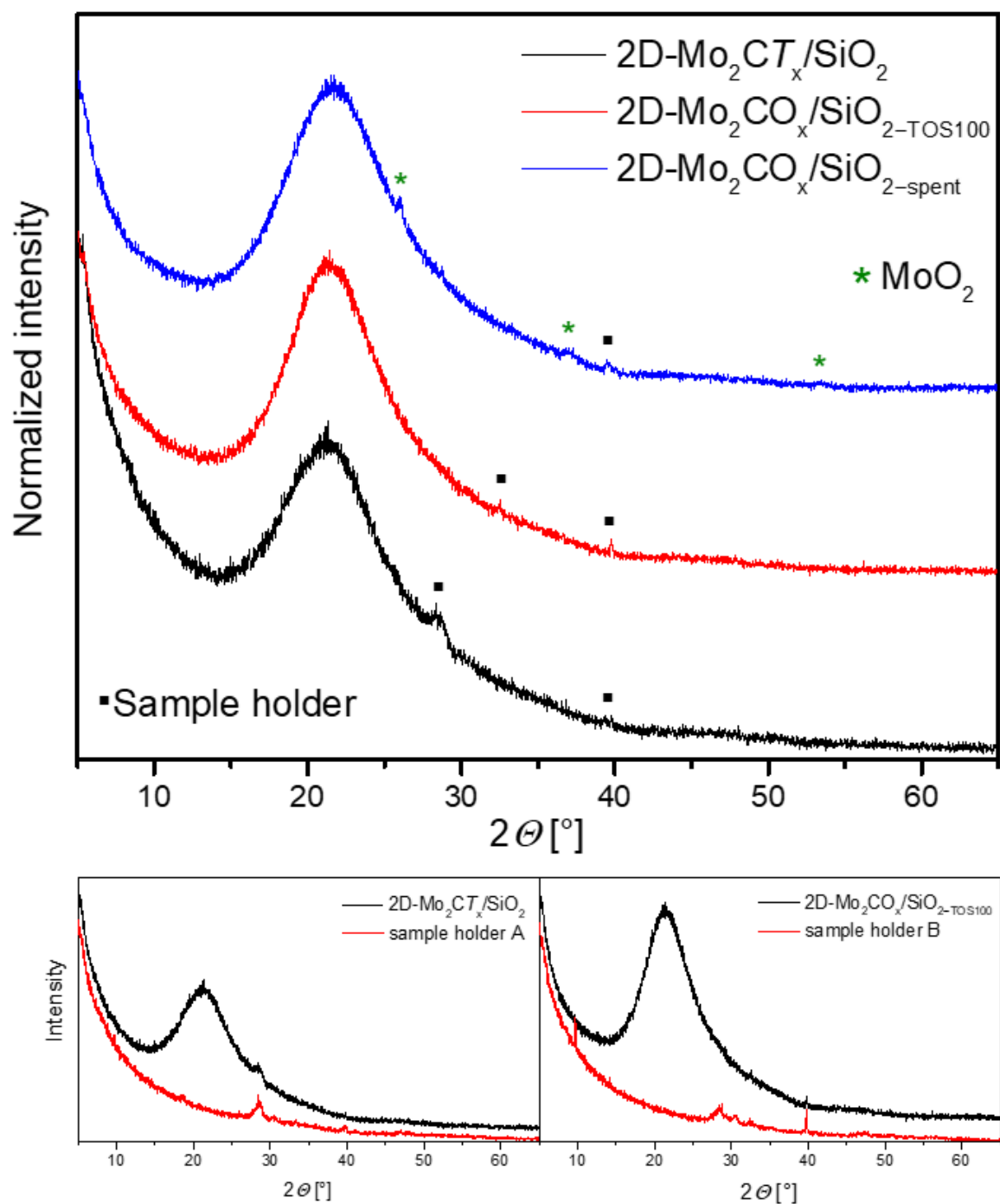


Figure F.6. XRD pattern of 2D-Mo₂CT_x/SiO₂, 2D-Mo₂CO_x/SiO_{2-TOS100} and 2D-Mo₂CO_x/SiO_{2-spent}.

XRD pattern of 2D-Mo₂CT_x/SiO₂ and 2D-Mo₂CO_x/SiO_{2-TOS100} show no presence of crystalline peaks confirming a good dispersion of individual Mo₂CT_x nanosheets and their impressive stability under DRM conditions.

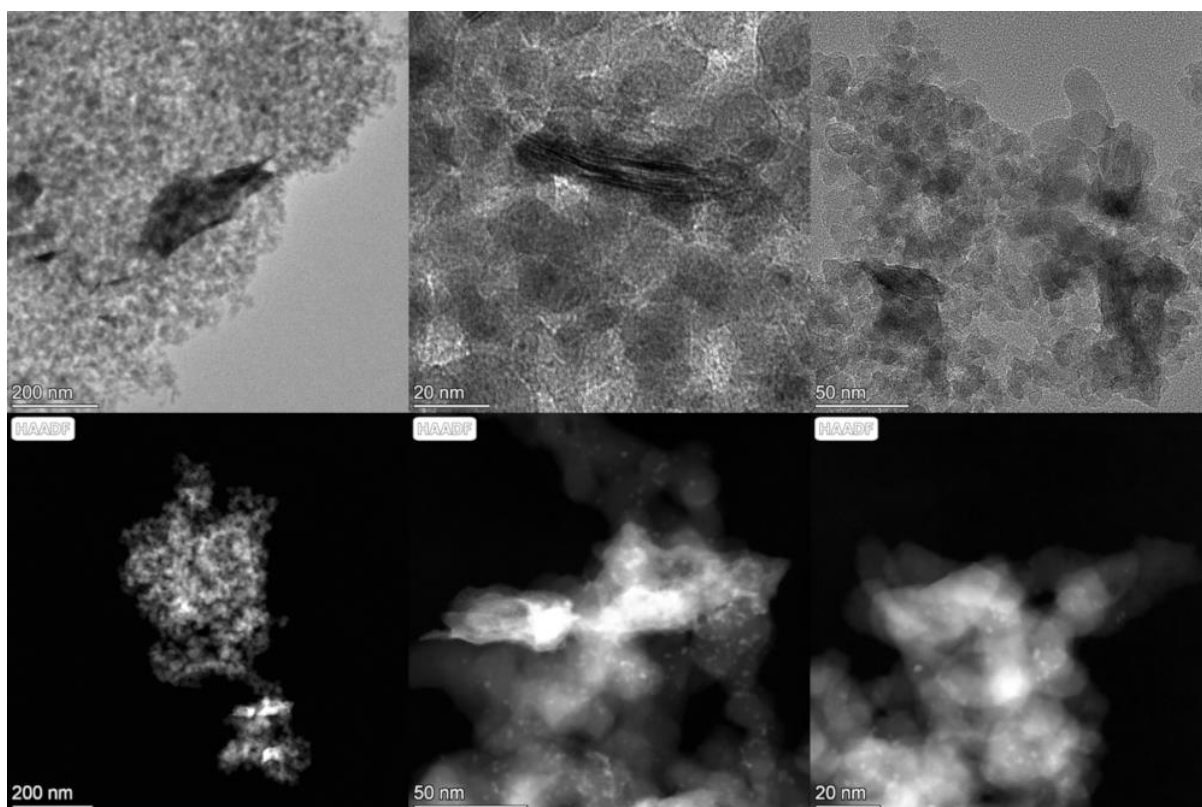


Figure F.7. TEM images of 2D-Mo₂CT_x/SiO₂ aged in air for ca. 1 month.

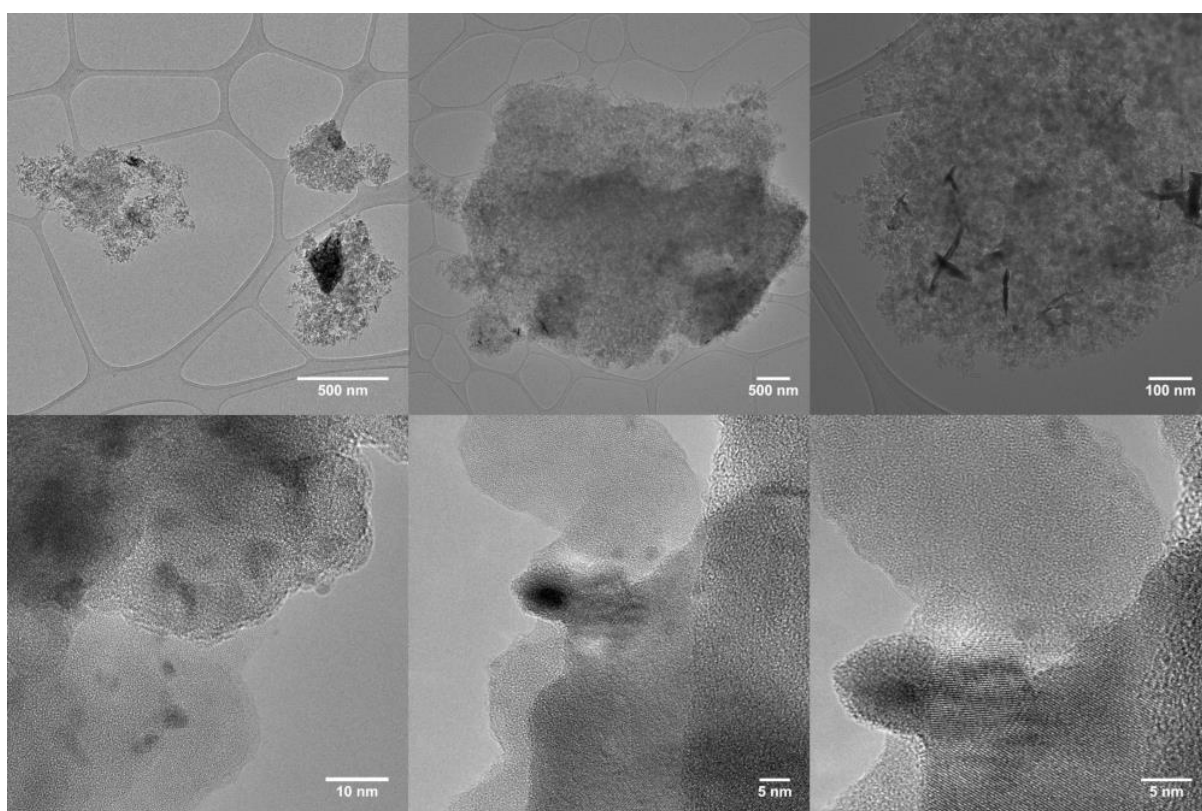


Figure F.8. TEM images of 2D-Mo₂C/SiO₂.

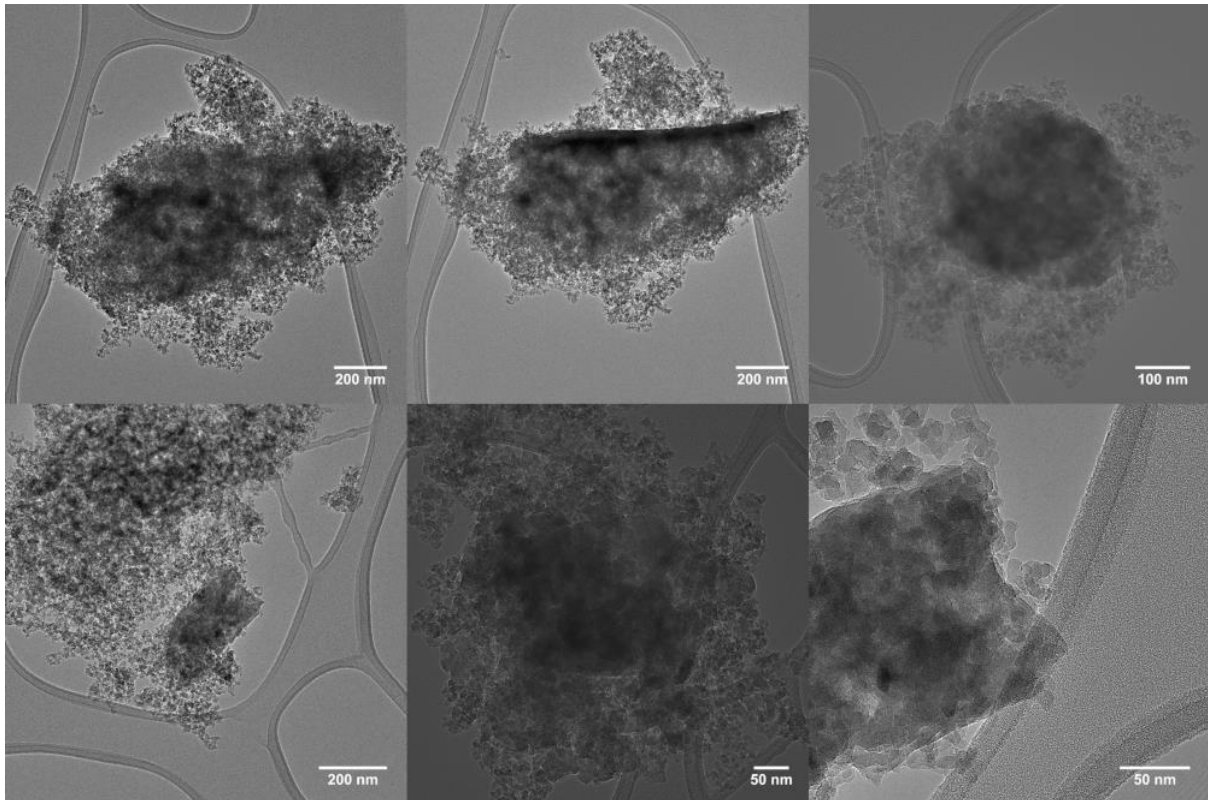


Figure F.9. TEM images of 2D-Mo₂CO_x/SiO₂.

Note that top left and top middle images represent the same agglomerate of Aerosil 300 particles. A scrolling of 2D-Mo₂CO_x nanosheets was observed after exposure of the specimen on the top left to the higher electron beam doze rate (top middle), confirming that the higher contrast structure on the top left image (and, therefore, on all other TEM images) corresponds to 2D-Mo₂CO_x nanosheets.

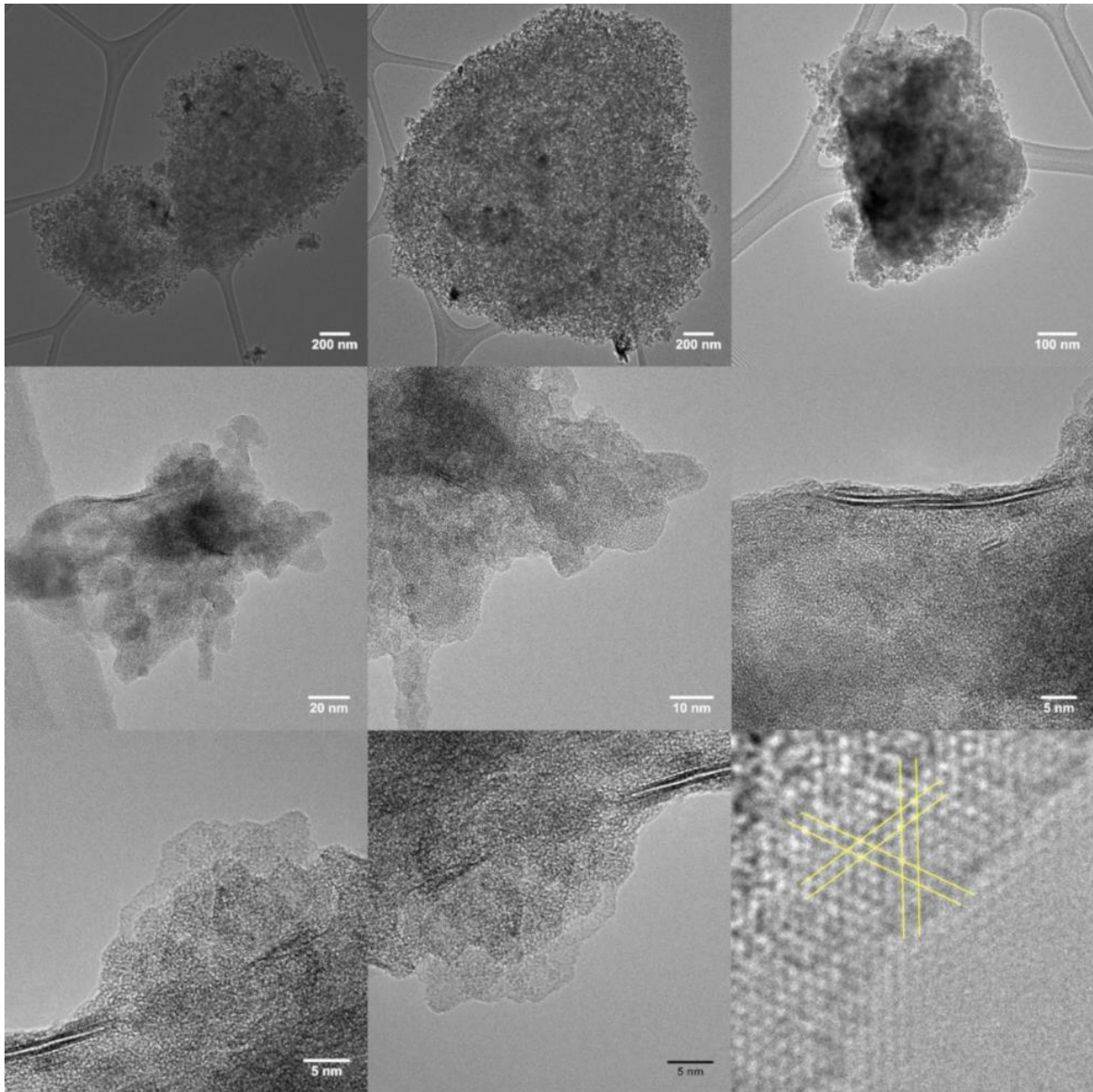


Figure F.10. TEM images of 2D-Mo₂CO_x/SiO₂-regen.

This sample was regenerated in CO₂ at 800 °C for 1 h after 100 min of DRM reaction.

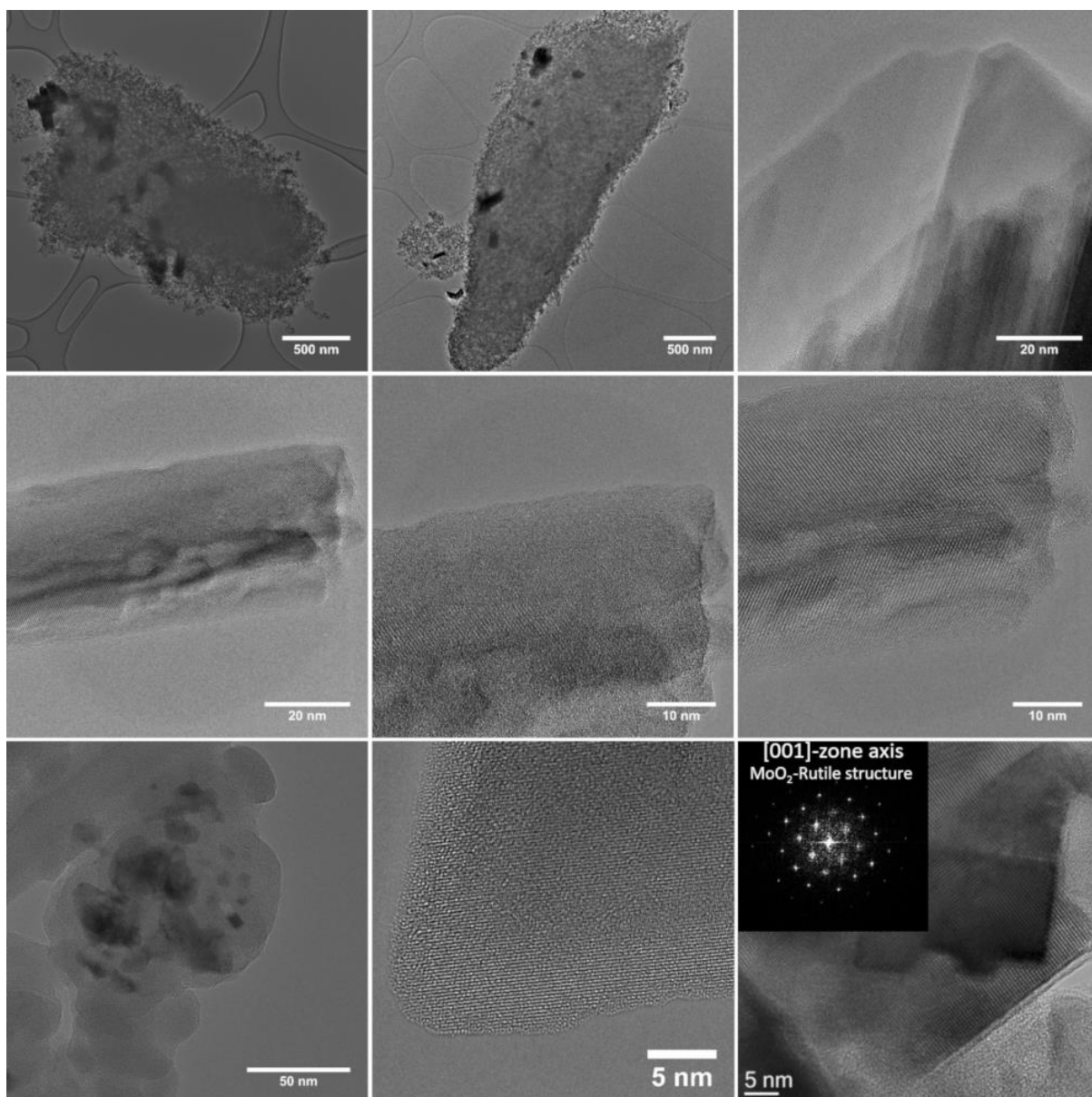


Figure F.11. TEM images of 2D-Mo₂CO_x/SiO₂-spent.

The presence of both 2D nanosheets and MoO₂ particles is observed

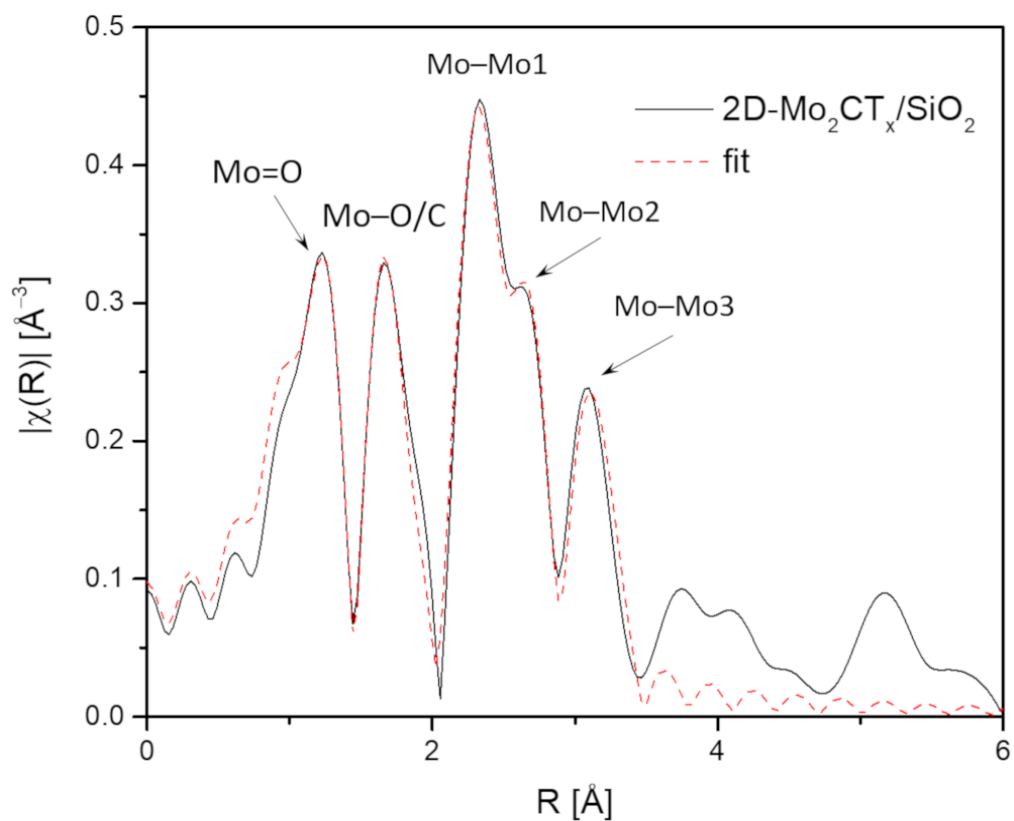


Figure F.12. EXAFS fitting of 2D-Mo₂CT_x/SiO₂.

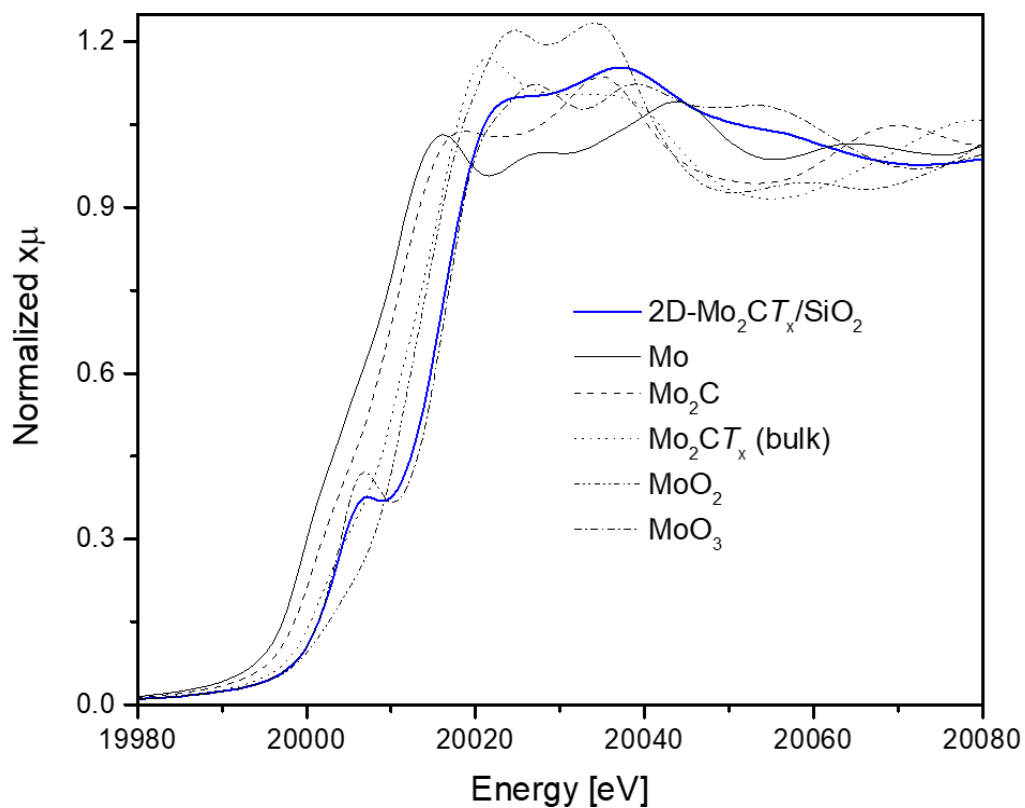


Figure F.13. XANES spectra of 2D-Mo₂CT_x/SiO₂ and reference materials.

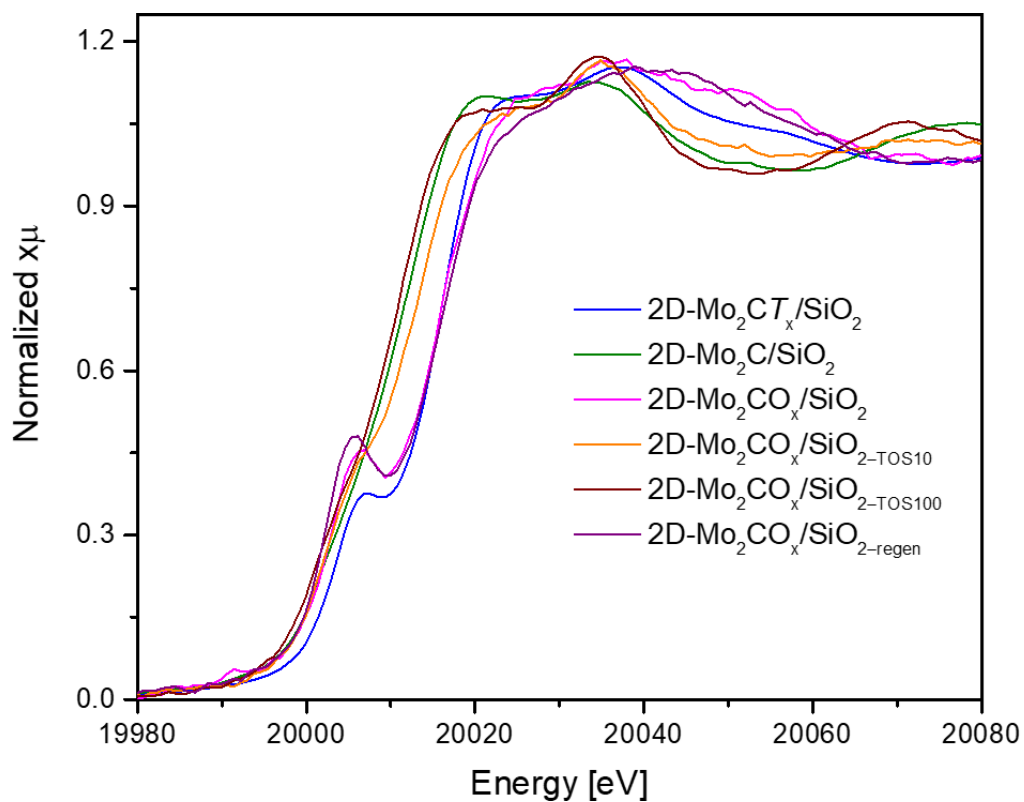


Figure F.14. XANES spectra of 2D-Mo₂CT_x/SiO₂ after different treatments.

Table F.1. Mo K edge position and calculated Mo oxidation state for 2D-Mo₂CT_x/SiO₂ treated under different conditions and reference materials.

Sample	Mo K-edge position [eV]	Mo oxidation state
2D-Mo ₂ CT _x /SiO ₂	20015.8	5.5
2D-Mo ₂ C/SiO ₂	20000.8	0.2
2D-Mo ₂ CO _x /SiO ₂	20015.7	5.5
2D-Mo ₂ CO _x /SiO ₂ -TOS10	20011.5	4.0
2D-Mo ₂ CO _x /SiO ₂ -TOS100	20009.0	3.0
2D-Mo ₂ CO _x /SiO ₂ -2-regen	20015.9	5.5
Mo	20000.0	0
β-Mo ₂ C	20000.7	0.2
MoO ₂	20011.4	4
MoO ₃	20017.0	6
Mo ₂ CT _x	20010.9	3.8

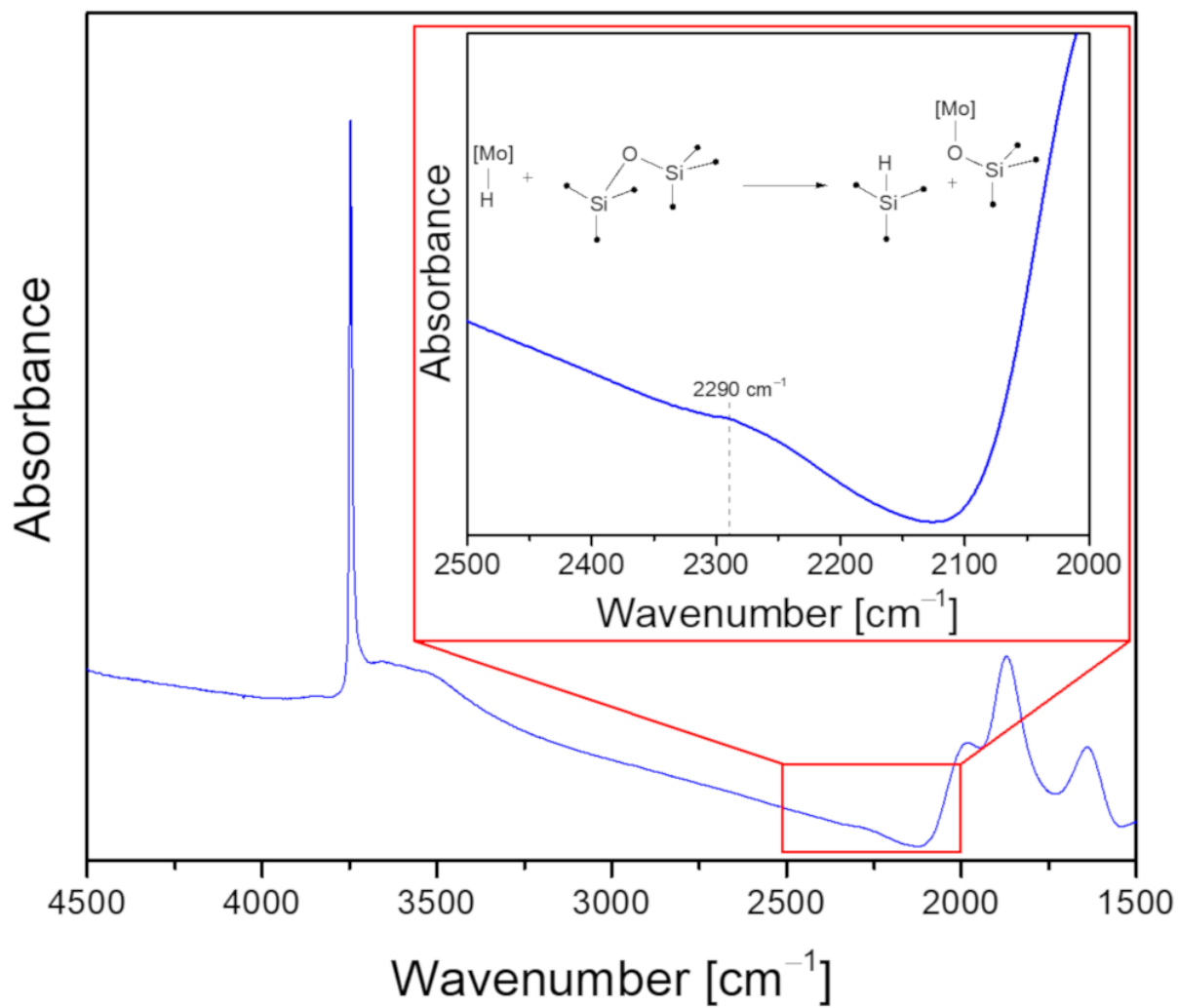


Figure F.15. IR spectrum of 2D-Mo₂C/SiO₂ with a zoomed in area of a [≡Si-H] region.

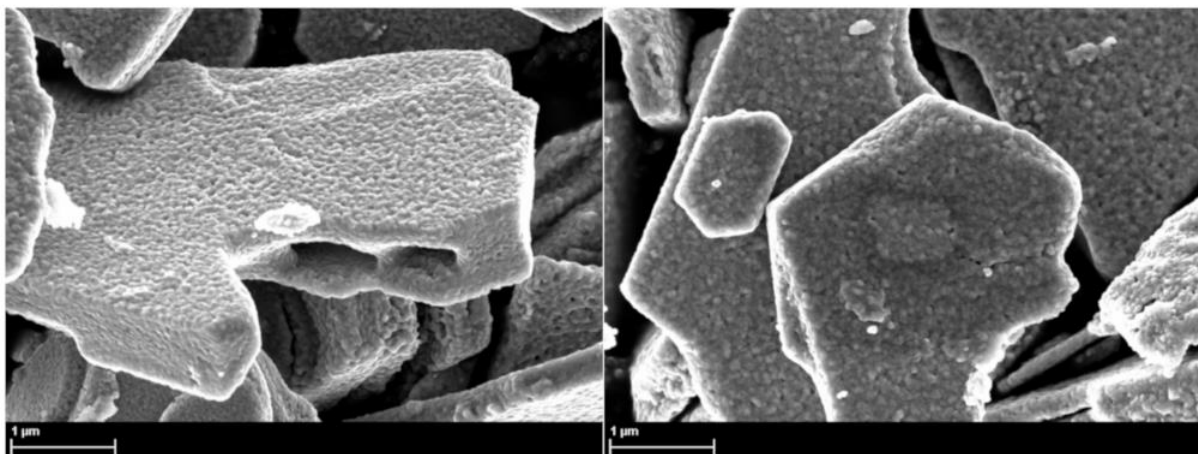
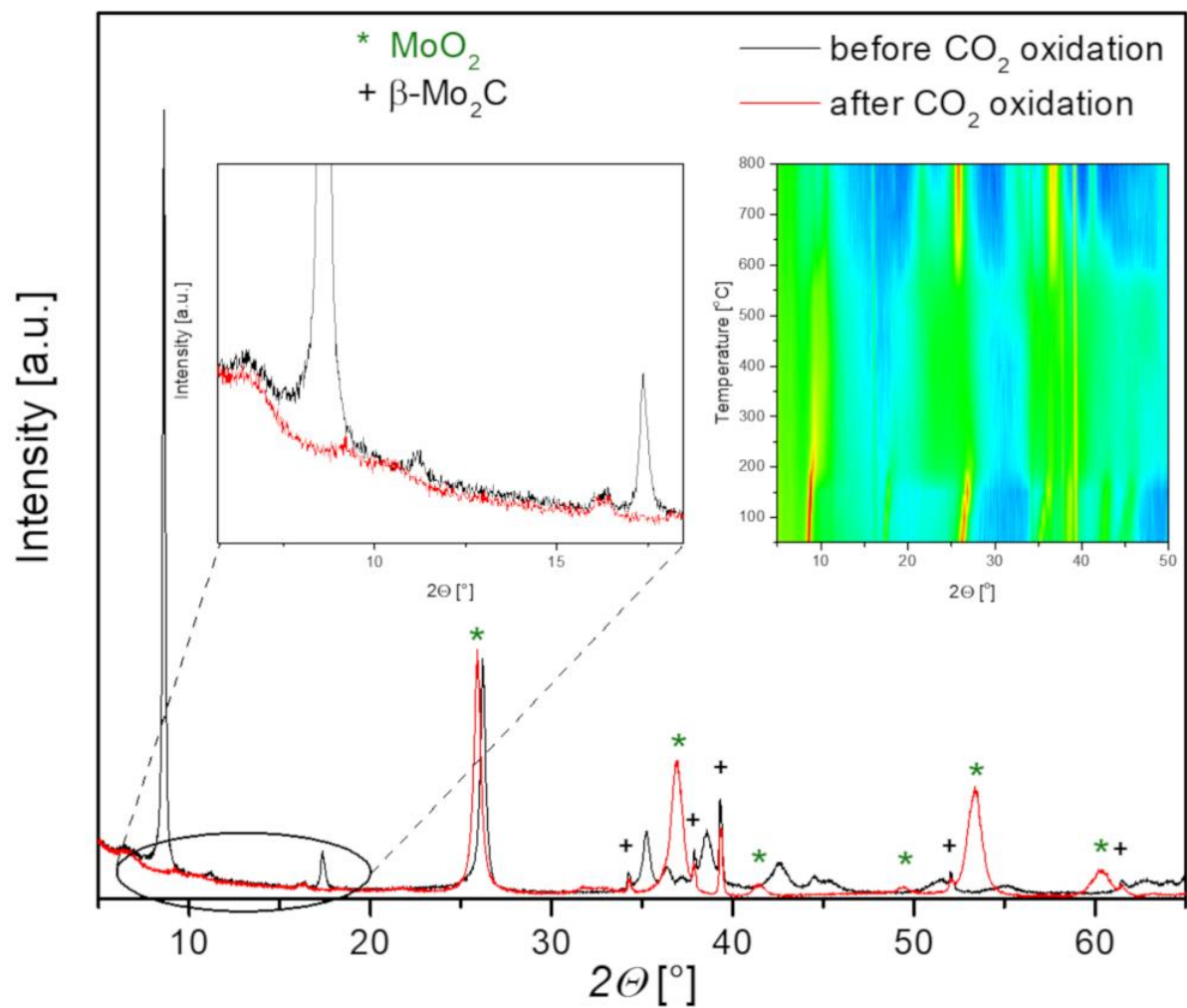


Figure F.16. Top: XRD pattern of $m\text{-Mo}_2\text{CT}_x$ before (black) and after (red) oxidation in CO_2 at 800 °C. Inset: *In situ* XRD pattern of bulk Mo_2CT_x oxidation in CO_2 (20 vol.% CO_2 in N_2 , XRD pattern every 50 °C). Bottom: SEM images of Mo_2CT_x annealed at 800 °C in pure CO_2 .

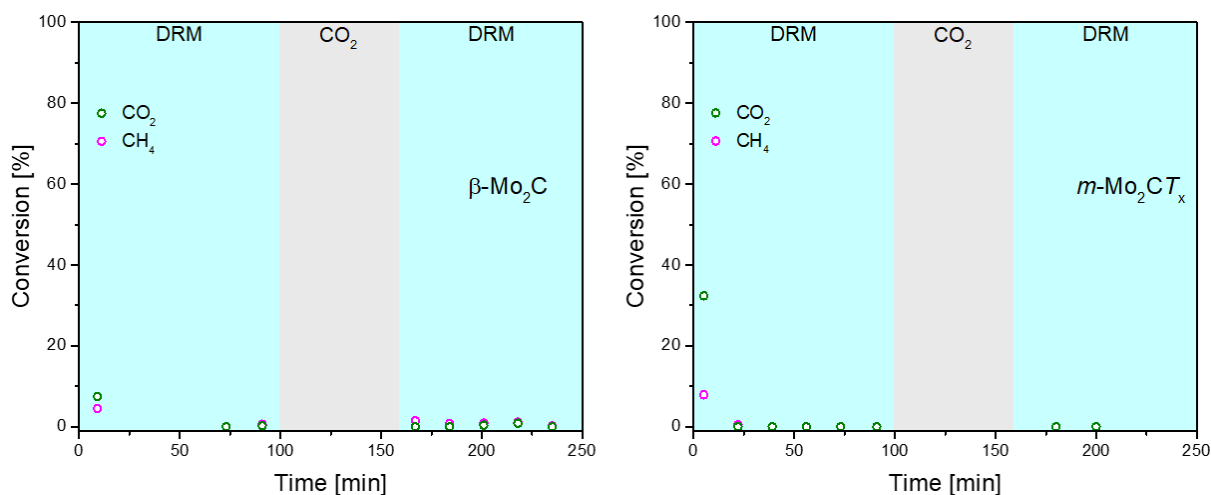


Figure F.17. Catalytic performance of $\beta\text{-Mo}_2\text{C}$ (left) and $m\text{-Mo}_2\text{CT}_x$ (right) in DRM.

Reaction conditions: 800 °C, 1 bar, $\text{CH}_4\text{:CO}_2 = 1\text{:}1$, total flow rate of 20 mL min^{-1} , 0.1 and 0.03 g of catalyst, respectively.

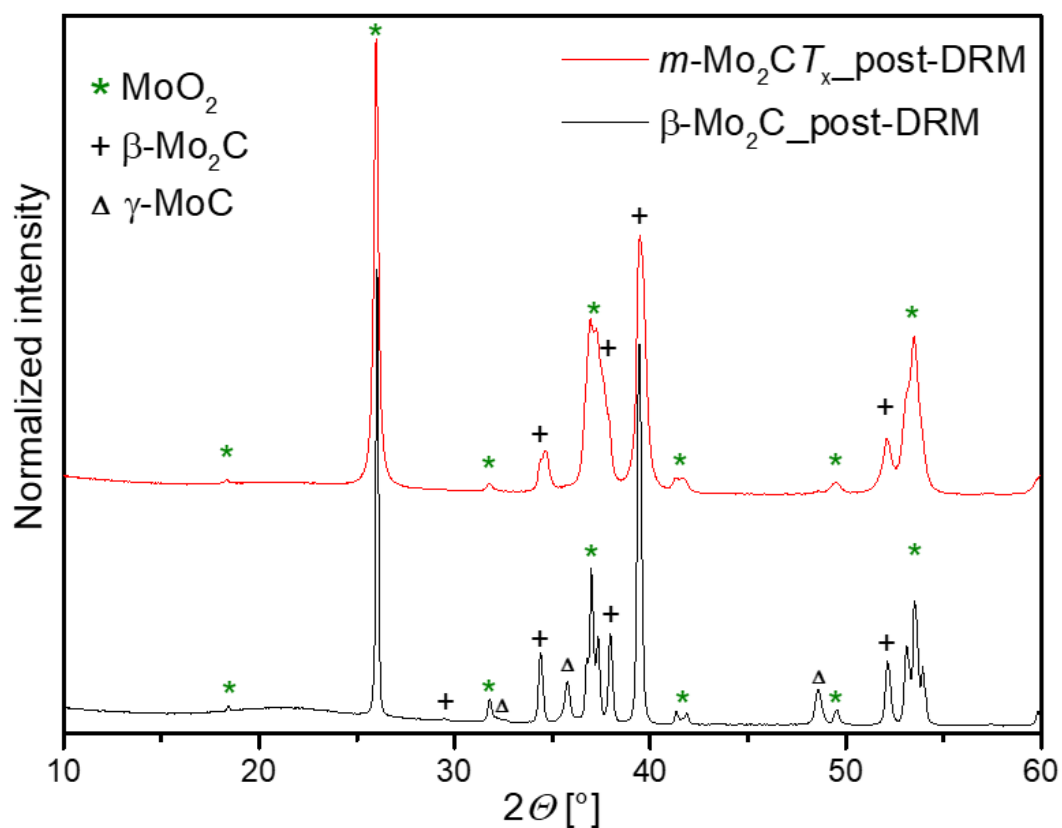


Figure F.18. XRD patterns of $\beta\text{-Mo}_2\text{C}$ and $m\text{-Mo}_2\text{CT}_x$ after the DRM catalytic test.

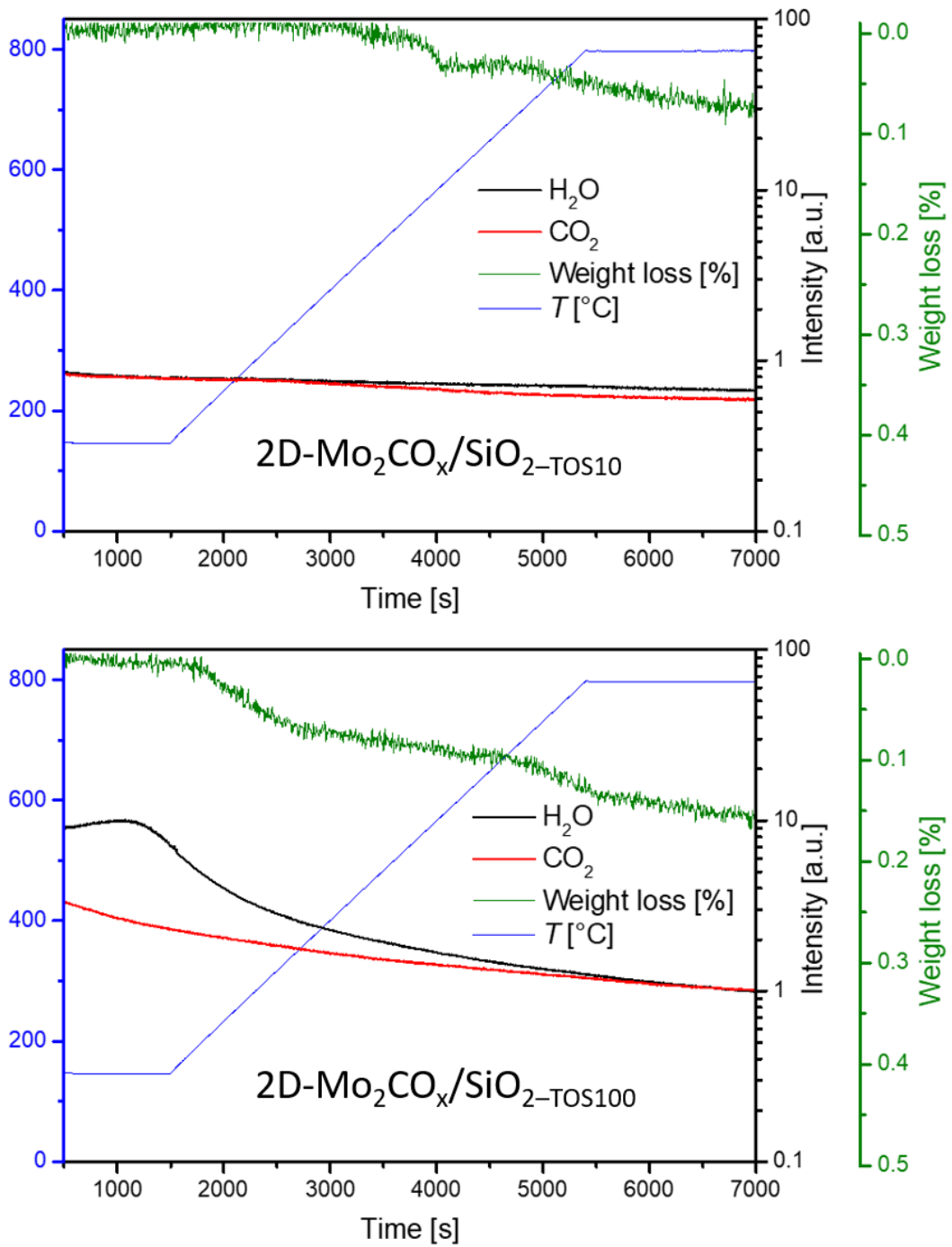


Figure F.19. A temperature programmed oxidation (TPO) of $2D-Mo_2CO_x/SiO_2-TOS10$ (top) and $2D-Mo_2CO_x/SiO_2-TOS100$ (bottom) in a TGA followed by MS.

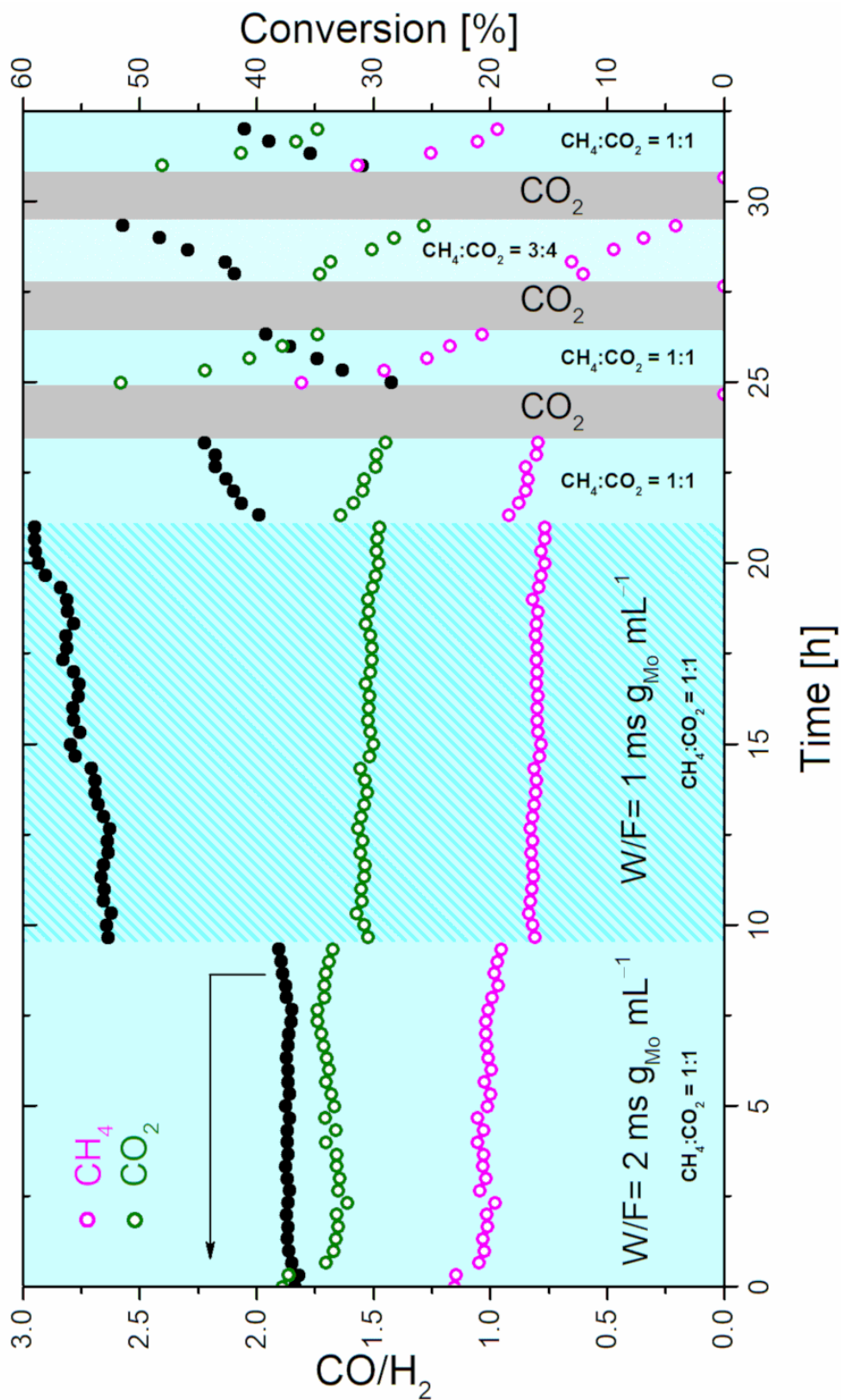


Figure F.20. DRM stability test of 2D-Mo₂CO_x/SiO₂ with several regeneration/deactivation cycles.

After the last data point, the sample was recovered for characterization (2D-Mo₂CO_x/SiO₂-spent)

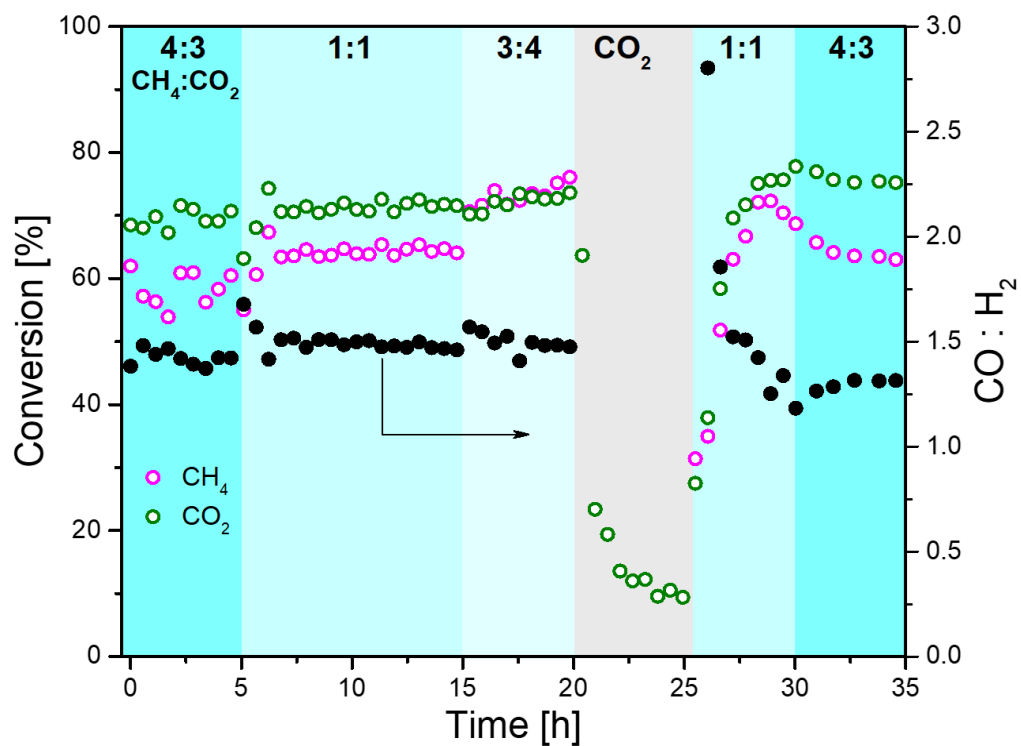


Figure F.21. Catalytic performance of 2D-Mo₂CT_x/SiO₂ in DRM at elevated pressure.

Reaction conditions: 800 °C, 8 bar, CH₄:CO₂= 1:1, total flow rate of 10 mL min⁻¹, 0.1 g of catalyst.

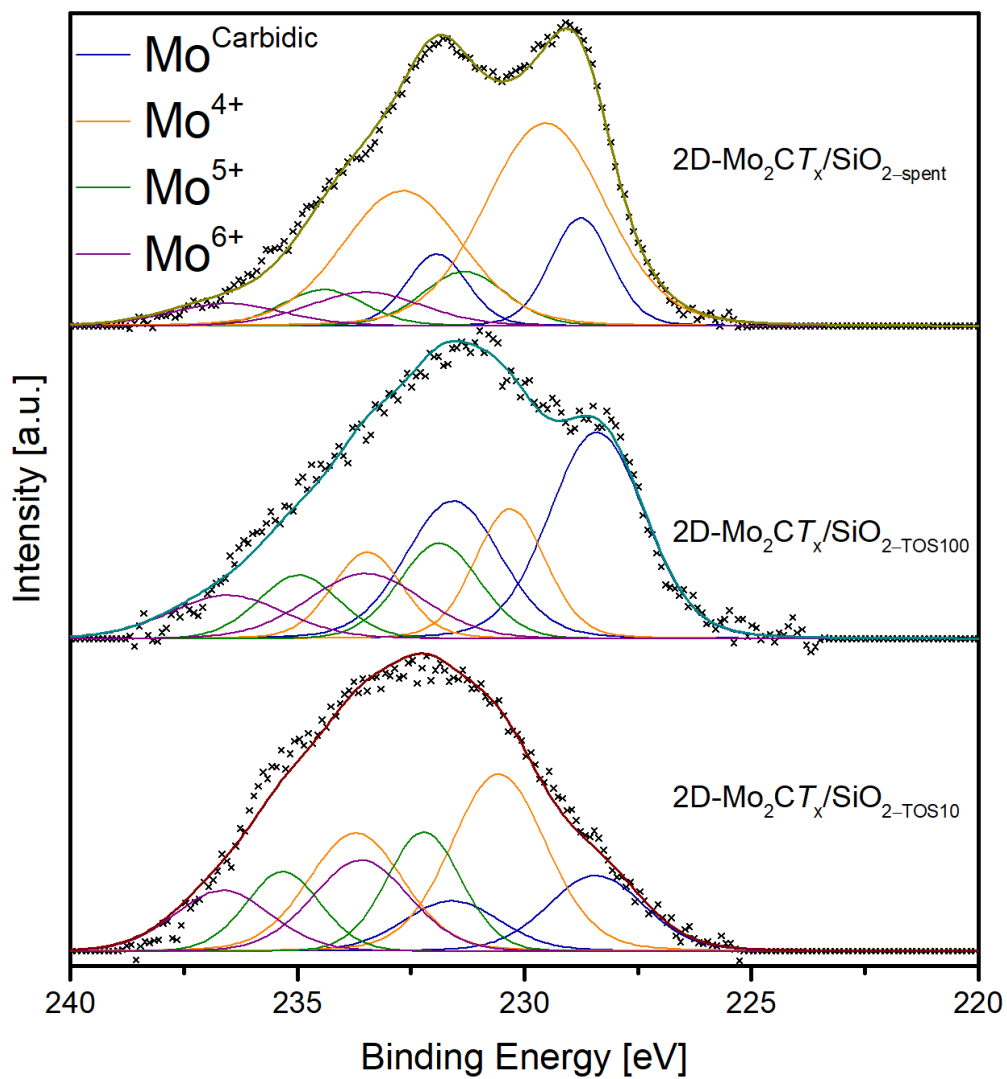


Figure F.22. Deconvolution of *ex situ* XPS data of the Mo 3d core levels of 2D-Mo₂CO_x/SiO₂-spent.

Table F.2. XPS fitting parameters for Mo₂CT_x, 2D-Mo₂CT_x/SiO₂, 2D-Mo₂C/SiO₂, 2D-Mo₂CO_x/SiO₂, 2D-Mo₂CO_x/SiO₂-DRM, β-Mo₂C and MoO₃.

State	Mo 3d _{5/2} B.E. [eV]	ΔB.E. [eV]	FWHM [eV]	Peak shape	Amount [%]
Mo₂CT_x					
Mo ⁴⁺	229.6	3.15	1.31	LA*	72
Mo ⁵⁺	232.6	3.06	2.62	GL#	28
2D-Mo₂CT_x/SiO₂					
Mo ⁴⁺	229.8	3.15	1.45	LA	9
Mo ⁵⁺	232.1	3.10	2.70	GL	40
Mo ⁶⁺	233.6	3.05	2.50	GL	51
2D-Mo₂C/SiO₂					
Carbodic	228.8	3.17	2.09	LA	53
Mo ⁴⁺	230.2	3.15	2.15	LA	29
Mo ⁶⁺	233.1	3.05	3.00	GL	18
2D-Mo₂CO_x/SiO₂					
Mo ⁰	228.0	3.17	2.00	LA	23
Mo ⁴⁺	230.1	3.10	2.24	LA	40
Mo ⁵⁺	232.1	3.10	1.86	GL	13
Mo ⁶⁺	233.5	3.05	3.00	GL	24
2D-Mo₂CO_x/SiO₂-TOS10					
Carbodic	228.4	3.17	2.50	LA	18
Mo ⁴⁺	230.6	3.15	2.46	LA	41
Mo ⁵⁺	232.2	3.10	1.93	GL	21
Mo ⁶⁺	233.6	3.05	2.50	GL	20
2D-Mo₂CO_x/SiO₂-TOS100					
Carbodic	228.4	3.17	2.50	LA	45
Mo ⁴⁺	230.3	3.15	1.84	LA	21
Mo ⁵⁺	231.9	3.10	2.10	GL	17
Mo ⁶⁺	233.5	3.05	2.99	GL	17
2D-Mo₂CO_x/SiO₂-spent					
Carbodic	228.8	3.17	1.58	LA	17
Mo ⁴⁺	229.5	3.15	3.11	LA	62
Mo ⁵⁺	231.3	3.10	2.17	GL	11
Mo ⁶⁺	233.5	3.05	3.00	GL	10
β-Mo₂C					
Carbodic	228.5	3.17	1.26	LA	100
MoO₃					
Mo ⁵⁺	232.2	3.05	2.24	GL	13
Mo ⁶⁺	233.3	3.13	1.41	GL	87

* LA- Lorentzian Asymmetric line shape, # GL- Gaussian/Lorentzian line shape.

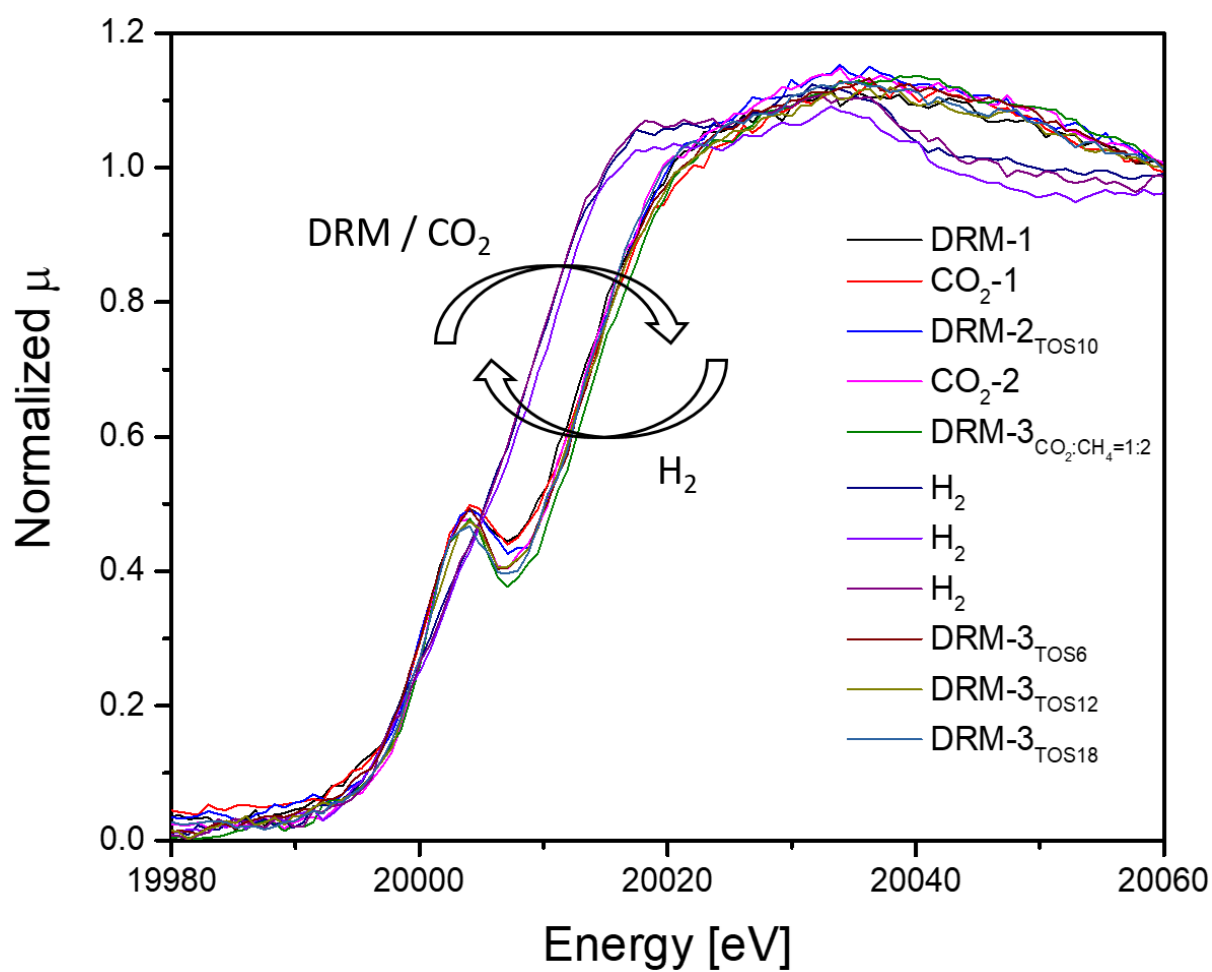


Figure F.23. XANES spectra of 2D-Mo₂CT_x derived materials under different conditions representing a complete reversibility between 2D-Mo₂C/SiO₂ and 2D-Mo₂CO_x/SiO₂.

Table F.3. Comparison of the DRM activity of 2D-Mo₂CO_x/SiO₂ with literature data for Mo-based catalysts.

	Catalyst	T °C	SV mL g ⁻¹ h ⁻¹	P bar	X(CH ₄) %	Activity		H ₂ :CO	Ref.
						mol _{CH₄}	mol _{Mo} ⁻¹ s ⁻¹		
1	30 wt.% Mo ₂ C/CNT	800	20400	1	10	0.003	–	[¹⁰⁶]	
2	6.3% Mo ₂ C/Al ₂ O ₃	800	20000 h ⁻¹	1	25.9	–	0.73	[³⁴⁰]	
3	5%Ni- 4.2%Mo ₂ C/Al ₂ O ₃	800	20000 h ⁻¹	1	78.6	–	0.89	[³⁴⁰]	
4	Ni/Mo ₂ C (1:9)	800	6000	1	80	0.003 and 0.028 [‡]	–	[¹¹⁴]	
5	β-Mo ₂ C	800	6000	1	<1	0	–	[¹¹⁴]	
6	4.4%Ni-14.6%Mo ₂ C/La ₂ O ₃	800	12000	1	66	0.033 and 0.067 [‡]	–	[¹¹³]	
7	Ni-Mo ₂ C (1:2)	800	12000	1	80	0.009 and 0.02 [‡]	–	[¹¹³]	
8	Mo ₂ C	800	6000	1	7	0.0002	<0.1	[¹¹¹]	
9	Ni-Mo ₂ C (1:1)	800	6000	1	82	0.005 and 0.005 [‡]	0.55	[¹¹¹]	
10	2D-Mo ₂ CO _x /SiO ₂	800	12000*	1	80	0.42	0.85 [#]	This work	
11	2D-Mo ₂ CO _x /SiO ₂	800	12000*	8	64	0.34	0.7	This work	
12	<i>m</i> -Mo ₂ CT _x	800	40000	1	8	0.002	0.33	This work	
13	β-Mo ₂ C	800	12000	1	4.5	0.0003	0.3	This work	
14	30 wt.% Mo ₂ C/CNT	850	18000	1	85	0.03	–	[¹⁰⁶]	
15	β-Mo ₂ C	850	18000	1	<1	0	–	[¹⁰⁶]	
16	α-MoC _{1-x}	850	6000	1	87	0.002	–	[¹⁰⁵]	
17	β-Mo ₂ C	850	6000	1	20	0.0005	–	[¹⁰⁵]	
18	18.3% Mo ₂ C/SiO ₂	850	2600 h ⁻¹	8	91	–	0.95	[¹⁰⁰]	
19	β-Mo ₂ C	850	2800 h ⁻¹	8.3	62.5	–	0.78	[²⁶⁰]	
20	5% Mo ₂ C/Al ₂ O ₃	850	2800 h ⁻¹	8.3	65.2	–	0.81	[²⁶⁰]	

* Per “g” of catalyst. 0.48 % Mo loading

[‡] Activity per mole of Ni: mol_{CH₄} mol_{Ni}⁻¹ s⁻¹

[#] Corresponds to the catalytic data presented in Figure 2 in the main text (entry 10), as well as in Figure F.21 (entry 11).

Table F.4. Total and areal CO capacity as well as the specific (Mo₂C) surface area of 2D-Mo₂C/SiO₂ and β-Mo₂C.

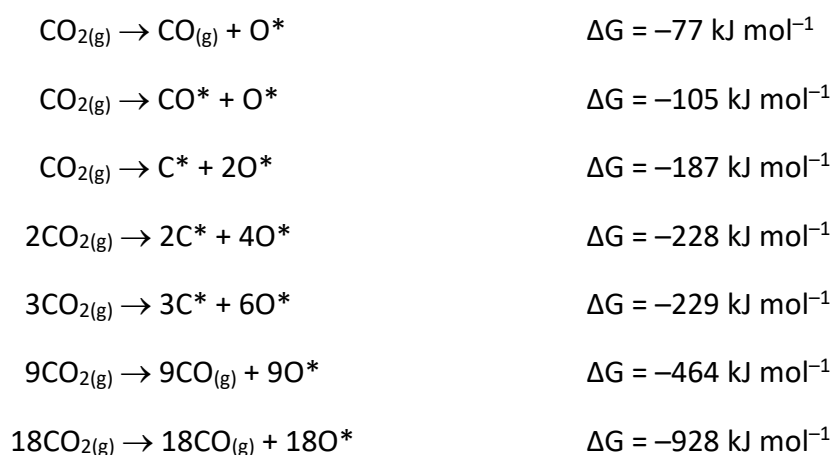
	2D-Mo ₂ C/SiO ₂	β-Mo ₂ C
CO adsorbed, 1-st isotherm, μmol g _{cat} ⁻¹	0.7	0.52
CO adsorbed, 2-nd isotherm, μmol g _{cat} ⁻¹	0.4	0.03
CO capacity, μmol g _{cat} ⁻¹	0.3	0.5
Specific Mo ₂ C surface area, m ² g _{cat} ⁻¹	1.34*	1-2
Areal CO capacity, μmol m ⁻²	0.22	0.25-0.5

* Estimated based on the crystal structure of Mo₂CT_x, see general experimental for details.

Computational Details

Structure of 2D-Mo₂C under CO₂ atmosphere

We evaluated different compositions of species on the 2D-Mo₂C slab and the resulting stabilities at 800 °C. For the reaction of one CO₂ molecule with the 2D-Mo₂C slab, the summary of reactions evaluated together with the resulting energetics is shown below.



The Gibbs energy of cleaving one CO₂ molecule, releasing one CO molecule in the gas phase and adsorbing one oxygen atom onto 2D-Mo₂C is exergonic by -77 kJ mol^{-1} . If CO* remains adsorbed, than the Gibbs energy is equal to -105 kJ mol^{-1} . This suggests that further CO* dissociation should be favored. Indeed, the formation of one C* and 2O* species is exergonic by -187 kJ mol^{-1} . If three CO₂ molecules are fully dissociated forming 3C* and 6O*, the Gibbs energies converges to a value equal to -229 kJ mol^{-1} . Nevertheless, the release of CO(g) together with the adsorption of atomic O* has less entropic penalty than the adsorption of all the species on the surface. For instance, if 9CO₂ molecules react on the top of the 2D-Mo₂C surface giving raise to 1 O ML on the top surface, this configuration is significantly more stable than all the previous ones, taking place in a highly exergonic process by -464 kJ mol^{-1} . Further addition of oxygen on the top surface by surface releasing another CO molecule in the gas phase or the formation of subsurface oxygen is an endergonic process. The adsorption of 9 additional oxygen atoms on the bottom layer of the Mo₂C slab, with the release of nine additional CO molecules has exactly the same energetics than the same reaction on the top layer, *i. e.* adsorbing a total of 18 oxygen atoms (9 per Mo layer) has an overall Gibbs energy exergonic by -928 kJ mol^{-1} . Thus, in atmosphere of pure CO₂ at 800 °C, 1 O ML is expected per Mo atom on both the top and the bottom layer, in agreement with

the experimental data. Since the adsorption on each side of the surface is very similar for next steps, we considered the surface with 1 O ML on one side of the slab.

Structure of the CO₂-treated 2D-Mo₂C surface under the DRM reaction conditions

As a starting point, we took the 2D-Mo₂C surface covered with 1 O ML on the top layer. Then, we evaluated possible reduction of the oxygen adsorbed on such 2D-Mo₂C surface since under DRM, the atmosphere is significantly more reducing than pure CO₂ (the latter atmosphere is oxidizing). We evaluated the reaction of the adsorbed oxygen with methane to form CO and H₂, and we found that it is thermodynamically favorable to reduce the coverage of oxygen of the Mo₂C surface previously treated with CO₂.



The results show that reducing the oxygen coverage is exergonic for one and two oxygen atoms and isoergonic for three oxygens. When evaluating the DRM reaction, we considered the surface with lower oxygen coverage than 1 O ML and to ease convergence, we selected 2D-Mo₂CO_x-0.67 O ML coverage.

Dry Reforming of Methane

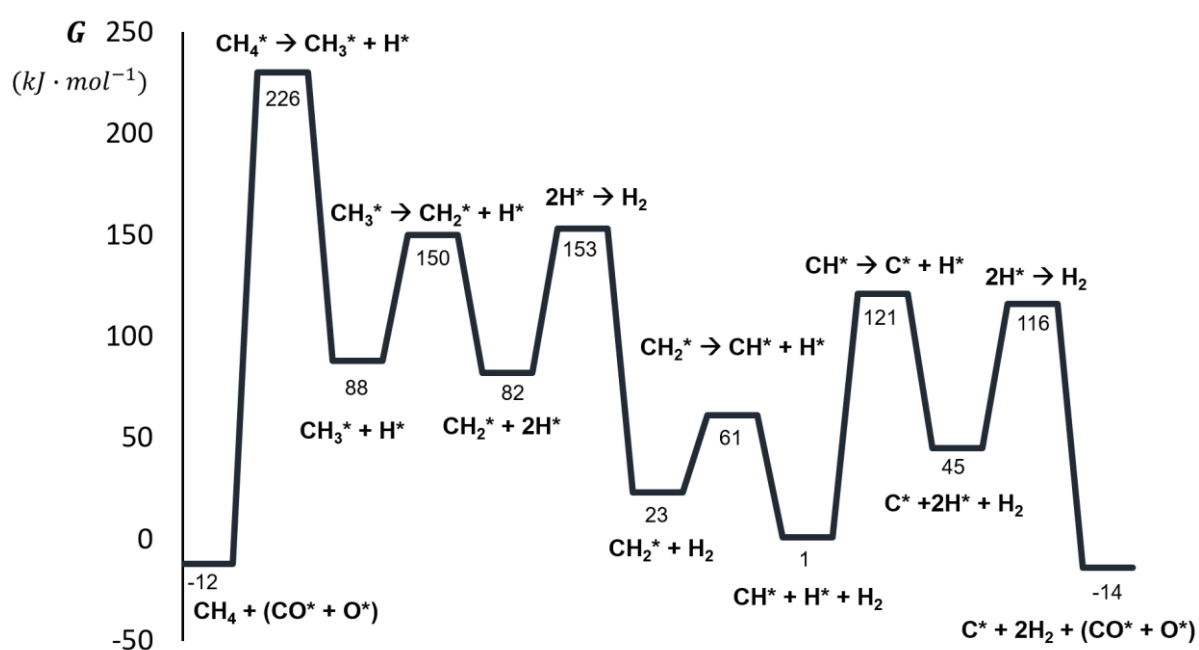


Figure F.24. Pathway to form C* and 2H₂ from CH₄ involving the H–H coupling steps. Gibbs energies are given with respect to CH₄ and CO₂ (in kJ mol⁻¹).

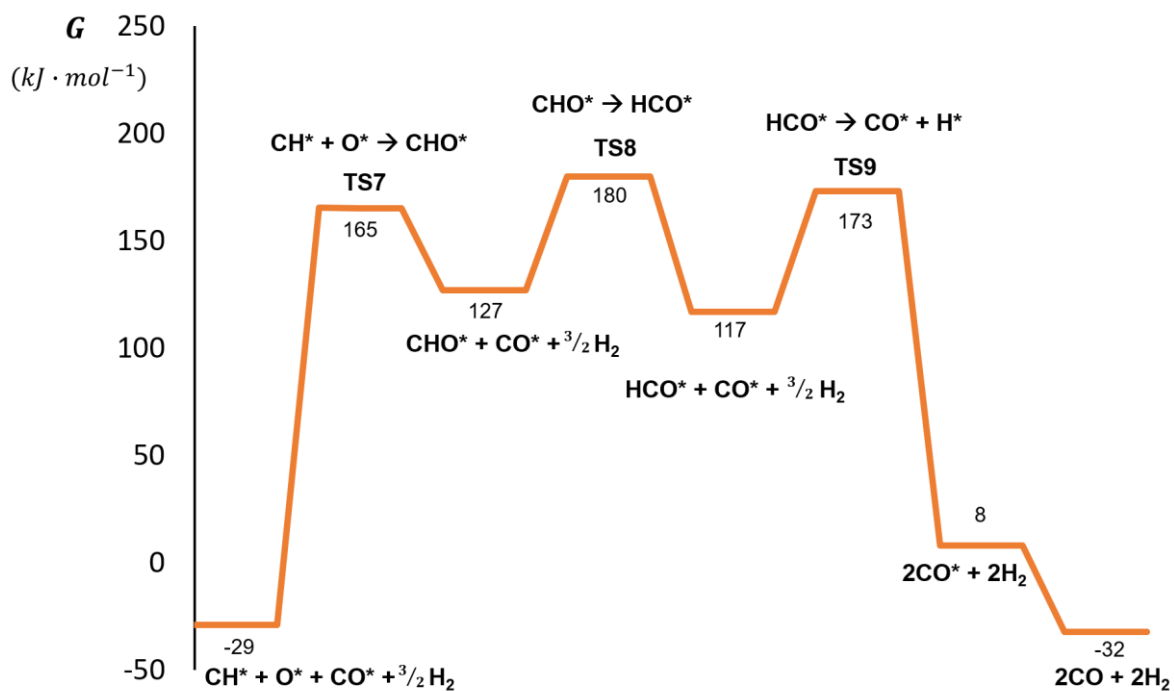


Figure F.25. Alternative oxidative pathway to form CO *via* the CHO* and HCO* intermediates. Gibbs energies are given with respect to CH₄ and CO₂ (in kJ mol⁻¹).

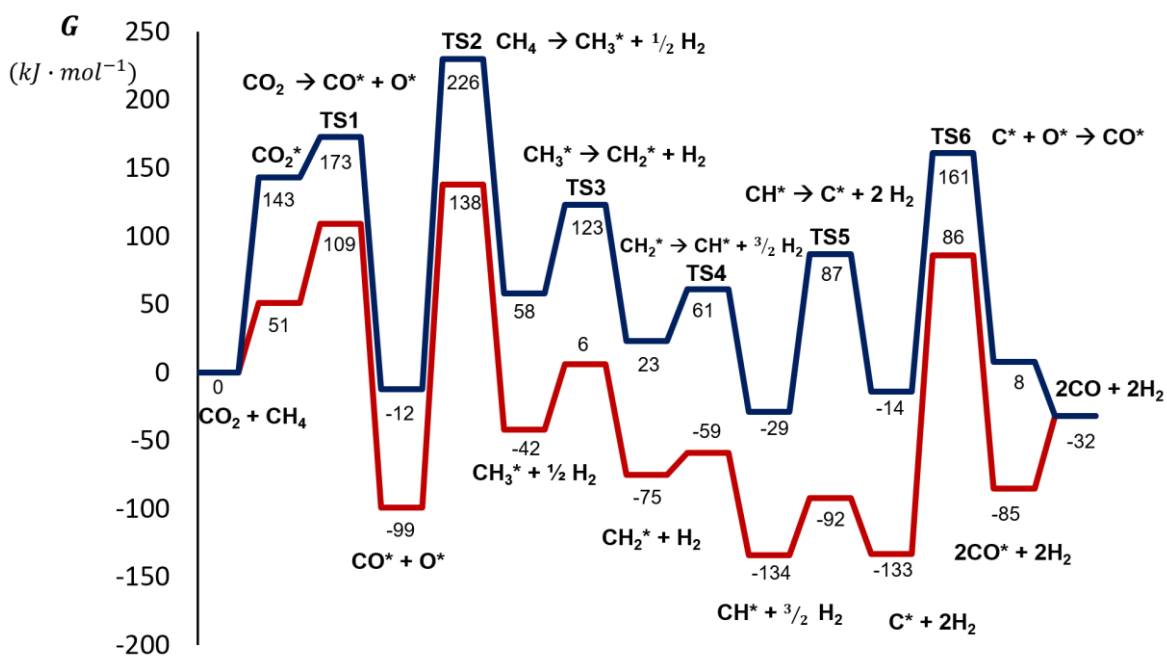


Figure F.26. Gibbs energy profile comparing the reactivities of 2D-Mo₂CO_x-0.67 O ML (blue) and 2D-Mo₂C (red) surfaces.

Gibbs energies are given with respect to initial reactants, CH₄ and CO₂ (in kJ mol⁻¹). A star (*) notation indicates surface species, and related species are compared for 2D-Mo₂CO_x-0.67 O ML and 2D-Mo₂C surfaces.

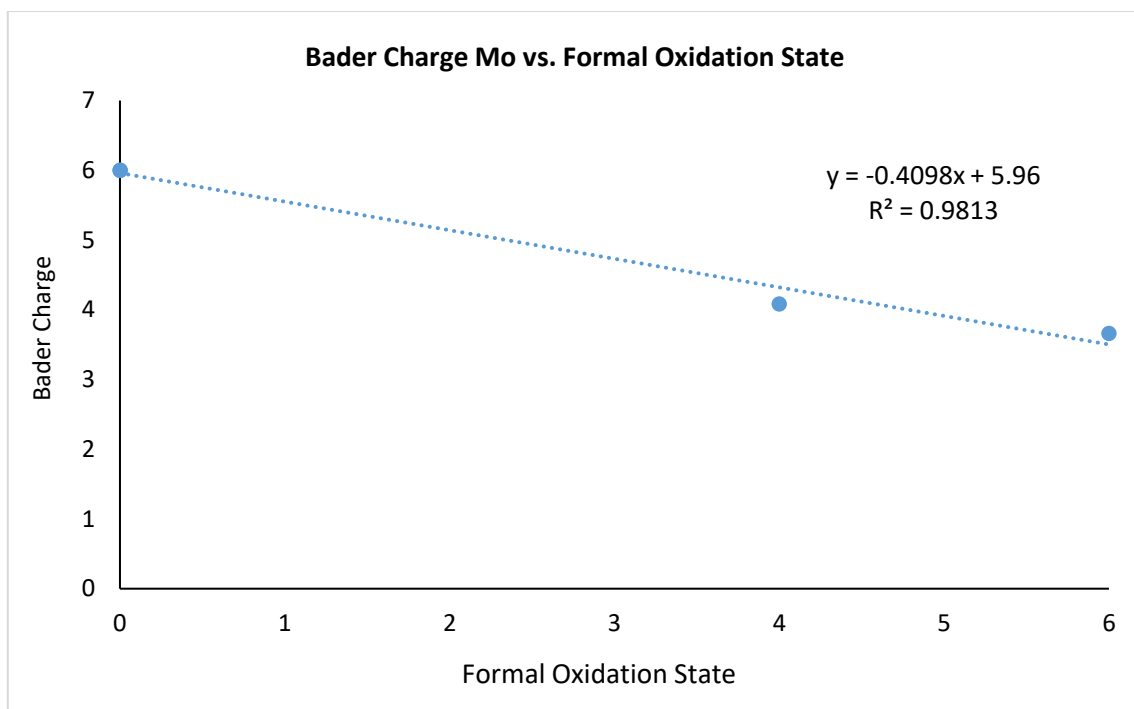


Figure F.27. Mo Bader charge dependence on the oxidation state (based on Mo, MoO₂ and MoO₃).

Table F.5. Oxidation states of the Mo atoms in the 2D-Mo₂C models with 1 O ML and 0.67 O ML oxygen coverage.

Oxidation State of Mo atoms (1.0 O ML)	Oxidation State of Mo atoms (0.67 O ML)
3.4	3.5
3.8	3.0
3.8	3.6
3.5	3.1
3.9	3.6
3.3	2.6
3.2	3.2
3.8	2.3
4.0	4.0
3.9	2.2
3.9	3.9
3.5	2.3
3.2	3.2
3.9	1.8
3.6	3.5
3.9	1.5
3.8	3.5
3.4	1.8

Table F.6. Comparison of the reactivity of 2D-Mo₂CO_x-0.67 O ML with respect to 2D-Mo₂C surface (in kJ mol⁻¹). Energies are given with respect to the initial reactants, CH₄ and CO₂. A star next to the species indicates the related species is adsorbed either on the 2D-Mo₂C or 2D-Mo₂CO_x-surface (*).

Reaction Step	2D-Mo ₂ CO _x -0.67 O ML G (kJ mol ⁻¹)	2D-Mo ₂ C G (kJ mol ⁻¹)
CO ₂ *	143	51
TS1 CO ₂ → CO + O	173	109
CO* + O*	-12	-99
TS2 CH ₄ → CH ₃ * + H*	226	138
CH ₃ * + 1/2 H ₂	58	-42
TS3 CH ₃ * → CH ₂ * + H*	123	6
CH ₂ * + H ₂	23	-75
TS4 CH ₂ * → CH* + H*	61	-59
CH* + 3/2 H ₂	-29	-134
TS 5 CH* → C* + H*	87	-92
C* + 2H ₂	-14	-133
TS6 C* + O* → CO*	161	86
2CO* + 2 H ₂	8	-85
2CO + 2 H ₂	-32	-32

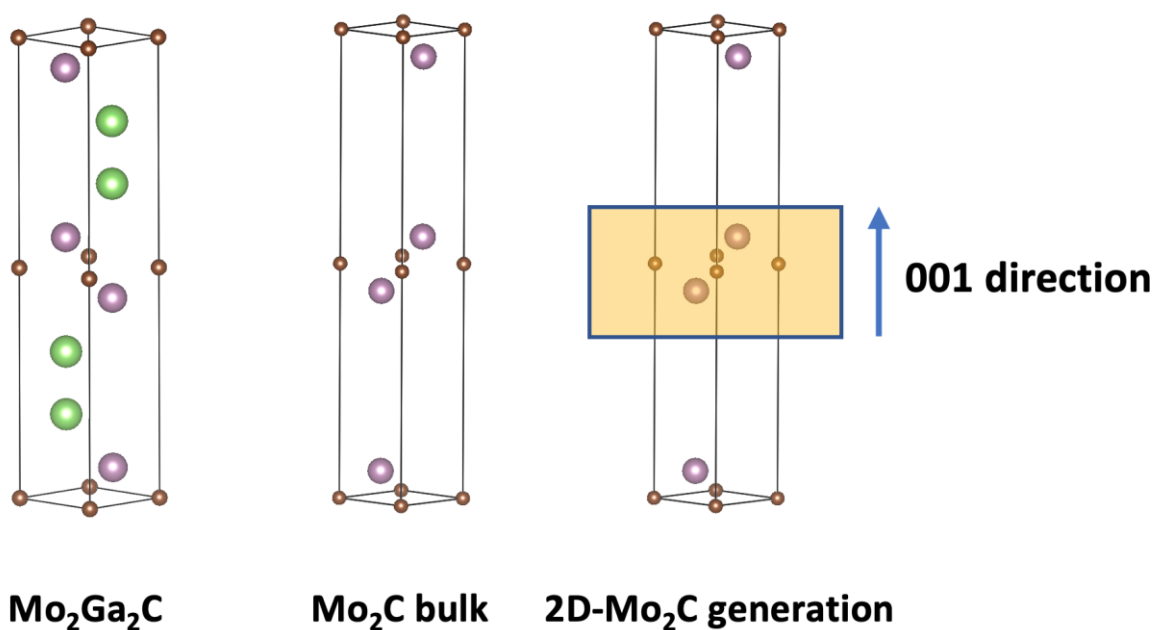


Figure F.28. Illustration of the construction of the theoretical model of the (001) facet of 2D-Mo₂C.

References

1. *Global Energy & CO₂ Status Report 2019*; IEA: Paris, 2019.
2. Dlugokencky, E.; Tans, P., NOAA/ESRL, [cited 2020].
3. *Climate Change 2014: Synthesis Report*; IPCC: Geneva, 2014.
4. Betts, R. A.; Boucher, O.; Collins, M.; Cox, P. M.; Falloon, P. D.; Gedney, N.; Hemming, D. L.; Huntingford, C.; Jones, C. D.; Sexton, D. M. H.; Webb, M. J., Projected increase in continental runoff due to plant responses to increasing carbon dioxide. *Nature* **2007**, *448*, 1037-1041.
5. *OECD environmental outlook to 2050: The consequences of inaction*; OECD: Paris, 2012.
6. *Energy Technology Perspectives 2016: Towards Sustainable Urban Energy Systems.*; IEA: Paris, 2016.
7. Benson, S. M.; Surles, T., Carbon Dioxide Capture and Storage: An Overview With Emphasis on Capture and Storage in Deep Geological Formations. *Proc. IEEE* **2006**, *94*, 1795-1805.
8. Figueroa, J. D.; Fout, T.; Plasynski, S.; McIlvried, H.; Srivastava, R. D., Advances in CO₂ capture technology—The U.S. Department of Energy's Carbon Sequestration Program. *Int. J. Greenh. Gas Con.* **2008**, *2*, 9-20.
9. Roefs, P.; Moretti, M.; Welkenhuysen, K.; Piessens, K.; Compernelle, T., CO₂-enhanced oil recovery and CO₂ capture and storage: An environmental economic trade-off analysis. *J. Environ. Manage.* **2019**, *239*, 167-177.
10. Metz, B.; Davidson, O.; de Coninck, H.; Loos, M.; Meyer, L. A. *IPCC special report on carbon dioxide capture and storage*; Cambridge: UK, 2005.
11. MacKenzie, A.; Granatstein, D. L.; Anthony, E. J.; Abanades, J. C., Economics of CO₂ capture using the calcium cycle with a pressurized fluidized bed combustor. *Energy Fuels* **2007**, *21*, 920-926.
12. Wall, T.; Liu, Y.; Spero, C.; Elliott, L.; Khare, S.; Rathnam, R.; Zeenathal, F.; Moghtaderi, B.; Buhre, B.; Sheng, C.; Gupta, R.; Yamada, T.; Makino, K.; Yu, J., An overview on oxyfuel coal combustion—State of the art research and technology development. *Chem. Eng. Res. Des.* **2009**, *87*, 1003-1016.
13. Rochelle, G. T., Amine Scrubbing for CO₂ Capture. *Science* **2009**, *325*, 1652-1654.
14. Veltman, K.; Singh, B.; Hertwich, E. G., Human and environmental impact assessment of postcombustion CO₂ capture focusing on emissions from amine-based scrubbing solvents to air. *Environ. Sci. Technol.* **2010**, *44*, 1496-1502.
15. Fine, N. A.; Nielsen, P. T.; Rochelle, G. T., Decomposition of nitrosamines in CO₂ capture by aqueous piperazine or monoethanolamine. *Environ. Sci. Technol.* **2014**, *48*, 5996-6002.
16. Yue, M. B.; Chun, Y.; Cao, Y.; Dong, X.; Zhu, J. H., CO₂ capture by As-prepared SBA-15 with an occluded organic template. *Adv. Funct. Mater.* **2006**, *16*, 1717-1722.
17. Qi, G. G.; Wang, Y. B.; Estevez, L.; Duan, X. N.; Anako, N.; Park, A. H. A.; Li, W.; Jones, C. W.; Giannelis, E. P., High efficiency nanocomposite sorbents for CO₂ capture based on amine-functionalized mesoporous capsules. *Energy Environ. Sci.* **2011**, *4*, 444-452.
18. Banerjee, R.; Phan, A.; Wang, B.; Knobler, C.; Furukawa, H.; O'Keeffe, M.; Yaghi, O. M., High-throughput synthesis of zeolitic imidazolate frameworks and application to CO₂ capture. *Science* **2008**, *319*, 939-943.

19. Lin, L. C.; Berger, A. H.; Martin, R. L.; Kim, J.; Swisher, J. A.; Jariwala, K.; Rycroft, C. H.; Bhowan, A. S.; Deem, M. W.; Haranczyk, M.; Smit, B., In silico screening of carbon-capture materials. *Nat. Mater.* **2012**, *11*, 633-641.
20. Wang, B.; Cote, A. P.; Furukawa, H.; O'Keeffe, M.; Yaghi, O. M., Colossal cages in zeolitic imidazolate frameworks as selective carbon dioxide reservoirs. *Nature* **2008**, *453*, 207-212.
21. Furukawa, H.; Ko, N.; Go, Y. B.; Aratani, N.; Choi, S. B.; Choi, E.; Yazaydin, A. O.; Snurr, R. Q.; O'Keeffe, M.; Kim, J.; Yaghi, O. M., Ultrahigh Porosity in Metal-Organic Frameworks. *Science* **2010**, *329*, 424-428.
22. Duan, Y.; Sorescu, D. C., CO₂ capture properties of alkaline earth metal oxides and hydroxides: A combined density functional theory and lattice phonon dynamics study. *J. Chem. Phys.* **2010**, *133*, 074508.
23. Zhang, K.; Li, X. S.; Li, W.-Z.; Rohatgi, A.; Duan, Y.; Singh, P.; Li, L.; King, D. L., Phase Transfer-Catalyzed Fast CO₂ Absorption by MgO-Based Absorbents with High Cycling Capacity. *Adv. Mater. Interfaces* **2014**, *1*, 1400030.
24. Harada, T.; Simeon, F.; Hamad, E. Z.; Hatton, T. A., Alkali Metal Nitrate-Promoted High-Capacity MgO Adsorbents for Regenerable CO₂ Capture at Moderate Temperatures. *Chem. Mater.* **2015**, *27*, 1943-1949.
25. Kierzkowska, A. M.; Pacciani, R.; Muller, C. R., CaO-based CO₂ sorbents: from fundamentals to the development of new, highly effective materials. *ChemSusChem* **2013**, *6*, 1130-1148.
26. Kierzkowska, A. M.; Muller, C. R., Development of calcium-based, copper-functionalised CO₂ sorbents to integrate chemical looping combustion into calcium looping. *Energy Environ. Sci.* **2012**, *5*, 6061-6065.
27. Song, Q. L.; Liu, W.; Bohn, C. D.; Harper, R. N.; Sivaniah, E.; Scott, S. A.; Dennis, J. S., A high performance oxygen storage material for chemical looping processes with CO₂ capture. *Energy Environ. Sci.* **2013**, *6*, 288-298.
28. Baker, E. H., The calcium oxide-carbon dioxide system in the pressure range 1–300 atmospheres. *J. Chem. Soc.* **1962**, *0*, 464-470.
29. Broda, M. Synthetic Calcium-based Sorbents for Pre-and Post-Combustion CO₂ Capture. ETH, 2014.
30. Abanades, J. C.; Alvarez, D., Conversion Limits in the Reaction of CO₂ with Lime. *Energy Fuels* **2003**, *17*, 308-315.
31. Grasa, G. S.; Abanades, J. C., CO₂ capture capacity of CaO in long series of carbonation/calcination cycles. *Ind. Eng. Chem. Res.* **2006**, *45*, 8846-8851.
32. Sun, P.; Grace, J. R.; Lim, C. J.; Anthony, E. J., The effect of CaO sintering on cyclic CO₂ capture in energy systems. *Aiche J.* **2007**, *53*, 2432-2442.
33. Barker, R., The reversibility of the reaction $\text{CaCO}_3 \rightleftharpoons \text{CaO} + \text{CO}_2$. *J. Appl. Chem. Biotechnol.* **1973**, *23*, 733-742.
34. Alvarez, D.; Abanades, J. C., Determination of the Critical Product Layer Thickness in the Reaction of CaO with CO₂. *Ind. Eng. Chem. Res.* **2005**, *44*, 5608-5615.
35. Sun, H.; Wang, J.; Liu, X.; Shen, B.; Parlett, Christopher M. A.; Adwek, G. O.; John Anthony, E.; Williams, P. T.; Wu, C., Fundamental studies of carbon capture using CaO-based materials. *J. Mater. Chem. A* **2019**, *7*, 9977-9987.
36. Arias, B.; Abanades, J. C.; Grasa, G. S., An analysis of the effect of carbonation conditions on CaO deactivation curves. *Chem. Eng. J.* **2011**, *167*, 255-261.

37. Chen, J.; Duan, L.; Sun, Z., Review on the Development of Sorbents for Calcium Looping. *Energy Fuels* **2020**, 10.1021/acs.energyfuels.0c00682.
38. Lu, H.; Khan, A.; Pratsinis, S. E.; Smirniotis, P. G., Flame-Made Durable Doped-CaO Nanosorbents for CO₂ Capture. *Energy Fuels* **2009**, *23*, 1093-1100.
39. Hu, Y.; Liu, W.; Chen, H.; Zhou, Z.; Wang, W.; Sun, J.; Yang, X.; Li, X.; Xu, M., Screening of inert solid supports for CaO-based sorbents for high temperature CO₂ capture. *Fuel* **2016**, *181*, 199-206.
40. Broda, M.; Kierzkowska, A. M.; Müller, C. R., Development of Highly Effective CaO-based, MgO-stabilized CO₂ Sorbents via a Scalable “One-Pot” Recrystallization Technique. *Adv. Funct. Mater.* **2014**, *24*, 5753-5761.
41. Zhang, X.; Li, Z.; Peng, Y.; Su, W.; Sun, X.; Li, J., Investigation on a novel CaO–Y₂O₃ sorbent for efficient CO₂ mitigation. *Chem. Eng. J.* **2014**, *243*, 297-304.
42. Broda, M.; Muller, C. R., Synthesis of highly efficient, Ca-based, Al₂O₃-stabilized, carbon gel-templated CO₂ sorbents. *Adv. Mater.* **2012**, *24*, 3059-3064.
43. Hassanzadeh, A.; Abbasian, J., Regenerable MgO-based sorbents for high-temperature CO₂ removal from syngas: 1. Sorbent development, evaluation, and reaction modeling. *Fuel* **2010**, *89*, 1287-1297.
44. Li, L.; King, D. L.; Nie, Z.; Howard, C., Magnesia-Stabilized Calcium Oxide Absorbents with Improved Durability for High Temperature CO₂ Capture. *Ind. Eng. Chem. Res.* **2009**, *48*, 10604-10613.
45. Sayyah, M.; Lu, Y.; Masel, R. I.; Suslick, K. S., Mechanical activation of CaO-based adsorbents for CO₂ capture. *ChemSusChem* **2013**, *6*, 193-198.
46. Luo, C.; Zheng, Y.; Xu, Y.; Ding, N.; Shen, Q.; Zheng, C., Wet mixing combustion synthesis of CaO-based sorbents for high temperature cyclic CO₂ capture. *Chem. Eng. J.* **2015**, *267*, 111-116.
47. Chen, H.; Zhang, P.; Duan, Y.; Zhao, C., CO₂ capture of calcium based sorbents developed by sol–gel technique in the presence of steam. *Chem. Eng. J.* **2016**, *295*, 218-226.
48. Naeem, M. A.; Armutlulu, A.; Kierzkowska, A.; Müller, C. R., Development of High-performance CaO-based CO₂ Sorbents Stabilized with Al₂O₃ or MgO. *Energy Procedia* **2017**, *114*, 158-166.
49. Naeem, M. A.; Armutlulu, A.; Imtiaz, Q.; Donat, F.; Schaublin, R.; Kierzkowska, A.; Muller, C. R., Optimization of the structural characteristics of CaO and its effective stabilization yield high-capacity CO₂ sorbents. *Nat. Commun.* **2018**, *9*, 2408.
50. Wu, S. F.; Li, Q. H.; Kim, J. N.; Yi, K. B., Properties of a Nano CaO/Al₂O₃CO₂ Sorbent. *Ind. Eng. Chem. Res.* **2008**, *47*, 180-184.
51. Benitez-Guerrero, M.; Valverde, J. M.; Sanchez-Jimenez, P. E.; Perejon, A.; Perez-Maqueda, L. A., Calcium-Looping performance of mechanically modified Al₂O₃-CaO composites for energy storage and CO₂ capture. *Chem. Eng. J.* **2018**, *334*, 2343-2355.
52. Florin, N. H.; Blamey, J.; Fennell, P. S., Synthetic CaO-Based Sorbent for CO₂ Capture from Large-Point Sources. *Energy Fuels* **2010**, *24*, 4598-4604.
53. Kierzkowska, A. M.; Poulikakos, L. V.; Broda, M.; Müller, C. R., Synthesis of calcium-based, Al₂O₃-stabilized sorbents for CO₂ capture using a co-precipitation technique. *Int. J. Greenh. Gas Con.* **2013**, *15*, 48-54.
54. Broda, M.; Kierzkowska, A. M.; Muller, C. R., Application of the sol-gel technique to develop synthetic calcium-based sorbents with excellent carbon dioxide capture characteristics. *ChemSusChem* **2012**, *5*, 411-418.

55. Zhao, C.; Zhou, Z.; Cheng, Z., Sol-gel-Derived Synthetic CaO-Based CO₂ Sorbents Incorporated with Different Inert Materials. *Ind. Eng. Chem. Res.* **2014**, *53*, 14065-14074.
56. Han, R.; Gao, J.; Wei, S.; Su, Y.; Qin, Y., Development of highly effective CaO@Al₂O₃ with hierarchical architecture CO₂ sorbents via a scalable limited-space chemical vapor deposition technique. *J. Mater. Chem. A* **2018**, *6*, 3462-3470.
57. Armutlulu, A.; Naeem, M. A.; Liu, H. J.; Kim, S. M.; Kierzkowska, A.; Fedorov, A.; Muller, C. R., Multishelled CaO Microspheres Stabilized by Atomic Layer Deposition of Al₂O₃ for Enhanced CO₂ Capture Performance. *Adv. Mater.* **2017**, *29*, 1702896.
58. Kim, S. M.; Liao, W.-C.; Kierzkowska, A. M.; Margossian, T.; Hosseini, D.; Yoon, S.; Broda, M.; Copéret, C.; Müller, C. R., In Situ XRD and Dynamic Nuclear Polarization Surface Enhanced NMR Spectroscopy Unravel the Deactivation Mechanism of CaO-Based, Ca₃Al₂O₆-Stabilized CO₂ Sorbents. *Chem. Mater.* **2018**, *30*, 1344-1352.
59. Dal Pozzo, A.; Armutlulu, A.; Rekhtina, M.; Abdala, P. M.; Müller, C. R., CO₂ Uptake and Cyclic Stability of MgO-Based CO₂ Sorbents Promoted with Alkali Metal Nitrates and Their Eutectic Mixtures. *ACS Appl. Energy Mater.* **2019**, *2*, 1295-1307.
60. Huang, L.; Zhang, Y.; Gao, W.; Harada, T.; Qin, Q.; Zheng, Q.; Hatton, T. A.; Wang, Q., Alkali Carbonate Molten Salt Coated Calcium Oxide with Highly Improved Carbon Dioxide Capture Capacity. *Energy Technol.* **2017**, *5*, 1328-1336.
61. Reddy, E. P.; Smirniotis, P. G., High-Temperature Sorbents for CO₂ Made of Alkali Metals Doped on CaO Supports. *J. Phys. Chem. B* **2004**, *108*, 7794-7800.
62. Salvador, C.; Lu, D.; Anthony, E. J.; Abanades, J. C., Enhancement of CaO for CO₂ capture in an FBC environment. *Chem. Eng. J.* **2003**, *96*, 187-195.
63. Al-Mamoori, A.; Thakkar, H.; Li, X.; Rownaghi, A. A.; Rezaei, F., Development of Potassium- and Sodium-Promoted CaO Adsorbents for CO₂ Capture at High Temperatures. *Ind. Eng. Chem. Res.* **2017**, *56*, 8292-8300.
64. Lee, C. H.; Choi, S. W.; Yoon, H. J.; Kwon, H. J.; Lee, H. C.; Jeon, S. G.; Lee, K. B., Na₂CO₃-doped CaO-based high-temperature CO₂ sorbent and its sorption kinetics. *Chem. Eng. J.* **2018**, *352*, 103-109.
65. Manovic, V.; Anthony, E. J.; Grasa, G.; Abanades, J. C., CO₂ Looping Cycle Performance of a High-Purity Limestone after Thermal Activation/Doping. *Energy Fuels* **2008**, *22*, 3258-3264.
66. Artz, J.; Muller, T. E.; Thenert, K.; Kleinekorte, J.; Meys, R.; Sternberg, A.; Bardow, A.; Leitner, W., Sustainable Conversion of Carbon Dioxide: An Integrated Review of Catalysis and Life Cycle Assessment. *Chem. Rev.* **2018**, *118*, 434-504.
67. Wang, L.; Yi, Y.; Wu, C.; Guo, H.; Tu, X., One-Step Reforming of CO₂ and CH₄ into High-Value Liquid Chemicals and Fuels at Room Temperature by Plasma-Driven Catalysis. *Angew. Chem., Int. Ed.* **2017**, *129*, 13867-13871.
68. Wu, Y.; Jiang, Z.; Lu, X.; Liang, Y.; Wang, H., Domino electroreduction of CO₂ to methanol on a molecular catalyst. *Nature* **2019**, *575*, 639-642.
69. Tsoukalou, A.; Abdala, P. M.; Stoian, D.; Huang, X.; Willinger, M. G.; Fedorov, A.; Muller, C. R., The Structural Evolution and Dynamics of an In₂O₃ Catalyst for CO₂ Hydrogenation to Methanol: an Operando XAS-XRD and in situ TEM Study. *J. Am. Chem. Soc.* **2019**, *141*, 13497-13505.
70. Fischer, F.; Tropsch, H., Über die direkte Synthese von Erdöl-Kohlenwasserstoffen bei gewöhnlichem Druck. (Erste Mitteilung). *Ber. Dtsch. Chem. Ges.* **1926**, *59*, 830-831.
71. Pakhare, D.; Spivey, J., A review of dry (CO₂) reforming of methane over noble metal catalysts. *Chem. Soc. Rev.* **2014**, *43*, 7813-7837.

72. Nikoo, M. K.; Amin, N. A. S., Thermodynamic analysis of carbon dioxide reforming of methane in view of solid carbon formation. *Fuel Process. Technol.* **2011**, *92*, 678-691.
73. Pakhare, D.; Shaw, C.; Haynes, D.; Shekhawat, D.; Spivey, J., Effect of reaction temperature on activity of Pt- and Ru-substituted lanthanum zirconate pyrochlores (La₂Zr₂O₇) for dry (CO₂) reforming of methane (DRM). *J. CO₂ Util.* **2013**, *1*, 37-42.
74. Wang, S.; Lu, G. Q.; Millar, G. J., Carbon Dioxide Reforming of Methane To Produce Synthesis Gas over Metal-Supported Catalysts: State of the Art. *Energy Fuels* **1996**, *10*, 896-904.
75. Bradford, M. C. J.; Vannice, M. A., CO₂ Reforming of CH₄. *Catal. Rev.* **1999**, *41*, 1-42.
76. Shah, Y. T.; Gardner, T. H., Dry Reforming of Hydrocarbon Feedstocks. *Catal. Rev.* **2014**, *56*, 476-536.
77. Ashcroft, A. T.; Cheetham, A. K.; Green, M. L. H.; Vernon, P. D. F., Partial oxidation of methane to synthesis gas using carbon dioxide. *Nature* **1991**, *352*, 225-226.
78. Kehres, J.; Jakobsen, J. G.; Andreasen, J. W.; Wagner, J. B.; Liu, H.; Molenbroek, A.; Sehested, J.; Chorkendorff, I.; Vegge, T., Dynamical Properties of a Ru/MgAl₂O₄ Catalyst during Reduction and Dry Methane Reforming. *J. Phys. Chem. C* **2012**, *116*, 21407-21415.
79. Hou, Z.; Yashima, T., Small amounts of Rh-promoted Ni catalysts for methane reforming with CO₂. *Catal Lett* **2003**, *89*, 193-197.
80. Steinhauer, B.; Kasireddy, M. R.; Radnik, J.; Martin, A., Development of Ni-Pd bimetallic catalysts for the utilization of carbon dioxide and methane by dry reforming. *Appl. Catal., A* **2009**, *366*, 333-341.
81. Hu, Y. H.; Ruckenstein, E., Catalytic Conversion of Methane to Synthesis Gas by Partial Oxidation and CO₂ Reforming. *Adv. Catal.* **2004**, *48*, 297-345.
82. Kim, S. M.; Abdala, P. M.; Margossian, T.; Hosseini, D.; Foppa, L.; Armutlulu, A.; van Beek, W.; Comas-Vives, A.; Coperet, C.; Muller, C., Cooperativity and Dynamics Increase the Performance of NiFe Dry Reforming Catalysts. *J. Am. Chem. Soc.* **2017**, *139*, 1937-1949.
83. Bian, Z.; Kawi, S., Highly carbon-resistant Ni-Co/SiO₂ catalysts derived from phyllosilicates for dry reforming of methane. *J. CO₂ Util.* **2017**, *18*, 345-352.
84. Sinfelt, J. H.; Yates, D. J., Effect of Carbiding on the Hydrogenolysis Activity of Molybdenum. *Nat. Phys. Sci.* **1971**, *229*, 27-28.
85. Levy, R. B.; Boudart, M., Platinum-Like Behavior of Tungsten Carbide in Surface Catalysis. *Science* **1973**, *181*, 547-549.
86. Patt, J.; Moon, D. J.; Phillips, C.; Thompson, L., Molybdenum carbide catalysts for water-gas shift. *Catal Lett* **2000**, *65*, 193-195.
87. Moon, D. J.; Ryu, J. W., Molybdenum carbide water-gas shift catalyst for fuel cell-powered vehicles applications. *Catal Lett* **2004**, *92*, 17-24.
88. Schweitzer, N. M.; Schaidle, J. A.; Ezekoye, O. K.; Pan, X.; Linic, S.; Thompson, L. T., High activity carbide supported catalysts for water gas shift. *J. Am. Chem. Soc.* **2011**, *133*, 2378-2381.
89. Wang, G.; Schaidle, J. A.; Katz, M. B.; Li, Y.; Pan, X.; Thompson, L. T., Alumina supported Pt-Mo₂C catalysts for the water-gas shift reaction. *J. Catal.* **2013**, *304*, 92-99.
90. Solymosi, F.; Cserényi, J.; Szöke, A.; Bánsági, T.; Oszkó, A., Aromatization of Methane over Supported and Unsupported Mo-Based Catalysts. *J. Catal.* **1997**, *165*, 150-161.
91. Sijaj, M.; Oudghiri-Hassani, H.; Maltais, C.; McBreen, P. H., Thermally Stable Alkylidene Groups on the Surface of β-Mo₂C: Relevance to Methane Aromatization and Olefin-Metathesis Catalysis. *J. Phys. Chem. C* **2007**, *111*, 1725-1732.

92. Wu, Q.; Christensen, J. M.; Chiarello, G. L.; Duchstein, L. D. L.; Wagner, J. B.; Temel, B.; Grunwaldt, J.-D.; Jensen, A. D., Supported molybdenum carbide for higher alcohol synthesis from syngas. *Catal. Today* **2013**, *215*, 162-168.
93. Schaidle, J. A.; Thompson, L. T., Fischer–Tropsch synthesis over early transition metal carbides and nitrides: CO activation and chain growth. *J. Catal.* **2015**, *329*, 325-334.
94. Marquart, W.; Morgan, D. J.; Hutchings, G. J.; Claeys, M.; Fischer, N., Oxygenate formation over K/ β -Mo₂C catalysts in the Fischer–Tropsch synthesis. *Catal. Sci. Technol.* **2018**, *8*, 3806-3817.
95. Porosoff, M. D.; Yang, X.; Boscoboinik, J. A.; Chen, J. G., Molybdenum carbide as alternative catalysts to precious metals for highly selective reduction of CO₂ to CO. *Angew. Chem., Int. Ed.* **2014**, *53*, 6705-6709.
96. Posada-Pérez, S.; Ramírez, P. J.; Gutiérrez, R. A.; Stacchiola, D. J.; Viñes, F.; Liu, P.; Illas, F.; Rodriguez, J. A., The conversion of CO₂ to methanol on orthorhombic β -Mo₂C and Cu/ β -Mo₂C catalysts: mechanism for admetal induced change in the selectivity and activity. *Catal. Sci. Technol.* **2016**, *6*, 6766-6777.
97. Claridge, J. B.; York, A. P. E.; Brungs, A. J.; Marquez-Alvarez, C.; Sloan, J.; Tsang, S. C.; Green, M. L. H., New Catalysts for the Conversion of Methane to Synthesis Gas: Molybdenum and Tungsten Carbide. *J. Catal.* **1998**, *180*, 85-100.
98. Schaidle, J. A.; Lausche, A. C.; Thompson, L. T., Effects of sulfur on Mo₂C and Pt/Mo₂C catalysts: Water gas shift reaction. *J. Catal.* **2010**, *272*, 235-245.
99. Da Costa, P.; Lemberon, J.-L.; Potvin, C.; Manoli, J.-M.; Perot, G.; Breyse, M.; Djega-Mariadassou, G., Tetralin hydrogenation catalyzed by Mo₂C/Al₂O₃ and WC/Al₂O₃ in the presence of H₂S. *Catal. Today* **2001**, *65*, 195-200.
100. Brungs, A. J.; York, A. P. E.; Claridge, J. B.; Marquez-Alvarez, C.; Green, M. L. H., Dry reforming of methane to synthesis gas over supported molybdenum carbide catalysts. *Catal Lett* **2000**, *70*, 117-122.
101. Xiao, T.; Wang, H.; Da, J.; Coleman, K. S.; Green, M. L. H., Study of the Preparation and Catalytic Performance of Molybdenum Carbide Catalysts Prepared with C₂H₂/H₂ Carburizing Mixture. *J. Catal.* **2002**, *211*, 183-191.
102. LaMont, D. C.; Gilligan, A. J.; Darujati, A. R. S.; Chellappa, A. S.; Thomson, W. J., The effect of Mo₂C synthesis and pretreatment on catalytic stability in oxidative reforming environments. *Appl. Catal., A* **2003**, *255*, 239-253.
103. LaMont, D. C.; Thomson, W. J., The influence of mass transfer conditions on the stability of molybdenum carbide for dry methane reforming. *Appl. Catal., A* **2004**, *274*, 173-178.
104. Naito, S., Mechanistic difference of the CO₂ reforming of CH₄ over unsupported and zirconia supported molybdenum carbide catalysts. *Catal. Today* **2002**, *77*, 161-165.
105. Liang, P.; Gao, H.; Yao, Z.; Jia, R.; Shi, Y.; Sun, Y.; Fan, Q.; Wang, H., Simple synthesis of ultrasmall β -Mo₂C and α -MoC_{1-x} nanoparticles and new insights into their catalytic mechanisms for dry reforming of methane. *Catal. Sci. Technol.* **2017**, *7*, 3312-3324.
106. Gao, H.; Yao, Z.; Shi, Y.; Jia, R.; Liang, F.; Sun, Y.; Mao, W.; Wang, H., Simple and large-scale synthesis of β -phase molybdenum carbides as highly stable catalysts for dry reforming of methane. *Inorg. Chem. Front.* **2018**, *5*, 90-99.
107. Gao, H.; Yao, Z.; Shi, Y.; Wang, S., Improvement of the catalytic stability of molybdenum carbide via encapsulation within carbon nanotubes in dry methane reforming. *Catal. Sci. Technol.* **2018**, *8*, 697-701.

108. Darujati, A. R. S.; Thomson, W. J., Stability of supported and promoted-molybdenum carbide catalysts in dry-methane reforming. *Appl. Catal., A* **2005**, *296*, 139-147.
109. Jung, K. T.; Kim, W. B.; Rhee, C. H.; Lee, J. S., Effects of Transition Metal Addition on the Solid-State Transformation of Molybdenum Trioxide to Molybdenum Carbides. *Chem. Mater.* **2004**, *16*, 307-314.
110. Cheng, J.; Huang, W., Effect of cobalt (nickel) content on the catalytic performance of molybdenum carbides in dry-methane reforming. *Fuel Process. Technol.* **2010**, *91*, 185-193.
111. Zhang, A.; Zhu, A.; Chen, B.; Zhang, S.; Au, C.; Shi, C., In-situ synthesis of nickel modified molybdenum carbide catalyst for dry reforming of methane. *Catal. Commun.* **2011**, *12*, 803-807.
112. Shi, C.; Zhang, A.; Li, X.; Zhang, S.; Zhu, A.; Ma, Y.; Au, C., Ni-modified Mo₂C catalysts for methane dry reforming. *Appl. Catal., A* **2012**, *431-432*, 164-170.
113. Zhang, S.; Shi, C.; Chen, B.; Zhang, Y.; Zhu, Y.; Qiu, J.; Au, C., Catalytic role of β-Mo₂C in DRM catalysts that contain Ni and Mo. *Catal. Today* **2015**, *258*, 676-683.
114. Yao, Z.; Jiang, J.; Zhao, Y.; Luan, F.; Zhu, J.; Shi, Y.; Gao, H.; Wang, H., Insights into the deactivation mechanism of metal carbide catalysts for dry reforming of methane *via* comparison of nickel-modified molybdenum and tungsten carbides. *RSC Adv.* **2016**, *6*, 19944-19951.
115. Sullivan, M. M.; Bhan, A., Effects of oxygen coverage on rates and selectivity of propane-CO₂ reactions on molybdenum carbide. *J. Catal.* **2018**, *357*, 195-205.
116. Naguib, M.; Kurtoglu, M.; Presser, V.; Lu, J.; Niu, J.; Heon, M.; Hultman, L.; Gogotsi, Y.; Barsoum, M. W., Two-dimensional nanocrystals produced by exfoliation of Ti₃AlC₂. *Adv. Mater.* **2011**, *23*, 4248-4253.
117. Naguib, M.; Mochalin, V. N.; Barsoum, M. W.; Gogotsi, Y., 25th anniversary article: MXenes: a new family of two-dimensional materials. *Adv. Mater.* **2014**, *26*, 992-1005.
118. Wang, H.-W.; Naguib, M.; Page, K.; Wesolowski, D. J.; Gogotsi, Y., Resolving the Structure of Ti₃C₂T_x MXenes through Multilevel Structural Modeling of the Atomic Pair Distribution Function. *Chem. Mater.* **2016**, *28*, 349-359.
119. Anasori, B.; Lukatskaya, M. R.; Gogotsi, Y., 2D metal carbides and nitrides (MXenes) for energy storage. *Nat. Rev. Mater.* **2017**, *2*, 16098.
120. Barsoum, M. W., The M_{N+1}AX_N phases: A new class of solids. *Prog. Solid State Chem.* **2000**, *28*, 201-281.
121. Naguib, M.; Mashtalir, O.; Carle, J.; Presser, V.; Lu, J.; Hultman, L.; Gogotsi, Y.; Barsoum, M. W., Two-dimensional transition metal carbides. *ACS Nano* **2012**, *6*, 1322-1331.
122. Deeva, E. B.; Kurllov, A.; Abdala, P. M.; Lebedev, D.; Kim, S. M.; Gordon, C. P.; Tsoukalou, A.; Fedorov, A.; Müller, C. R., *In Situ* XANES/XRD Study of the Structural Stability of Two-Dimensional Molybdenum Carbide Mo₂CT_x: Implications for the Catalytic Activity in the Water–Gas Shift Reaction. *Chem. Mater.* **2019**, *31*, 4505-4513.
123. Naguib, M.; Halim, J.; Lu, J.; Cook, K. M.; Hultman, L.; Gogotsi, Y.; Barsoum, M. W., New two-dimensional niobium and vanadium carbides as promising materials for Li-ion batteries. *J. Am. Chem. Soc.* **2013**, *135*, 15966-15969.
124. Lukatskaya, M. R.; Mashtalir, O.; Ren, C. E.; Dall'Agnese, Y.; Rozier, P.; Taberna, P. L.; Naguib, M.; Simon, P.; Barsoum, M. W.; Gogotsi, Y., Cation intercalation and high volumetric capacitance of two-dimensional titanium carbide. *Science* **2013**, *341*, 1502-1505.
125. Anasori, B.; Gogotsi, Y., *2D Metal Carbides and Nitrides (MXenes)*. Springer: 2019, 10.1007/978-3-030-19026-2.

126. Xie, Y.; Naguib, M.; Mochalin, V. N.; Barsoum, M. W.; Gogotsi, Y.; Yu, X.; Nam, K. W.; Yang, X. Q.; Kolesnikov, A. I.; Kent, P. R., Role of surface structure on Li-ion energy storage capacity of two-dimensional transition-metal carbides. *J. Am. Chem. Soc.* **2014**, *136*, 6385-6394.
127. Liang, X.; Garsuch, A.; Nazar, L. F., Sulfur cathodes based on conductive MXene nanosheets for high-performance lithium-sulfur batteries. *Angew. Chem., Int. Ed.* **2015**, *54*, 3907-3911.
128. Dall'Agness, Y.; Taberna, P. L.; Gogotsi, Y.; Simon, P., Two-Dimensional Vanadium Carbide (MXene) as Positive Electrode for Sodium-Ion Capacitors. *J. Phys. Chem. Lett.* **2015**, *6*, 2305-2309.
129. Ghidui, M.; Lukatskaya, M. R.; Zhao, M. Q.; Gogotsi, Y.; Barsoum, M. W., Conductive two-dimensional titanium carbide 'clay' with high volumetric capacitance. *Nature* **2014**, *516*, 78-81.
130. Zhao, M. Q.; Ren, C. E.; Ling, Z.; Lukatskaya, M. R.; Zhang, C.; Van Aken, K. L.; Barsoum, M. W.; Gogotsi, Y., Flexible MXene/carbon nanotube composite paper with high volumetric capacitance. *Adv. Mater.* **2015**, *27*, 339-345.
131. Cao, S.; Shen, B.; Tong, T.; Fu, J.; Yu, J., 2D/2D Heterojunction of Ultrathin MXene/Bi₂WO₆ Nanosheets for Improved Photocatalytic CO₂ Reduction. *Adv. Funct. Mater.* **2018**, *28*, 1800136.
132. Ran, J.; Gao, G.; Li, F. T.; Ma, T. Y.; Du, A.; Qiao, S. Z., Ti₃C₂ MXene co-catalyst on metal sulfide photo-absorbers for enhanced visible-light photocatalytic hydrogen production. *Nat. Commun.* **2017**, *8*, 13907.
133. Kuznetsov, D. A.; Chen, Z.; Kumar, P. V.; Tsoukalou, A.; Kierzkowska, A.; Abdala, P. M.; Safonova, O. V.; Fedorov, A.; Muller, C. R., Single Site Cobalt Substitution in 2D Molybdenum Carbide (MXene) Enhances Catalytic Activity in the Hydrogen Evolution Reaction. *J. Am. Chem. Soc.* **2019**, *141*, 17809-17816.
134. Chia, X.; Pumera, M., Characteristics and performance of two-dimensional materials for electrocatalysis. *Nat. Catal.* **2018**, *1*, 909-921.
135. Xie, X.; Chen, S.; Ding, W.; Nie, Y.; Wei, Z., An extraordinarily stable catalyst: Pt NPs supported on two-dimensional Ti₃C₂X₂ (X = OH, F) nanosheets for oxygen reduction reaction. *Chem. Commun.* **2013**, *49*, 10112-10114.
136. Gao, G.; O'Mullane, A. P.; Du, A., 2D MXenes: A New Family of Promising Catalysts for the Hydrogen Evolution Reaction. *ACS Catal.* **2016**, *7*, 494-500.
137. Zhang, J. Q.; Zhao, Y. F.; Guo, X.; Chen, C.; Dong, C. L.; Liu, R. S.; Han, C. P.; Li, Y. D.; Gogotsi, Y.; Wang, G. X., Single platinum atoms immobilized on an MXene as an efficient catalyst for the hydrogen evolution reaction. *Nat. Catal.* **2018**, *1*, 985-992.
138. Li, Z.; Cui, Y.; Wu, Z.; Milligan, C.; Zhou, L.; Mitchell, G.; Xu, B.; Shi, E.; Miller, J. T.; Ribeiro, F. H.; Wu, Y., Reactive metal-support interactions at moderate temperature in two-dimensional niobium-carbide-supported platinum catalysts. *Nat. Catal.* **2018**, *1*, 349-355.
139. Li, Z.; Yu, L.; Milligan, C.; Ma, T.; Zhou, L.; Cui, Y.; Qi, Z.; Libretto, N.; Xu, B.; Luo, J.; Shi, E.; Wu, Z.; Xin, H.; Delgass, W. N.; Miller, J. T.; Wu, Y., Two-dimensional transition metal carbides as supports for tuning the chemistry of catalytic nanoparticles. *Nat. Commun.* **2018**, *9*, 5258.
140. Zhao, D.; Chen, Z.; Yang, W.; Liu, S.; Zhang, X.; Yu, Y.; Cheong, W. C.; Zheng, L.; Ren, F.; Ying, G.; Cao, X.; Wang, D.; Peng, Q.; Wang, G.; Chen, C., MXene (Ti₃C₂) Vacancy Confined Single-Atom Catalyst for Efficient Functionalization of CO₂. *J. Am. Chem. Soc.* **2019**, *141*, 4086-4093.

141. Diao, J.; Hu, M.; Lian, Z.; Li, Z.; Zhang, H.; Huang, F.; Li, B.; Wang, X.; Su, D. S.; Liu, H., $Ti_3C_2T_x$ MXene Catalyzed Ethylbenzene Dehydrogenation: Active Sites and Mechanism Exploration from both Experimental and Theoretical Aspects. *ACS Catal.* **2018**, *8*, 10051-10057.
142. Ghassemi, H.; Harlow, W.; Mashtalir, O.; Beidaghi, M.; Lukatskaya, M. R.; Gogotsi, Y.; Taheri, M. L., In situ environmental transmission electron microscopy study of oxidation of two-dimensional Ti_3C_2 and formation of carbon-supported TiO_2 . *J. Mater. Chem. A* **2014**, *2*, 14339–14343.
143. Mashtalir, O.; Cook, K. M.; Mochalin, V. N.; Crowe, M.; Barsoum, M. W.; Gogotsi, Y., Dye adsorption and decomposition on two-dimensional titanium carbide in aqueous media. *J. Mater. Chem. A* **2014**, *2*, 14334-14338.
144. Maleski, K.; Mochalin, V. N.; Gogotsi, Y., Dispersions of Two-Dimensional Titanium Carbide MXene in Organic Solvents. *Chem. Mater.* **2017**, *29*, 1632-1640.
145. Habib, T.; Zhao, X.; Shah, S. A.; Chen, Y.; Sun, W.; An, H.; Lutkenhaus, J. L.; Radovic, M.; Green, M. J., Oxidation stability of $Ti_3C_2T_x$ MXene nanosheets in solvents and composite films. *NPJ 2D Mater. Appl.* **2019**, *3*, 8.
146. Cobden, P. D.; van Beurden, P.; Reijers, H. T. J.; Elzinga, G. D.; Kluiters, S. C. A.; Dijkstra, J. W.; Jansen, D.; van den Brink, R. W., Sorption-enhanced hydrogen production for pre-combustion CO_2 capture: Thermodynamic analysis and experimental results. *Int. J. Greenh. Gas Con.* **2007**, *1*, 170-179.
147. Bohn, C. D.; Müller, C. R.; Cleeton, J. P.; Hayhurst, A. N.; Davidson, J. F.; Scott, S. A.; Dennis, J. S., Production of Very Pure Hydrogen with Simultaneous Capture of Carbon Dioxide using the Redox Reactions of Iron Oxides in Packed Beds. *Ind. Eng. Chem. Res.* **2008**, *47*, 7623-7630.
148. Pozdnyakova, O.; Teschner, D.; Wootsch, A.; Krohnert, J.; Steinhauer, B.; Sauer, H.; Toth, L.; Jentoft, F.; Knopgericke, A.; Paal, Z., Preferential CO oxidation in hydrogen (PROX) on ceria-supported catalysts, part I: Oxidation state and surface species on Pt/CeO₂ under reaction conditions. *J. Catal.* **2006**, *237*, 1-16.
149. Han, C.; Harrison, D. P., Simultaneous shift reaction and carbon dioxide separation for the direct production of hydrogen. *Chem. Eng. Sci.* **1994**, *49*, 5875-5883.
150. Johnsen, K.; Grace, J. R.; Elnashaie, S. S. E. H.; Kolbeinsen, L.; Eriksen, D., Modeling of Sorption-Enhanced Steam Reforming in a Dual Fluidized Bubbling Bed Reactor. *Ind. Eng. Chem. Res.* **2006**, *45*, 4133-4144.
151. Le Chatelier, H., Sur un énoncé général des lois des équilibres chimiques. *C. R. Acad. Sci.* **1884**, *99*, 786-789.
152. Ochoa-Fernández, E.; Haugen, G.; Zhao, T.; Rønning, M.; Aartun, I.; Børresen, B.; Rytter, E.; Rønnekleiv, M.; Chen, D., Process design simulation of H₂ production by sorption enhanced steam methane reforming: evaluation of potential CO₂ acceptors. *Green Chem.* **2007**, *9*, 654-662.
153. Dou, B.; Wang, C.; Song, Y.; Chen, H.; Jiang, B.; Yang, M.; Xu, Y., Solid sorbents for in-situ CO₂ removal during sorption-enhanced steam reforming process: A review. *Renew. Sust. Energ. Rev.* **2016**, *53*, 536-546.
154. Broda, M.; Kierzkowska, A. M.; Baudouin, D.; Imtiaz, Q.; Copéret, C.; Müller, C. R., Sorbent-Enhanced Methane Reforming over a Ni–Ca-Based, Bifunctional Catalyst Sorbent. *ACS Catal.* **2012**, *2*, 1635-1646.
155. Kim, S. M.; Abdala, P. M.; Hosseini, D.; Armutlulu, A.; Margossian, T.; Copéret, C.; Müller, C., Bi-functional Ru/Ca₃Al₂O₆–CaO catalyst-CO₂ sorbent for the production of high

- purity hydrogen via sorption-enhanced steam methane reforming. *Catal. Sci. Technol.* **2019**, *9*, 5745-5756.
156. Halabi, M. H.; de Croon, M. H. J. M.; van der Schaaf, J.; Cobden, P. D.; Schouten, J. C., A novel catalyst–sorber system for an efficient H₂ production with in-situ CO₂ capture. *Int. J. Hydrogen Energy* **2012**, *37*, 4987-4996.
157. Balasubramanian, B.; Lopez Ortiz, A.; Kaytakoglu, S.; Harrison, D. P., Hydrogen from methane in a single-step process. *Chem. Eng. Sci.* **1999**, *54*, 3543-3552.
158. Lopez Ortiz, A.; Harrison, D. P., Hydrogen Production Using Sorption-Enhanced Reaction. *Ind. Eng. Chem. Res.* **2001**, *40*, 5102-5109.
159. Johnsen, K.; Ryu, H. J.; Grace, J. R.; Lim, C. J., Sorption-enhanced steam reforming of methane in a fluidized bed reactor with dolomite as CO₂-acceptor. *Chem. Eng. Sci.* **2006**, *61*, 1195-1202.
160. Li, Z.-s.; Cai, N.-s.; Yang, J.-b., Continuous Production of Hydrogen from Sorption-Enhanced Steam Methane Reforming in Two Parallel Fixed-Bed Reactors Operated in a Cyclic Manner. *Ind. Eng. Chem. Res.* **2006**, *45*, 8788-8793.
161. Martavaltzi, C. S.; Lemonidou, A. A., Hydrogen production via sorption enhanced reforming of methane: Development of a novel hybrid material—reforming catalyst and CO₂ sorber. *Chem. Eng. Sci.* **2010**, *65*, 4134-4140.
162. Di Giuliano, A.; Giancaterino, F.; Courson, C.; Foscolo, P. U.; Gallucci, K., Development of a Ni-CaO-mayenite combined sorber-catalyst material for multicycle sorption enhanced steam methane reforming. *Fuel* **2018**, *234*, 687-699.
163. Pecharaumporn, P.; Wongsakulphasatch, S.; Glinrun, T.; Maneedaeng, A.; Hassan, Z.; Assabumrungrat, S., Synthetic CaO-based sorber for high-temperature CO₂ capture in sorption-enhanced hydrogen production. *Int. J. Hydrogen Energy* **2019**, *44*, 20663-20677.
164. Keith, D. W., Why Capture CO₂ from the Atmosphere? *Science* **2009**, *325*, 1654-1655.
165. MacDowell, N.; Florin, N.; Buchard, A.; Hallett, J.; Galindo, A.; Jackson, G.; Adjiman, C. S.; Williams, C. K.; Shah, N.; Fennell, P., An overview of CO₂ capture technologies. *Energy Environ. Sci.* **2010**, *3*, 1645-1669.
166. Boot-Handford, M. E.; Abanades, J. C.; Anthony, E. J.; Blunt, M. J.; Brandani, S.; Mac Dowell, N.; Fernandez, J. R.; Ferrari, M. C.; Gross, R.; Hallett, J. P.; Haszeldine, R. S.; Heptonstall, P.; Lyngfelt, A.; Makuch, Z.; Mangano, E.; Porter, R. T. J.; Pourkashanian, M.; Rochelle, G. T.; Shah, N.; Yao, J. G.; Fennell, P. S., Carbon capture and storage update. *Energy Environ. Sci.* **2014**, *7*, 130-189.
167. Jacobson, M. Z., Review of solutions to global warming, air pollution, and energy security. *Energy Environ. Sci.* **2009**, *2*, 148-173.
168. Orr, F. M.; Taber, J. J., Use of Carbon Dioxide in Enhanced Oil Recovery. *Science* **1984**, *224*, 563-569.
169. Torp, T. A.; Gale, J., Demonstrating storage of CO₂ in geological reservoirs: The sleipner and SACS projects. *Energy* **2004**, *29*, 1361-1369.
170. Gadipelli, S.; Patel, H. A.; Guo, Z. X., An Ultrahigh Pore Volume Drives Up the Amine Stability and Cyclic CO₂ Capacity of a Solid-Amine@Carbon Sorber. *Adv. Mater.* **2015**, *27*, 4903-4909.
171. Drese, J. H.; Choi, S.; Lively, R. P.; Koros, W. J.; Fauth, D. J.; Gray, M. L.; Jones, C. W., Synthesis-Structure-Property Relationships for Hyperbranched Aminosilica CO₂ Adsorbents. *Adv. Funct. Mater.* **2009**, *19*, 3821-3832.

172. Sumida, K.; Rogow, D. L.; Mason, J. A.; McDonald, T. M.; Bloch, E. D.; Herm, Z. R.; Bae, T. H.; Long, J. R., Carbon Dioxide Capture in Metal-Organic Frameworks. *Chem. Rev.* **2012**, *112*, 724-781.
173. Duan, J. G.; Higuchi, M.; Horike, S.; Foo, M. L.; Rao, K. P.; Inubushi, Y.; Fukushima, T.; Kitagawa, S., High CO₂/CH₄ and C₂ Hydrocarbons/CH₄ Selectivity in a Chemically Robust Porous Coordination Polymer. *Adv. Funct. Mater.* **2013**, *23*, 3525-3530.
174. Lopez-Maya, E.; Montoro, C.; Colombo, V.; Barea, E.; Navarro, J. A. R., Improved CO₂ Capture from Flue Gas by Basic Sites, Charge Gradients, and Missing Linker Defects on Nickel Face Cubic Centered MOFs. *Adv. Funct. Mater.* **2014**, *24*, 6130-6135.
175. Lan, Y. Q.; Jiang, H. L.; Li, S. L.; Xu, Q., Mesoporous Metal-Organic Frameworks with Size-tunable Cages: Selective CO₂ Uptake, Encapsulation of Ln³⁺ Cations for Luminescence, and Column-Chromatographic Dye Separation. *Adv. Mater.* **2011**, *23*, 5015-5020.
176. Dennis, J. S.; Pacciani, R., The rate and extent of uptake of CO₂ by a synthetic, CaO-containing sorbent. *Chem. Eng. Sci.* **2009**, *64*, 2147-2157.
177. Charitos, A.; Rodríguez, N.; Hawthorne, C.; Alonso, M. n.; Zieba, M.; Arias, B.; Kopanakis, G.; Scheffknecht, G. n.; Abanades, J. C., Experimental Validation of the Calcium Looping CO₂ Capture Process with Two Circulating Fluidized Bed Carbonator Reactors. *Ind. Eng. Chem. Res.* **2011**, *50*, 9685-9695.
178. Chang, P. H.; Chang, Y. P.; Chen, S. Y.; Yu, C. T.; Chyou, Y. P., Ca-Rich Ca-Al-Oxide, High-Temperature-Stable Sorbents Prepared from Hydrotalcite Precursors: Synthesis, Characterization, and CO₂ Capture Capacity. *ChemSusChem* **2011**, *4*, 1844-1851.
179. Liu, F.-Q.; Li, W.-H.; Liu, B.-C.; Li, R.-X., Synthesis, characterization, and high temperature CO₂ capture of new CaO based hollow sphere sorbents. *J. Mater. Chem. A* **2013**, *1*, 8037-8044.
180. Wang, M.; Lee, C.-G., Absorption of CO₂ on CaSiO₃ at high temperatures. *Energy Convers. Manag.* **2009**, *50*, 636-638.
181. Valverde, J. M.; Perejon, A.; Perez-Maqueda, L. A., Enhancement of fast CO₂ capture by a nano-SiO₂/CaO composite at Ca-looping conditions. *Environ. Sci. Technol.* **2012**, *46*, 6401-6408.
182. Huang, C.-H.; Chang, K.-P.; Yu, C.-T.; Chiang, P.-C.; Wang, C.-F., Development of high-temperature CO₂ sorbents made of CaO-based mesoporous silica. *Chem. Eng. J.* **2010**, *161*, 129-135.
183. Vieille, L.; Govin, A.; Grosseau, P., Improvements of calcium oxide based sorbents for multiple CO₂ capture cycles. *Powder Technol.* **2012**, *228*, 319-323.
184. Wu, S. F.; Zhu, Y. Q., Behavior of CaTiO₃/Nano-CaO as a CO₂ Reactive Adsorbent. *Ind. Eng. Chem. Res.* **2010**, *49*, 2701-2706.
185. Wang, Y.; Zhu, Y.; Wu, S., A new nano CaO-based CO₂ adsorbent prepared using an adsorption phase technique. *Chem. Eng. J.* **2013**, *218*, 39-45.
186. Derevschikov, V. S.; Lysikov, A. I.; Okunev, A. G., High Temperature CaO/Y₂O₃ Carbon Dioxide Absorbent with Enhanced Stability for Sorption-Enhanced Reforming Applications. *Ind. Eng. Chem. Res.* **2011**, *50*, 12741-12749.
187. Manovic, V.; Anthony, E. J., CaO-based pellets supported by calcium aluminate cements for high-temperature CO₂ capture. *Environ. Sci. Technol.* **2009**, *43*, 7117-7122.
188. Qin, C.; Yin, J.; An, H.; Liu, W.; Feng, B., Performance of Extruded Particles from Calcium Hydroxide and Cement for CO₂ Capture. *Energy Fuels* **2011**, *26*, 154-161.

189. Ridha, F. N.; Manovic, V.; Macchi, A.; Anthony, E. J., High-temperature CO₂ capture cycles for CaO-based pellets with kaolin-based binders. *Int. J. Greenh. Gas. Con.* **2012**, *6*, 164-170.
190. Brunauer, S.; Emmett, P. H.; Teller, E., Adsorption of Gases in Multimolecular Layers. *J. Am. Chem. Soc.* **1938**, *60*, 309-319.
191. Barrett, E. P.; Joyner, L. G.; Halenda, P. P., The Determination of Pore Volume and Area Distributions in Porous Substances. I. Computations from Nitrogen Isotherms. *J. Am. Chem. Soc.* **1951**, *73*, 373-380.
192. Washburn, E. W., The Dynamics of Capillary Flow. *Phys. Rev.* **1921**, *17*, 273-283.
193. Burns, J. H.; Bredig, M. A., Transformation of Calcite to Aragonite by Grinding. *J. Chem. Phys.* **1956**, *25*, 1281-1281.
194. Li, T.; Sui, F.; Li, F.; Cai, Y.; Jin, Z., Effects of dry grinding on the structure and granularity of calcite and its polymorphic transformation into aragonite. *Powder Technol.* **2014**, *254*, 338-343.
195. Borgwardt, R. H., Calcium Oxide Sintering in Atmospheres Containing Water and Carbon Dioxide. *Ind. Eng. Chem. Res.* **1989**, *28*, 493-500.
196. Hacker, B. R.; Kirby, S. H.; Bohlen, S. R., Time and Metamorphic Petrology: Calcite to Aragonite Experiments. *Science* **1992**, *258*, 110-112.
197. Lin, S.-J.; Huang, W.-L., Polycrystalline calcite to aragonite transformation kinetics: experiments in synthetic systems. *Contrib. Mineral. Petrol.* **2004**, *147*, 604-614.
198. Malliaris, A.; Turner, D. T., Influence of Particle Size on the Electrical Resistivity of Compacted Mixtures of Polymeric and Metallic Powders. *J Appl Phys* **1971**, *42*, 614-618.
199. Kryuchkov, Y. N., Percolation estimation of the conductivity and elasticity of heterogeneous two-phase systems. *Theor. Found. Chem. Eng.* **2000**, *34*, 281-285.
200. Alvarez, D.; Abanades, J. C., Pore-Size and Shape Effects on the Recarbonation Performance of Calcium Oxide Submitted to Repeated Calcination/Recarbonation Cycles. *Energy Fuels* **2005**, *19*, 270-278.
201. Abanades, J. C.; Anthony, E. J.; Lu, D. Y.; Salvador, C.; Alvarez, D., Capture of CO₂ from combustion gases in a fluidized bed of CaO. *Aiche J.* **2004**, *50*, 1614-1622.
202. Bhatia, S. K.; Perlmutter, D. D., Effect of the Product Layer on the Kinetics of the CO₂-Lime Reaction. *Aiche J.* **1983**, *29*, 79-86.
203. *World Energy Balances 2019*; IEA: Paris, 2019.
204. Liu, W.; An, H.; Qin, C.; Yin, J.; Wang, G.; Feng, B.; Xu, M., Performance Enhancement of Calcium Oxide Sorbents for Cyclic CO₂ Capture—A Review. *Energy Fuels* **2012**, *26*, 2751-2767.
205. Kurlov, A.; Broda, M.; Hosseini, D.; Mitchell, S. J.; Perez-Ramirez, J.; Muller, C. R., Mechanochemically Activated, Calcium Oxide-Based, Magnesium Oxide-Stabilized Carbon Dioxide Sorbents. *ChemSusChem* **2016**, *9*, 2380-2390.
206. Ravel, B.; Newville, M., ATHENA, ARTEMIS, HEPHAESTUS: data analysis for X-ray absorption spectroscopy using IFEFFIT. *J. Synchrotron Rad.* **2005**, *12*, 537-541.
207. Prado, R. J.; Flank, A. M., Sodium K Edge XANES Calculation in 'NaCl' Type Structures. *Phys. Scr.* **2005**, *T115*, 165-167.
208. Kim, J.-W.; Lee, H.-G., Thermal and carbothermic decomposition of Na₂CO₃ and Li₂CO₃. *Metall. Mater. Trans. B* **2001**, *32*, 17-24.
209. Gavryushkin, P. N.; Thomas, V. G.; Bolotina, N. B.; Bakakin, V. V.; Golovin, A. V.; Seryotkin, Y. V.; Fursenko, D. A.; Litasov, K. D., Hydrothermal Synthesis and Structure Solution

- of $\text{Na}_2\text{Ca}(\text{CO}_3)_2$: “Synthetic Analogue” of Mineral Nyerereite. *Cryst. Growth Des.* **2016**, *16*, 1893-1902.
210. Mitchell, R. H.; Kjarsgaard, B. A., EXPERIMENTAL STUDIES OF THE SYSTEM $\text{Na}_2\text{Ca}(\text{CO}_3)_2$ - NaCl - KCl AT 0.1 GPa: IMPLICATIONS FOR THE DIFFERENTIATION AND LOW-TEMPERATURE CRYSTALLIZATION OF NATROCARBONATITE. *Can. Mineral.* **2008**, *46*, 971-980.
211. Gibbins, J.; Chalmers, H., Carbon capture and storage. *Energ Policy* **2008**, *36*, 4317-4322.
212. Wang, J. Y.; Huang, L.; Yang, R. Y.; Zhang, Z.; Wu, J. W.; Gao, Y. S.; Wang, Q.; O'Hare, D.; Zhong, Z. Y., Recent advances in solid sorbents for CO_2 capture and new development trends. *Energy Environ. Sci.* **2014**, *7*, 3478-3518.
213. Erans, M.; Manovic, V.; Anthony, E. J., Calcium looping sorbents for CO_2 capture. *Appl. Energy* **2016**, *180*, 722-742.
214. Manovic, V.; Anthony, E. J., Thermal Activation of CaO-Based Sorbent and Self-Reactivation during CO_2 Capture Looping Cycles. *Environ. Sci. Technol.* **2008**, *42*, 4170-4174.
215. Chen, Z.; Song, H. S.; Portillo, M.; Lim, C. J.; Grace, J. R.; Anthony, E. J., Long-Term Calcination/Carbonation Cycling and Thermal Pretreatment for CO_2 Capture by Limestone and Dolomite. *Energy Fuels* **2009**, *23*, 1437-1444.
216. Manovic, V.; Anthony, E. J., Steam Reactivation of Spent CaO-Based Sorbent for Multiple CO_2 Capture Cycles. *Environ. Sci. Technol.* **2007**, *41*, 1420-1425.
217. Manovic, V.; Anthony, E. J., Reactivation and remaking of calcium aluminate pellets for CO_2 capture. *Fuel* **2011**, *90*, 233-239.
218. Fennell, P. S.; Pacciani, R.; Dennis, J. S.; Davidson, J. F.; Hayhurst, A. N., The effects of repeated cycles of calcination and carbonation on a variety of different limestones, as measured in a hot fluidized bed of sand. *Energy Fuels* **2007**, *21*, 2072-2081.
219. Wu, Y.; Manovic, V.; He, I.; Anthony, E. J., Modified lime-based pellet sorbents for high-temperature CO_2 capture: Reactivity and attrition behavior. *Fuel* **2012**, *96*, 454-461.
220. Chen, H.; Zhao, C.; Yang, Y., Enhancement of attrition resistance and cyclic CO_2 capture of calcium-based sorbent pellets. *Fuel Process. Technol.* **2013**, *116*, 116-122.
221. Arias, B.; Alonso, M.; Abanades, C., CO_2 Capture by Calcium Looping at Relevant Conditions for Cement Plants: Experimental Testing in a 30 kW_{th} Pilot Plant. *Ind. Eng. Chem. Res.* **2017**, *56*, 2634-2640.
222. Harrison, D. P., Sorption-Enhanced Hydrogen Production: A Review. *Ind. Eng. Chem. Res.* **2008**, *47*, 6486-6501.
223. Fernández, J. R.; Abanades, J. C., Optimized design and operation strategy of a Ca Cu chemical looping process for hydrogen production. *Chem. Eng. Sci.* **2017**, *166*, 144-160.
224. Westbye, A.; Aranda, A.; Grasa, G.; Dietzel, P. D. C.; Martínez, I.; Di Felice, L., Fixed Bed Reactor Validation of a Mayenite Based Combined Calcium–Copper Material for Hydrogen Production through Ca–Cu Looping. *Ind. Eng. Chem. Res.* **2019**, *58*, 14664-14677.
225. Chen, J.; Duan, L.; Shi, T.; Bian, R.; Lu, Y.; Donat, F.; Anthony, E. J., A facile one-pot synthesis of CaO/CuO hollow microspheres featuring highly porous shells for enhanced CO_2 capture in a combined Ca–Cu looping process via a template-free synthesis approach. *J. Mater. Chem. A* **2019**, *7*, 21096-21105.
226. Díez-Martín, L.; López, J. M.; Fernández, J. R.; Martínez, I.; Grasa, G.; Murillo, R., Complete Ca/Cu cycle for H_2 production via CH_4 sorption enhanced reforming in a Lab-Scale fixed bed reactor. *Chemical Engineering Journal* **2018**, *350*, 1010-1021.
227. Mitchell, S.; Michels, N. L.; Kunze, K.; Perez-Ramirez, J., Visualization of hierarchically structured zeolite bodies from macro to nano length scales. *Nat. Chem.* **2012**, *4*, 825-831.

228. Yang, X. Y.; Chen, L. H.; Li, Y.; Rooke, J. C.; Sanchez, C.; Su, B. L., Hierarchically porous materials: synthesis strategies and structure design. *Chem. Soc. Rev.* **2017**, *46*, 481-558.
229. Wang, Y.; Arandiyana, H.; Scott, J.; Dai, H. X.; Amal, R., Hierarchically Porous Network-Like Ni/Co₃O₄: Noble Metal-Free Catalysts for Carbon Dioxide Methanation. *Adv Sustain Syst* **2018**, *2*, 1700119.
230. Srinivas, G.; Krungleviciute, V.; Guo, Z.-X.; Yildirim, T., Exceptional CO₂ capture in a hierarchically porous carbon with simultaneous high surface area and pore volume. *Energy Environ. Sci.* **2014**, *7*, 335-342.
231. Butler, R.; Davies, C. M.; Cooper, A. I., Emulsion templating using high internal phase supercritical fluid emulsions. *Adv. Mater.* **2001**, *13*, 1459-1463.
232. Zhang, H.; Cooper, A. I., Synthesis and applications of emulsion-templated porous materials. *Soft Matter*. **2005**, *1*, 107-113.
233. Gonzenbach, U. T.; Studart, A. R.; Tervoort, E.; Gauckler, L. J., Macroporous ceramics from particle-stabilized wet foams. *J. Am. Ceram. Soc.* **2007**, *90*, 16-22.
234. Deville, S.; Saiz, E.; Tomsia, A. P., Ice-templated porous alumina structures. *Acta Mater* **2007**, *55*, 1965-1974.
235. Mann, S.; Burkett, S. L.; Davis, S. A.; Fowler, C. E.; Mendelson, N. H.; Sims, S. D.; Walsh, D.; Whilton, N. T., Sol-Gel Synthesis of Organized Matter. *Chem. Mater.* **1997**, *9*, 2300-2310.
236. Studart, A. R.; Studer, J.; Xu, L.; Yoon, K.; Shum, H. C.; Weitz, D. A., Hierarchical porous materials made by drying complex suspensions. *Langmuir* **2011**, *27*, 955-964.
237. Erb, R. M.; Obrist, D.; Chen, P. W.; Studer, J.; Studart, A. R., Predicting sizes of droplets made by microfluidic flow-induced dripping. *Soft Matter*. **2011**, *7*, 8757-8761.
238. Ofner, A.; Moore, D. G.; Rühls, P. A.; Schwendimann, P.; Eggersdorfer, M.; Amstad, E.; Weitz, D. A.; Studart, A. R., High-Throughput Step Emulsification for the Production of Functional Materials Using a Glass Microfluidic Device. *Macromol. Chem. Phys.* **2017**, *218*, 1600472.
239. Li, Z.-s.; Cai, N.-s.; Huang, Y.-y.; Han, H.-j., Synthesis, Experimental Studies, and Analysis of a New Calcium-Based Carbon Dioxide Absorbent. *Energy Fuels* **2005**, *19*, 1447-1452.
240. Barker, R., The reversibility of the reaction $\text{CaCO}_3 \rightleftharpoons \text{CaO} + \text{CO}_2$. *J. Appl. Chem. Biotechnol.* **2007**, *23*, 733-742.
241. Oyama, S. T., *The Chemistry of Transition Metal Carbides and Nitrides*. Springer: 1996, 10.1007/978-94-009-1565-7.
242. Hwu, H. H.; Chen, J. G., Surface chemistry of transition metal carbides. *Chem. Rev.* **2005**, *105*, 185-212.
243. Alexander, A. M.; Hargreaves, J. S., Alternative catalytic materials: carbides, nitrides, phosphides and amorphous boron alloys. *Chem. Soc. Rev.* **2010**, *39*, 4388-4401.
244. Stottlemeyer, A. L.; Kelly, T. G.; Meng, Q.; Chen, J. G., Reactions of oxygen-containing molecules on transition metal carbides: Surface science insight into potential applications in catalysis and electrocatalysis. *Surf. Sci. Rep.* **2012**, *67*, 201-232.
245. Chen, W. F.; Muckerman, J. T.; Fujita, E., Recent developments in transition metal carbides and nitrides as hydrogen evolution electrocatalysts. *Chem. Commun.* **2013**, *49*, 8896-909.
246. Ma, Y.; Guan, G.; Hao, X.; Cao, J.; Abudula, A., Molybdenum carbide as alternative catalyst for hydrogen production – A review. *Renew. Sust. Energy Rev.* **2017**, *75*, 1101-1129.
247. Wan, W.; Tackett, B. M.; Chen, J. G., Reactions of water and C1 molecules on carbide and metal-modified carbide surfaces. *Chem. Soc. Rev.* **2017**, *46*, 1807-1823.

248. Moyer, M. M.; Karakaya, C.; Kee, R. J.; Trewyn, B. G., In Situ Formation of Metal Carbide Catalysts. *ChemCatChem* **2017**, *9*, 3090-3101.
249. Dronskowski, R.; Kikkawa, S.; Stein, A., *Handbook of Solid State Chemistry*. Wiley: 2017, 10.1002/9783527691036.
250. Lezcano-Gonzalez, I.; Oord, R.; Rovezzi, M.; Glatzel, P.; Botchway, S. W.; Weckhuysen, B. M.; Beale, A. M., Molybdenum Speciation and its Impact on Catalytic Activity during Methane Dehydroaromatization in Zeolite ZSM-5 as Revealed by Operando X-Ray Methods. *Angew. Chem., Int. Ed.* **2016**, *55*, 5215-5219.
251. Kosinov, N.; Coumans, F. J. A. G.; Uslamin, E. A.; Wijpkema, A. S. G.; Mezari, B.; Hensen, E. J. M., Methane Dehydroaromatization by Mo/HZSM-5: Mono- or Bifunctional Catalysis? *ACS Catal.* **2016**, *7*, 520-529.
252. Liu, P.; Rodriguez, J. A., Water-gas-shift reaction on molybdenum carbide surfaces: essential role of the oxycarbide. *J. Phys. Chem. B* **2006**, *110*, 19418-19425.
253. Lee, W.-S.; Kumar, A.; Wang, Z.; Bhan, A., Chemical Titration and Transient Kinetic Studies of Site Requirements in Mo₂C-Catalyzed Vapor Phase Anisole Hydrodeoxygenation. *ACS Catal.* **2015**, *5*, 4104-4114.
254. Schaidle, J. A.; Blackburn, J.; Farberow, C. A.; Nash, C.; Steirer, K. X.; Clark, J.; Robichaud, D. J.; Ruddy, D. A., Experimental and Computational Investigation of Acetic Acid Deoxygenation over Oxophilic Molybdenum Carbide: Surface Chemistry and Active Site Identity. *ACS Catal.* **2016**, *6*, 1181-1197.
255. Sullivan, M. M.; Chen, C.-J.; Bhan, A., Catalytic deoxygenation on transition metal carbide catalysts. *Catal. Sci. Technol.* **2016**, *6*, 602-616.
256. Wang, H.; Liu, S.; Smith, K. J., Synthesis and Hydrodeoxygenation Activity of Carbon Supported Molybdenum Carbide and Oxycarbide Catalysts. *Energy Fuels* **2016**, *30*, 6039-6049.
257. Xu, W.; Ramirez, P. J.; Stacchiola, D.; Rodriguez, J. A., Synthesis of α -MoC_{1-x} and β -MoC_y Catalysts for CO₂ Hydrogenation by Thermal Carburization of Mo-oxide in Hydrocarbon and Hydrogen Mixtures. *Catal Lett* **2014**, *144*, 1418-1424.
258. Bradford, M. C. J.; Vannice, M. A., CO₂ Reforming of CH₄ over Supported Ru Catalysts. *J. Catal.* **1999**, *183*, 69-75.
259. Xiao, T.-c.; Hanif, A.; York, A. P. E.; Nishizaka, Y.; Green, M. L. H., Study on the mechanism of partial oxidation of methane to synthesis gas over molybdenum carbide catalyst. *Phys. Chem. Chem. Phys.* **2002**, *4*, 4549-4554.
260. York, A. P. E.; Claridge, J. B.; Brungs, A. J.; Tsang, S. C.; Green, M. L. H., Molybdenum and tungsten carbides as catalysts for the conversion of methane to synthesis gas using stoichiometric feedstocks. *Chem. Commun.* **1997**, *1*, 39-40.
261. LaMont, D. C.; Thomson, W. J., Dry reforming kinetics over a bulk molybdenum carbide catalyst. *Chem. Eng. Sci.* **2005**, *60*, 3553-3559.
262. Lee, J. S.; Oyama, S. T.; Boudart, M., Molybdenum Carbide Catalysts: I. Synthesis of Unsupported Powders. *J. Catal.* **1987**, *106*, 125-133.
263. Chaudhury, S.; Mukerjee, S. K.; Vaidya, V. N.; Venugopal, V., Kinetics and mechanism of carbothermic reduction of MoO₃ to Mo₂C. *J. Alloys Compd.* **1997**, *261*, 105-113.
264. Wang, H. M.; Wang, X. H.; Zhang, M. H.; Du, X. Y.; Li, W.; Tao, K. Y., Synthesis of bulk and supported molybdenum carbide by a single-step thermal carburization method. *Chem. Mater.* **2007**, *19*, 1801-1807.
265. Ochoa, E.; Torres, D.; Moreira, R.; Pinilla, J. L.; Suelves, I., Carbon nanofiber supported Mo₂C catalysts for hydrodeoxygenation of guaiacol: The importance of the carburization process. *Appl. Catal., B* **2018**, *239*, 463-474.

266. Naeem, M. A.; Abdala, P. M.; Armutlulu, A.; Kim, S. M.; Fedorov, A.; Müller, C. R., Exsolution of Metallic Ru Nanoparticles from Defective, Fluorite-Type Solid Solutions $\text{Sm}_2\text{Ru}_x\text{Ce}_{2-x}\text{O}_7$ To Impart Stability on Dry Reforming Catalysts. *ACS Catal.* **2020**, *10*, 1923-1937.
267. Chithambararaj, A.; Rajeswari Yogamalar, N.; Bose, A. C., Hydrothermally Synthesized h-MoO₃ and α -MoO₃ Nanocrystals: New Findings on Crystal-Structure-Dependent Charge Transport. *Cryst. Growth Des.* **2016**, *16*, 1984-1995.
268. Ji, F.; Ren, X.; Zheng, X.; Liu, Y.; Pang, L.; Jiang, J.; Liu, S., 2D-MoO₃ nanosheets for superior gas sensors. *Nanoscale* **2016**, *8*, 8696-8703.
269. Titirici, M.-M.; Antonietti, M.; Baccile, N., Hydrothermal carbon from biomass: a comparison of the local structure from poly- to monosaccharides and pentoses/hexoses. *Green Chem.* **2008**, *10*, 1204-1212.
270. Abdala, P. M.; Mauroy, H.; van Beek, W., A large-area CMOS detector for high-energy synchrotron powder diffraction and total scattering experiments. *J. Appl. Crystallogr.* **2014**, *47*, 449-457.
271. van Beek, W.; Safonova, O. V.; Wiker, G.; Emerich, H., SNBL, a dedicated beamline for combined in situ X-ray diffraction, X-ray absorption and Raman scattering experiments. *Phase Transit.* **2011**, *84*, 726-732.
272. Jaumot, J.; de Juan, A.; Tauler, R., MCR-ALS GUI 2.0: New features and applications. *Chemom. Intell. Lab. Syst.* **2015**, *140*, 1-12.
273. Martini, A.; Borfecchia, E.; Lomachenko, K. A.; Pankin, I. A.; Negri, C.; Berlier, G.; Beato, P.; Falsig, H.; Bordiga, S.; Lamberti, C., Composition-driven Cu-speciation and reducibility in Cu-CHA zeolite catalysts: a multivariate XAS/FTIR approach to complexity. *Chem. Sci.* **2017**, *8*, 6836-6851.
274. Wang, D.; Su, D. S.; Schlögl, R., Electron Beam Induced Transformation of MoO₃ to MoO₂ and a New Phase MoO. *Zeitschrift für anorganische und allgemeine Chemie* **2004**, *630*, 1007-1014.
275. Lajaunie, L.; Boucher, F.; Dessapt, R.; Moreau, P., Quantitative use of electron energy-loss spectroscopy Mo-M_{2,3} edges for the study of molybdenum oxides. *Ultramicroscopy* **2015**, *149*, 1-8.
276. Wu, W.; Wu, Z.; Liang, C.; Ying, P.; Feng, Z.; Li, C., An IR study on the surface passivation of Mo₂C/Al₂O₃ catalyst with O₂, H₂O and CO₂. *Phys. Chem. Chem. Phys.* **2004**, *6*, 5603-5608
277. Guzmán, H. J.; Xu, W.; Stacchiola, D.; Vitale, G.; Scott, C. E.; Rodríguez, J. A.; Pereira-Almao, P., In situ time-resolved X-ray diffraction study of the synthesis of Mo₂C with different carburization agents. *Canad. J. Chem.* **2013**, *91*, 573-582.
278. Vitale, G.; Guzmán, H.; Frauwallner, M. L.; Scott, C. E.; Pereira-Almao, P., Synthesis of nanocrystalline molybdenum carbide materials and their characterization. *Catal. Today* **2015**, *250*, 123-133.
279. Chen, W. F.; Wang, C. H.; Sasaki, K.; Marinkovic, N.; Xu, W.; Muckerman, J. T.; Zhu, Y.; Adzic, R. R., Highly active and durable nanostructured molybdenum carbide electrocatalysts for hydrogen production. *Energy Environ. Sci.* **2013**, *6*, 943-951.
280. Takenaka, S.; Tanaka, T.; Funabiki, T.; Yoshida, S., Structures of molybdenum species in silica-supported molybdenum oxide and alkali-ion-modified silica-supported molybdenum oxide. *J. Phys. Chem. B* **1998**, *102*, 2960-2969.
281. Beale, A. M.; Sankar, G., In Situ Study of the Formation of Crystalline Bismuth Molybdate Materials under Hydrothermal Conditions. *Chem. Mater.* **2003**, *15*, 146-153.

282. Likith, S. R. J.; Farberow, C. A.; Manna, S.; Abdulslam, A.; Stevanović, V.; Ruddy, D. A.; Schaidle, J. A.; Robichaud, D. J.; Ciobanu, C. V., Thermodynamic Stability of Molybdenum Oxycarbides Formed from Orthorhombic Mo₂C in Oxygen-Rich Environments. *J. Phys. Chem. C* **2018**, *122*, 1223-1233.
283. Zheng, Y.; Tang, Y.; Gallagher, J. R.; Gao, J.; Miller, J. T.; Wachs, I. E.; Podkolzin, S. G., Molybdenum Oxide, Oxycarbide and Carbide: Controlling the Dynamic Composition, Size and Catalytic Activity of Zeolite-Supported Nanostructures. *J. Phys. Chem. C* **2019**, *123*, 22281-22292.
284. Seh, Z. W.; Fredrickson, K. D.; Anasori, B.; Kibsgaard, J.; Strickler, A. L.; Lukatskaya, M. R.; Gogotsi, Y.; Jaramillo, T. F.; Vojvodic, A., Two-Dimensional Molybdenum Carbide (MXene) as an Efficient Electrocatalyst for Hydrogen Evolution. *ACS Energy Lett.* **2016**, *1*, 589-594.
285. Sang, X.; Xie, Y.; Yilmaz, D. E.; Lotfi, R.; Alhabeb, M.; Ostadhossein, A.; Anasori, B.; Sun, W.; Li, X.; Xiao, K.; Kent, P. R. C.; van Duin, A. C. T.; Gogotsi, Y.; Unocic, R. R., In situ atomistic insight into the growth mechanisms of single layer 2D transition metal carbides. *Nat. Commun.* **2018**, *9*, 2266.
286. Rakhi, R. B.; Ahmed, B.; Hedhili, M. N.; Anjum, D. H.; Alshareef, H. N., Effect of Postetch Annealing Gas Composition on the Structural and Electrochemical Properties of Ti₂CT_x MXene Electrodes for Supercapacitor Applications. *Chem. Mater.* **2015**, *27*, 5314-5323.
287. Hart, J. L.; Hantanasirisakul, K.; Lang, A. C.; Anasori, B.; Pinto, D.; Pivak, Y.; van Omme, J. T.; May, S. J.; Gogotsi, Y.; Taheri, M. L., Control of MXenes' electronic properties through termination and intercalation. *Nat. Commun.* **2019**, *10*, 522.
288. Tsakoumis, N. E.; Voronov, A.; Rønning, M.; van Beek, W.; Borg, Ø.; Rytter, E.; Holmen, A., Fischer–Tropsch synthesis: An XAS/XRPD combined in situ study from catalyst activation to deactivation. *J. Catal.* **2012**, *291*, 138-148.
289. Tsakoumis, N. E.; Walmsley, J. C.; Ronning, M.; van Beek, W.; Rytter, E.; Holmen, A., Evaluation of Reoxidation Thresholds for gamma-Al₂O₃-Supported Cobalt Catalysts under Fischer-Tropsch Synthesis Conditions. *J. Am. Chem. Soc.* **2017**, *139*, 3706-3715.
290. Hu, C.; Lai, C. C.; Tao, Q.; Lu, J.; Halim, J.; Sun, L.; Zhang, J.; Yang, J.; Anasori, B.; Wang, J.; Sakka, Y.; Hultman, L.; Eklund, P.; Rosen, J.; Barsoum, M. W., Mo₂Ga₂C: a new ternary nanolaminated carbide. *Chem. Commun.* **2015**, *51*, 6560-6563.
291. Halim, J.; Kota, S.; Lukatskaya, M. R.; Naguib, M.; Zhao, M.-Q.; Moon, E. J.; Pitcock, J.; Nanda, J.; May, S. J.; Gogotsi, Y.; Barsoum, M. W., Synthesis and Characterization of 2D Molybdenum Carbide (MXene). *Adv. Funct. Mater.* **2016**, *26*, 3118-3127.
292. Cossu, G.; Rossi, A.; Arcifa, A.; Spencer, N. D., Development and Application of a Cost-Effective Transfer Cell for X-ray Photoelectron Spectroscopy. *Incontro di Spettroscopia Analitica ISA* **2018**, *Cagliari*.
293. Shirley, D. A., High-Resolution X-Ray Photoemission Spectrum of the Valence Bands of Gold. *Phys. Rev. B* **1972**, *5*, 4709-4714.
294. Scofield, J. H., Hartree-Slater Subshell Photoionization Cross-Sections at 1254 and 1487 eV. *J. Electron Spectros. Relat. Phenomena* **1976**, *8*, 129-137.
295. Rietveld, H. M., A Profile Refinement Method for Nuclear and Magnetic Structures. *J. Appl. Crystallogr.* **1969**, *2*, 65-71.
296. Le Bail, A.; Duroy, H.; Fourquet, J. L., Ab-Initio Structure Determination of LiSbWO₆ by X-ray Powder Diffraction. *Mater. Res. Bull.* **1988**, *23*, 447-452.
297. Rodríguez-Carvajal, J., Recent advances in magnetic structure determination by neutron powder diffraction. *Physica B Condens. Matter* **1993**, *192*, 55-69.

298. Cramer, S. P.; Eccles, T. K.; Kutzler, F. W.; Hodgson, K. O.; Mortenson, L. E., Molybdenum X-ray Absorption Edge Spectra. The Chemical State of Molybdenum in Nitrogenase. *J. Am. Chem. Soc.* **1976**, *98*, 1287-1288.
299. Ressler, T.; Wienold, J.; Jentoft, R. E.; Neisius, T., Bulk structural investigation of the reduction of MoO₃ with propene and the oxidation of MoO₂ with oxygen. *J. Catal.* **2002**, *210*, 67-83.
300. Lukatskaya, M. R.; Bak, S. M.; Yu, X. Q.; Yang, X. Q.; Barsoum, M. W.; Gogotsi, Y., Probing the Mechanism of High Capacitance in 2D Titanium Carbide Using In Situ X-Ray Absorption Spectroscopy. *Adv. Energy Mater.* **2015**, *5*, 1500589.
301. Xiao, T. C.; York, A. P. E.; Williams, V. C.; Al-Megren, H.; Hanif, A.; Zhou, X. Y.; Green, M. L. H., Preparation of molybdenum carbides using butane and their catalytic performance. *Chem. Mater.* **2000**, *12*, 3896-3905.
302. Xiao, T.; York, A. P. E.; Coleman, K. S.; Claridge, J. B.; Sloan, J.; Charnock, J.; Green, M. L. H., Effect of carburising agent on the structure of molybdenum carbides. *J. Mater. Chem.* **2001**, *11*, 3094-3098.
303. Hope, M. A.; Forse, A. C.; Griffith, K. J.; Lukatskaya, M. R.; Ghidui, M.; Gogotsi, Y.; Grey, C. P., NMR reveals the surface functionalisation of Ti₃C₂ MXene. *Phys. Chem. Chem. Phys.* **2016**, *18*, 5099-5102.
304. Harris, K. J.; Bugnet, M.; Naguib, M.; Barsoum, M. W.; Goward, G. R., Direct Measurement of Surface Termination Groups and Their Connectivity in the 2D MXene V₂CT_x Using NMR Spectroscopy. *J. Phys. Chem. C* **2015**, *119*, 13713-13720.
305. Halim, J.; Cook, K. M.; Naguib, M.; Eklund, P.; Gogotsi, Y.; Rosen, J.; Barsoum, M. W., X-ray photoelectron spectroscopy of select multi-layered transition metal carbides (MXenes). *Appl. Surf. Sci.* **2016**, *362*, 406-417.
306. Damma, D.; Boningari, T.; Smirniotis, P. G., High-temperature water-gas shift over Fe/Ce/Co spinel catalysts: Study of the promotional effect of Ce and Co. *Mol Catal* **2018**, *451*, 20-32.
307. Yao, S.; Zhang, X.; Zhou, W.; Gao, R.; Xu, W.; Ye, Y.; Lin, L.; Wen, X.; Liu, P.; Chen, B.; Crumlin, E.; Guo, J.; Zuo, Z.; Li, W.; Xie, J.; Lu, L.; Kiely, C. J.; Gu, L.; Shi, C.; Rodriguez, J. A.; Ma, D., Atomic-layered Au clusters on α -MoC as catalysts for the low-temperature water-gas shift reaction. *Science* **2017**, *357*, 389-393.
308. Shou, H.; Davis, R. J., Multi-product steady-state isotopic transient kinetic analysis of CO hydrogenation over supported molybdenum carbide. *J. Catal.* **2013**, *306*, 91-99.
309. Naito, S.; Takada, A.; Tokizawa, S.; Miyao, T., Mechanistic study on the methane activation over various supported molybdenum carbide catalysts with isotopic tracer methods. *Appl. Catal., A* **2005**, *289*, 22-27.
310. Chorkendorff, I.; Niemantsverdriet, J. W., *Concepts of Modern Catalysis and Kinetics*. Wiley: 2003, 10.1002/3527602658.
311. Chen, C.-J.; Bhan, A., Mo₂C Modification by CO₂, H₂O, and O₂: Effects of Oxygen Content and Oxygen Source on Rates and Selectivity of m-Cresol Hydrodeoxygenation. *ACS Catal.* **2017**, *7*, 1113-1122.
312. Li, Z.; Wu, Y., 2D Early Transition Metal Carbides (MXenes) for Catalysis. *Small* **2019**, *15*, e1804736.
313. Kresse, G.; Hafner, J., *Ab initio* molecular dynamics for liquid metals. *Phys. Rev. B* **1993**, *47*, 558-561.
314. Kresse, G.; Hafner, J., *Ab initio* molecular-dynamics simulation of the liquid-metal-amorphous-semiconductor transition in germanium. *Phys. Rev. B* **1994**, *49*, 14251-14269.

315. Kresse, G.; Furthmüller, J., Efficiency of ab-initio total energy calculations for metals and semiconductors using a plane-wave basis set. *Comput. Mater. Sci.* **1996**, *6*, 15-50.
316. Blochl, P. E., Projector augmented-wave method. *Phys. Rev. B* **1994**, *50*, 17953-17979.
317. Wellendorff, J.; Lundgaard, K. T.; Møgelhøj, A.; Petzold, V.; Landis, D. D.; Nørskov, J. K.; Bligaard, T.; Jacobsen, K. W., Density functionals for surface science: Exchange-correlation model development with Bayesian error estimation. *Phys. Rev. B* **2012**, *85*, 235149.
318. Monkhorst, H. J.; Pack, J. D., Special points for Brillouin-zone integrations. *Phys. Rev. B* **1976**, *13*, 5188-5192.
319. Henkelman, G.; Uberuaga, B. P.; Jónsson, H., A climbing image nudged elastic band method for finding saddle points and minimum energy paths. *J. Chem. Phys.* **2000**, *113*, 9901-9904.
320. Shah, S. A.; Habib, T.; Gao, H.; Gao, P.; Sun, W.; Green, M. J.; Radovic, M., Template-free 3D titanium carbide ($Ti_3C_2T_x$) MXene particles crumpled by capillary forces. *Chem. Commun.* **2017**, *53*, 400-403.
321. Graham, P. M.; Buschhaus, M. S. A.; Baillie, R. A.; Semproni, S. P.; Legzdins, P., Hydroperoxide-Initiated Intramolecular Insertions of NO into Metal–Carbon Bonds. *Organometallics* **2010**, *29*, 5068-5072.
322. Varjas, C. J.; Powell, D. R.; Thomson, R. K., Rapid Access to an Oxido-Alkylidene Complex of Mo(VI). *Organometallics* **2015**, *34*, 4806-4809.
323. Thakur, R.; VahidMohammadi, A.; Moncada, J.; Adams, W. R.; Chi, M.; Tatarchuk, B.; Beidaghi, M.; Carrero, C. A., Insights into the thermal and chemical stability of multilayered V_2CT_x MXene. *Nanoscale* **2019**, *11*, 10716-10726.
324. Saggio, G.; de Mallmann, A.; Maunders, B.; Taoufik, M.; Thivolle-Cazat, J.; Basset, J.-M., Synthesis, Characterization, and Reactivity of the Highly Unsaturated Silica-Supported Trisiloxy Tantalum: $(:SiO)_3Ta^{(III)}$. *Organometallics* **2002**, *21*, 5167-5171.
325. Coperet, C.; Comas-Vives, A.; Conley, M. P.; Estes, D. P.; Fedorov, A.; Mougél, V.; Nagee, H.; Nunez-Zarur, F.; Zhizhko, P. A., Surface Organometallic and Coordination Chemistry toward Single-Site Heterogeneous Catalysts: Strategies, Methods, Structures, and Activities. *Chem. Rev.* **2016**, *116*, 323-421.
326. Steib, M.; Lou, Y.; Jentys, A.; Lercher, J. A., Enhanced Activity in Methane Dry Reforming by Carbon Dioxide Induced Metal-Oxide Interface Restructuring of Nickel/Zirconia. *ChemCatChem* **2017**, *9*, 3809-3813.
327. Theofanidis, S. A.; Batchu, R.; Galvita, V. V.; Poelman, H.; Marin, G. B., Carbon gasification from Fe–Ni catalysts after methane dry reforming. *Appl. Catal., B* **2016**, *185*, 42-55.
328. Medford, A. J.; Vojvodic, A.; Studt, F.; Abild-Pedersen, F.; Nørskov, J. K., Elementary steps of syngas reactions on $Mo_2C(001)$: Adsorption thermochemistry and bond dissociation. *J. Catal.* **2012**, *290*, 108-117.
329. Foppa, L.; Silaghi, M.-C.; Larmier, K.; Comas-Vives, A., Intrinsic reactivity of Ni, Pd and Pt surfaces in dry reforming and competitive reactions: Insights from first principles calculations and microkinetic modeling simulations. *J. Catal.* **2016**, *343*, 196-207.
330. Kunkel, C.; Viñes, F.; Illas, F., Transition metal carbides as novel materials for CO_2 capture, storage, and activation. *Energy Environ. Sci.* **2016**, *9*, 141-144.
331. Asara, G. G.; Ricart, J. M.; Rodriguez, J. A.; Illas, F., Exploring the activity of a novel Au/TiC(001) model catalyst towards CO and CO_2 hydrogenation. *Surf. Sci.* **2015**, *640*, 141-149.

332. Silaghi, M.-C.; Comas-Vives, A.; Copéret, C., CO₂ Activation on Ni/ γ -Al₂O₃ Catalysts by First-Principles Calculations: From Ideal Surfaces to Supported Nanoparticles. *ACS Catal.* **2016**, *6*, 4501-4505.
333. Foppa, L.; Margossian, T.; Kim, S. M.; Muller, C.; Coperet, C.; Larmier, K.; Comas-Vives, A., Contrasting the Role of Ni/Al₂O₃ Interfaces in Water-Gas Shift and Dry Reforming of Methane. *J. Am. Chem. Soc.* **2017**, *139*, 17128-17139.
334. Lam, E.; Corral-Perez, J. J.; Larmier, K.; Noh, G.; Wolf, P.; Comas-Vives, A.; Urakawa, A.; Coperet, C., CO₂ Hydrogenation on Cu/Al₂O₃ : Role of the Metal/Support Interface in Driving Activity and Selectivity of a Bifunctional Catalyst. *Angew. Chem., Int. Ed.* **2019**, *58*, 13989-13996.
335. Posada-Perez, S.; Vines, F.; Ramirez, P. J.; Vidal, A. B.; Rodriguez, J. A.; Illas, F., The bending machine: CO₂ activation and hydrogenation on δ -MoC(001) and β -Mo₂C(001) surfaces. *Phys. Chem. Chem. Phys.* **2014**, *16*, 14912-14921.
336. Damaskinos, C. M.; Vasiliades, M. A.; Efstathiou, A. M., The effect of Ti⁴⁺ dopant in the 5 wt% Ni/Ce_{1-x}Ti_xO_{2- δ} catalyst on the carbon pathways of dry reforming of methane studied by various transient and isotopic techniques. *Appl. Catal., A* **2019**, *579*, 116-129.
337. Rietveld, H. M., Line profiles of neutron powder-diffraction peaks for structure refinement. *Acta Cryst.* **1967**, *22*, 151-152.
338. Teo, B. K., *EXAFS: Basic Principles and Data Analysis*. Springer: Berlin, Heidelberg, 1986, 10.1007/978-3-642-50031-2.
339. van Oversteeg, C. H.; Doan, H. Q.; de Groot, F. M.; Cuk, T., In situ X-ray absorption spectroscopy of transition metal based water oxidation catalysts. *Chem. Soc. Rev.* **2017**, *46*, 102-125.
340. Yao, L.; Wang, Y.; Galvez, M. E.; Hu, C.; Da Costa, P., Ni–Mo₂C supported on alumina as a substitute for Ni–Mo reduced catalysts supported on alumina material for dry reforming of methane. *C. R. Chimie* **2018**, *21*, 247-252.

Curriculum vitae

Alexey Kurlov

Education

- 2014 – 2020** **PhD candidate 2020 at ETH Zürich**
Department of Mechanical and Processing Engineering
Research advisor: Prof. Dr. Christoph R. Müller
- 2010 – 2013** **Master degree at ETH Zürich**
Department of Materials
Major in Materials Analysis and Properties
- 2006 – 2010** **Bachelor degree at Lomonosov MSU**
Material Science Department
Major in Chemistry, Physics and Mechanics of Materials

Publications

- A. Kurlov**, E. B. Deeva, P. M. Abdala, D. Lebedev, A. Tsoukalou, A. Comas-Vives, A. Fedorov, C. R. Müller, Exploiting two-dimensional morphology of molybdenum oxycarbide to enable efficient catalytic dry reforming of methane, *Nat. Commun.*, **2020**, 11, 4920
- A. Kurlov**, A. M. Kierzkowska, T. Huthwelkerb, P. M. Abdala, C. R. Müller, Na₂CO₃-modified CaO-based CO₂ Sorbents: The Effects of Structure and Morphology on CO₂ Uptake, *Phys. Chem. Chem. Phys.*, **2020**, 22, 24697-24703
- A. Kurlov**, X. Huang, E. B. Deeva, P. M. Abdala, A. Fedorov, C. R. Müller, Molybdenum Carbide and Oxycarbide from Carbon-Supported MoO₃ Nanosheets: Phase Evolution and DRM Catalytic Activity Assessed by TEM and *in situ* XANES/XRD Methods, *Nanoscale*, **2020**, 12, 13086-13094
- A. Kurlov**, A. Armutlulu, F. Donat, A. R. Studart, C. R. Müller, CaO-Based CO₂ Sorbents with a Hierarchical Porous Structure Made *via* Microfluidic Droplet Templating, *Ind. Eng. Chem. Res.*, **2020**, 59, 7182–7188
- E. B. Deeva, **A. Kurlov**, P. M. Abdala, D. Lebedev, S. M. Kim, C. P. Gordon, A. Tsoukalou, A. Fedorov, C. R. Müller, *In Situ* XANES/XRD Study of the Structural Stability of Two-Dimensional Molybdenum Carbide Mo₂CT_x: Implications for the Catalytic Activity in the Water–Gas Shift Reaction, *Chem. Mater.*, **2019**, 31, 4505-4513

A. Kurlov, M. Broda, D. Hosseini, S. J. Mitchell, J. Pérez-Ramírez, C. R. Müller, Mechanochemically Activated, Calcium Oxide-Based, Magnesium Oxide-Stabilized Carbon Dioxide Sorbents, *ChemSusChem*, **2016**, 9, 2380-2390

N. S. Yüzbaşı, A. M. Kierzkowska, Q. Imtiaz, P. M. Abdala, **A. Kurlov**, J. L. M. Rupp, C. R. Müller, ZrO₂-Supported Fe₂O₃ for Chemical-Looping-Based Hydrogen Production: Effect of pH on Its Structure and Performance As Probed by X-ray Absorption Spectroscopy and Electrical Conductivity Measurements, *J. Phys. Chem. C*, **2016**, 120, 18977-18985

Q. Imtiaz, **A. Kurlov**, J. L. M. Rupp, C. R. Müller, Highly Efficient Oxygen-Storage Material with Intrinsic Coke Resistance for Chemical Looping Combustion-Based CO₂ Capture, *ChemSusChem*, **2015**, 8, 2055-2065

M. V. F. Schlupp, **A. Kurlov**, J. Hwang, Z. Yáng, M. Döbeli, J. Martynczuk, M. Prestat, J-W. Son, L. J. Gauckler, Gadolinia doped ceria thin films prepared by aerosol assisted chemical vapor deposition and applications in intermediate-temperature solid oxide fuel cells, *Fuel Cells*, **2013**, 13, 658-665

J. Bisschop, **A. Kurlov**, A flow-through method for measuring the dissolution rate of alite and Portland cement clinker, *Cem. Concr. Res.*, **2013**, 51, 47-56

S. Ya. Istomin, **A.V. Kurlov**, S. M. Kazakov, E. V. Antipov, Crystal structure and thermal expansion of LaCr_{1-x}Mg_xO₃, 0 < x ≤ 0.25, *Mat. Res. Bulletin*, **2012**, 47, 1176-1180